



HAL
open science

High-repetition rate CEP-stable few-cycle OPCPA sources in the short wavelength infrared/mid-infrared

Gaëtan Jargot

► **To cite this version:**

Gaëtan Jargot. High-repetition rate CEP-stable few-cycle OPCPA sources in the short wavelength infrared/mid-infrared. Optics [physics.optics]. Université Paris Saclay (COMUE), 2019. English. NNT : 2019SACLO020 . tel-03907316

HAL Id: tel-03907316

<https://pastel.hal.science/tel-03907316>

Submitted on 20 Dec 2022

HAL is a multi-disciplinary open access archive for the deposit and dissemination of scientific research documents, whether they are published or not. The documents may come from teaching and research institutions in France or abroad, or from public or private research centers.

L'archive ouverte pluridisciplinaire **HAL**, est destinée au dépôt et à la diffusion de documents scientifiques de niveau recherche, publiés ou non, émanant des établissements d'enseignement et de recherche français ou étrangers, des laboratoires publics ou privés.

High-repetition rate CEP-stable few-cycle OPCPA sources in the short wave infrared/mid-infrared

Thèse de doctorat de l'Université Paris-Saclay
préparée à Institut d'Optique Graduate School

École doctorale n°572 Ondes et Matière (EDOM)
Spécialité de doctorat: Physique

Thèse présentée et soutenue à Palaiseau, le 19 12 2019, par

Gaëtan Jargot

Composition du Jury :

Aurélie Jullien Chargée de recherche, INPHYNI (Nice)	Rapporteuse
Thibaut Sylvestre Directeur de recherche, FEMTO-ST (Besançon)	Rapporteur
Sophie Kazamias Professeure des universités, LPGP (Orsay)	Examinatrice
Patricia Segonds Professeure des universités, NEEL (Grenoble)	Examinatrice
Marc Hanna Chargé de recherche, LCF (Palaiseau)	Directeur de thèse
Nicolas Forget Directeur R&D, Fastlite (Antibes)	Invité

Contents

Résumé en français	7
Introduction	9
I Fundamentals of ultrafast pulse propagation	13
1 Femtosecond pulses	15
1.1 Pulse description	15
1.2 Time and spectral domain	16
2 Propagation in materials	16
2.1 Propagation equations	16
2.2 Dispersion	19
2.3 First order of spectral phase	20
2.4 Second order of spectral phase	20
2.5 Higher orders of spectral phase	21
2.6 Control of the dispersion	23
2.6.1 Pulse shaper: 4f configuration with a SLM	23
2.6.2 Dazzler	23
3 Second-order nonlinear optics	25
3.1 Description of the polarization for intense fields: nonlinear response	25
3.2 Coupled wave equations for optical parametric amplification	25
3.2.1 Solutions for the coupled wave equations.	26
3.3 Phase matching considerations	27
3.3.1 Birefringent phase matching	27
3.3.2 Angular aspects of phase matching	29
3.3.3 Quasi-phase matching	30
3.3.4 Broadband parametric amplification	31
3.4 Noncollinear parametric amplification	32
3.5 Second Harmonic Generation	33
4 Kerr effect	34
4.1 Self-Phase Modulation	35
4.2 Self-focusing	35
II Yb laser-pumped OPCPA systems and techniques	39
1 OPCPA systems	40
1.1 Pump lasers	40
1.2 Signal generation	42
1.3 Chirped Pulse Amplification (CPA)	44

1.4	Nonlinear crystals	46
1.5	Passive CEP stable systems	47
1.5.1	Definitions	47
1.5.2	CEP characterization	49
1.5.3	Passive CEP stabilization	49
1.5.4	Inter-pulse CEP stabilization	50
1.5.5	Intra-pulse CEP stabilization	51
1.6	State of the art	51
2	Nonlinear compression	53
2.1	Principles	53
2.1.1	Nonlinear compression in wave guides	54
2.1.2	Compression in bulk medium	55
2.1.3	Soliton compression	57
III CEP-stable mid-infrared OPCPA		61
1	Goals and specifications for the mid-IR OPCPA	63
2	First architecture: DFG from a 515 nm pump laser	64
2.1	SHG of the pump laser	66
2.2	Seed generation: supercontinuum generation	67
2.3	DFG stage	69
2.3.1	Numerical simulation	70
2.3.2	Experimental results	71
2.4	Dispersion management	72
2.5	Second amplifier stage	75
2.6	Overall system results and discussions	77
2.6.1	Central wavelength	77
2.6.2	Compressed pulse energy	77
2.6.3	Pulse duration	77
2.6.4	Pulse-to-pulse and long term power stability	79
2.6.5	CEP stability	80
2.6.6	Spatial profile: Strehl ratio	82
2.6.7	Pointing stability	83
2.6.8	Uninterrupted operation	83
2.6.9	Conclusion	83
3	Second architecture: DFG from a 1030 nm pump laser	84
3.1	Seed generation from an all inline DFG scheme	86
3.1.1	Layout	86
3.1.2	Experimental results	87
3.2	First amplifier stage	88
3.3	Dispersion management	89
3.4	Second amplifier	90
3.5	Output measurements and discussion	91
3.5.1	Pulse duration	91
3.5.2	Strehl ratio	91
3.5.3	Pointing stability	93
3.5.4	Energy and CEP stability	93
3.5.5	Conclusion	96

IV Self-compression in a MultiPass Cell	99
1 Introduction	100
2 SWIR OPCPA architecture	101
3 MultiPass Cell concept	102
3.1 Principle	102
3.1.1 B-integral calculation	103
3.2 State of the art	105
4 MPC in anomalous dispersion regime: self-compression regime	105
4.1 Experimental setup	105
4.2 Nonlinear propagation regime	106
4.3 Numerical simulations	106
4.4 Experimental results	108
5 Conclusion	111
Conclusion	115
Bibliography	117

Résumé en français

La génération d'impulsions de quelques cycles optiques stabilisées en CEP dans le moyen infrarouge utilisant la technique d'amplification paramétrique optique (OPCPA) à haut taux de répétition est d'un grand intérêt pour diverses études de dynamiques ultra-brèves de la matière et la génération d'harmonique d'ordre élevé (HHG). En effet l'étude des dynamiques électroniques ainsi que l'étude des rotations moléculaires à une échelle de temps ultra brève et la résolution spatiale plus importante en utilisant de l'imagerie par diffraction cohérente est accessible avec ces sources. Les travaux de cette thèse sont directement inscrits dans ce cadre.

Dans une première partie nous décrivons deux systèmes OPCPA émettant des impulsions dont le spectre est centré à $2.1 \mu\text{m}$ dont la CEP est stabilisée. Le premier système présente une architecture classique de type Mach-Zehnder pour réaliser l'étage de différence de fréquences. Cependant, cette architecture ne permet pas d'obtenir de faibles fluctuations tir-à-tir de CEP au cours du temps. C'est pourquoi nous avons dans un second temps développé une seconde architecture qui permet de s'affranchir du Mach-Zehnder traditionnel pour avoir un étage de différence de fréquences totalement colinéaire. Nous avons ainsi obtenu des impulsions avec des durées de 19.5 fs et des énergies de $31 \mu\text{J}$ opérant à 10 kHz possédant une stabilité en énergie RMS de 0.54% . Ce système se distingue de l'état de l'art par la mise en œuvre d'une technique de différence de fréquences en ligne permettant d'obtenir une stabilité de la CEP tir-à-tir de 107 mrad pendant quatre heures.

La deuxième partie de cette thèse a permis le développement d'un dispositif émettant des impulsions de quelques cycles optiques à $1.55 \mu\text{m}$ opérant à haut taux de répétition (125 kHz). Ce système est le résultat de l'assemblage d'un amplificateur paramétrique optique et d'un système de compression non-linéaire dans une cellule multi-passage. En effet, les systèmes OPCPA ne possèdent pas forcément en sortie des impulsions ultra-brèves suite aux contraintes imposées notamment par les cristaux non-linéaires. Ainsi pour raccourcir la durée des impulsions nous avons utilisé une cellule multi-passage. La propagation non linéaire périodique dans la cellule en régime de dispersion anormale permet une compression solitonique, tout en moyennant les effets spatiaux de la nonlinéarité sur le faisceau. Nous démontrons ainsi la première autocompression en régime de dispersion anormale dans une cellule multi-passage d'impulsions initiales de $19 \mu\text{J}$, 63 fs vers des impulsions en sortie de $14 \mu\text{J}$ et 22 fs .

Enfin, les sources que nous avons développées ont été utilisées pour des expériences de génération d'harmoniques d'ordre élevé dans des gaz et dans les solides. Plusieurs expériences ont pris place lors de cette thèse avec deux équipes du LIDYL (CEA Saclay). Dans un premier temps, nous avons démontré la première génération d'harmonique d'ordre élevé à haut taux de répétition (125 kHz) à $1.55 \mu\text{m}$. Afin de compenser la faible intensité du faisceau laser, nous avons opté pour une focale très courte afin de diminuer le foyer au niveau du jet de gaz. De ce fait, nous avons pu observer des modulations spatio-spectrales induites par cette configuration de focalisation. En effet, en fonction de la pression de gaz utilisée il est possible de favoriser un certain type de trajectoire (longues ou courtes). Ensuite, la deuxième expérience de HHG dans les solides a permis de démontrer le transfert d'un moment angulaire orbitale (AOM) du laser de pompe vers les harmoniques. Pour ce faire, à l'aide de lames d'ondes, un moment angulaire a été fourni au faisceau laser fondamental puis a été focalisé

dans un échantillon afin d'en générer les harmoniques. Deux mesures de profils d'intensité et de front d'onde ont permis d'attester du transfert de l'AOM.

Introduction

Physics is a field that aims at describing and explaining nature. For that purpose, a lot of tools, theories and concepts have been developed since ancient Greece. To properly observe and understand a dynamic phenomenon, experiments in physics must bring a sufficient time resolution. More specifically, this time resolution should be shorter than all the time scales that we wish to observe. Today, the most used tool to achieve a time resolution below the picosecond is laser pulses. Indeed, shortly after the first realization of a laser (light amplification by stimulated emission of radiation) in 1960 by Maiman [Maiman 60], scientists realized that locking the phase of the longitudinal modes of a laser resulted in the generation of picosecond and femtosecond pulses. These sources have been denoted as "ultrafast lasers". A wide variety of applications have been made possible by this technology. Scientific applications include the ultimate metrology of time, high intensity physics, a very broad range of time-resolved spectroscopy techniques allowing the study of ultrafast dynamics in all kinds of physical systems, multiphoton imaging, and the development of secondary sources of radiation (from the THz to the XUV) and particles through, e.g. laser-based electron acceleration. On the more applied side, ultrafast lasers have been used for micromachining in a wide variety of materials including biological tissues to perform eye surgery, glass to fabricate smartphone screens, or large silicon wafers in the semiconductor industry.

During my thesis we focused our work on the generation of extremely short pulsed laser. Since light is an electromagnetic wave with a carrier, we can consider pulses of light which duration is only a few times the carrier period, denoted as "few-cycle pulses". Working with pulsed lasers implies to manage three different key features of the laser source: energy, pulse duration and repetition rate. Average power is directly the amount of energy per pulse multiplied by the repetition rate and the peak power corresponds to the energy divided by the temporal duration.

In terms of laser technology, the first successful few-cycle sources were based on titanium-doped sapphire (Ti:Sa) crystals, generating few-cycle pulses with high energy, with an average power limited to few tens of watts. On the other hand, ytterbium and thulium-based lasers provide high repetition rates and high average powers, with a pulse duration of a few hundreds of femtoseconds. A common feature of both of these laser types is the fixed central wavelength (800 nm for Ti:Sa, 1030 nm for ytterbium-based lasers, and 1950 nm for thulium-based lasers) which is not suitable for some applications.

An alternative way to scale the average power, allow wavelength tunability, and provide high peak powers is to use a technique called optical parametric chirped-pulse amplification (OPCPA). This will be the focus of the work described in this manuscript. The application that triggered this thesis work is high intensity physics, and in particular the process known as high harmonic generation (HHG), both in gases and in dense media. This process was discovered in 1988 [Ferray 88], and generates attosecond (10^{-18} s) pulses in bursts or isolated, at wavelengths that span the EUV to soft X-rays domains (wavelengths between 1 and 50 nm, or photon energies from 20 eV to 1 keV). These attosecond pulses can be further used to probe electron dynamics in atomic or molecular systems, which constitutes today's

frontier of short time scales accessible to physics experiments. HHG also constitutes a tabletop alternative to the only other coherent sources in this frequency range that are both based on large facilities: synchrotron sources and free electron lasers.

HHG is often described using the three step model [Krause 92]. Let us consider one atom irradiated by an ultra-intense laser 1. The three steps are described by:

- (1) An outer shell electron is tunnel-ionized from the atom because the large electric field bends the Coulomb potential sufficiently.
- (2) The now free electron is accelerated by the laser field first away from, then back towards the parent ion.
- (3) The electron recombines with the parent ion emitting an XUV photon.

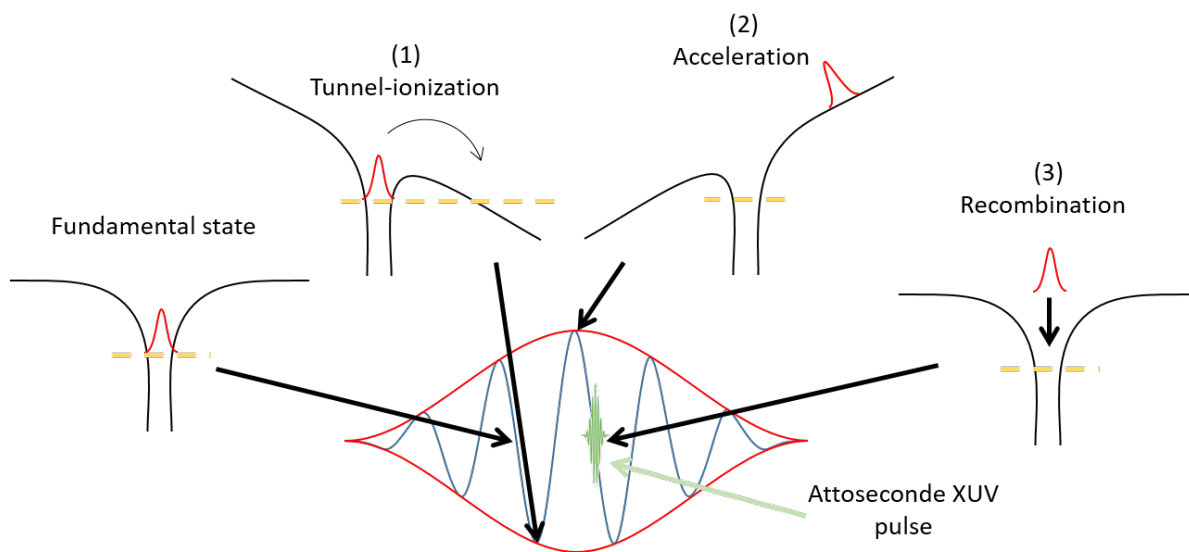


Figure 1 – Three steps model for HHG generation.

From this model, a number of conclusions can be drawn. An XUV pulse of tens to hundreds of attoseconds is emitted at each half-optical cycle of the ultrashort driving laser. As a consequence, the perfect control of the driving pulse at the electric field level is essential to generate attosecond pulses in a controlled manner. The carrier envelope phase (CEP) is the quantity that allows us to control the electric field. Furthermore, the generation of isolated attosecond pulses require a driving pulse with an optical duration of the order of a few optical cycles. The wavelength of the driving laser also plays an important role on the generated XUV pulses. The longer the wavelength, the more kinetic energy the free electron can accumulate before recombination. As a consequence, the cutoff photon energy in the XUV scales as the square of the driver laser wavelength. In solids, the HHG mechanism is more complex owing to the fact that electrons are promoted to upper conduction bands by the electric laser field instead of being considered free from the atomic potential. However, driving HHG in solids with a short pulse duration and long wavelength laser is also of considerable interest because of the larger ponderomotive energy associated with longer wavelengths, like for gases, and because the damage thresholds are typically higher at longer wavelengths. This enables higher overall electric fields in the medium, and therefore stronger effects. In solids, the cutoff XUV photon energy was shown to scale like the wavelength in some cases.

The driving laser wavelength, energy and pulse duration combined with a high repetition rate are the main interests that drove the development of high repetition rate CEP-stable few-cycle OPCPA

sources in the short wavelength infrared (SWIR)/Mid-IR described in this thesis. It is composed of four chapters as follows.

Chapter 1: The first chapter is an introduction to the formalism of femtosecond pulses and their propagation in linear optics. Afterwards, nonlinear propagation with second-order nonlinear effects and the Kerr effect are discussed.

Chapter 2: This chapter describes some technical aspects of ultrafast source design. It is divided into two parts. First, an overview of OPCPA architectures and a brief state of the art is provided. Second, the principles of nonlinear temporal compression are exposed, along with a short state of the art.

Chapter 3: In this chapter we present a Mid-IR OPCPA with features beyond the state of the art. These features are the pulse duration, CEP stability, and energy per pulse. The emphasis is placed on an innovative difference frequency generation (DFG) stage design that allows extreme performances in terms of CEP stability.

Chapter 4: The last chapter presents an ultrashort SWIR OPCPA source. The original contribution in this part is the implementation of a new nonlinear compression setup based on a multipass cell in anomalous dispersion regime, leading to self-compression of the pulses.

This thesis was done in the framework of a collaboration between the laser group at Laboratoire Charles Fabry and the company Fastlite.

Chapter I

Fundamentals of ultrafast pulse propagation

Objectives

This first chapter gives an overlook of ultrashort pulses propagation. We introduce the formalism of femtosecond pulses and how they propagate in the framework of linear optics. Then, nonlinear propagation is discussed starting with second-order non linear optics. Finally a third-order phenomenon, the Kerr effect, is discussed.

Contents

1 Femtosecond pulses	15
1.1 Pulse description	15
1.2 Time and spectral domain	16
2 Propagation in materials	16
2.1 Propagation equations	16
2.2 Dispersion	19
2.3 First order of spectral phase	20
2.4 Second order of spectral phase	20
2.5 Higher orders of spectral phase	21
2.6 Control of the dispersion	23
2.6.1 Pulse shaper: 4f configuration with a SLM	23
2.6.2 Dazzler	23
3 Second-order nonlinear optics	25
3.1 Description of the polarization for intense fields: nonlinear response	25
3.2 Coupled wave equations for optical parametric amplification	25
3.2.1 Solutions for the coupled wave equations.	26
3.3 Phase matching considerations	27
3.3.1 Birefringent phase matching	27
3.3.2 Angular aspects of phase matching	29
3.3.3 Quasi-phase matching	30
3.3.4 Broadband parametric amplification	31
3.4 Noncollinear parametric amplification	32
3.5 Second Harmonic Generation	33

4 Kerr effect	34
4.1 Self-Phase Modulation	35
4.2 Self-focusing	35

1 Femtosecond pulses

1.1 Pulse description

Light pulses are electromagnetic waves and can be entirely described by a real vector quantity $\vec{\mathbf{E}}(r, t)$ space ($r = x, y, z$) and time dependent. To introduce some basic concepts, we consider the temporal dependence of the scalar electric field $\mathbf{E}(t)$, representing one of the components of the electric field. We can describe pulses with relevant physical quantities such as the angular frequency ω_0 and the carrier envelope phase ϕ_{ce} as follows:

$$\mathbf{E}(t) = \Re(E(t)e^{i\omega_0 t + \phi_{ce}}). \quad (\text{I.1})$$

In that case $E(t)$ represents the slowly varying complex envelope modulated by a fast sinusoidal oscillation called the carrier. We define the wavelength λ_0 in vacuum as the spatial period of the carrier by:

$$\lambda_0 = \frac{2\pi c}{\omega_0},$$

where c represents the speed of light in vacuum. We also introduce the optical cycle T :

$$T = \frac{\lambda_0}{c}.$$

During this thesis we predominatly work with three different wavelengths: $1.55 \mu\text{m}$, $2.1 \mu\text{m}$ and $3.1 \mu\text{m}$. The corresponding optical cycles for each wavelength are 5.1 fs, 7 fs and 10.3 fs.

The carrier envelope phase ϕ_{ce} represents the relative position between the carrier wave and the maximum of the envelope. The figure I.1 shows two 10 fs pulses (in blue and orange) with their envelope (dash green line) at a central wavelength of $1.55 \mu\text{m}$.

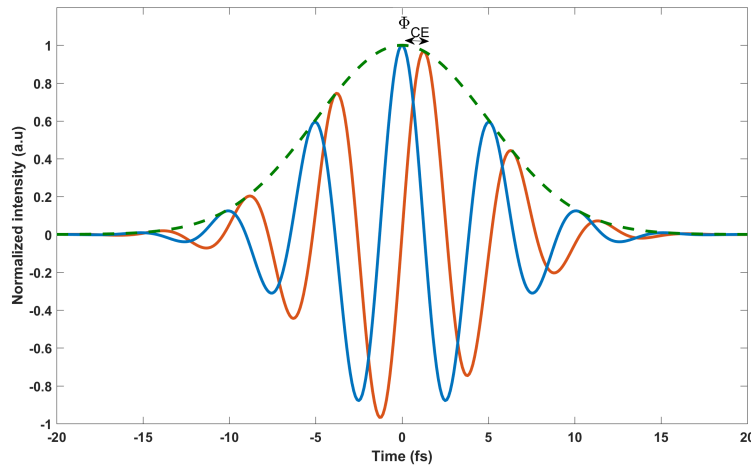


Figure I.1 – Electric fields of two short pulses (10 fs). Both pulses have the same envelope (dash green line) but a different carrier envelope phase offset, $\phi_{ce} = 0$ (solid blue line) and $\phi_{ce} = \frac{3\pi}{2}$ (solid orange line). The central wavelength of these pulses is $1.55 \mu\text{m}$.

1.2 Time and spectral domain

The electric field can be represented in the frequency domain. The complex envelope $E(t)$ in the time domain is connected to $\tilde{E}(\omega)$ in the spectral domain by the Fourier transform:

$$\tilde{E}(\omega) = FT\{E(t)\} = \int_{-\infty}^{+\infty} E(t)e^{i\omega t} dt \quad (\text{I.2})$$

This representation allows us to describe completely the laser pulse. Indeed, based on the spectral intensity and the spectral phase, it is possible to compute the temporal intensity and phase of the pulse. A criterion to determine if a pulse is as short as possible given a spectral intensity is to look at the spectral phase. If the spectral components exhibit a constant or linear phase, the pulse is as short as it can be. The pulse is then said to be Fourier Transformed Limited (FTL).

If the spectral phase varies nonlinearly over the spectrum bandwidth the pulse duration increases, the pulse is chirped. We frequently deal with the spectral and temporal domains, it is convenient to define the time bandwidth product:

$$\Delta t \Delta \nu \geq K.$$

For a Gaussian pulse, and defining Δt and $\Delta \nu$ as Full Widths at Half Maximum (FWHM) in the time and frequency domains, the coefficient K equals 0.44.

This is a useful concept, allowing to translate spectral properties to temporal properties. As an example, in most lab environments, the spectrum is measured in order to aim at a specific pulse duration. Spectral phase management is needed to achieve this targeted value.

2 Propagation in materials

This section presents a discussion on the origin of dispersion in a material and the temporal consequences for the pulses propagating through it. The chromatic dispersion is directly related to the fact that each spectral component of the pulse does not travel at the same speed inside a material. This is due to the fact that the refractive index $n(\lambda)$ of every medium is not constant on the spectral range covered by the pulse. A description of the medium resonances called the Sellmeier equation provides a relationship between a specific material refractive index and the wavelength:

$$n(\lambda)^2 = 1 + \frac{B_1\lambda^2}{\lambda^2 - C_1} + \frac{B_2\lambda^2}{\lambda^2 C_2} + \frac{B_3\lambda^2}{\lambda^2 - C_3}.$$

Where $B_{1,2,3}$ and $C_{1,2,3}$ are experimentally determined coefficients.

2.1 Propagation equations

Maxwell's equations describe every electromagnetic phenomena. These equations describe the evolution of the electric field due to the current and the charge densities. They can be written as follows:

$$\nabla \cdot \vec{\mathbf{D}} = \frac{\rho}{\epsilon_0} \quad (\text{I.3a})$$

$$\nabla \cdot \vec{\mathbf{B}} = 0 \quad (\text{I.3b})$$

$$\nabla \wedge \vec{\mathbf{E}} = -\frac{\partial \vec{\mathbf{B}}}{\partial t} \quad (\text{I.3c})$$

$$\nabla \wedge \vec{\mathbf{H}} = \frac{\partial \vec{\mathbf{D}}}{\partial t} + \vec{\mathbf{J}}. \quad (\text{I.3d})$$

Where \mathbf{E} and \mathbf{H} represent the electric field [V/m] and the magnetic field [A/m], ϵ_0 is the permittivity of vacuum. \mathbf{D} and \mathbf{B} are the electric [C/m²] and magnetic [Wb/m² or Tesla T] flux densities. Moreover, ρ and \mathbf{J} are the volume charge density [C/m³] and the current density [A/m²] of any external charges.

In our case, we consider nonmagnetic materials so a simple relation relates \mathbf{B} and \mathbf{H} :

$$\mathbf{H} = \frac{\mathbf{B}}{\mu_0},$$

where μ_0 is the permeability of vacuum.

Inside a material, an electric-dipole polarization \mathbf{P} occurs when a laser pulse interacts with it, as:

$$\mathbf{D} = \mathbf{E}\epsilon_0 + \mathbf{P},$$

The vector \mathbf{P} fully describes the response of the medium to the incident electric field. Now, we ignore the free charges and currents in the medium and apply the ∇ operator on [I.3c](#). The resulting equation is as follows:

$$\nabla \wedge (\nabla \wedge \mathbf{E}) = \nabla \cdot (\nabla \cdot \mathbf{E}) - \Delta \mathbf{E} = -\frac{1}{c^2} \frac{\partial^2}{\partial t^2} - \frac{1}{\epsilon_0 c^2} \frac{\partial^2 \vec{\mathbf{P}}}{\partial t^2}, \quad (\text{I.4})$$

with $\epsilon_0 \mu_0 c^2 = 1$.

In the equation [I.4](#) we remove the term $\nabla \cdot (\nabla \cdot \mathbf{E})$ because $\nabla \cdot \mathbf{D} = 0$ implies that $\nabla \cdot \mathbf{E} = 0$. The wave equation can be expressed as:

$$\nabla^2 \mathbf{E} + \mu_0 \epsilon_0 \frac{\partial^2 \mathbf{E}}{\partial t^2} = -\mu_0 \frac{\partial^2 \mathbf{P}}{\partial t^2}. \quad (\text{I.5})$$

This equation can be solved for pulse propagation in a medium with both a linear and nonlinear response. To simplify the problem, more approximations are needed. The electric field is assumed to propagate in the z-direction (also called scalar approximation) and is polarized along a constant direction in the plane (xy). Describing the fields as plane waves, the electric field can be written as:

$$E(z, t) = E_0(z, t)e^{i(\omega_0 t - k_0 z)}.$$

In this case, the wave equation can be written as follows:

$$\frac{\partial^2 \mathbf{E}(z, t)}{\partial z^2} + \mu_0 \epsilon_0 \frac{\partial^2 \mathbf{E}(z, t)}{\partial t^2} = -\mu_0 \frac{\partial^2 \mathbf{P}(z, t)}{\partial t^2}. \quad (\text{I.6})$$

The wave vector is defined as:

$$k_0 = \frac{2\pi}{\lambda} n(\omega_0) = \frac{\omega_0}{c_0} n(\omega_0).$$

The same formalism can be used for the polarization fields P :

$$P(z, t) = P(z, t)e^{i(\omega_0 t - k_0 z)}.$$

The electric and polarization fields can be expressed in the Fourier domain:

$$\begin{cases} \tilde{E}(z, \omega) = FT\{E(z, t)\} = \tilde{E}_0(\omega', t)e^{ik_0z}, \\ \tilde{P}(z, \omega) = FT\{P(z, t)\} = \tilde{P}_0(\omega', t)e^{ik_0z}, \end{cases}$$

with $\omega' = \omega - \omega_0$.

As a consequence, equation (I.6) becomes:

$$e^{-ik_0z} \left[\frac{\partial^2 \tilde{E}_0}{\partial z^2} - 2ik_0 \frac{\partial \tilde{E}_0}{\partial z} - \left(k_0^2 - \frac{\omega^2}{c_0^2} \right) \tilde{E}_0 \right] = -\mu_0 \omega^2 \tilde{P}_0 e^{-ik_0z}. \quad (\text{I.7})$$

For weak fields (non-intense), the response of the dielectric medium is linear. The electric field interacts with the dielectric and induces oriented dipoles. The overall electronic distribution is modified and acts as an electric field inside the medium. That macroscopic phenomenon is described by the polarization P with:

$$P_0(\omega) = (\epsilon_r(\omega) - 1)\epsilon_0 E_0(\omega)$$

For now (in the next section a more accurate definition will be given), we introduce the electric susceptibility $\chi^{(1)}(\omega) = \epsilon_r(\omega) - 1$, so:

$$P(\omega) = \chi^{(1)}(\omega)\epsilon_0 E(\omega).$$

Moreover, the refractive index $n(\omega)$ can be defined through:

$$n(\omega) = \sqrt{1 + \chi^{(1)}(\omega)} = \sqrt{\epsilon_r}$$

The frequency dependence of the refractive index is the direct source of dispersion in dielectric material. This feature will be further discussed in the following section.

From the last definition, the polarization can be written as:

$$\tilde{P}_0(\omega', t) = \epsilon_0 [n_0^2(\omega) - 1] \tilde{E}_0(\omega', t) e^{ik_0z}. \quad (\text{I.8})$$

Concerning the slowly varying envelope approximation, the variations of the envelope in space are supposed to be negligible compared to the carrier wavelength so that:

$$\frac{\partial^2 \tilde{E}_0}{\partial z^2} \ll \frac{2\pi}{\lambda_0} \frac{\partial \tilde{E}_0}{\partial z}.$$

In conclusion, the wave equation can be expressed:

$$-2ik_0 \frac{\partial \tilde{E}_0}{\partial z} + \left[k(\omega)^2 - k_0^2 \right] \tilde{E}_0 = 0. (\text{I.9})$$

2.2 Dispersion

The spectrum of the pulse is centered at ω_0 and $n(\omega)$ is slowly varying with the frequency so the difference between k_0 and $k(\omega)$ is small. We can therefore write:

$$k(\omega)^2 - k_0^2 \simeq 2k_0(k(\omega) - k_0).$$

And the propagation equation becomes:

$$\frac{\partial \tilde{E}_0}{\partial z} = -i [k(\omega) - k_0] \tilde{E}_0.$$

We can also Taylor expand $k(\omega)$ as follows:

$$k(\omega) \simeq \sum_{n=0}^{\infty} \frac{k^{(n)}(\omega_0)}{n!} (\omega - \omega_0)^n \simeq k(\omega_0) + \left. \frac{\partial k}{\partial \omega} \right|_{\omega_0} (\omega - \omega_0) + \frac{1}{2} \left. \frac{\partial^2 k}{\partial \omega^2} \right|_{\omega_0} (\omega - \omega_0)^2 + \frac{1}{6} \left. \frac{\partial^3 k}{\partial \omega^3} \right|_{\omega_0} (\omega - \omega_0)^3 + \dots$$

Since each spectral component is affected by a specific value of $n(\omega)$, we can define the phase velocity, which corresponds to the wavefront speed of a single wave by:

$$v_p = \frac{\omega}{k} = \frac{c_0}{n(\omega)}. \quad (\text{I.10})$$

As mentioned above, a laser pulse is described by a product of a carrier with a defined frequency ω_0 propagating at $v_p(\omega_0)$ and an envelope. Since the envelope gathers a lot of frequencies, its propagation cannot be defined by a single phase velocity but rather by the so called group velocity v_g with:

$$v_g = \frac{\partial \omega}{\partial k}. \quad (\text{I.11})$$

Previously, we introduced the CEP which provides the phase difference between the peak of the envelope and the carrier frequency. In pulsed lasers, slippage of the CEP occurs pulse to pulse, and these variations are easily caused by dispersion. Indeed, the envelope ($v_g = \frac{\partial \omega}{\partial k}$) and the carrier wave ($v_p = \frac{\omega}{k} = \frac{c_0}{n(\omega)}$) experience different speeds in material. For few-cycle pulses, the CEP is crucial because each CEP shift will cause a variation in the maximum electric field. This variation is important for many applications.

Group velocity corresponds directly to the first order Taylor expansion term of $k(\omega)$. Another important notion is group-velocity dispersion (GVD), corresponding to the second-order term. Each spectral component has a different group velocity while propagating inside a medium and that stretches the pulse in time:

$$GVD = \left. \frac{\partial^2 k}{\partial \omega^2} \right|_{\omega_0} = \frac{\partial \frac{1}{v_g}}{\partial \omega}. \quad (\text{I.12})$$

The GVD is often expressed in fs^2 . The next section will break down the different orders of spectral phase. Following this, the different methods used to control the dispersion will be discussed.

2.3 First order of spectral phase

Propagation of the pulse inside the dielectric therefore impacts a varying phase shift on each single spectral component of the pulse. This phase shift is given by $\phi(\omega) = k(\omega)z$ and can be written as:

$$\phi(\omega) \simeq \sum_{n=0}^{\infty} \frac{\phi^{(n)}(\omega_0)}{n!} (\omega - \omega_0)^n \simeq \phi(\omega_0) + \left. \frac{\partial \phi}{\partial \omega} \right|_{\omega_0} (\omega - \omega_0) + \frac{1}{2} \left. \frac{\partial^2 \phi}{\partial \omega^2} \right|_{\omega_0} (\omega - \omega_0)^2 + \frac{1}{6} \left. \frac{\partial^3 \phi}{\partial \omega^3} \right|_{\omega_0} (\omega - \omega_0)^3 + \dots$$

The first order of the spectral phase, also called the group delay, represents the time interval that the pulse takes to travel through a certain amount of material (length L). The propagation of the pulse, over a defined length, introduces a delay and can be described as:

$$\tau_g = \left. \frac{\partial \phi}{\partial \omega} \right|_{\omega_0}.$$

The linear part of the spectral phase corresponds to a pure delay, without any deformation of the envelope.

2.4 Second order of spectral phase

The second order of dispersion, as mentioned earlier, has an impact on the pulse duration. The group delay dispersion (GDD) quantifies the stretching factor that the pulse experiences during propagation inside a medium of length L):

$$GDD = GVD \times L = \left. \frac{\partial^2 \phi}{\partial \omega^2} \right|_{\omega_0}. \quad (\text{I.13})$$

Let us describe the effect of GVD on an initially unchirped Gaussian pulse of length τ_p written in the time and spectral domains as:

$$\begin{cases} E(0, t) = E_0 e^{-\frac{t^2}{\tau_p^2}} \\ \tilde{E}(0, \omega) = E_0 \sqrt{2\pi} \tau_p e^{-\frac{\omega^2 \tau_p^2}{2}} \end{cases} \quad (\text{I.14})$$

By inserting this field in equation 2.2 and isolating the GVD effect it can be shown that the output field is given by:

$$E(z, t) = \frac{E_0 \tau_p}{\sqrt{\tau_p^2 + iGDD}} e^{\frac{t^2 \tau_p^2}{2(\tau_p^4 + GDD^2)}} e^{-\frac{i}{2} \frac{t^2 GDD}{(\tau_p^4 + GDD^2)}}.$$

A few comments can be made about this result. First, the amplitude term can be expressed with a new quantity τ_{out} . It represents the pulse duration after propagation in a dielectric:

$$\frac{t^2 \tau_p^2}{2(\tau_p^4 + GDD^2)} = \frac{t^2}{2\tau_{out}^2} \rightarrow \tau_{out} = \tau_p \sqrt{1 + \left(\frac{GDD}{\tau_p^2}\right)^2}.$$

Thus, from this equation, we see that the shorter the pulse, the more sensitive it is to GVD. The phase term, can be rewritten:

$$\Phi(t) = -\frac{t^2 GDD}{2(\tau_p^4 + GDD^2)}.$$

We can define the instantaneous frequency $\omega_i(t)$ by the temporal derivative of the phase with :

$$\omega_i(t) = \frac{d\varphi}{dt} = \omega_0 + \frac{tGDD}{\tau_p^4 + GDD^2}. \quad (I.15)$$

This directly describes the frequency chirp of a pulse. While traveling through a dielectric each spectral component arrives at different times. In that case, the pulse is stretched after propagating inside a medium. By convention, the pulse is up-chirped if ω_i increases during time and the pulse is down-chirped if ω_i decreases during time.

The focus of this thesis is on ultra broadband pulses and higher orders of dispersion need to be considered, as explained in the next section.

2.5 Higher orders of spectral phase

When working with ultra broadband pulses it is often required to consider higher orders of dispersion and break down, in depth, the wave vector. Let us consider the Third Order of Dispersion (TOD), defined as:

$$TOD = \frac{\partial^3 \phi}{\partial \omega^3} \quad (I.16)$$

This order of dispersion results in an asymmetric broadening of the pulse and creates a pattern of interference in the time domain. All dielectric media provide a positive TOD, which is a problem that is faced at the output of a laser chain. Later, we will see some techniques that can be used to compensate the TOD. TOD is often expressed in fs^3 .

We can also define the fourth order of dispersion (FOD) like:

$$FOD = \frac{\partial^4 \phi}{\partial \omega^4}. \quad (I.17)$$

FOD is often expressed in fs^4 . The number of terms that must be taken into account in the Taylor expansion of the phase mostly depends on the considered bandwidth. For extremely short pulses, numerical simulations that take into account the full dispersion are used. To design our ultrafast sources, we mostly consider dispersion up to the third order.

Figure I.2 shows a 20 fs pulse at 1550 nm without any dispersion (a,b) and the corresponding spectrum with its spectral phase. Then in (c,d) we have the pulse after experiencing the GVD corresponding to 500 μm of silicon (1100 fs^2 at 1550 nm). We can clearly see the impact on the temporal shape. We can also observe the parabolic spectral phase. In regions (e,f) we introduced on the pulse TOD corresponding to 5 mm of silicon (this arbitrary number was chosen to emphasize the impact on the temporal structure). The temporal shape shows interferences and the spectral curve has a cubic shape.

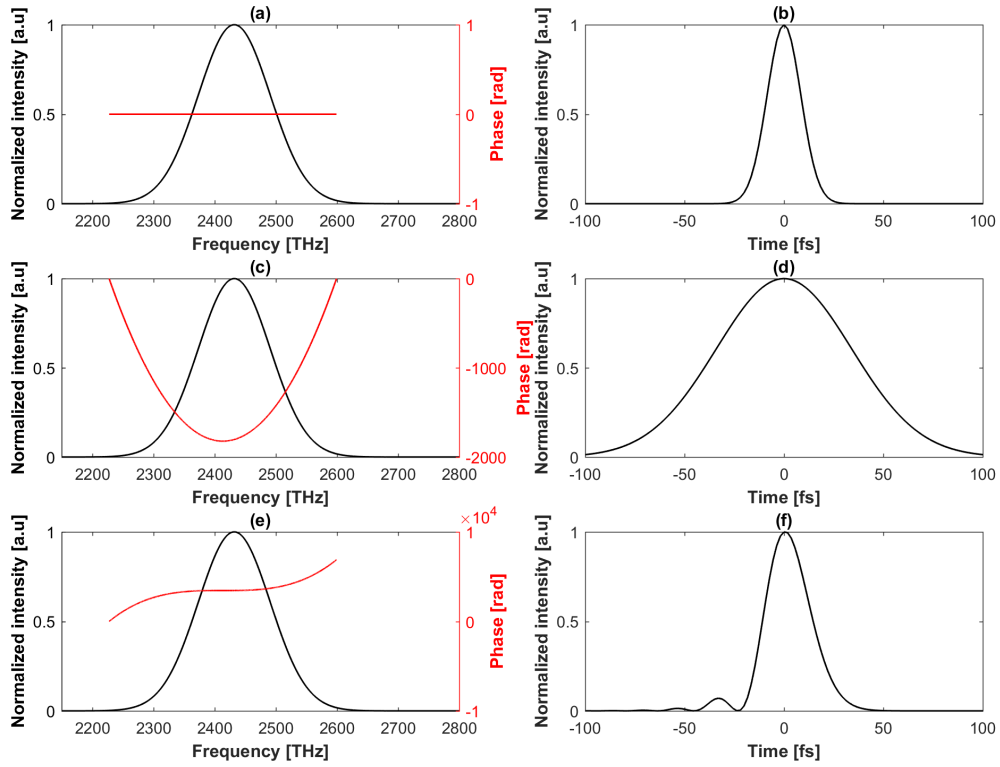


Figure I.2 – (a) Pulse spectrum (black line) centered at 1.55 μm and the spectral phase (red line). (b) Temporal profile for the FTL pulse at 20 fs. (c) Same pulse spectrum as (a) and the spectral phase after propagation of 500 μm of silicon inducing 550 fs^2 of GDD. (d) The corresponding stretched temporal profile of the pulse. (e) Same pulse spectrum than (a) and the spectral phase after propagation of 500 μm of silicon inducing 680 fs^3 of TOD. (f) Temporal profile with temporal modulation.

Table I.1 shows the different orders of dispersion for five materials often used during this thesis: fused silica SiO_2 , silicon Si, YAG (yttrium aluminium garnet), lithium niobate LiNbO_3 and calcium fluoride CaF_2 at three different wavelengths.

To summarize this section we analyzed the impact of the different orders of dispersion upon propagation of an ultrashort pulse in a dielectric media. In the next section we discuss two different methods used to control the spectral phase with active devices.

	λ (μm)	ng	GVD (fs^2)	TOD (fs^3)	FOD (fs^4)
Si	1.5	3.6	1114	1354	3090
	2.1	3.52	766	972	505
	3.1	3.46	501	871	225
SiO ₂	1.5	1.46	-28	153	-505
	2.1	1.46	-123	572	-3010
	3.1	1.49	-614	4360	-41500
YAG	1.5	1.83	13	145	-335
	2.1	1.83	-80	467	-2075
	3.1	1.85	-408	2540	-19750
LiNbO ₃	1.5	2.19	122	360	-475
	2.1	2.26	-74	925	-3600
	3.1	2.27	-675	4575	-35000
CaF ₂	1.5	1.43	2	45	-105
	2.1	1.43	-27	142	-595
	3.1	1.44	-120	669	-4600

Table I.1 – This table gives the different orders of dispersion for fused silica SiO₂, silicon Si, YAG, LiNbO₃ and calcium fluoride CaF₂ at 1.5 μm , 2.1 μm and 3.1 μm .

2.6 Control of the dispersion

Temporal shaping of ultrashort pulses is usually performed in the spectral domain, since direct temporal approaches are limited to bandwidths of around 100 GHz. In the following sections we discuss two different options to temporally shape ultrafast pulses. The first method is based on Fourier optics and a Spatial Light Modulator (SLM) using a 4f scheme. The second method relies on an acousto-optic programmable dispersive filter (AOPDF) [Tournois 97], and is commercialized by Fastlite under the name "Dazzler".

2.6.1 Pulse shaper: 4f configuration with a SLM

The concept is presented in figure (I.3). The beam to be shaped is sent to a diffraction grating that maps each wavelength to an angle. A 2f lens setup, in turn, maps the angle to position in the Fourier plane. As a result, the spectrum is mapped to position in this plane, in which a SLM is placed in order to adjust the phase and amplitude of each spectral component by adjusting the matrix of liquid crystals. A symmetrical setup is used to recombine the spectral components in a single spatial beam at the output.

In the example of figure (I.3), the pulse shaper is used to compress a pulse by carefully adjusting the spectral phase.

2.6.2 Dazzler

The Dazzler is based on an AOPDF, this method was invented by Tournois in the late nineties. The principle is based on the interaction of an acoustic polychromatic wave and a polychromatic light pulse co-propagating inside a birefringent crystal as shown in figure (I.4).

The acoustic wave induces a vibration inside the crystal matrix. Since the acoustic wave is very slow

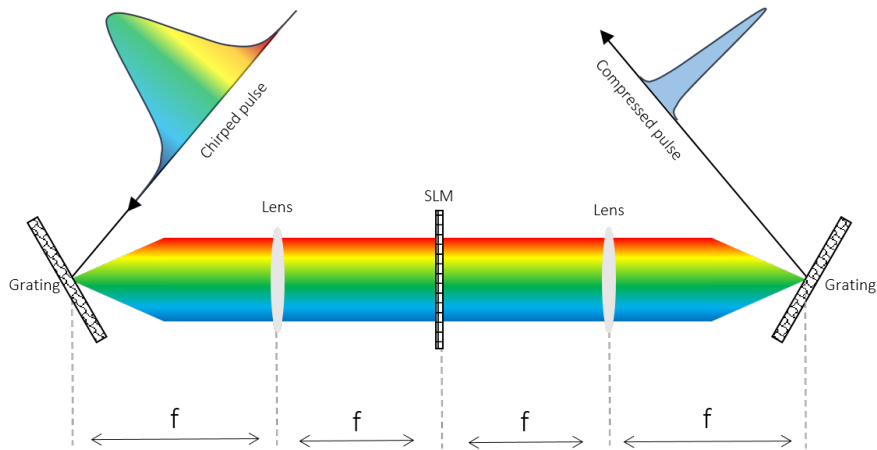


Figure I.3 – This figure shows a 4f scheme with a chirped pulse at the input and compressed at the output. The SLM is the light shaper in that blueprint controlled by a computer.

($v=765$ m/s) compared to the light pulse, the latter one sees it as a stationary wave. The acoustic wave creates an index grating that, if properly phase-matched, can diffract the incoming light pulse on the orthogonal polarization state through birefringence. Since the acoustic wave frequency can be controlled, this interaction can be phase-matched at different locations in the crystal for different input spectral components. This is equivalent to controlling the group delay for each spectral component, thereby allowing pulse shaping. In particular, as mentioned before, the Dazzler can be used to pre-compensate the positive TOD induced by material dispersion.

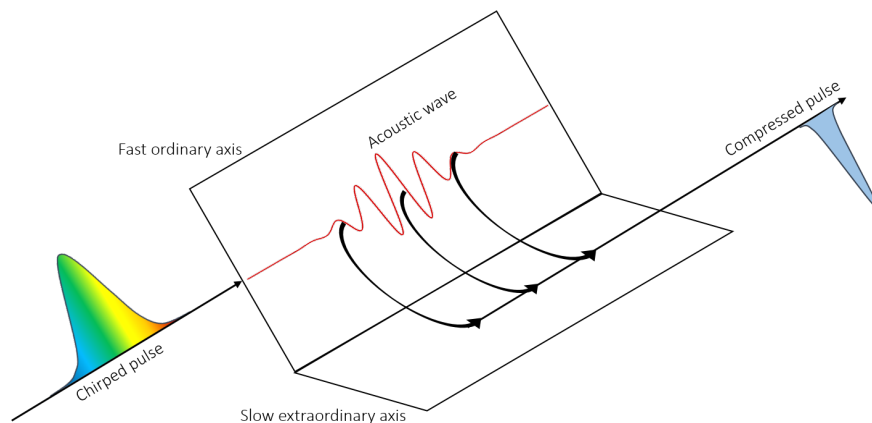


Figure I.4 – AOPDF schematic.

These setups are also able to shape the spectral intensity. During amplification, gain narrowing appears and can be a problem when amplifying the entire spectrum (and preserve the temporal duration). By pre-compensating the gain with losses in the spectrum, it is possible to amplify the entire bandwidth of the laser.

3 Second-order nonlinear optics

3.1 Description of the polarization for intense fields: nonlinear response

For stronger fields, another description for the polarization is needed because the response of the medium deviates from a simple linear response. We will consider fields strong enough to induce non linearity in the medium without generating any ionization process or any damages. A common approach to describe the polarization is to expand \mathbf{P} into a power series of \mathbf{E} :

$$\mathbf{P} = \epsilon_0 \chi^{(1)} \mathbf{E} + \frac{1}{2} \epsilon_0 \chi^{(2)} \mathbf{E}^2 + \dots + \frac{1}{n!} \epsilon_0 \chi^{(n)} \mathbf{E}^n,$$

The quantities χ^n are known as the nonlinear optical susceptibilities of the n^{th} order. We can also introduce $\mathbf{P}^{(L)}$ and $\mathbf{P}^{(NL)}$ like :

$$\mathbf{P} = \mathbf{P}^{(L)} + \mathbf{P}^{(NL)},$$

with :

$$\begin{cases} \mathbf{P}^{(L)} = \epsilon_0 \chi^{(1)} \mathbf{E} \\ \mathbf{P}^{(NL)} = \frac{1}{2} \epsilon_0 \chi^{(2)} \mathbf{E}^2 + \dots + \frac{1}{n!} \epsilon_0 \chi^{(n)} \mathbf{E}^n. \end{cases} \quad (\text{I.18})$$

The derivation of propagation equations for intense fields can be found in ([Shen 84],[Boyd 03]). To consider the dispersion of the medium, the description of the polarization needs to be adjusted: we should take into account the effect of the field at earlier times $t < t_0$. The polarization in that case depends on the history of the field so the first and the second orders of polarization become:

$$\begin{cases} \mathbf{P}^{(1)}(t) = \epsilon_0 \int_{-\infty}^t dt' \chi^{(1)}(t-t') \mathbf{E}(t-t'), \\ \mathbf{P}^{(2)}(t) = \epsilon_0 \int_{-\infty}^t dt' \int_{-\infty}^t dt'' \chi^{(2)}(t', t'') \mathbf{E}(t-t') \mathbf{E}(t-t''). \end{cases} \quad (\text{I.19})$$

Like before, in (1.2), we can Fourier transform the equations to obtain the polarization in the frequency domain:

$$\begin{cases} \mathbf{P}^{(1)}(\omega) = \epsilon_0 \chi^{(1)}(\omega) \mathbf{E}(\omega) \\ \mathbf{P}^{(2)}(\omega_3) = \epsilon_0 \chi^{(2)}(\omega_3, \omega_2, \omega_1) : \mathbf{E}(\omega_1) \mathbf{E}(\omega_2), \end{cases}$$

where, since in this part we focus our attention on the second order of nonlinear optics, we have omitted order 3 and higher for the nonlinear polarization. A new expression of the coupled wave equation can be expressed as follows:

$$\nabla^2 \mathbf{E} - \frac{\epsilon_r}{c^2} \frac{\partial^2 \mathbf{E}}{\partial t^2} = \frac{1}{\epsilon_0 c^2} \frac{\partial^2 \mathbf{P}^{(2)}}{\partial t^2}, \quad (\text{I.20})$$

with $\epsilon_r = \chi^{(1)} + 1$ the relative dielectric constant.

3.2 Coupled wave equations for optical parametric amplification

Optical parametric amplification (OPA) is a three wave mixing process based on $\chi^{(2)}$ nonlinearities. During this process, two optical fields $\omega_1 > \omega_2$ are combined in a nonlinear crystal in order to generate a third wave ω_3 such that:

$$\omega_3 = \omega_1 - \omega_2.$$

The fig (1.5) depicts the process.

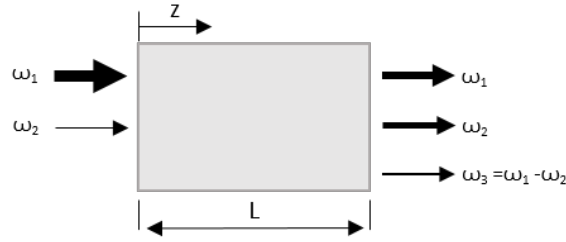


Figure I.5 – Optical parametric amplification process.

Due to the conservation of energy, for each photon of frequency ω_3 and ω_2 generated, one photon of higher energy ω_1 is annihilated. For practical reasons, ω_1 , ω_2 , ω_3 are called the pump (ω_p), signal (ω_s) and idler (ω_i). In this thesis, we will use the convention that the pump has the higher frequency and the idler has the lower one $\omega_p > \omega_s > \omega_i$, regardless of what wave is seeded at the input. Each interacting wave is described as a plane wave:

$$E_i(z, t) = A_i e^{i(k_i z - \omega_i t)} + c.c \quad (\text{I.21})$$

Considering three monochromatic plane waves for the signal, pump and idler and using the propagation equation I.20, it can be established that the three waves evolve according to:

$$\begin{cases} \frac{\partial A_i}{\partial z} = \frac{-2id_{eff}\omega_i^2}{k_i c^2} A_p A_s^* e^{i\Delta k z} \\ \frac{\partial A_p}{\partial z} = \frac{-2id_{eff}\omega_p^2}{k_p c^2} A_s A_i e^{-i\Delta k z} \\ \frac{\partial A_s}{\partial z} = \frac{-2id_{eff}\omega_s^2}{k_s c^2} A_p A_i^* e^{i\Delta k z}. \end{cases} \quad (\text{I.22})$$

with $d_{eff} = \frac{\chi_{eff}}{2}$. $\Delta k = (k_p - k_i - k_s)$, is the wavevector mismatch.

Before solving these equations, we can notice that:

$$\frac{dA_s}{dz} \times A_s^* \times \frac{\omega_i}{n_i} = \frac{dA_i}{dz} \times A_i^* \times \frac{\omega_s}{n_s}. \quad (\text{I.23})$$

Those equations directly represent the fact that the creation of a signal photon is associated to the creation of an idler one.

3.2.1 Solutions for the coupled wave equations.

The general solution of I.22 has been provided in [Armstrong 62]. Here, we neglect the pump depletion, so A_p is constant. We will, in the next chapter, consider a more accurate version with numerical simulations. It can be shown that the idler and the signal evolutions during propagation are given by:

$$A_s(z) = (A_s(0)(ch(\gamma z) - i\frac{\Delta k}{2\gamma}sh(\gamma z) + \frac{2id_{eff}\omega_s^2}{\gamma k_s c^2} A_i^*(0)sh(\gamma z))e^{i\frac{\Delta k}{2}z} \quad (\text{I.24a})$$

$$A_i(z) = (A_i(0)(ch(\gamma z) - i\frac{\Delta k}{2\gamma}sh(\gamma z) + \frac{2id_{eff}\omega_s^2}{\gamma k_s c^2} A_s^*(0)sh(\gamma z))e^{i\frac{\Delta k}{2}z}. \quad (\text{I.24b})$$

Where γ the parametric gain is defined by:

$$\gamma = \sqrt{\frac{2\omega_i\omega_s d_{eff}^2 I_p}{n_s n_p n_i \epsilon_0 c^3} - \left(\frac{\Delta k}{2}\right)^2}. \quad (I.25)$$

The amplification of the signal and the idler, when neglecting the pump depletion and considering zero idler power at the input of the system [Cerullo 03] are given by:

$$\begin{cases} I_s(z) = I_s(0) \left(1 + \frac{\Gamma^2}{\gamma^2} \text{sh}^2(\gamma z)\right) \\ I_i(z) = I_s(0) \frac{\omega_i \Gamma^2}{\omega_s \gamma^2} \text{sh}^2(\gamma z) \end{cases} \quad (I.26)$$

The signal gain is then:

$$G(z) = \frac{I_s(z)}{I_s(0)} = 1 + \frac{\Gamma^2}{\gamma^2} \text{sh}^2(\gamma z). \quad (I.27)$$

If the phase matching is perfect, $\Delta k = 0$ and $\gamma = \Gamma$. Thus, the expression can be simplified in the large gain approximation $\Gamma z \gg 1$:

$$G(z) = \frac{1}{4} e^{2\Gamma z}. \quad (I.28)$$

The approximation is valid for pre-amplifier stages. For example, when the signal is the result of a supercontinuum generation in a medium. Only few nJ are available, in the bandwidth of interest, to seed the amplifier. The gain for this particular case follows an exponential curve. The results also explain why OPAs have very high single pass gains.

Nevertheless, when the energy transfers significantly from the pump to the signal, the approximation $\frac{dA_p}{dz} = 0$ is not valid anymore. The resolution of coupled wave equations [Moses 11], [Armstrong 62] describes the evolution of each wave with a Jacobi elliptic function.

3.3 Phase matching considerations

Phase matching is arranged in two geometries displayed in figure (I.6). In the following section, we discuss collinear phase matching, then expand to describe noncollinear phase matching.

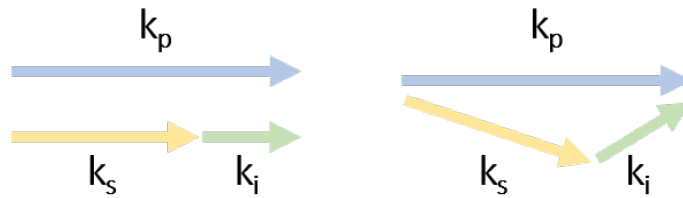


Figure I.6 – Phase matching geometry. Collinear phase matching (left), noncollinear phase matching (right)

3.3.1 Birefringent phase matching

As mentioned before, the phase matching is a very important criterion to optimize the amplification. The phase mismatch is given by:

$$\Delta k = \frac{n_p \omega_p - n_s \omega_s - n_i \omega_i}{c}. \quad (I.29)$$

Given that we must satisfy the conservation of energy and that refractive indices typically increase with frequency in the optical range, it is not possible to obtain phase matching in isotropic crystals. Birefringent crystals are typically used to realize this condition for second order nonlinear processes, by exploiting the polarization-dependent refractive index. By carefully choosing the polarization for the pump and for the signal it is possible to satisfy both the energy and momentum conservation.

For example, BBO is a negative uniaxial crystal ($n_e < n_o$) widely used in laboratories. The crystal structure is such that a direction is preferred and called the optical axis. While propagating co-linear to this axis, the refractive index is invariant regardless of the input polarization. However, beams propagating perpendicular to the optical axis either experience a low refractive index n_e or a high refractive index n_o . In intermediate situations where the beams propagate at an angle θ with respect to the optical axis, the effective extraordinary index can be adjusted between the ordinary and extraordinary values.

Two different types of phase matching are available for uniaxial crystals called type I (idler and signal pulses have the same polarization orthogonal to pump pulse) and type II (idler and signal pulses have orthogonal polarization). In table (I.2) these configurations are summarized.

Table I.2 – Type I and type II phase matching configurations for uniaxial crystals.

	positive uniaxial	negative uniaxial
Type I	$n_{op}\omega_p = n_{es}\omega_s + n_{ei}\omega_i$	$n_{ep}\omega_p = n_{os}\omega_s + n_{oi}\omega_i$
Type II	$n_{op}\omega_p = n_{os}\omega_s + n_{ei}\omega_i$	$n_{ep}\omega_p = n_{os}\omega_s + n_{ei}\omega_i$
	$n_{op}\omega_p = n_{es}\omega_s + n_{oi}\omega_i$	$n_{ep}\omega_p = n_{es}\omega_s + n_{oi}\omega_i$

Once each polarization is chosen, it is important to adjust, very precisely, each refractive index seen by the beams. The ordinary index is constant regardless of the beam propagation direction, which is not the case for the extraordinary index. To adjust the phase matching, it is possible to adjust the amplified wavelength by changing the crystal orientation with respect to the the extraordinary axis. Experimentally, we adjust the angle θ made by the optical axis and the wave vector as seen on figure I.7. The refractive index experienced by the extraordinary axis can be tuned continuously between n_e ($\theta = \pi/2$) and n_o ($\theta = 0$).

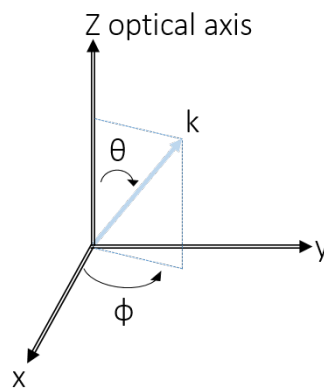


Figure I.7 – Definition of phase matching angles in uniaxial birefringent crystals.

3.3.2 Angular aspects of phase matching

The extraordinary index angular dependence is given by:

$$\frac{1}{n_e^2(\theta)} = \frac{\cos^2(\theta)}{n_o^2} + \frac{\sin^2(\theta)}{n_e^2} \quad (\text{I.30})$$

Angular phase matching is limited by two factors. First, the laser is a Gaussian beam with a finite diameter focused into the crystal (to reach the desired peak intensity in order to trigger an efficient conversion). So each beam presents some angular dispersion. Since the index seen by the extraordinary polarization is angular dependent, that leads to a decrease of the conversion efficiency [Barnes 76]. We can define the angular acceptance $\Delta\Theta$ corresponding to an angle where $\Delta k = \pi$. The angular acceptance is inversely proportional to the crystal length.

Walk-off

On another hand, the walk-off angle also decreases the conversion efficiency. Inside the crystal, the energy direction is dictated by the Poynting vector $\vec{P} = \vec{E} \wedge \vec{B}$. The wave vector and the Poynting vector generate an angle ρ or walk-off angle given by:

$$\rho = \arctan\left[\tan \theta \frac{1 - \frac{n_e^2}{n_o^2}}{\frac{n_e^2}{n_o^2} + \tan^2 \theta}\right]. \quad (\text{I.31})$$

When the phase matching angle is different from 0 or $\frac{\pi}{2}$, ρ is different from zero. As a consequence the ordinary and extraordinary beams do not propagate along the same direction and progressively separate, as show in fig(I.8). If we consider w_0 the diameter of the beams, we can define the interaction length of the two beams L_{w0} after which the two beams are not interacting anymore by the effect of the walk-off by:

$$L_{w0} = \frac{w_0}{\tan \rho}. \quad (\text{I.32})$$

Depending of the length of the crystal, the walk-off of the beams causes the decrease of the efficiency and can also manifest as a spatial deformation that will induce elliptical beams at the output.

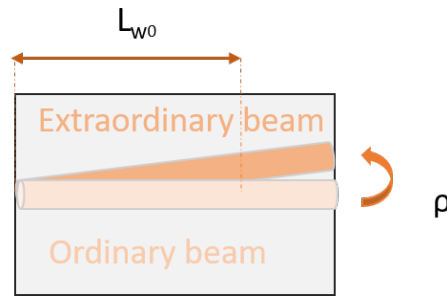


Figure I.8 – Walk-off angle in a birefringent crystal.

3.3.3 Quasi-phase matching

The quasi-phase matching (QPM) principle was proposed in the early sixties [Armstrong 62], but has been implemented almost thirty years later [Lim 89] due to some manufacturing process issues. The idea is to counterbalance the periodic effect of the imperfect phase matching by directly shaping the nonlinear coefficient of the material figure (I.9).

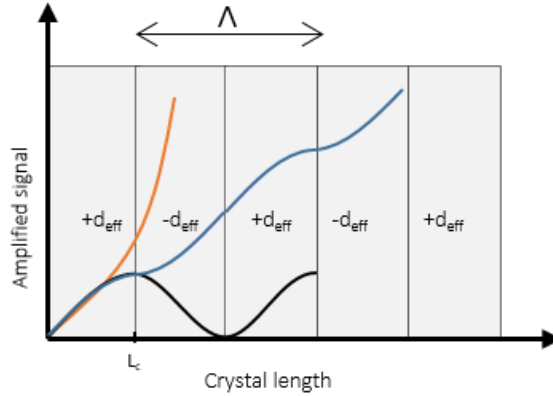


Figure I.9 – Gain comparison as a function of the length of the nonlinear crystal, for a phase matched interaction (orange line), without any phase matching (black line) and by using QPM (blue line).

In the case of perfect phase matching, the gain follows an exponential law (equation I.28). But, without any phase matching, the gain follows a periodical law where the half period is named the coherence length $L_c = \frac{1}{\Gamma}$. During propagation inside the crystal, the gain increases until a maximum obtained at L_c . Then, back conversion occurs (from the signal and the idler to the pump) until $2L_c$.

The QPM technique consists in inverting the sign of the nonlinear coefficient d_{eff} at every L_c in order to keep the gain growing during propagation. Consequently, at each position, in the crystal we have constructive interferences to increase the gain. The phase matching condition changes a little bit because we need to take into account the spatial inversion of the non linearities:

$$\Delta k = k_p - k_s - k_i - \frac{2\pi}{\Lambda} \quad (\text{I.33})$$

The inversion of d_{eff} can be done in ferroelectrics applying a large electric field with isolating masks with a period of $\Lambda = 2L_c$. The order of magnitude of Λ is typically few microns. The applied field is maintained for a few milliseconds, causing permanent poling. Once this periodicity is established inside the crystal, it is still possible to adjust the phase matching with the temperature. One big advantage of this technique is that it grants access to the largest d_{eff} coefficients, including for interaction where all the waves are polarized along the same direction. For example periodically poled Lithium Niobate (PPLN) has d_{eff} of 14 pm/V. Another advantage is the non existence of the walkoff. There are two other different types of PPLN which are the fanout PPLN and the so called chirped PPLN, displayed in figure (I.10).

For the fanout PPLN, the poling period changes across the transverse axis of the propagation beam. These types of crystals are used to implement tunability in the system. And when we look at the chirped PPLN, the period changes along the axis of the propagation beam. These crystals are used to increase the overall phase matching bandwidth and create ultra broadband pulses. However, there are at least two downsides associated to the use of periodically poled crystals. First, the transverse size (the height) is limited by the method used for the polling. A very strong electric field can be applied

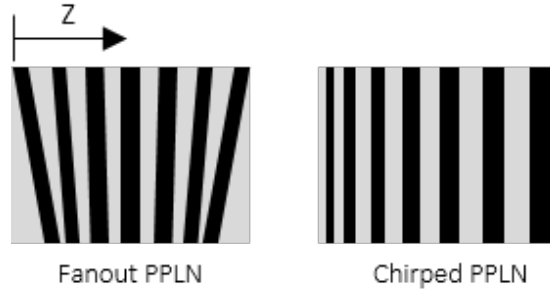


Figure I.10 – Blueprints of a fanout and a chirped PPLN.

on the crystals, but the penetration depth is still limited. In practice this limits the useable transverse size of the crystal to a few mm, thereby limiting the energy scaling of systems in which these crystals are used. Another disadvantage is the price compared to usual bulk crystals.

3.3.4 Broadband parametric amplification

Group velocity effects

Dealing with ultrashort pulses, we need to take into account the broad spectrum and in particular the group velocities v_g . It can be shown [Boyd 03] that the coupled wave equations then become:

$$(I.34) \quad \left\{ \begin{array}{l} \frac{\partial A_i}{\partial z} + \frac{1}{v_{gi}} \frac{\partial A_i}{\partial t} = \frac{i\omega_i d_{eff}}{cn_i} A_s^* A_p e^{i\Delta kz} \\ \frac{\partial A_s}{\partial z} + \frac{1}{v_{gs}} \frac{\partial A_s}{\partial t} = \frac{i\omega_s d_{eff}}{cn_s} A_i^* A_p e^{i\Delta kz} \\ \frac{\partial A_p}{\partial z} + \frac{1}{v_{gp}} \frac{\partial A_p}{\partial t} = \frac{i\omega_p d_{eff}}{cn_p} A_s A_i e^{-i\Delta kz} \end{array} \right.$$

Generally we re-write the equation with the change of variable $\tau = t - \frac{z}{v_{gp}}$, so now the temporal reference corresponds to the pump pulse:

$$(I.35) \quad \left\{ \begin{array}{l} \frac{\partial A_i}{\partial z} + \left(\frac{1}{v_{gi}} - \frac{1}{v_{gp}}\right) \frac{\partial A_i}{\partial \tau} = \frac{i\omega_i d_{eff}}{cn_i} A_s^* A_p e^{i\Delta kz} \\ \frac{\partial A_s}{\partial z} + \left(\frac{1}{v_{gs}} - \frac{1}{v_{gp}}\right) \frac{\partial A_s}{\partial \tau} = \frac{i\omega_s d_{eff}}{cn_s} A_i^* A_p e^{i\Delta kz} \\ \frac{\partial A_p}{\partial z} = \frac{i\omega_p d_{eff}}{cn_p} A_s A_i e^{-i\Delta kz} \end{array} \right.$$

These equations point out the fact that one of the most important parameters of the amplification of femtosecond pulses is the difference between the group velocity between the different beams GVM (Group Velocity Mismatch). First, the GVM between the pump and the signal causes them to gradually slip upon propagation in the crystal. Similarly to L_{w0} the distance where both beams do not overlap anymore due to the *walk-off*, we can define the interaction length L_{GVM} where the pump and the signal do not overlap in the time domain. If $\delta_{j,p} = \frac{1}{v_{gj}} - \frac{1}{v_{gp}}$ is the GVM between the signal (or idler)

and the pump and τ_p is the duration of the pump then:

$$L_{GVM} = \min\left(\frac{\tau_p}{\delta_{ip}}, \frac{\tau_p}{\delta_{sp}}\right). \quad (I.36)$$

The direct consequence is that the shorter the pulses are, the shorter the crystal needs to be. The effect is related to dispersion of the materials and has nothing to do with the nonlinearities induced in it. It is useful to consider two cases, when the product $\delta_{ip}\delta_{sp}$ is either positive or negative. For the first case when $\delta_{ip}\delta_{sp} > 0$, the idler and the signal get separated from the pump in the same direction, so the gain is provided only when $L < L_{GVM}$. But if $\delta_{ip}\delta_{sp} < 0$ the gain is still occurring for long crystals: since the idler and the signal are shifted temporally in opposite directions, the pump is continuously turned into new signal/idler photon pairs.

Spectral acceptance

Since indices of refraction are a function of optical frequency, phase matching is only achieved at one given wavelength for the signal. This limits the amplification of short pulses that necessarily exhibit broad spectral bandwidth. Similarly to the concept of angular acceptance, we can define a bandwidth for the signal over which the phase mismatch is kept below $\Delta k < \pi$. Like for spectral acceptance, this bandwidth is inversely proportional to the crystal length.

3.4 Noncollinear parametric amplification

To achieve wider phase matching bandwidths, a noncollinear geometry can be used as shown in figure (I.11).

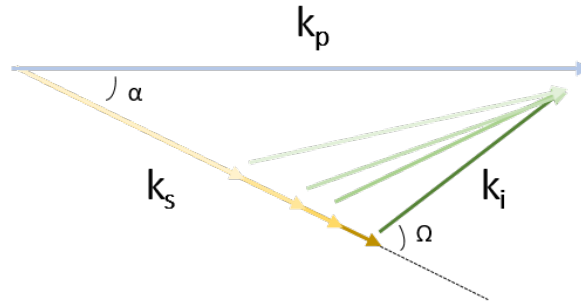


Figure I.11 – Noncollinear phase matching for OPA. α is the noncollinear angle between the pump and the signal. Ω is the frequency-dependent angle between the signal and the idler which achieves phase matching.

From figure (I.11) phase matching can be decomposed into perpendicular and parallel vector with respect to the signal beam:

$$\begin{cases} k_p \cos \alpha = k_s + k_i \cos \Omega \\ k_p \sin \alpha = k_i \sin \Omega \end{cases} \quad (I.37)$$

After Taylor expansion of both expressions and simplification using trigonometric identities, a simple expression for group velocities is obtained:

$$v_{gs} = v_{gi} \cos \Omega. \quad (I.38)$$

For some values of the angle Ω , the idler and the signal experience the same group velocity, therefore allowing amplification of a broad spectrum as shown in figure (I.12).

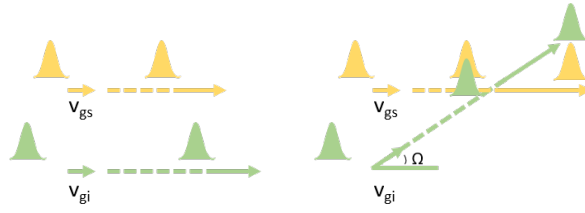


Figure I.12 – Temporal evolution between signal and idler beams in a collinear geometry (left) and in a noncollinear geometry (right).

Nevertheless, when using noncollinear amplification, the beam that is not seeded is angularly dispersed, and thus harder to use. This can prevent simultaneous use of the signal and the idler at the output.

3.5 Second Harmonic Generation

In this section we present the description of the second harmonic generation (SHG) process depicted in figure (I.13), where second-order nonlinearities are used to generate an optical beam at twice the frequency of the input beam.

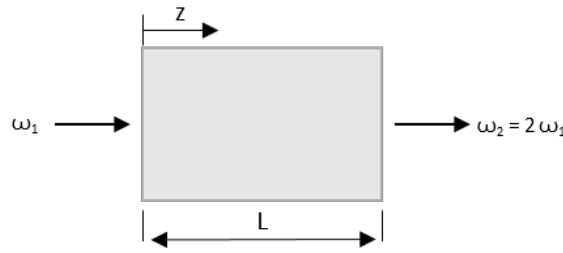


Figure I.13 – SHG process.

When we look at the total electric field within the medium we have:

$$E(z, t) = E_1(z, t) + E_2(z, t). \quad (\text{I.39})$$

Where:

$$\begin{cases} E_1 = A_1 e^{i(\omega_1 t - k_1 z)} + c.c \\ E_2 = A_2 e^{i(\omega_2 t - k_2 z)} + c.c \end{cases}$$

E_2 has twice the frequency of E_1 . With all approximations done before for the polarization field and the wave equation, we find [Boyd 03]:

$$\frac{\partial A_1}{\partial z} = \frac{2i\omega_1^2 d_{eff}}{k_1 c^2} A_2 A_1^* e^{i\Delta k z} \quad (\text{I.40})$$

and

$$\frac{\partial A_2}{\partial z} = \frac{2i\omega_2^2 d_{eff}}{k_2 c^2} A_1^2 e^{i\Delta k z} \quad (\text{I.41})$$

with $\Delta k = 2k_1 - k_2$.

In figure (I.14), what is being depicted is the phase matching angle for type I SHG of a signal as a function of wavelength in a BBO ($\beta - BaB_2O_4$) crystal. In chapter 3 these calculations will be relevant, since we will convert a femtosecond laser at 1030 nm to 515 nm. With the first graph on the left, we notice that our crystal needs to be cut at an angle of 23.4° in order to phase match the process. The second graph on the left shows the two refractive indices.

We now describe a class of third-order nonlinear effects that will be useful to understand the development of pulse compression systems in chapter 4.

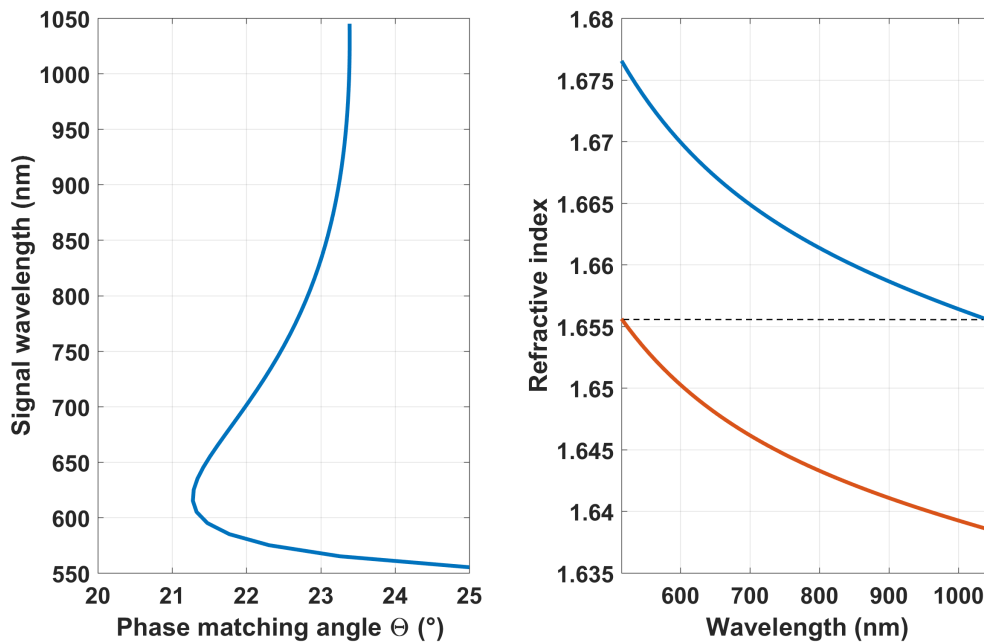


Figure I.14 – Phase matching angle in a BBO crystal (left), refractive index differences (right), ordinary refractive index (blue) and extraordinary refractive index (orange) for $\Theta=23.4^\circ$.

4 Kerr effect

The Kerr effect is a nonlinearity of third order. Its effects can be described by considering that the refractive index n of the medium is modified locally and instantaneously by an optical wave with intensity I . A nonlinear refractive index n_2 appears and the refractive index can be written as follows:

$$n = n_0 + n_2 I, \quad (\text{I.42})$$

where $n_2 = \frac{3}{8n_0} \Re(\chi^{(3)})$.

The intensity dependence of the refractive index will have two main impact on pulses. First, in the time domain, a nonlinear phase shift occurs called Self-Phase Modulation (SPM). The phase shift can be used to induce spectral broadening. Second, in the space domain, a convergent lens is induced and leads to self-focusing. Both of these effects can have desired and undesired consequences on the laser beam. These effects are discussed in the following sections.

4.1 Self-Phase Modulation

SPM is often used to compress pulses in the time domain. Indeed, some applications require very short pulses that might not be easily available from common ultrafast sources, and a post compression setup is needed to shorten the pulses (this part will be discussed in chapter 4). This setup is based on SPM and chirp compensation.

Propagation in a medium exhibiting solely SPM can be described by the following equation:

$$\frac{\partial A}{\partial z} = i\gamma_{SPM}A|A|^2.$$

Where γ_{SPM} is given by:

$$\gamma_{SPM} = \frac{n_2\omega_0}{cA_{eff}}, \quad (I.43)$$

where A_{eff} represents the effective mode area of the beam, equal to πw^2 for a Gaussian beam of waist w . In this equation the complex amplitude A is normalized so that $|A|^2$ is the optical power carried by the beam. The solution to this partial differential equation is simply given by:

$$A(z, t) = A(0, t)e^{i\gamma_{SPM}P(0,t)z}.$$

With this solution we notice that in the temporal domain the profile is not impacted, only the phase is changing. That leads to a change of the spectral phase. In order to look at the evolution of the spectrum, we must analyze the instantaneous optical frequency $\Omega(t)$.

$$\Omega(t) = \frac{d}{dt}(\omega_0 t + \gamma_{SPM}P(z, t)z) = \omega + \delta\omega. \quad (I.44)$$

It becomes evident that the generated frequencies are given by the time derivative of the intensity. The leading ledge of the pulse gives rise to a red shift (lower frequencies), on the other hand the trailing edge causes blue shifts (higher frequencies).

A parallel can be made here: when a pulse is propagating linearly inside a media, it is chirped due to the second order of dispersion but its spectrum remains the same. However, when a pulse experiences SPM, its spectra is broadened but the pulse keeps the same time duration.

To quantify the nonlinearity of the propagation over a length L , the B integral is often used. It is given by the nonlinear phase accumulated in the temporal center of the pulse where the peak power is the highest:

$$B = \int_0^L \gamma_{SPM}P_{peak}(z)dz. \quad (I.45)$$

It can be shown, as illustrated in figure I.15, that the spectral broadening of an initially unchirped pulse is proportional to the B integral [Agrawal 06].

4.2 Self-focusing

Self-focusing is the spatial manifestation of the Kerr effect. Since the local index is proportional to the intensity in the plane transverse to propagation, a Kerr medium is equivalent to a positive lens for a Gaussian beam.

Then, if the Kerr lens is too important, the beam can self-focus inside the medium and severely damage it. This phenomenon appears when the critical power P_{crit} is overcome, for a Gaussian beam it is defined as:

$$P_{crit} = \frac{\lambda^2}{8n_0n_2}. \quad (I.46)$$

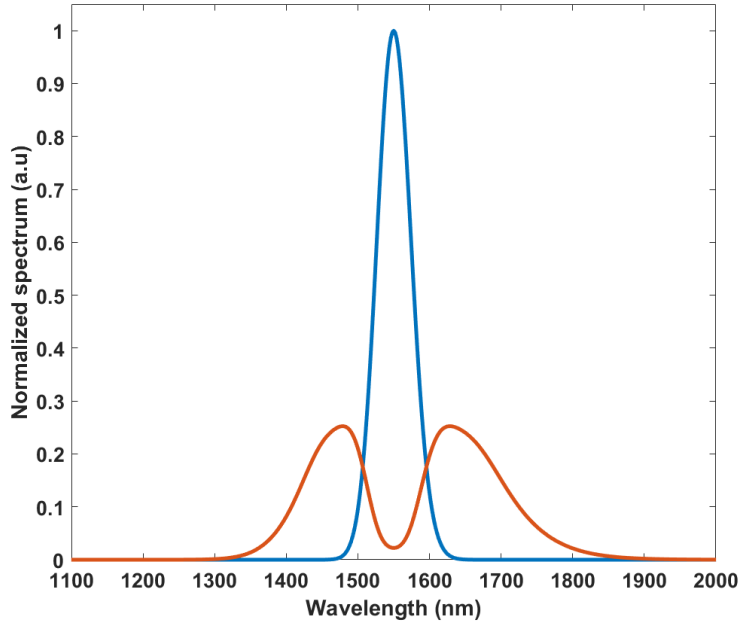


Figure I.15 – Input of an unchirped 60 fs pulse spectrum centered at $1.55 \mu\text{m}$ (blue) with $19 \mu\text{J}$ of energy. Same pulse after propagating in 1 cm of fused silica (orange). The radius of the beam is $150 \mu\text{m}$ and the non linear refractive index of the material is $2.7 \times 10^{-20} \text{ m}^2 \cdot \text{W}^{-1}$. The B integral is 1.5π rad.

To prevent any damages due to self-focusing, we can introduce two parameters: f_{Kerr} is the focal length of the lens induced by the Kerr effect while z_{sf} is the length of the medium that corresponds to the catastrophic collapse of the beam [Boyd 03].

$$\begin{cases} f_{Kerr} = \frac{\pi\omega^4}{4n_2dP_{peak}} \\ z_{sf} = \frac{2n_0\omega^2}{\lambda\sqrt{\frac{P_{peak}}{P_{crit}} - 1}} \end{cases} \quad (\text{I.47})$$

These two parameters give us a good estimation for the propagation of an intense beam and any beam divergence due to the Kerr lens. The figure (I.16) shows us the impact of the spatial Kerr effect on a beam. The first diagram (a) shows directly that we need to consider the spatial Kerr effect on the divergence of our optical system. The second diagram (b) illustrates the catastrophic collapse of the beam inside the material.

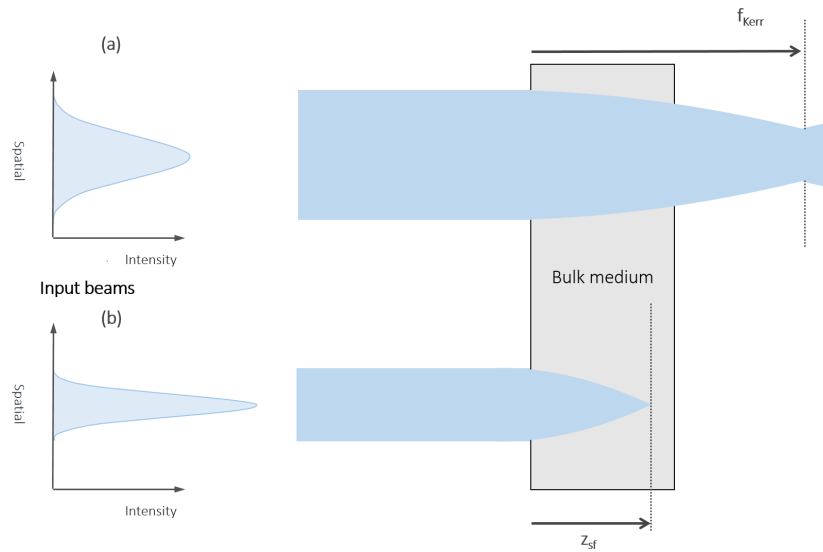


Figure I.16 – (a) The Kerr lens focal lens is longer than the medium length, so the beam is focused after the medium. (b) The self focusing distance is shorter than the medium length, so self collapse occurs and destroys it.

Conclusion

In this chapter, we discussed linear and nonlinear propagation of ultrashort pulses. We have seen that second-order nonlinear optics can be used to amplify and convert the optical frequency of ultrashort pulses. Linear effects such as dispersion can limit the efficiency of these processes. Third-order non-linearity can be used to broaden the spectrum of femtosecond pulses, hence reducing their duration if the spectral phase can be compensated. The Kerr effect also imposes a limitation to the peak power that can be launched into a material due to self-focusing. In the next chapter, these fundamentals effects will be considered as tools to engineer ultrafast laser sources.

Chapter II

Yb laser-pumped OPCPA systems and techniques

Objectives

This chapter is devoted to more technical aspects of ultrafast source design, and is composed of two parts. In the first part, we give an overview on OPCPA architectures used during this thesis and describe each subsystem. Then a state of the art of these sources is presented. Secondly, the nonlinear compression principle is presented, also with a brief state of the art.

Contents

1 OPCPA systems	40
1.1 Pump lasers	40
1.2 Signal generation	42
1.3 Chirped Pulse Amplification (CPA)	44
1.4 Nonlinear crystals	46
1.5 Passive CEP stable systems	47
1.5.1 Definitions	47
1.5.2 CEP characterization	49
1.5.3 Passive CEP stabilization	49
1.5.4 Inter-pulse CEP stabilization	50
1.5.5 Intra-pulse CEP stabilization	51
1.6 State of the art	51
2 Nonlinear compression	53
2.1 Principles	53
2.1.1 Nonlinear compression in wave guides	54
2.1.2 Compression in bulk medium	55
2.1.3 Soliton compression	57

1 OPCPA systems

OPCPA sources are unique tools in ultrafast optics. Their main advantages include an availability at wavelengths from the UV to the MIR, a high contrast and potentially very short pulse durations. Although a large variety of architectures have been developed in the last 25 years, the current trend is to use Yb-based lasers as a pump, and to generate and synchronize the signal optically. We now detail this architecture used in this thesis. It relies on the principle shown in figure (II.1).

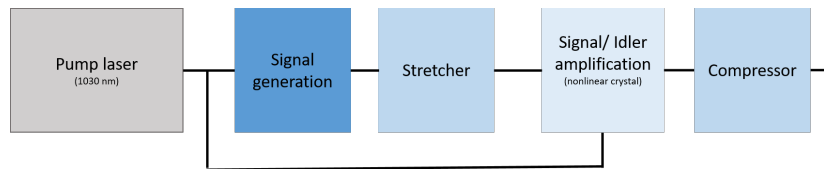


Figure II.1 – From left to right, pump laser emits pulses at 1030 nm, signal is generated via supercontinuum generation (SCG). Signal is then stretched and amplified in a nonlinear crystal. At the output, a compressor is used to compress the amplified signal close to its FTL.

First, a pump laser emits ultrashort pulses (from 300 fs to 900 fs) at 1030 nm. These sources, based on ytterbium-doped materials, are described in the next section.

Then, the generation of the signal is studied. It is generated via SCG from a small portion of the energy provided by the pump laser. Thus, optical synchronization is obtained directly from this method [Van de Walle 16], no electronics synchronization is required. A simple delay line is required to adjust the temporal overlap of both pulses inside the amplification medium, active stabilization is not required.

After, the Chirp Pulse Amplification (CPA) technique is introduced and explained. Benefits of this scheme are presented. In particular we explain our choices on stretchers and compressors in the systems developed during this thesis.

The following section is dedicated to nonlinear crystals. We explain our choices about nonlinear crystals used in our systems, that involve transparency windows, phase matching and nonlinear coefficients. To conclude, technical aspects of CEP characterization are explained, and passive CEP stabilization by difference frequency generation (DFG) is described. Finally, a few references typical from the current state of the art of such systems are shortly described.

1.1 Pump lasers

Since the 1990s lasers based on Ti:Sa crystals are the workhorse of ultrashort optics, characterized by a bandwidth that allows pulses below 20 fs with several mJ energy. These lasers are limited in average power to around 10-50 W by thermal problems induced by a high quantum defect inside the crystal as shown in figure (II.2).

During the last two decades, ytterbium-doped material-based lasers have emerged [Paschotta 97]. Compactness, reliability and high average power have made them dominant, in particular for industrial applications. Their thermal management is facilitated by the low quantum defect, as depicted figure (II.3) (taken from [Paschotta 97]). As a consequence these lasers can emit average power up to 1 kW in the femtoseconde regime using the fiber geometry [Muller 16], the thin disk geometry [Nubbemeyer 17] and the slab geometry [Russbuedt 10].

First, fiber-based Yb systems benefit from the potential for integration of fiber-based technology. Nevertheless, the energy per pulse is limited by the small area of the fiber core. When peak power increases, some detrimental nonlinear effects can appear in the fiber during amplification. To solve those

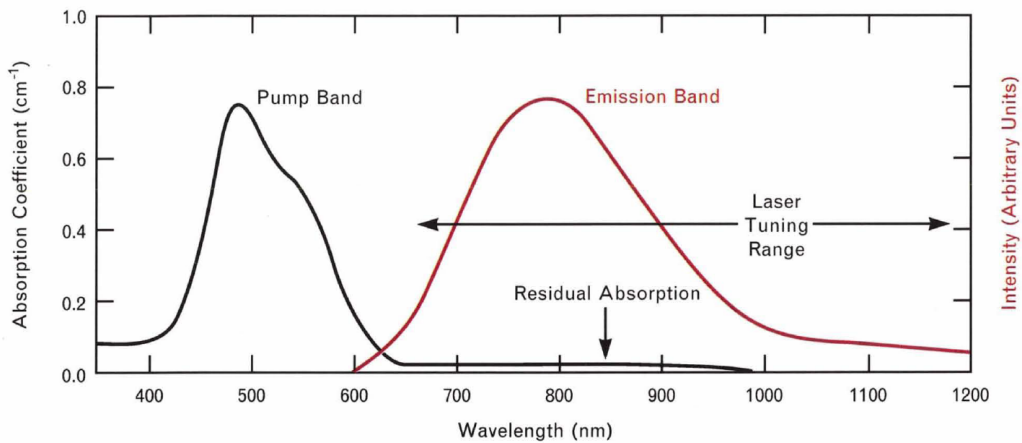


Figure II.2 – Emission and absorption bands of Ti:Sa [Wall 90].

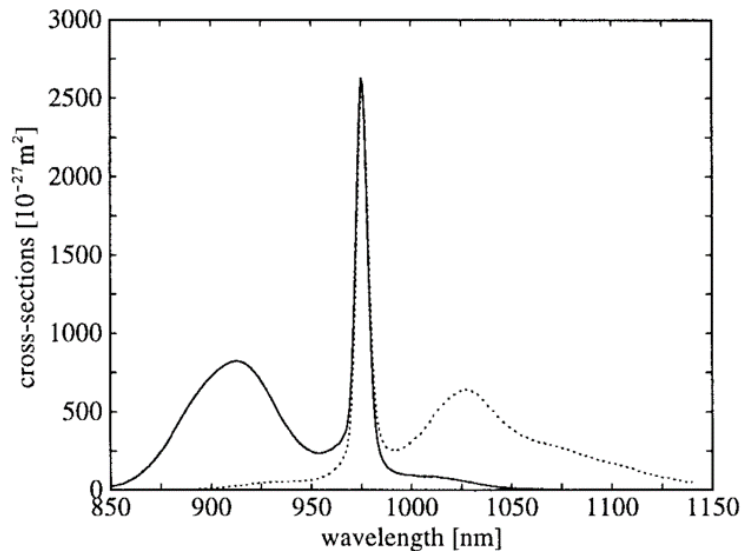


Figure II.3 – Absorption (solid) and emission (dotted) cross sections of Yb in germanosilicate glass [Paschotta 97].

problems, a lot of efforts to increase fiber diameters while retaining a single transverse mode (from $7\ \mu\text{m}$ to $100\ \mu\text{m}$ due to new manufacturing techniques) have been made. Also, the CPA [Strickland 85] architecture (developed in the next section) allows ytterbium doped fiber systems to produce hundreds of μJ of energy, up to 2 mJ [Eidam 11]. Coherent combining can also be used to increase the pulse energy to 10 mJ [Kienel 16].

An alternative to ytterbium-doped fiber amplifiers is thin-disk ytterbium-doped YAG laser amplifiers invented in 1994 by Giesen et al. [Giesen 94]. The general layout of thin-disk-based architectures is shown in figure (II.4) taken from [Saraceno 19]. The gain medium is very thin and shaped like a disk. It has a very large diameter compared to its thickness. The back side of the disk is coated by a highly reflective coating (for the appropriate wavelengths) and the front side is coated with an anti-reflection coating. Back side of the disk is in contact with a heatsink. In that way the medium is water-cooled very efficiently. The thin-gain medium necessitates a clever pump recycling optical system.

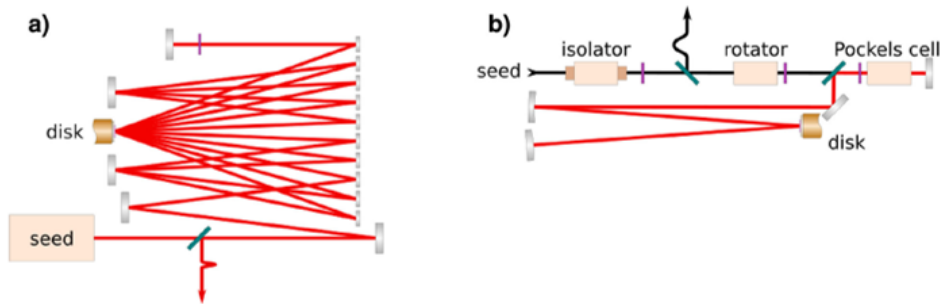


Figure II.4 – Schematics of a thin-disk laser amplifier. a) Multi-pass amplifier b) regenerative amplifier [Saraceno 19].

For multi-pass thin-disk amplifiers depicted in figure (II.4a), an array of mirrors allows the geometrical folding of the seed beam to the disk. In the regenerative configuration shown in figure (II.4b) multipass through the gain medium is obtained by controlling the polarization and therefore the number of passes inside the cavity with a Pockels cell. When the pulse is strongly amplified, the pulse is ejected outside the cavity. Such systems can deliver powers up to 1 kW with pulse durations around 1 ps [Nubbemeyer 17].

During this thesis we use two commercial laser sources: first, an ytterbium doped fiber laser (Tangerine, Amplitude Laser) that delivers pulses with 400 fs duration and 400 μJ at a repetition rate of 125 kHz. Second we developed another OPCPA pumped by a thin disk laser (Dira, TRUMPF) that delivers pulses with 800 fs duration and an energy of 500 μJ at a repetition rate of 10 kHz.

1.2 Signal generation

One fundamental element of an OPCPA source architecture is the generation of a signal or idler seed, that needs to be synchronized with the pump laser. When the pump laser delivers short enough pulses, it is possible to do so via supercontinuum generation. This has been recognized since the nineties [Reed 94] with Ti:Sa lasers. The SCG from Yb-doped lasers has also been studied more recently by different teams [Bradler 14, de Walle 15].

The phenomenon of supercontinuum generation results in spectral broadening of an incoming fs pulses over up to several octaves. This effect was observed for the first time in 1970 by Alfano and Shapiro [Alfano 70]. They used a 530 nm laser with 5 mJ and 4-8 ps duration pulses focused in a borosilicate (BK-7) glass. The output spectrum was observed to spread over the whole visible, giving it its other name: white-light generation (WLG). This phenomenon is also observed and studied in optical fibers for various applications [Dudley 06], such as spectroscopy or pulse compression.

SCG is the outcome of high peak power pulse propagation, with a large number of nonlinear and linear effects being involved. In bulk media, SPM, self focusing, Raman scattering and ionization trigger the WLG process. In our case, this is a good starting point for our broadband OPAs, because it will provide a coherent broadband pulse that is optically synchronized with the pump. For all of these reasons, we use during this thesis this same scheme to generate our broadband seed for our systems.

Several questions must be answered:

- What parameters control the output WL spectrum?
- What type of crystals do we need to use?

In one of the developed OPCPA, we will want to generate our seed around $1.5 \mu\text{m}$. A good candidate for our experiments seems to be YAG (Yttrium aluminum garnet) crystals. Indeed, this crystal is transparent at these wavelengths and damage threshold is high, around 20 GW/cm^2 .

Self-focusing plays an important role during the WLG process. We saw that for a Gaussian beam the refractive index changes and acts like a convergent lens (Kerr lens). If the critical power is overcome, the beam focuses inside the medium. That effect leads to the creation of plasma in the crystal. This partial ionization of the medium generates the inverse effect of the Kerr-lens, the beam then defocuses due to the free electrons in the medium. These two effects can combine and result in the generation of a so-called filament associated with the SCG phenomenon. As the intensity is increased, another regime is observed corresponding to the multi-filament regime. In that case, the filamentation regime is reached in different points inside the medium and generates several filaments. Each filament generates a new source and interferes with the next one.

We focus our experimental condition on the single-filamentation regime. A picture in figure (II.5) shows the white-light generation in the single filamentation regime in a 10 mm YAG crystal.

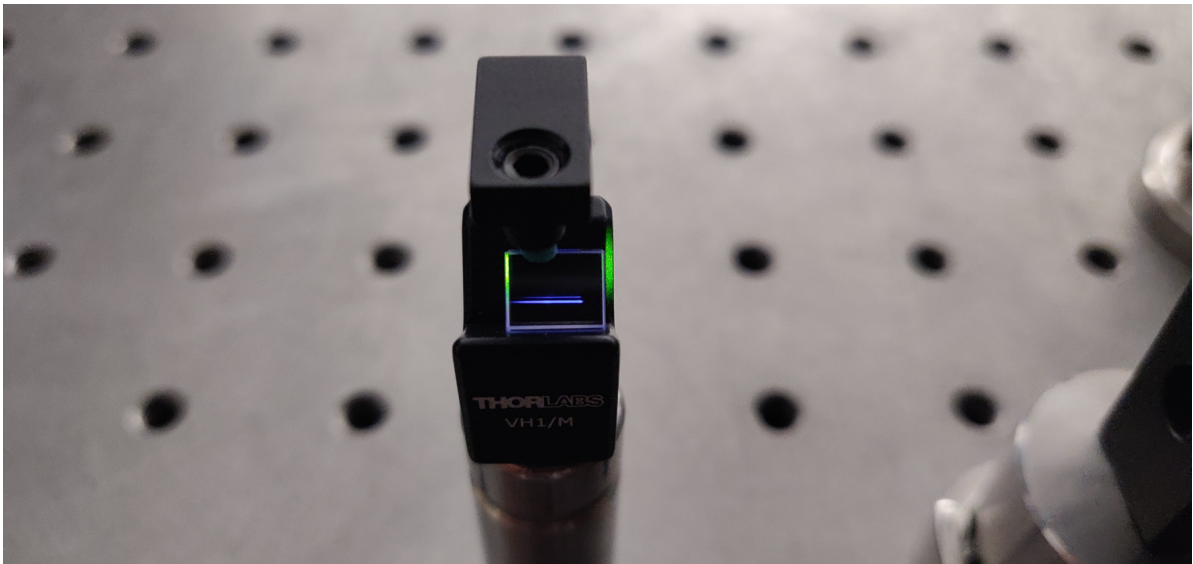


Figure II.5 – Picture of a white-light generation in a 10 mm YAG crystal.

A lot of different input parameters play a role in SCG, and the final operation point is often the result of experimental tests in a given situation. However some general considerations can be followed. The central wavelength determines the starting point from where the spectrum starts to broaden. The broadening is asymmetrical, in our case for the OPCPAs that we built, the pump wavelength is in the normal dispersion regime. The extension to shorter wavelengths reaches a limit. Broadening towards short wavelengths is related to plasma generation and limited by the bandgap energy. This sets the maximum broadening for a given crystal. In YAG the bottom limit is around 480 nm [Bradler 09].

Pulse duration has also a big impact on the WLG process. In particular, the spectral broadening is easier to obtain for shorter pulses. As pulse duration increase, the threshold for WLG approaches the damage threshold. As far as energy per pulse is concerned, a sufficient peak power is necessary (in the femtosecond regime, typically we use few μJ). The generated spectrum is also very sensitive to the input pulse energy. The crystal choice is related to damage threshold, transparency range, nonlinear coefficients, band gap energy and zero dispersion wavelength.

The last important parameter is the focal lens used to focus inside the crystal. Experimentally, [Jukna 14] shows the influence of the focal lens on spectral broadening. The longer the lens, the fur-

ther the extension in the infrared. The tradeoff here is to use higher energy per pulse to compensate the decrease of the peak intensity and still reach the filamentation regime while remaining below damage threshold.

On figure (II.6) three SC spectra filtered with a short pass filter (at 1350 nm) in a 10 mm long YAG crystal are shown. To obtain these spectra, we used an Yb-doped fiber amplifier with a 125 kHz repetition rate and a pulse duration of 400 fs. Here, we cut off the visible part first because we are not interested in those wavelengths, and want to avoid saturation of our spectrometer (NIRQuest512-2.5, Ocean optics).

We can clearly notice the influence of the focal length and the input energy. For the same focal length (blue and orange), with different energies, the more energetic pulse spreads more toward the infrared part of the spectrum. The central wavelength shifts a little toward higher wavelengths. And for a longer focal length and higher energy, the central wavelength is shifted to higher wavelengths. We clearly see that the whole SWIR wavelength range is accessible, allowing a great freedom for OPCPA system design.

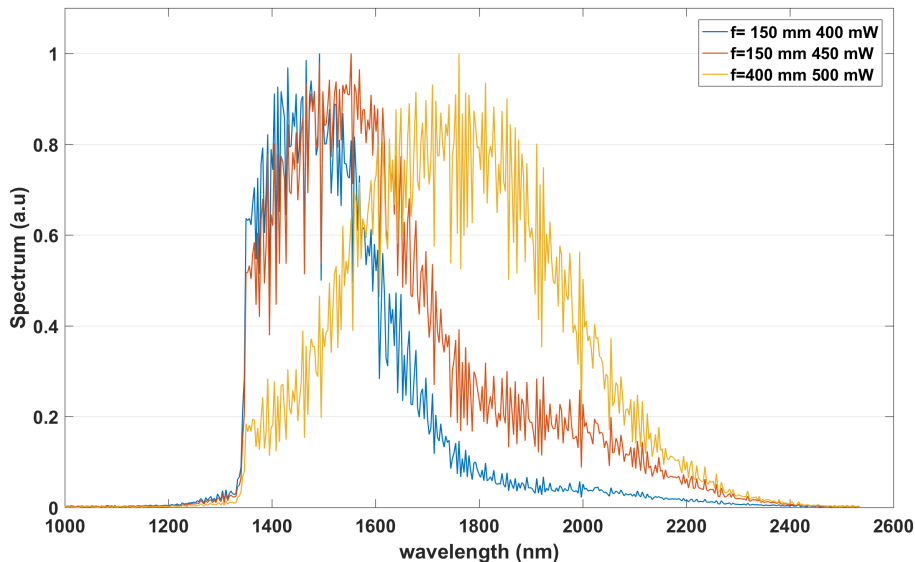


Figure II.6 – Three supercontinua spectra filtered with a short pass filter at 1350 nm in a 10 mm YAG crystal with (blue) a focal length of 150 mm and 400 mW, with (orange) a focal length of 150 and 450 mW and with (yellow) a focal length of 400 mm and 500 mW.

1.3 Chirped Pulse Amplification (CPA)

The Chirped Pulse Amplification (CPA) technique was introduced in 1985 by Strickland and Mourou [Strickland 85] and made possible to increase the pulse peak power at the output of ultrafast lasers by several orders of magnitude (figure (II.7), from [Roso 17]).

The CPA scheme uses the properties of dispersion (presented in chapter 1) in order to overcome the limitations of amplification. The CPA principle is shown figure (II.8). This process is divided in three steps, stretching, amplification and compression of the pulse. First, the pulse is short and presents a relatively high peak power. Sending the pulse directly into the amplification medium can cause optical damages. The pulse is stretched in time, and as a consequence, the peak power decreases by several

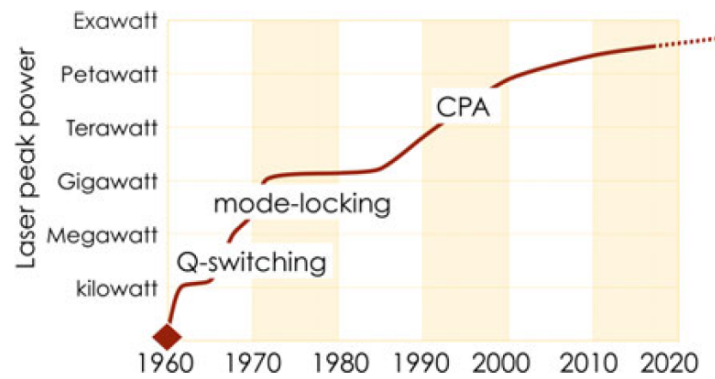


Figure II.7 – Evolution of peak power from 1960 to nowadays.

order of magnitude. The stretching ratio depends on the type of laser chain and the type of stretcher used. The pulse is then amplified. Finally, the dispersion added in the first step is compensated in the compressor at the output of the laser chain.

As an example, in Ti:Sa lasers, the input pulse is 20 fs long with a nJ energy level. It is stretched to 200 ps and amplified to the mJ level. And then at the output, the pulse is compressed back to its original temporal duration.

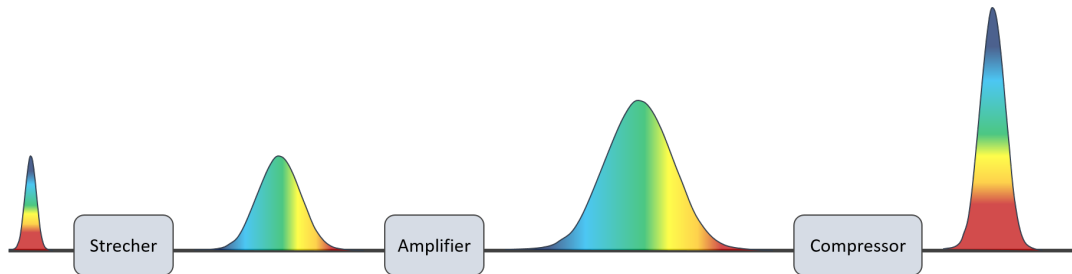


Figure II.8 – Chirped pulse amplification scheme.

The OPA and CPA techniques are often used in conjunction, resulting in the moniker Optical Parametric Chirped Pulse Amplification (OPCPA). In these systems, CPA is used as a way to match the signal/idler pulse duration to the pump pulse duration, rather than, or in addition to manage the peak power.

We have seen that the seed is produced via WLG. Since we produce ultrashort SWIR pulses around 60 fs, we need to take into account that the pump laser emits pulses around few hundreds of femtoseconds. In order to maximize the temporal overlap in the nonlinear medium between the pump and the signal, we stretch the signal. In our system we use the dispersion properties of bulk materials to stretch the seed. This is possible because of the small amounts of stretching needed. As an example, for the signal at $1.5 \mu\text{m}$ we can use a plate of silicon with positive dispersion ($3333 \text{ fs}^2/\text{mm}$). The whole setup will be detailed in chapter 4.

To compress the pulses, we also use bulk materials with the opposite sign of dispersion. For the previous example we use fused silica (SiO_2) that exhibits anomalous dispersion ($-28 \text{ fs}^2/\text{mm}$) in that wavelength region. Since the idler beam is generated with a chirp opposite to the signal, normal dis-

person is required to compress it in this example. As tabulated in table (I.1) silicon exhibits normal dispersion at 3.1 μm and can be used to compress the idler.

1.4 Nonlinear crystals

There is a plethora of nonlinear crystals, during this thesis we only use a few of them. Their choice depends on various characteristics such as transparency domain, nonlinear coefficient, phase-matching type, damage threshold. Table (II.1) gives an overview of nonlinear crystals for broadband generation in the Mid-IR (from [Pires 15]).

<i>Mid-IR non linear crystals</i>	<i>Transparency range (μm)</i>	<i>d_{eff} (pm/V)</i>
Oxide crystals		
KNO (KNbO ₃)	0.4 – 4.5	8
KTA (KTiOAsO ₄)	0.4 – 4	2.1
KTP (KTiOPO ₄)	0.4 – 4.5	2.3
LIO (LiIO ₃)	0.3 – 6	2
LNO (LiNbO ₃)	0.3 – 5.5	4
MgO: PPLN (MgO:LiNbO ₃)	0.3 – 5.5	14
LTO (LiTaO ₃)	0.3 – 5.5	7
LBO (LiB ₃ O ₅)	0.16 – 2.6	4.4
BBO (β -BaB ₂ O ₄)	0.41 – 3.5	2
Non-oxide crystals		
AGS (AgGaS ₂)	0.5 – 1.3	23
AGSe (AgGaSe ₂)	0.7 – 18	41
CSP (CdSiP ₂)	0.7 – 9	85
GaSe	0.7 – 18	54
HGS (HgGaS ₄)	0.5 – 13	31
LGS (LiGaS ₂)	0.3 – 11	10
LGSe (LiGaSe ₂)	0.4 – 13	18
LIS (LiInS ₂)	0.4 – 12	16
LISe (LiInSe ₂)	0.5 – 12	10
ZGP (ZnGeP ₂)	2 – 11	75

Table II.1 – Overview of nonlinear crystals for Mid-IR parametric amplifications.

These crystals are separated in two categories, oxide and non-oxide crystals. Non-oxide crystals have transparency range up to 20 μm . They are complex inorganic crystals, in general they require more complex growth processes which lead to the increase of the defects and cause residual losses. Nonetheless, big improvements in terms of crystal quality have been achieved in the last two decades. During this thesis we focus our work on the SWIR and Mid-IR wavelength regions (up to 3.1 μm). We use four oxide crystals in our different setups which are BBO, LBO, PPLN and KTA crystals.

We used BBO crystals in two different parts in the OPCPA system described in chapter 3. First, we use it to generate the second harmonic (515 nm) of the pump laser at 1030 nm. Phase matching curves are shown in chapter 1. We also use it as a DFG crystal in order to generate a CEP stable idler at 2.1 μm , by mixing a 675 nm pulse and a 1030 nm pulse. LBO crystal is used in order to generate an idler at 2.1 μm by mixing a 515 nm pulse and a 682 nm pulse.

We use a KTA crystal in a non-collinear geometry as the last amplification stage of the system presented in chapter 4 in order to transfer the energy from the pump at 1030 nm to the signal at 1550 nm (in

a low gain configuration).

Finally, we used PPLN crystals in a lot of different places in our systems due to its very broadband amplification and high nonlinear coefficient. Its only drawback is the fact that detrimental parasitic effects such as photorefractive effect or green-induced infrared absorption [Baudisch 14] limit the average power that can be handled in these crystals.

1.5 Passive CEP stable systems

The control of CEP has become a key feature for ultrashort lasers in particular few-cycle sources used in attosecond science. Indeed, due to the wide range of applications for ultrafast lasers, the degree of control over all parameters of the pulses has increased. A lot of well-established methods for pulse diagnostics are used in most systems. They allow the characterization of the pulse duration and of the spectral phase by for example using a second harmonic generation frequency resolved optical gating [Trebino 97] (SHG FROG). These characterizations are exhaustive for describing non linear phenomena in the perturbative regime ($I < 10^{13} \text{W/cm}^2$).

Nevertheless, for strong field applications, such as HHG, that are ultimately determined by the oscillating electric field, more detailed degree of control on pulses is needed. These processes are triggered by ultra intense lasers, meaning that the pulse energy increases and the pulse duration decreases. At a certain point it is relevant to consider the varying electric field instead of the envelope. Recent breakthrough in laser technologies gave rise to ultrashort system approaching the few-cycle regime with pulse duration of 4 fs at 800 nm [Bohle 14] and 6.8 fs at $1.03 \mu\text{m}$ [Lavenu 19]. Depending on the relative bandwidth of the pulse $\Delta\omega_0$, the carrier can oscillate only a few times during the pulse envelope. A precise control of the electric field and the maximum of the envelope is therefore needed to perform strong field experiments. The parameter that defines the shift between the maximum of the envelope and the main peak of the electric field is the CEP.

1.5.1 Definitions

In the first chapter we defined CEP and showed in figure (II) the difference of the CEP on two ultrashort pulses. From there, when we consider ultrashort pulses, the carrier of the electric field of these pulses has to be taken into account. When the pulse has an arbitrary ϕ_{CE} at a given position, then propagates in a medium, we introduced in the first chapter that the envelope is traveling with a group velocity v_g and the carrier propagates with a phase velocity v_ϕ . As it propagates in a medium, the pulse CEP is modified according to:

$$\Delta\phi_{CEP}(z) = \omega_0 z \left(\frac{1}{v_g(\omega_0)} - \frac{1}{v_p(\omega_0)} \right), \quad (\text{II.1})$$

showing that a slip occurs linearly with the distance of propagation. As an example, let us consider a pulse around $2.1 \mu\text{m}$ and the effect on CEP shift while propagating in the air and in calcium fluoride. The chromatic dispersion in the air and CaF_2 is respectively $-3.3365\text{e-}7 \mu\text{m}^{-1}$ and $-5.2352\text{e-}3 \mu\text{m}^{-1}$. In order to operate a CEP shift of π , the propagation in the air and CaF_2 is:

$$\Delta L_\pi(\text{air}) = 1.499 \text{ m} \quad (\text{II.2})$$

$$\Delta L_\pi(\text{CaF}_2) = 95.5 \mu\text{m} \quad (\text{II.3})$$

These equations show how the CEP is sensitive to dispersion and how it can be difficult to control and stabilize it.

From the beginning we only considered one pulse, now we consider a mode-locked laser. In the

time domain, the laser is represented by a pulse train equally spaced with $T_R = \frac{1}{f_{rep}}$, where each pulse has its own ϕ_{CEP} , as depicted in figure (II.9). Considering that in the first approximation there is no

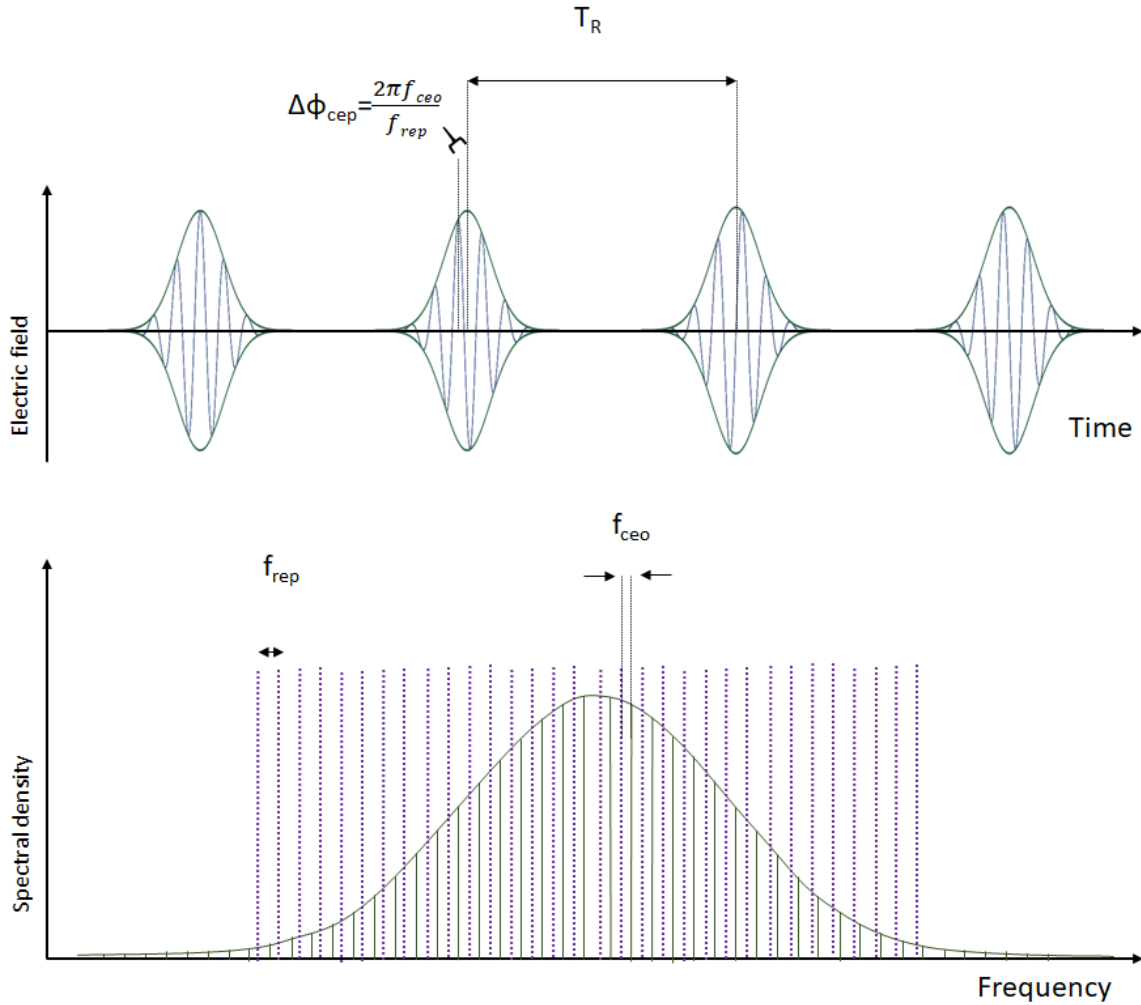


Figure II.9 – Time and frequency domains representation of a mode-locked laser output. The pulse train is spaced in time by T_R , corresponding to a comb in the frequency domain. The frequency offset of the comb f_{ceo} is related to the pulse to pulse CEP phase shift.

perturbation in the laser cavity, we can state that the CEP shift $\Delta\phi_{CE}$ of consecutive pulses is constant. The frequency f_{CEO} as defined in figure (II.9) is:

$$f_{CEO} = \frac{\Delta\phi_{CEP} f_{rep}}{2\pi}. \quad (II.4)$$

It represents the frequency offset on the frequency comb of a mode-locked laser. Any frequency component belonging to the mode-locked frequency comb can be written as:

$$f_n = n f_{rep} + f_{CEO}. \quad (II.5)$$

Let us now take a look at different factors that can induce a time dependency on the CEP shift. These noise sources can be classified into different time characteristics. Environmental factors in the laboratory can induce perturbations on a long time scale (from 1 s to hours). For example, temperature variations, humidity and air flows can induce perturbations in the gain medium refractive index. Other

sources of noises are present such as mechanical vibrations (time scale 1 ms to 1 s). At higher frequencies, pump fluctuations and driving electronics noise (kHz to MHz) can also perturb the optical phase and the CEP.

1.5.2 CEP characterization

The first technique to measure CEP shift in the time domain appeared in the late nineties [Xu 96], this technique is based on a cross-correlator. A few years later, the most used technique for CEP measurement was introduced [Telle 99]. It is a self-referencing technique based on the so-called f-to-2f interferometer. The principle of this technique relies on the definition on f_{CEO} for the frequency comb instead of measuring the $\Delta\phi_{CE}$ of two subsequent pulses. The principle is depicted in figure (II.10). The second harmonic of the lower part of the fundamental spectrum is generated with the proper non-

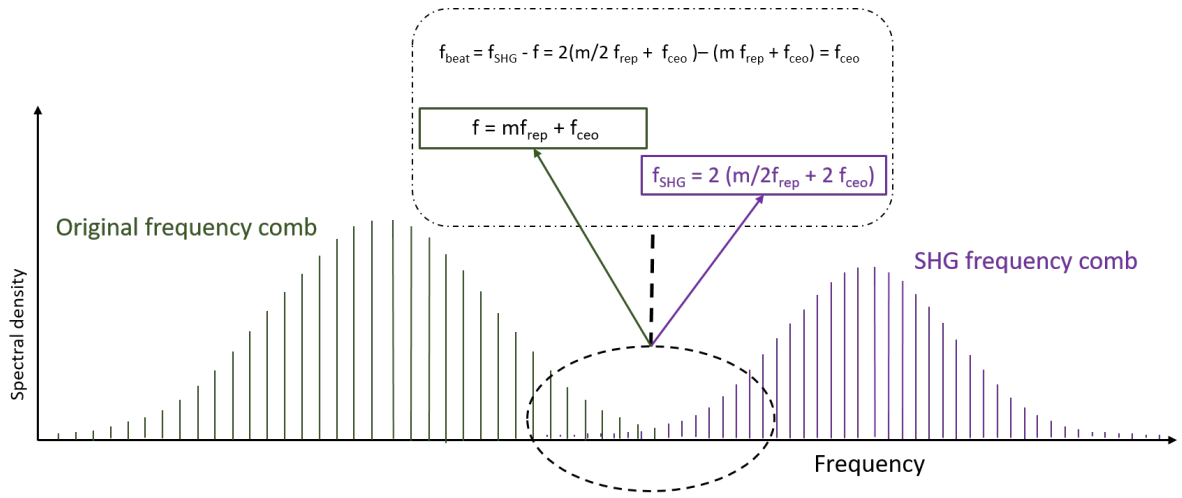


Figure II.10 – Principle of f-to-2f interferometer.

linear crystal. Frequencies of the fundamental comb are $f = m f_{rep} + f_{CEO}$, and the second harmonic of these frequencies correspond to $f_{SHG} = 2(\frac{m}{2} f_{rep} + f_{CEO})$. If the fundamental spectrum expands over an octave, frequency beats between the fundamental and SHG combs can be measured. To obtain these very broad spectrum, a WLG process can be used, since it can be shown to preserve the comb coherence in certain conditions.

A polarizing cube is used to project all the components (fundamental and SHG) on the same polarization axis. Then the signal is filtered out around the region of interest, where both combs overlap. The superposition of these two combs on a detector results in the heterodyne beat-signal at frequency f_{CEO} .

$$f_{beat} = f_{SHG} - f = 2(\frac{m}{2} f_{rep} + f_{CEO}) - (m f_{rep} + f_{CEO}) = f_{CEO} \quad (\text{II.6})$$

This beat-signal is accessible as a radio frequency (RF) signal and can be detected by an Electrical Spectrum Analyser (ESA). It can also be used as an error signal in a feedback loop to lock the f_{CEO} of an oscillator.

1.5.3 Passive CEP stabilization

To obtain self-CEP stabilized pulses a nonlinear process can be used. This scheme was presented by Baltuska et al. in 2002 [Baltuska 02]. By using a DFG process of two pulses sharing the same f_{CEO} , the f_{CEO} of the DFG pulses is automatically set to zero. Indeed for the DFG process, the phase of the

idler is [Cerullo 10]:

$$\Phi_i = \Phi_p - \Phi_s - \pi/2. \quad (\text{II.7})$$

To obtain a CEP stable idler, we just need to ensure that $\Phi_p = \Phi_s$. To satisfy this condition, the generation of very broadband and coherent frequency comb is needed. The WLG process allows this [Brodeur 99], then the phase of the pump and the signal are the same, therefore the idler phase after DFG process is constant. In the two next sections, two techniques are described to passively stabilize the CEP. Figure (II.11) depicts both of these techniques.

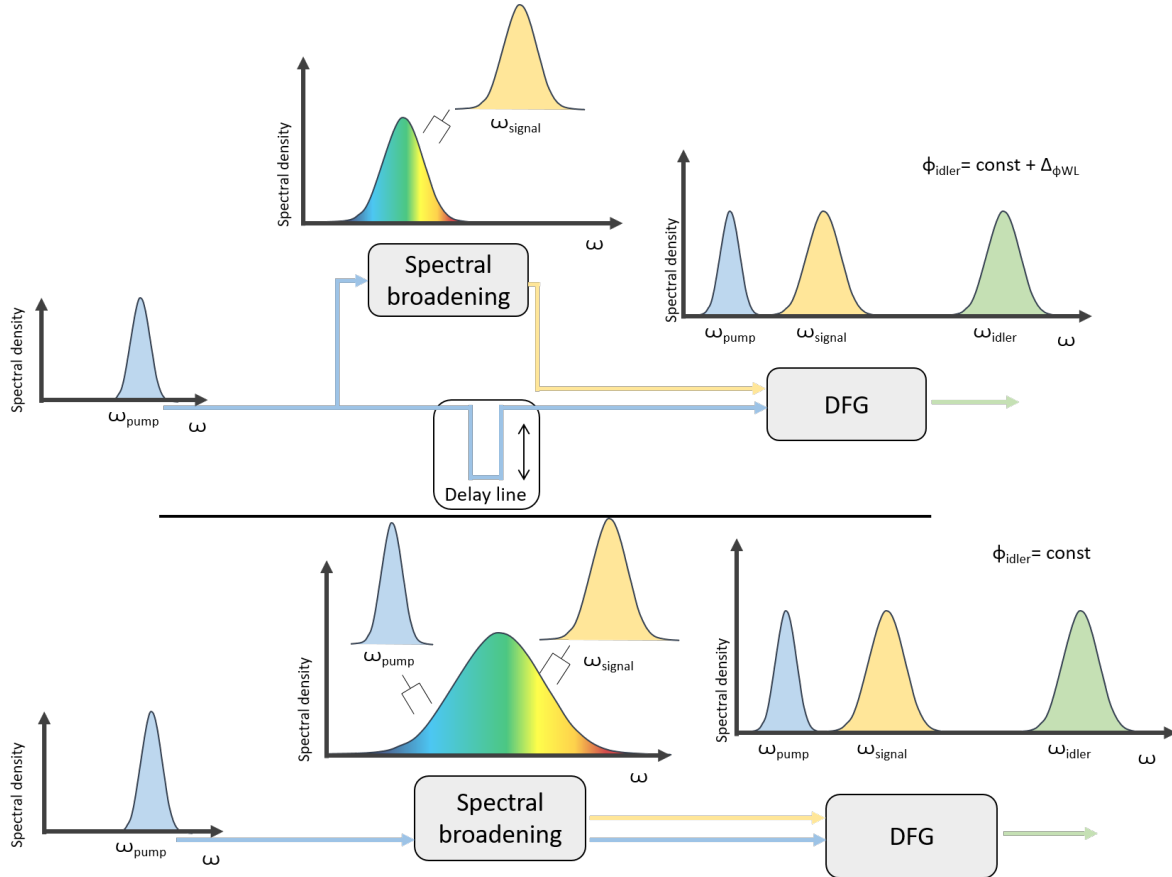


Figure II.11 – Top: Principle and scheme of inter-pulse CEP stabilization principle. Bottom: Principle and scheme of intra-pulse CEP stabilization principle.

1.5.4 Inter-pulse CEP stabilization

In order to stabilize the CEP of the idler, the pump and the signal need to have the same ϕ_{CEP} . The most used technique is to spectrally broaden the pump in order to generate the signal. Most of the time it is done in a photonic crystal fiber (PCF) or a YAG crystal [Thiré 17, Thai 11]. As shown on the top of figure (II.11), the signal is generated during WLG. To ensure temporal overlap of the pulses, a delay line is placed in one arm of the interferometer. Nevertheless, the delay line and the WLG can add some optical phase noise and therefore CEP phase shift. For the interferometer, the additional path added in the delay line directly induces CEP instabilities at the output. Regarding the WLG on the signal arm, since it is a very high nonlinear process, pump intensity instabilities can be transferred to the phase. It can be detrimental for the output CEP stability [Baltuska 02].

1.5.5 Intra-pulse CEP stabilization

The previous technique shows some limitations due to the fact that it is an interferometer with two physically separated arms. As a consequence, any fluctuation from one arm can severely hinder the CEP stability. To overcome this problem, the DFG can be done directly within two different spectral parts of the same pulse as shown at the bottom in figure (II.11). Since the pump and the signal are sharing the same optical path, their phase fluctuations are highly correlated. This scheme can also be used to generate Mid-IR pulses [Pupeza 15, Fuji 06].

As a downside, this technique is not flexible in terms of wavelength because the broadened spectrum is directly related to the amount of energy available at the input of the system. Moreover, the energy of the CEP-stable seed is very low, since the energy of the pump is limited to the single filament regime, and the DFG process efficiency is low. This technique will constitute the main original point of the system presented in chapter 3.

1.6 State of the art

In this section we present two systems with high performances in terms of energy, average power, pulse duration, dual output and CEP stability. These systems have been chosen as good representation of the current state of the art, but there have been tens of reports of such sources in recent years.

The first system [Mero 18] is shown in figure (II.12) and was developed the Max Born Institut in Berlin.

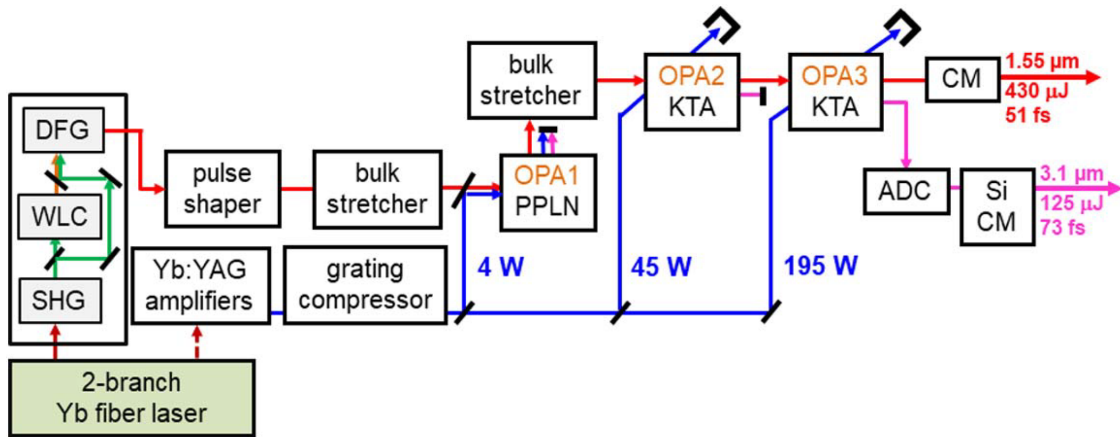


Figure II.12 – Scheme of a high average power OPCPA taken from [Mero 18].

A two-branch Yb-fiber laser operating at 100 kHz seeds the system. The first branch delivers 20 μJ with a pulse duration of 290 fs, and is used to generate the second harmonic of the pump. The beam is splitted into two parts. One part is used for WLG and the second part serves to pump a DFG unit based on a 2-mm-long BBO crystal. At the output of the DFG a passively-CEP stabilized signal with 180 nJ at 1.55 μm with a FTL at 39 fs is available to seed the OPCPA. The second branch delivers few-10 nJ. With a fiber, this pulse is stretched and amplified into a Yb:YAG amplifier system. After chirp compensation the Yb:YAG Innoslab amplifier delivers 244 W with a pulse duration of 1.1 ps.

The OPCPA is based on three amplifier stages. First, the seed is stretched by a pulse shaper and a bulk medium to 430 fs. Then the seed is combined by using a dichroic mirror with the pump. The first OPCPA stage is based on an antireflection (AR)-coated 2-mm-long fanout MgO:PPLN in collinear

geometry. It is pumped by 4 W, the seed is amplified from 50 nJ to 3.3 μJ .

Before the second stage, the seed is stretched by using a 47 mm-long piece of SF57 to reach a pulse duration of 600 fs. The amplifier is a 4 mm-long, type II KTA crystal used in a noncollinear geometry. This stage is pumped by 45 W and amplifies the signal from 3.3 μJ to 100 μJ . The angularly dispersed idler generated (50 μJ at 3.1 μm) is dumped. Nevertheless, they tried to compensate the angular dispersion with an AR-coated silicon prism. This leads to astigmatism and laterally varying chirp in the beam. In order to compensate the angular dispersion, a design based on reflection gratings is necessary due to the broad spectral bandwidth.

The last stage is also based on a 2 mm-long, type II KTA crystal used in a noncollinear geometry. It is pumped with 1.95 mJ and the signal is amplified from 100 μJ to 490 μJ and 190 μJ of angularly dispersed idler at 3.1 μm is generated.

Regarding the compression, the signal is compressed with chirped mirrors (24 bounces with -300 fs^2 each). After fine tuning of the pulse shaper, the compressor transmission is 91% leading to 430 μJ close to FTL pulses. The pulse duration is 51 fs measured with a SHG-FROG, close to 47 fs FTL estimated by the measuring device. The open-loop CEP stability of the 1.55 μm is 390 mrad over 10 s. It is characterized by a f-to-2f interferometer.

For the idler beam, the angular dispersion is compensated by using a grating on copper substrate (due to the scalability for high average power). Compression is achieved using a 10-mm-long AR-coated silicon window and eight reflections on chirped mirrors (+500 fs^2 / bounce) are used. The total transmission for angular and temporal chirp compensation is 66%, leading to a pulse energy of 125 μJ . The pulses are compressed down to 73 fs measured with a SHG-FROG (FTL is estimated to 71 fs).

This system is remarkable on several aspects. The system is CEP stable. It is an energetic, high-flux, stable (both beams have RMS average power below 0.5%) dual output system with ultrashort pulses. Indeed, 22% of the pump is transferred to the signal and the idler. The angular dispersion compensation of the idler is a salient feature of this work, found in very few other reports in the literature.

The next section is dedicated to the description of a system built by our team in Fastlite [Thiré 18]. Figure (II.13) shows the layout of the system, let us describe each key component of it.

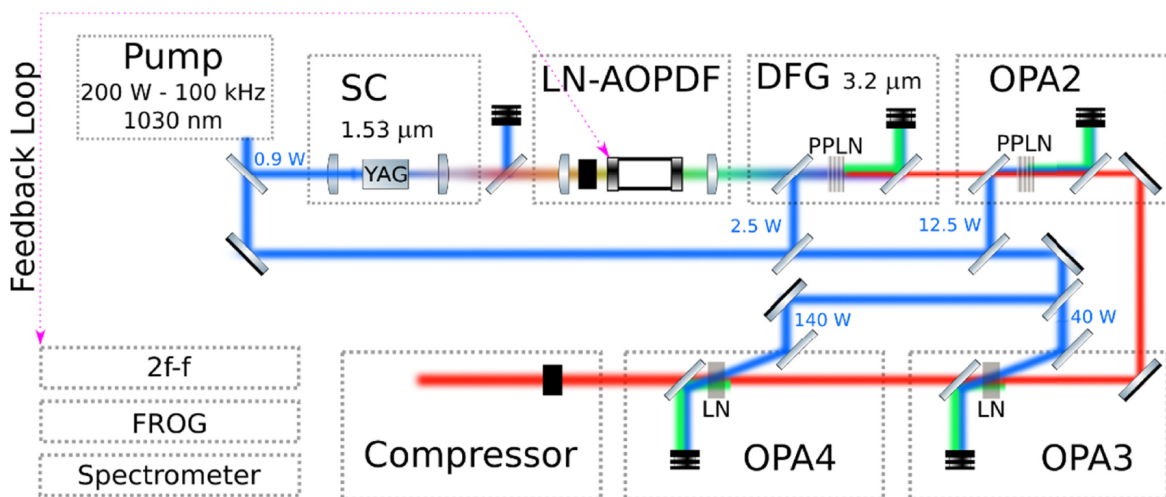


Figure II.13 – High average power, CEP stable OPCPA scheme taken from [Thiré 18].

The OPCPA is pumped by a 100 kHz, 2 mJ Yb:YAG thin-disk regenerative amplifier (Dira, TRUMPF). It emits pulses with 1.1 ps duration with a pulse-to-pulse energy stability of 1% RMS. A 10 mm YAG in one filamentation regime is used to generate the signal (1.3-1.9 μm) pumped by a

small amount (10 μJ) of energy. The signal is shaped by an AOPDF (Dazzler). The AOPDF is used to shape the seed (to match the pump duration), select the spectrum (acts as a spectral filter) and to pre-compensate higher order of spectral phase induced in the overall system. This device is also used to stabilize the CEP of the system via an error signal from the f-to-2f interferometer.

The first OPA stage is based on a 1 mm long MgO:PPLN. A large effort has been made on the compactness of the first OPA stage in order to preserve the CEP stabilization. In this system, the idler with a central wavelength of 3.2 μm is kept and amplified in the subsequent OPA stages. OPA2 is based on a 0.7 mm long MgO:PPLN and both two last stages are based on non-collinear, type I 1.5 mm bulk LiNbO₃ crystals. At the output of OPA4, 16.5 W of 3.2 μm is available.

The beam is temporally compressed with a 20 mm long Si plate. 15.2 W are available for the experiment after the compressor and sampling for diagnostics. These consist of a SH-FROG (Frozzler, Fastlite), MidIR-spectrometer (1-5 μm scanning acousto-optic spectrometer Mozza, Fastlite) and CEP stability (f-to-2f interferometer Fringezz, Fastlite). For the beam quality, a wavefront sensor (SWIR-SID4, Phasics) and a MidIR camera were used to determine the spatial Strehl ratio.

The spectrum spans from 2.8 μm to 3.65 μm . Regarding the pulse duration, 38.2 fs was measured close to its FTL (35.5 fs). The Strehl ratio is good with a calculated value of 0.87 and a M^2 value of 1.4 on both axis. The energy output stability is less than 0.7% RMS during 8 h.

CEP fluctuations were measured via an f-to-2f interferometer. The second harmonic of the beam is generated through a thin AgGaS₂ crystal and interfere with a stable continuum generated in a YAG crystal. Both beams are coupled with a 45° polarizer and a spectral beating occurs at 1.55 μm . This signal was recorded during 8 hours at 10 kHz with 2 μs of integration time (meaning that the acquisition system is single shot every 10 shots). The digital output is directly used in a feedback loop on the AOPDF. The CEP noise measured over 8 h is 65 mrad RMS. The low noise and the stability of the CEP is due to two principal aspects, first the passive stability of the DFG and the active feedback loop.

Performances of this source are well suited for strong field experiments due to the low single shot CEP noise and the high peak power available.

These two references are good comparison points for Yb-doped laser pumped OPCPAs in the SWIR and MIR, and have been developed while I was working towards my PhD thesis. More complete reviews of the state of the art can be found in [Biegert 12]. We now turn to a related subject, that allows better performances in terms of pulse duration: nonlinear compression.

2 Nonlinear compression

In the previous section we discussed OPCPA systems and their flexibility in terms of energy, wavelength, repetition rate and pulse duration. Sometimes, the output duration is not short enough for demanding applications (HHG, multidimensional spectroscopy). In order to generate even shorter pulses, in the few-cycle regime, a nonlinear post compression setup can be required. In the following section, this nonlinear setup is explained and then the state of the art of this technique is overviewed.

2.1 Principles

Spectral broadening using SPM

The first demonstration of this method was performed fifty years ago [Fisher 69]. The authors injected a pulse in a CS₂-filled cell in order to broaden the spectrum and compress the pulse from 5 ps down to 50 fs. Since this breakthrough, a lot of compression schemes have been implemented with various types of lasers. From Neodymium-YAG [Zysset 86] and dye lasers [Rolland 88] to Ti:Sa [Bohle 14,

Park 09, Chen 09], ytterbium doped fiber laser [Lavenu 17, Hadrich 16] and finally OPCPAs [Elu 17, Schmidt 10].

An in-depth theoretical study of post compression systems based on SPM in fiber is presented in [Tomlinson 84]. The general scheme is depicted in figure(II.14). The basic concept is to send a FTL pulse into a medium in order to induce mostly SPM. As a consequence (cf chapter 1), the temporal profile of the pulse remains unchanged but the spectrum is significantly broadened, meaning that the pulse is chirped.

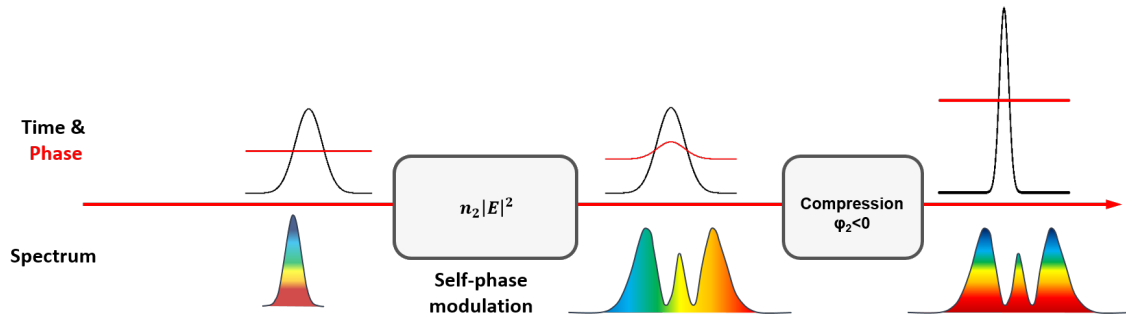


Figure II.14 – Nonlinear compression principle.

This chirped pulse is sent into a compressor in order to compensate the added spectral phase due to the SPM. A number of solutions can be used to induce this compensating dispersion, ranging from pairs of gratings and prisms to Gires Tournois Interferometer (GTI) mirrors [Gires 64] and chirped mirrors. Chirped mirrors are made of successive dielectric layers with varying thickness. With the control of the thickness of each layer, it is possible to control the dispersion induced on the pulse. These mirrors allow the compression of ultrashort pulses (spectral bandwidths can reach up to one octave) but the dispersion induced by bounce is generally low. A scheme of chirped mirrors is presented in figure (II.15). They are therefore well suited to the compression to short pulse durations. The other significant design choice resides in the nonlinear medium for a post compression setup. Two main possibilities have been explored: waveguides and bulk media.

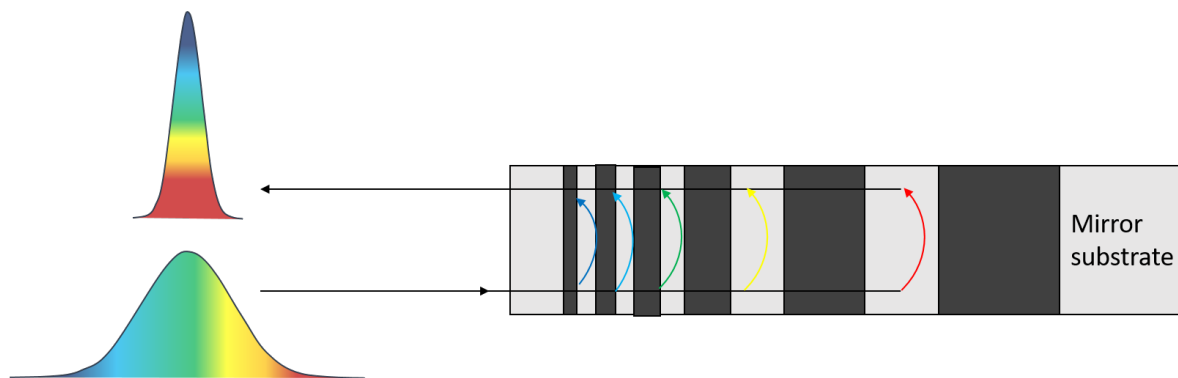


Figure II.15 – Chirped mirror principle.

2.1.1 Nonlinear compression in wave guides

One popular design choice for the nonlinear medium is to use single transverse mode waveguides, so that the spatial properties of the beam are fixed. The Kerr lens acts as a slight perturbation to the propagating mode, and large B integrals can be accumulated. The nonlinearity is brought by the

material constituting the guide, often fused silica for optical fibers, or a rare gas in the case of hollow core fibers and capillaries. The peak power is limited by the critical power associated to the nonlinear medium, around 10 MW for fused silica at 1550 nm, and three order of magnitude more (~ 10 GW) for gases at atmospheric pressures.

This explains the technical choices of waveguides for different types of lasers:

- Fused silica optical fibers for ps pulses with an energy less than 1 μJ
- Hollow core Kagome or antiresonant fibers filled with rare gases, with a diameter of a few tens of micrometers, for pulse energies ranging from 1 to 100 μJ [Mak 13, Emaury 13].
- Gas-filled capillaries, with a diameter of several hundred μm for pulses exceeding 100 μJ , and up to 70 mJ [Emaury 13, Chen 09].

Compression factors in terms of pulse duration obtained in these systems can be of several tens [Jeong 18]. However, it is increasingly difficult to obtain high compression ratios as the fractional bandwidth increases [Lavenu 19]. This is mostly due to self-steepening and to the more complex management of the spectral phase.

2.1.2 Compression in bulk medium

Another possibility is to use free propagation in bulk media. These systems allow more compact systems compared to waveguide-based compressors, often with highly transmission. However, since the B-integral varies in the transverse section of the beam, the output beam usually exhibits spatio-spectral couplings. It can be easily conceived that the spectral broadening is larger in the central part of the beam where the intensity is higher. To limit this effect, the compression factor often kept low (2-4) and spatial filters are used to get a homogeneous beam at the output.

As an example, a post compression setup is implemented in [Seidel 16] at the output of an oscillator. They use two stages both based on 15 mm quartz crystals. Compression with chirped mirrors allows them to reach few-cycle pulse duration from 250 fs pulses with an efficiency of 60%.

Multiple-plate compression

Multiple-plate compression [Beetar 18] is an extension of single bulk medium compression. The principle of multiple-plate compression is depicted in figure (II.16).

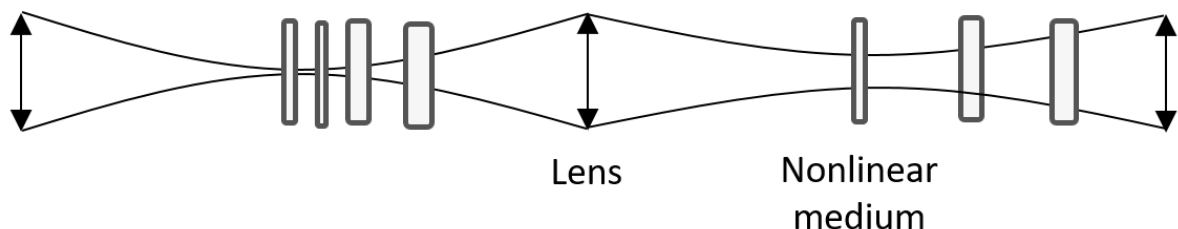


Figure II.16 – Multiple-plate compression principle.

The FTL pulse is focused into a bulk medium in order to broaden the spectrum and the beam propagates before going through another lens to focus into another bulk medium this process can be cascaded a number of times, often 4 times. Here, in this scheme (II.16), the free space propagation of the pulse helps to spatially homogenize the spectral broadening induced by the Kerr effect. So when the pulse is

going into the next bulk medium, the broadening occurs in another part of the beam, as a consequence the beam is less prone to showing spatio-spectral couplings.

As a significant example of this technique, we discuss the work reported in [Lu 18a]. The authors have used the output of a CEP stable non-collinear OPCPA (NOPCPA) to compress pulse down to 3.7 fs by using thin quartz plates and air. Generation of sub-two-cycle CEP stable at 3.5 μm is reported by [Lu 18b]. We briefly present the NOPA and then go into the details of the post compression.

The pump laser is a Ti:Sa multipass amplifier. It delivers 5.5 mJ energy with a pulse duration of 70 fs at 300 Hz. The pump is splitted in three different arms, 1% is used for the WLG in a 4 mm long YAG crystal to generate a seed at 1.03 μm . 19% of the pump are used to pump the first NOPA based on a 4 mm long KTA crystal used in type II configuration in order to amplify the signal. And 80% of the pump is used to pump the last collinear (in order not to introduce angular chirp on the idler) OPA based on a 2 mm long KTA. As a result, the output centered at 3.5 μm has 149 μJ of energy and a bandwidth of 150 nm. They measured a pulse duration of 120 fs.

The scheme of their empirically designed compressor setup is depicted in (II.17).

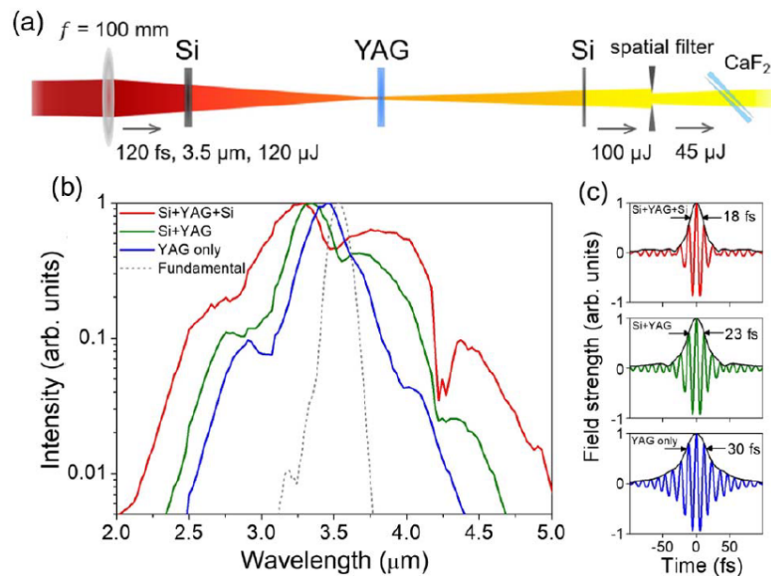


Figure II.17 – a) Scheme of the multiple-plate compressor taken from ([Lu 18a]). b) Results of spectral broadening. c) Corresponding FTL pulses calculated from the spectra (b).

First the beam is focused with a 100 mm CaF_2 lens that exhibits negative dispersion at this wavelength ($-180 \text{ fs}^2/\text{mm}$) and three plates of respectively 2 mm of Si (with positive dispersion of $440 \text{ fs}^2/\text{mm}$), 2 mm of YAG (with negative dispersion of $650 \text{ fs}^2/\text{mm}$) and 1 mm of Si are placed. The first Si plate is placed at 30 mm from the lens and the estimated laser intensity is $7 \text{ GW}/\text{cm}^2$. The beam is focused 103 mm from the lens, the YAG is placed slightly after the focus at 108 mm. The laser intensity estimated is $1000 \text{ GW}/\text{cm}^2$, then at 190 mm from the lens, the last plate of Si is placed. The laser intensity estimated is $50 \text{ GW}/\text{cm}^2$. The net dispersion of these materials is negative. Nevertheless, the broadening adds positive second-order spectral phase, that is why a pair of CaF_2 wedges (4 mm of material is the optimal result) is used to compress the output pulse.

A spatial filter is added at the output of the compression scheme in order to select the homogeneous part of the beam and have a Gaussian like shape (45% of transmission). Edges of the beam were not broadened due to the intensity dependence of the spectral broadening. The pulse duration mea-

sured is 21 fs, corresponding to 1.8 optical cycle at 3.5 μm . Moreover, they measured via an f-to-2f interferometer the CEP stability of the output. They obtained 283 mrad RMS over 500 s.

Note that in these schemes where the pulses propagate in thin plates, the peak power can exceed the critical power as long as no catastrophic collapse occur in the material.

2.1.3 Soliton compression

Instead of inducing spectral broadening and negative dispersion in sequence, it is possible to perform both at the same time in nonlinear media exhibiting anomalous dispersion. In this case, the pulses are compressed at the output of the nonlinear medium, a phenomenon denoted as "self-compression" or "soliton compression".

Soliton compression is illustrated in figure (II.18). A FTL pulse is sent into a nonlinear medium and the spectrum is broadened. SPM initially dominates, this enhances the effect of the negative GVD, which compensates for the nonlinear phase and results in self-compression of the pulse.

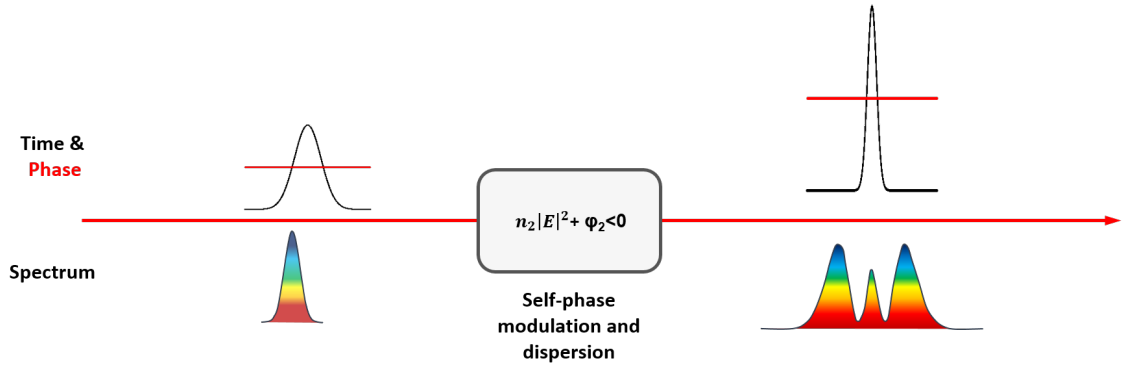


Figure II.18 – Soliton compression principle.

The propagation equation that takes into account both SPM and dispersion is expressed as followed:

$$\frac{\partial A}{\partial z} + i\frac{\beta_2}{2}\frac{\partial^2 A}{\partial t^2} = i\gamma_{SPM}A|A|^2.$$

It is possible to define L_D , dispersion length, and L_{SPM} , characteristic length for SPM as:

$$\left\{ \begin{array}{l} L_D = \frac{T_0^2}{\beta_2} \\ L_{SPM} = \frac{1}{\gamma_{SPM}P_{peak}} \end{array} \right. \quad (\text{II.8})$$

And we can define N (soliton number) as the ratio between these characteristic lengths.

$$N^2 = \frac{L_D}{L_{SPM}} = \frac{\gamma_{SPM}P_{peak}T_0^2}{\beta_2}. \quad (\text{II.9})$$

Self-compression is possible for propagation at soliton orders $N = \sqrt{L_D/L_{SPM}} > 1$. Under such conditions, the accumulated linear dispersion is balanced by nonlinear dispersion, and negative GVD causes new frequency components (generated via SPM) at the leading and trailing parts of the pulse to move toward the pulse center. Thus, the pulse self-compresses by a factor that is inversely proportional to N upon propagating a distance $\sim L_D/N$. This distance becomes longer as higher order dispersion terms become more important and for chirped input pulses. As the soliton order increases, the nonlinear chirp introduced by SPM is no longer balanced by negative GVD so that the amount of

energy contained in the compressed pulse peak, rather than in its pedestal, decreases. As a result, small values of N are required to achieve clean compression ($N < 5$) [Tomlinson 84, Agrawal 06].

As an example, a team in ICFO [Elu 17] managed to post compress a mid-IR OPCPA via self-compression inside a gas-filled antiresonant-guiding photonic crystal fiber. The figure (II.19) shows the entire layout of the system.

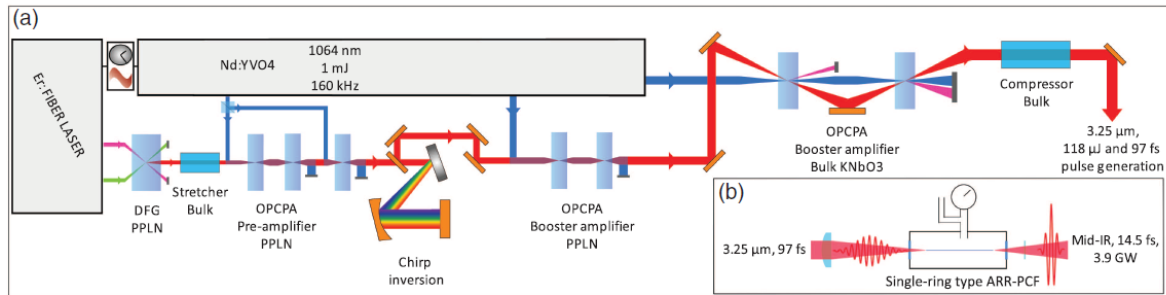


Figure II.19 – Postcompressed OPCPA via self-compression inside a gas-filled antiresonant-guiding photonic crystal fiber, taken from [Elu 17].

The first part of the system is the OPCPA shown in figure (II.19)a). This system delivers short and energetic pulses at $3.2 \mu\text{m}$. A major difference occurs in the synchronization between the signal and the pump compared to the other presented systems. The seed is generated via a DFG process inside a PPLN crystal fed by an erbium fiber laser system with two outputs (one at 1550 nm and the other one at 1050 nm). The pump is based on a Nd:YVO4 providing 1.1 mJ , 9 ps at 1064 nm and 160 kHz repetition rate. The temporal overlap between the pump and the seed is ensured via electronic synchronization (better than 300 fs). The OPCPA is divided into three parts, a preamplification section composed of three PPLN crystals in collinear configuration and a booster section with four different amplification stages. Regarding the preamplification stage, the energy at the output reaches $2.6 \mu\text{J}$ after the three stages. For the boost section, the two first PPLN are pumped by $250 \mu\text{J}$ (the pump is recycled to the second amplifier in order to increase the efficiency). That results in $18 \mu\text{J}$ of signal energy at the output of these two crystals. Then, the two last stages are based on KNbO_3 crystals in a noncollinear geometry. These two final stages reach $77 \mu\text{J}$ and $131 \mu\text{J}$ respectively, corresponding to an average power of 21 W with a pulse duration after compression of 97 fs .

The inset (II.19b)), shows the compression setup at the output of the system. They matched the beam inside a gas-filled hollow core antiresonant-reflection photonic crystal fiber (ARR-PCF). They used argon at a pressure of 12 bar inside the chamber where the 14.9 cm long ARR-PCF is maintained. With these parameters they calculated a soliton number $N=4.8$, and they reached a pulse duration of 14.5 fs at $3.3 \mu\text{m}$ (1.35 optical cycles). Nevertheless, only 60% of the energy is contained in the main peak.

We will present in chapter 4 an implementation of a soliton effect compressor in an extension of the multi plate setup, where a multipass cell is used to increase the number of elementary nonlinear and dispersive steps.

Conclusion

In this chapter we looked at the overall architecture of OPCPA systems that we will use in this thesis. We have seen that with the control of a few elements (pump laser, nonlinear crystals, dispersion management) it is possible to generate ultrashort and energetic pulses. Nonetheless, these systems remain limited in terms of pulse duration. In the second part we discussed nonlinear post compression setups.

Third-order nonlinearity and dispersion compensation can be used to compress pulses to even shorter pulse durations. In the next chapter, we will show the design and implementation of an ultrashort OPCPA system, that features an original subsystem to ensure high CEP stability performances.

Chapter III

CEP-stable mid-infrared OPCPA

Objectives

This chapter presents the design and development of a Mid-IR OPCPA. Specifications of this system are beyond the state of the art in terms of combined performances of CEP-stability, energy per pulse and pulse duration. In the first part we present the specifications of this source. In the second part, we present a first approach that consists in pumping the DFG process with the second harmonic of the pump laser. In the last part, we present a new DFG architecture that allows significantly improved performances in terms of CEP stability.

Contents

1	Goals and specifications for the mid-IR OPCPA	63
2	First architecture: DFG from a 515 nm pump laser	64
2.1	SHG of the pump laser	66
2.2	Seed generation: supercontinuum generation	67
2.3	DFG stage	69
2.3.1	Numerical simulation	70
2.3.2	Experimental results	71
2.4	Dispersion management	72
2.5	Second amplifier stage	75
2.6	Overall system results and discussions	77
2.6.1	Central wavelength	77
2.6.2	Compressed pulse energy	77
2.6.3	Pulse duration	77
2.6.4	Pulse-to-pulse and long term power stability	79
2.6.5	CEP stability	80
2.6.6	Spatial profile: Strehl ratio	82
2.6.7	Pointing stability	83
2.6.8	Uninterrupted operation	83
2.6.9	Conclusion	83
3	Second architecture: DFG from a 1030 nm pump laser	84
3.1	Seed generation from an all inline DFG scheme	86
3.1.1	Layout	86
3.1.2	Experimental results	87
3.2	First amplifier stage	88
3.3	Dispersion management	89
3.4	Second amplifier	90
3.5	Output measurements and discussion	91
3.5.1	Pulse duration	91
3.5.2	Strehl ratio	91
3.5.3	Pointing stability	93
3.5.4	Energy and CEP stability	93
3.5.5	Conclusion	96

1 Goals and specifications for the mid-IR OPCPA

The work presented in this chapter was triggered by one of Fastlite’s scientific client’s request for a custom OPCPA frontend. The goal is to study proton acceleration with ultrashort pulses. This requires an intense laser (multi-mJ energy with a pulse duration under 20 fs) at 2 μm central wavelength, with a controlled electric field shape, i.e. CEP-stabilized. The request is focused on the frontend of the source that delivers pulse energies on the order of a few tens of μJ , the power amplifier being treated separately. The client owns a pump laser that delivers 50 mJ pulses at 10 kHz and 1030 nm central wavelength. This laser has two outputs, first, the energetic one with more than 49 mJ with a pulse duration of 8 ps. This part of the pump laser is used to pump the last OPCPA stages in order to increase the energy. During our development of the front-end we therefore did not operate with this beam line. The other beam line delivers shorter pulses (around 900 fs) with 500 μJ of energy, and is the basis for the system designed in this part.

In this first section, we give the specifications for this mid-IR front-end OPCPA and the characteristics of the pump laser that we used to develop the OPCPA. In table (III.1) all specifications are summarized.

Specifications	Values	Units
Central wavelength	2100 \pm 100	nm
Compressed pulse energy	> 30	μJ
Repetition rate	10 or 20	kHz
Pulse duration FWHM	< 20	fs
Pulse-to-pulse stability (over 1000 shots)	1.5 times the pump stability	% RMS
Long term power stability (8h)	1.5 times the pump stability	% RMS
CEP stability	< 150	mrad RMS, single-shot
Strehl Ratio	> 0.8	-
Pointing stability	0.1x diffracted limited beam divergence	RMS
Uninterrupted operation	>8	hours
Warm up time	<1	hours

Table III.1 – OPCPA output specifications.

Compared to the literature, this system is beyond the state of the art regarding the CEP stability. As a comparison, our team in Fastlite has designed a CEP-stable OPCPA system with better CEP stability [Thiré 18], albeit at a larger central wavelength. As a side note, CEP stability is, as is well known for phase properties in general, increasingly sensitive to perturbation as the wavelength decreases, simply because a given phase translates to a longer propagation length. To our knowledge, and at the time it was designed, the specifications of this system were never reported before.

Another specification that is not present in the previous table is the compactness of the system. Indeed, it has to be mounted on a metric breadboard and housed in an aluminum enclosure (ready for dry air or Nitrogen purge). Dimensions of the housing are 750x1200x260 mm³.

Both systems presented in the next section are implemented with the following devices:

- Computer, in order to run the entire system.
- Security rack, that permits a safe use. It is linked with a beam blocker at the input of the OPCPA source and directly connected to the power supply of the pump laser. If any problem occurs, users can shut down the system quickly.
- Octopuzz synchronization unit. This device is fed by the internal trigger of the pump laser. It

allows us to trig any devices used in this chain, applying any delay desired and even downsample to trigger a lower repetition rate device.

- Dazzler, running at the repetition rate of the pump laser triggered by the Octopuzz. This device allows us to manage the entire dispersion in the system.
- BigBrozzer. It is a monitoring unit that allows recording at up to 100 kHz. This device is triggered by the Octopuzz and allows us to record spectra and pulse energies simultaneously at the repetition rate of the pump laser.

A typical rack built with all this equipment is shown in figure (III.1).

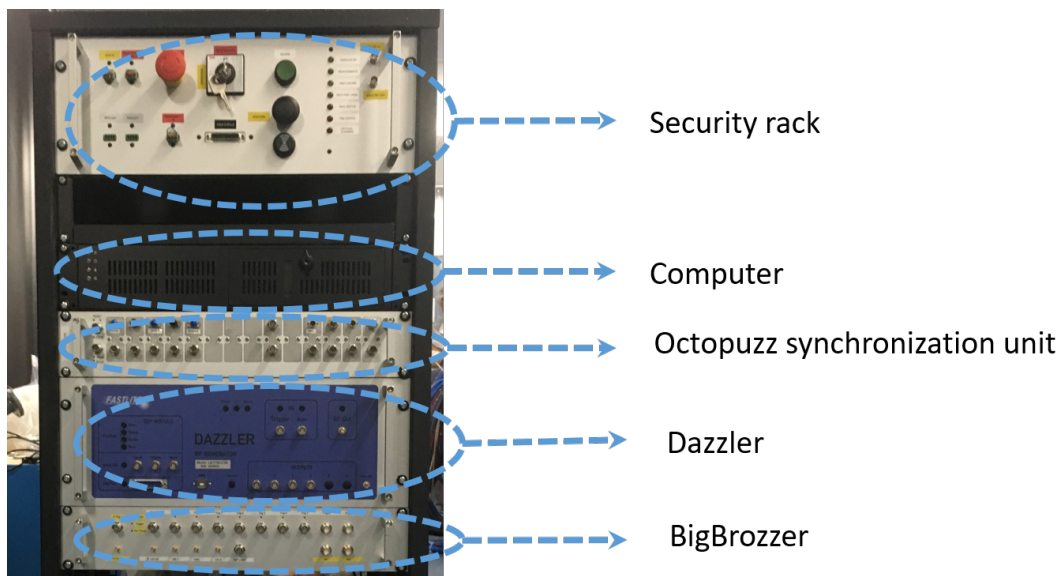


Figure III.1 – Rack built with a security rack, Bigbrozzer, Dazzler, Octopuzz synchronization unit and a computer.

2 First architecture: DFG from a 515 nm pump laser

The scheme of the OPCPA is depicted in figure (III.2).

In order to generate these few-cycle pulses, as mentioned above, the final pump laser (Trumpf) is based on Yb:YAG TDL technology delivering pulses of 0.5 mJ at a repetition rate of 10 or 20 kHz and with less than 1 ps pulse duration. Nevertheless, the development of the OPCPA was made at the Fastlite premises with another pump laser (Amplitude S-pulse). This system delivers pulses with 500 μJ at 1 kHz with a 600 fs FTL pulses as shown figure (III.3 1)) measured with a commercial SHG-FROG by Fastlite (Frozzler).

In order to match the pulse duration delivered by the customer's pump laser, we chirped the pulses to 825 fs (III.3 2)) by slightly detuning the output compressor of the laser.

The pump laser has an astigmatic spatial profile with an elliptical ratio of 70 % in the near field and 99 % in the far field. The beam size measured in the near-field is $1272 \times 900 \mu\text{m}^2$ (III.4 a)). The far-field measured with a 750 mm long focal length has a Gaussian shape and measure $431 \times 436 \mu\text{m}^2$ (III.4 b)). Both measurements were performed using a silicon-based camera (Basler with a pixel size of $9.9 \mu\text{m}$).

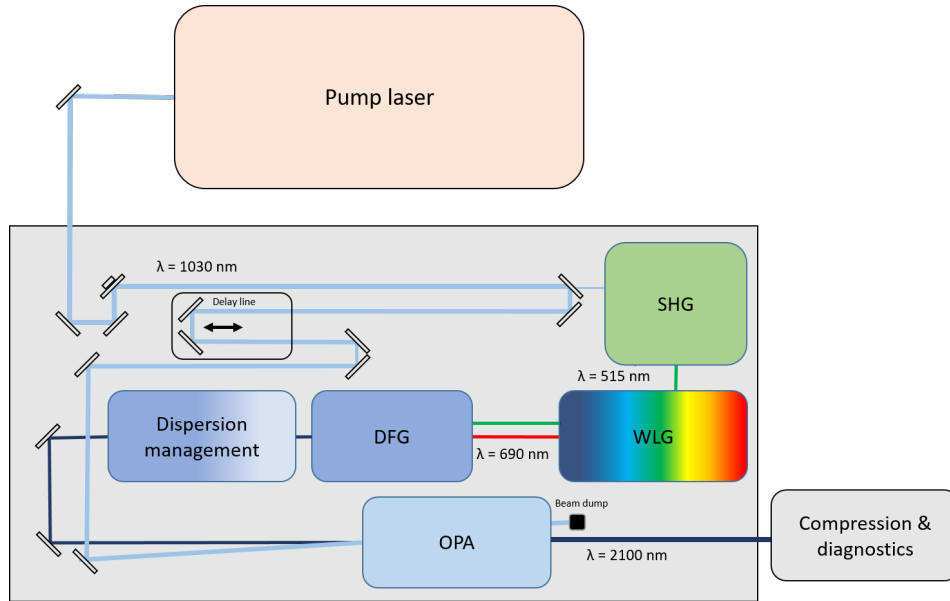


Figure III.2 – Layout of the OPCPA with the DFG pumped at 515 nm.

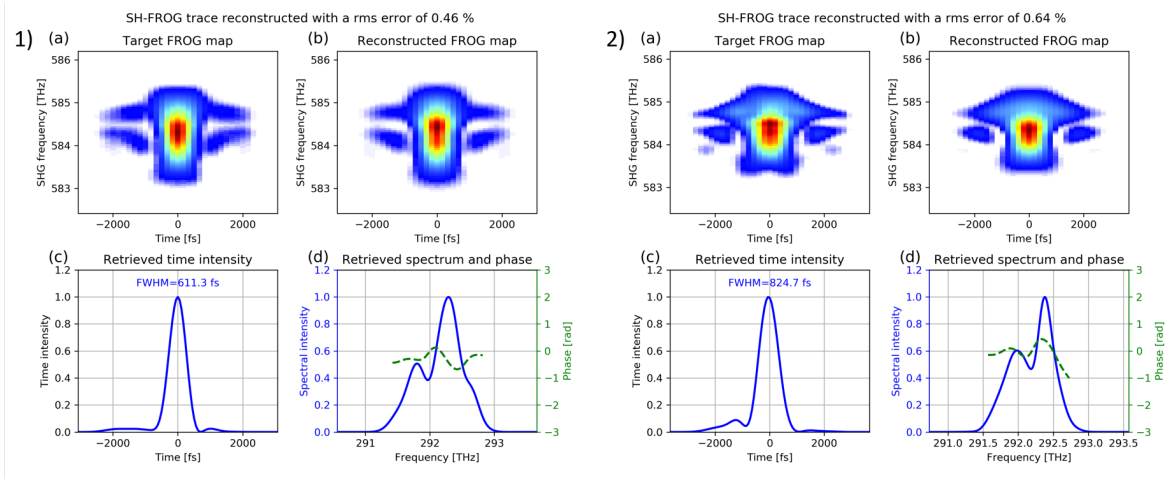


Figure III.3 – 1) SH-FROG of the compressed pump laser. (a) Measured FROG trace (b) Reconstructed FROG with a RMS error of 0.46 % (c) Retrieved time intensity of the pulse with a duration of 611 fs (d) Retrieved spectrum and phase of the pump laser. 2) SH-FROG of the chirped pump laser. (a) Measured FROG trace (b) Reconstructed FROG with a RMS error of 0.64 % (c) Retrieved time intensity of the pulse with a duration of 825 fs, (d) Retrieved spectrum and phase of the pump laser.

The DFG in this first layout generates intrinsically a constant CEP as seen in table (III.2). This is due to the fact that the pump and signal seed originate from the same beam (pump SHG beam).

From the pump laser, the beam is sent into the breadboard. At the input of the system an active beam pointing/position stabilization system is mounted on two mirrors. This system ensures a stable pointing of the beam. Then the beam goes onto a beam splitter, where the major reflected part is used to pump the OPA stage. The transmitted part of the beam is used to generate a CEP stable seed through DFG: the second harmonic of the beam is generated (2.1), then a small portion of the beam is used to generate the signal through WLG (2.2). Via a DFG process between the signal and the SHG of the pump, a CEP stable idler is generated (2.3). Then, the beam goes to a dispersion management setup including a Dazzler and carefully chosen bulk materials (2.4). At the end of our system, an amplifier

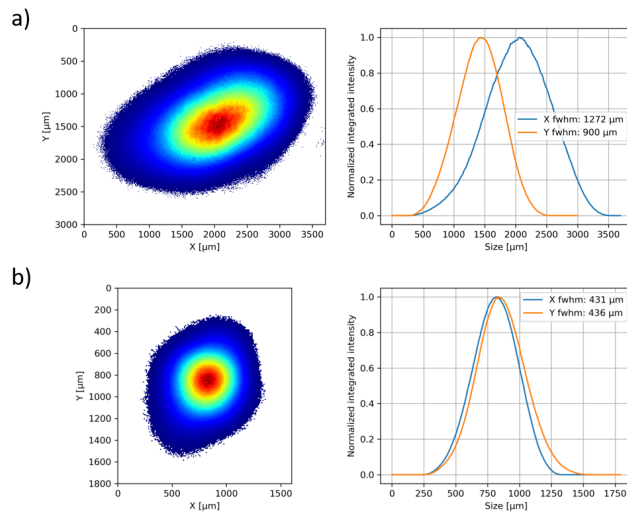


Figure III.4 – a) Spatial profile in the near field of the pump laser. b) Spatial profile in the far field of the pump laser focused with a 750 mm lens.

	DFG	OPA
Pump frequency	$2\omega_0$	ω_0
Pump phase	$\Phi_p=2\Phi_0-\frac{\pi}{2}$	$\Phi_p=\Phi_0$
Signal phase	$\Phi_s=2\Phi_0-\pi$	$\Phi_{s out} = 0$
Idler phase	$\Phi_i=0$	$\Phi_{i out} = \Phi_0-\frac{\pi}{2}$

Table III.2 – Phases and frequencies of each beam in the OPCPA. Fundamental frequency and phase are ω_0 and Φ_0 at the output of the pump laser.

stage is implemented to reach the targeted energy (2.5). At the output, the beam is compressed and characterized thoroughly.

2.1 SHG of the pump laser

In this section, we describe the first part of the system the SHG of the pump depicted in figure (III.5).

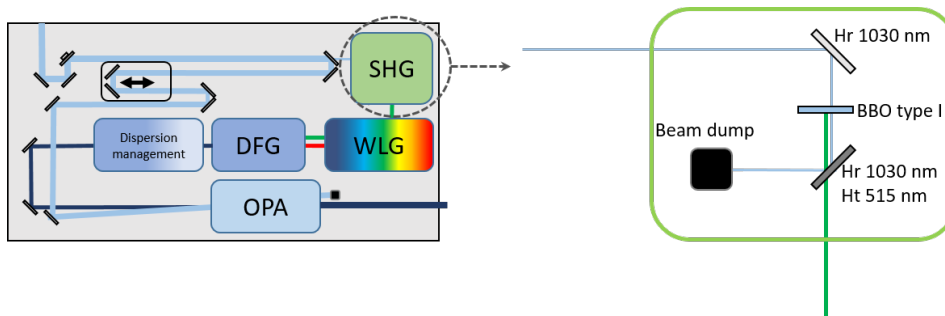


Figure III.5 – Second harmonic generation stage.

A 25 % fraction off the pump beam energy is sampled using a splitter (Eksma) to be frequency doubled. We saturate the SHG process with a long nonlinear crystal in order to have a more stable signal. The beam is not focused into the crystal so we estimate it has the same size as the pump laser (III.4 a)). We use a 2.5 mm long BBO crystal in type I configuration with an angle $\Theta=23.4^\circ$. The

incoming beam has 117 μJ energy and 52 μJ are converted into a 515 nm beam. That represents 44 % of conversion efficiency. The spectrum of the SHG beam is shown in figure (III.6).

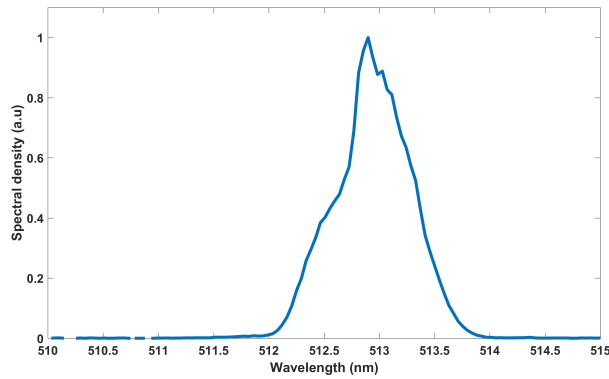


Figure III.6 – Second harmonic spectrum of the pump laser using a 2.5 mm long BBO type I cut at 23.4 °.

This SHG beam is then used to generate the CEP signal.

2.2 Seed generation: supercontinuum generation

This section is dedicated to the WLГ of the system, which scheme is depicted in figure (III.7).

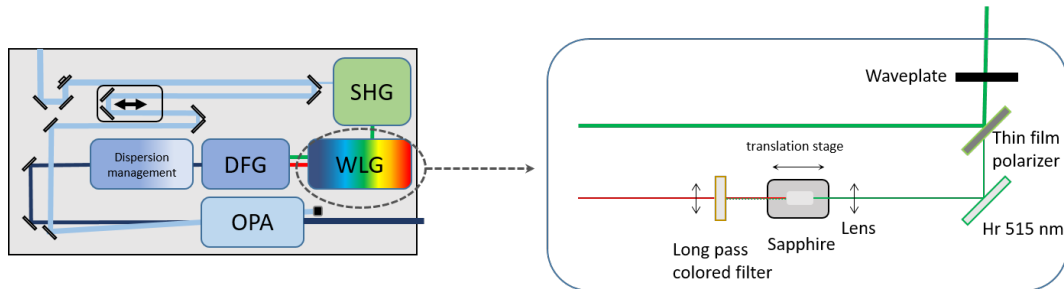


Figure III.7 – White light generation stage.

For this system, we need to generate pulses at 2.1 μm with a pulse duration of less than 20 fs. In the spectral domain, the targeted bandwidth (idler) is 1720-2700 nm. As a consequence the corresponding signal beam must cover a 644-745 nm bandwidth.

In chapter 2 we explained the importance of the crystal for WLГ. During the development of this system, we tested two crystals for WLГ. The first one is a YAG crystal and the second one is a sapphire crystal. Other critical characteristics need to be taken into account, such as the focal lens used to focus into the crystal, the energy used. In figure (III.8) WLГ from a YAG is shown with different input energies.

In order to perform these measurements, we used a filter that blocks the input beam to a large extent. However, since this SHG beam is intense compared to the generated signal, we can observe on the short wavelength region a residual of it.

From these spectra, we can see that the best configuration is for lowest input energy (with an energy of (640 nJ). Both other spectra do not cover the entire required bandwidth on the long wavelength side. We also want to look at how far the extension to the red part is. In order to do so, we use a longpass colored glass filter at 715 nm (fgl715 from Thorlabs). The spectrum spans up to 755 nm, it

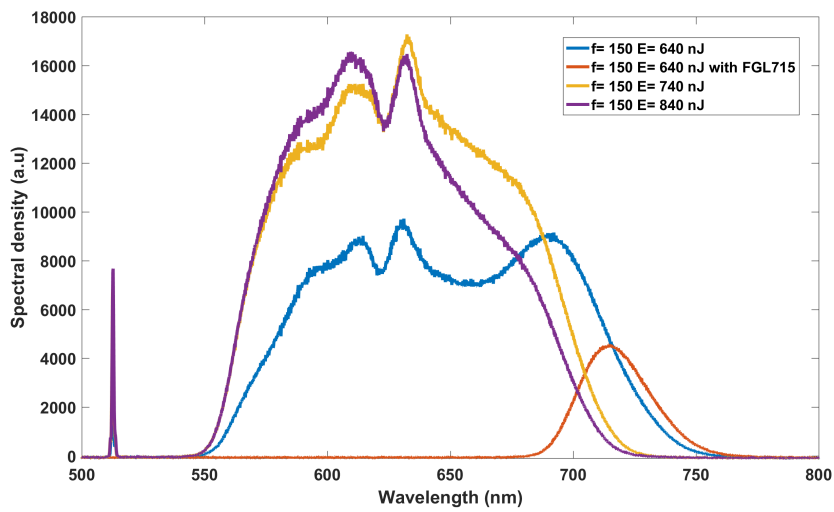


Figure III.8 – WLG in YAG for an input energy of 840 nJ in purple, 740 nJ in yellow and 640 nJ in blue, all focused with the same 150 mm lens. The red spectrum represents WLG in the same conditions as the blue one with a longpass colored filter at 715 nm.

is in adequacy with the targeted bandwidth. Nevertheless, the spectrum decreases rapidly on the long wavelength side, indicating that a low power is available to perform the DFG. That is why we tried another crystal as a WLG medium.

For our second crystal, we used sapphire. In figure (III.9) spectra obtained with sapphire and YAG are shown.

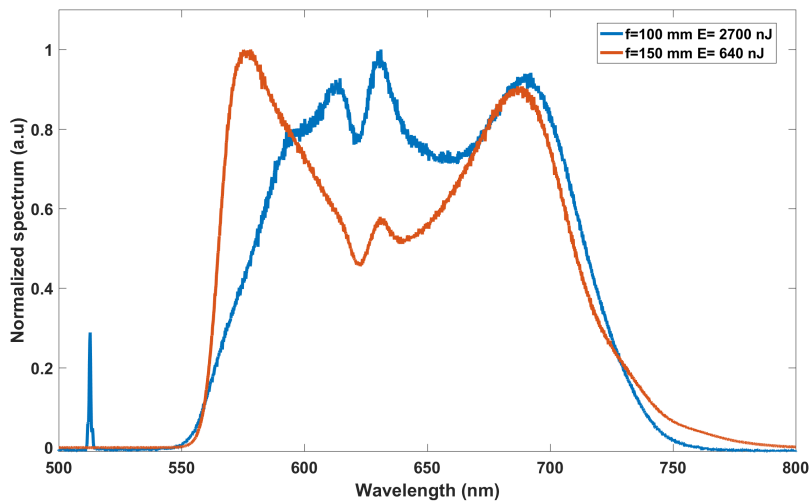


Figure III.9 – WLG for an input energy of 640 nJ in blue focused with a 150 mm lens in a YAG crystal. The red spectrum is obtained through WLG for an input energy of 2700 nJ focused with a 100 mm lens in a sapphire crystal.

The spectrum in blue is the one obtained previously (figure III.8) for an input energy of 640 nJ and a focal lens of 150 mm in a YAG crystal. The red spectrum shows WLG in a sapphire crystal, with an input energy of 2700 nJ and a focal length of 100 mm. We can see that the red spectrum extends toward longer wavelengths. The spectrum now has a bandwidth that extends from 550 nm to almost 800 nm. That spectrum fits the specifications better.

We now look at the spatial shape of the WL created. During different tests, we sometimes observed spatial chirp due to a conical emission [Dubietis 17] that can be detrimental for the DFG stage. Each spectral component is not focusing with the same size at the same longitudinal position. For a given focal length, the red part of the spectrum is focusing closer to the lens than the blue part of the spectrum. This is probably due to the fact that the divergence of the longer wavelength is larger and because the red part of the spectrum is created earlier in the crystal. Experimentally, the sapphire crystal is mounted on a translation stage, moving along the propagation axis. It is possible to control different foci into the DFG crystal by slightly translating it. After generating the signal, a color filter glass is used to remove the pump beam. Now that the signal is generated, let us look at the DFG stage in the following section.

2.3 DFG stage

The DFG stage is depicted in figure (III.10). The signal centered at 680 nm from the WLG is focused into a nonlinear crystal and spatially overlapped with the pump centered at 513 nm. They are combined with a dichroic mirror that reflects the pump and is transparent for the signal wavelength. The incoming pump beam energy is controlled by a TFP and a waveplate. A delay line allows both beams to be temporally overlapped.

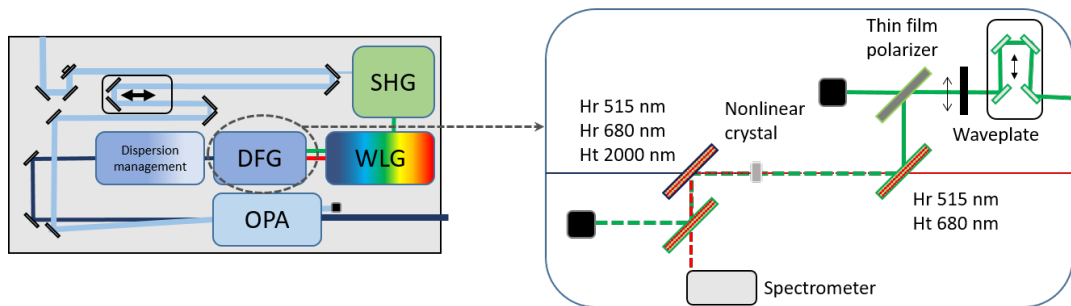


Figure III.10 – Difference frequency generation stage.

For this stage, we compared two different crystals, BBO and LBO. In figure (III.11) are presented both gains as a function of phase matching angle and wavelength of the signal. For a number of phase matching angles, the gain is also represented as a function of the idler wavelength.

In figure (III.11) on the top left, the signal gain is depicted in a BBO crystal with a length of 0.7 mm and an input pump intensity of 100 GW/cm^2 . In the bandwidth of interest, around 650 nm, a gain of 150 can be reached with a phase matching angle of 21.5° . As depicted in the figure (III.11 bottom left), obtained with the same input characteristics than the simulation before, for a phase matching angle of 21.7° , the bandwidth for the idler spreads from 1850 to 2650 nm.

On the right side of figure (III.11), the signal (a) and idler (b) gain are depicted in a 1.9 mm long LBO crystal with an input pump intensity of 100 GW/cm^2 . For this crystal, a phase matching angle of 9° in the XY plane corresponds to the desired bandwidth and can reach for the signal a gain of 500. For this phase matching angle, we can notice a turnaround point in the 2D phase matching map, which explains the very broad spectral gain curve. This shape is directly transmitted to the idler spectrum as depicted in (III.13 c)). Later in this section it is also shown experimentally. Regarding the corresponding idler bandwidth, it spreads from 1700 to more than 2700 nm. Both figure displays up to 2700 nm because of the transmission drop induced by these crystals beyond this wavelength (figure III.12).

Since these two crystals seem to be suitable candidates to use in the DFG stage, we perform numerical simulation on the LBO crystal. Indeed, this crystal allows a higher gain and a larger bandwidth in

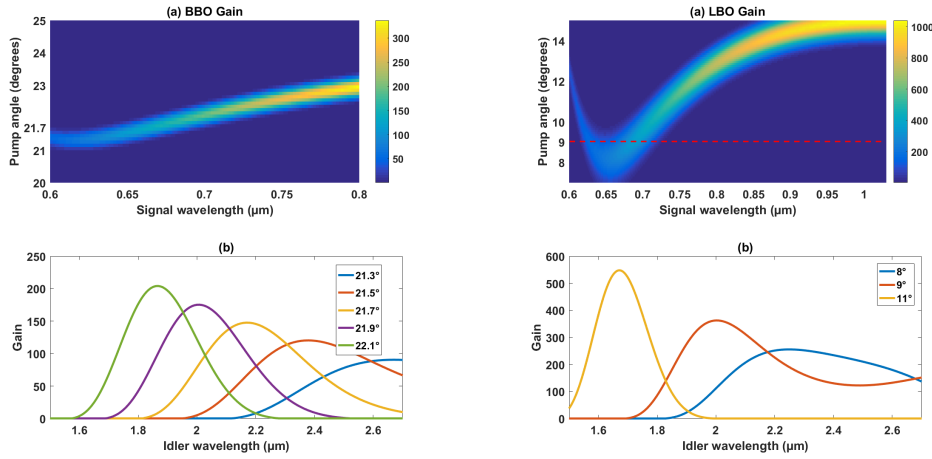


Figure III.11 – Small signal gain maps for a pump intensity of 100 GW/cm^2 . Left: (a) Signal gain in a 0.7 mm long BBO. (b) Idler gain for selected phase matching angles. Right: (a) Signal gain in a 1.9 mm long LBO crystal. (b) Idler gain for selected phase matching angles.

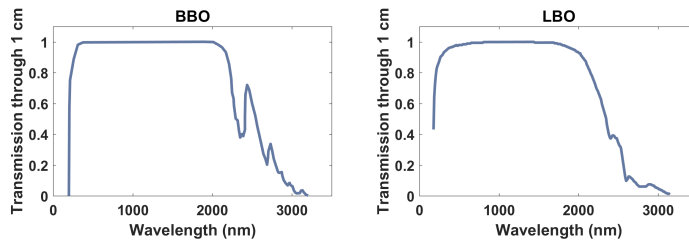


Figure III.12 – BBO (left) and LBO (right) transmission after propagation in 1 cm of material (data from SNLO).

the MID-IR.

2.3.1 Numerical simulation

In this section, we discuss the numerical simulations used during this thesis, and an application on the DFG stage is demonstrated.

Simulations for ultrafast OPAs are often based on the split-step Fourier method. This technique consists in dividing the propagation phenomena into two parts. Linear phenomena such as dispersion are taken into account in the Fourier domain, and nonlinear phenomena are implemented in the temporal domain. This technique is capable of solving propagation equations very efficiently by using fast Fourier transform routines available in most software libraries. The simulations presented here were achieved with the software Matlab. The code solves six nonlinearly coupled propagation equations corresponding to the pump, signal, idler, and second harmonic of each of these waves. The SHG of each wave is considered because it is one of the most frequent parasitic process encountered in such OPAs. The numerical method was inspired and adapted from reference [Bromage 11]. The full dispersion and phase matching characteristics are taken into account by modelling the refractive indices through a Sellmeier equation for the ordinary and extraordinary indices. Spatial effects such as diffraction and walkoff are not modelled, because the beams are not tightly focused in these high power femtosecond systems. However, to obtain a realistic value for the efficiency, a Gaussian spatial profile is considered

and the temporal equations are solved for multiple points in this profile, allowing to observe spatial depletion and obtain integrated values for conversion efficiencies.

When using this numerical simulation, different input parameters for the amplification process can be adjusted in order to obtain a result that fits the gain, conversion efficiency, and spectral bandwidth. These parameters includes beam sizes (pump and signal), input energies, and the delay between the pump and the signal at the input facet of the crystal. This last parameter allows us to maximize the temporal overlap inside the crystal, therefore modifying the delay induced by GVM.

In figure (III.13) we performed numerical simulations in a 1.9 mm LBO crystal for a phase matching angle in the XY plane of 9° and we consider a nonlinear coefficient of 0.841 pm/V . The pump beam diameter at $1/e^2$ in intensity at 513 nm is $150 \mu\text{m}$ with an input energy of $45 \mu\text{J}$ and a temporal duration of 850 fs . For the seed, it is centered at 680 nm with a diameter of $100 \mu\text{m}$ and a temporal duration of 17 fs chirped to 500 fs . The input seed energy is difficult to estimate because it is coming from the WLG, in our case we estimated it to be 0.3 nJ .

All spectra presented in (III.13) are taken at the beam center. The output pump spectrum is depleted due to the high gain configuration (20000 for the simulations). The output signal spectrum features a profile that is characteristic of the gain curve shown previously, in the vicinity of the turning point for the phase matching 2D map. We also clearly observe that this spectral shape is transmitted to the idler. These simulations confirm that the chosen phase matching condition allows the amplification of a broad spectrum that matches the target specifications. In the next section, the experimental results of the DFG stage are presented

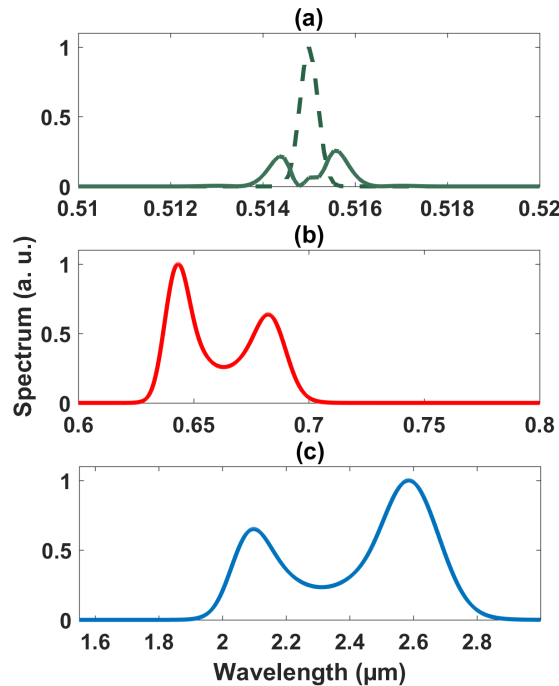


Figure III.13 – Numerical simulations (a) dashed line input pump spectrum and solid line output pump spectrum, (b) output signal spectrum and (c) output idler spectrum.

2.3.2 Experimental results

In this section we present the results obtained experimentally with three different crystals, one BBO and two LBO crystals with different lengths.

The focused pump has a spot size of $167 \times 134 \mu\text{m}^2$ and the seed is imaged with a 19 mm lens after the WLG with a focused spot size of $102 \times 103 \mu\text{m}^2$. Both beam profiles are shown in figure (III.14). Even if the seed is generated from a WLG process, it has a Gaussian shape, suitable for our use in the OPCPA. For the seed it is not possible for us to perfectly calculate the intensity inside the nonlinear crystal due to the fact that the output energy from the WLG is low. For the pump we estimate it to be 231 GW/cm^2 for an energy of $49 \mu\text{J}$. These values are experimentally observed to be close to the damage threshold for the crystal.

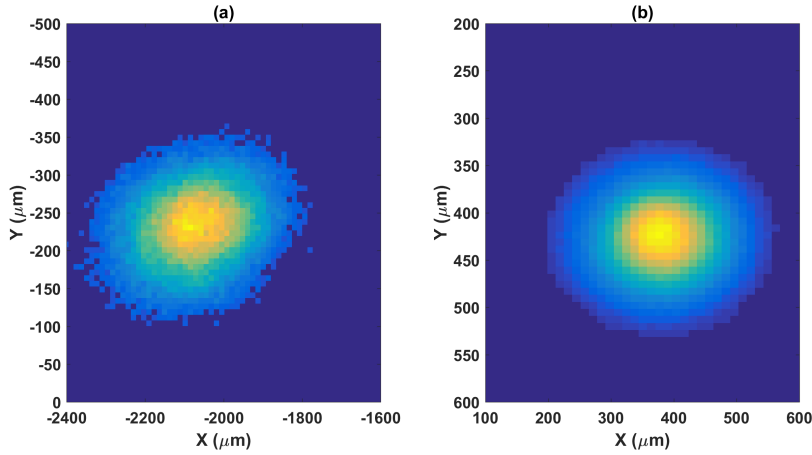


Figure III.14 – (a) Spatial profile of the pump beam for the DFG stage (b) Signal beam profile for the DFG stage.

Both beams are spatially and temporally overlapped in the three tested crystals. The resulting output spectra are plotted in figure (III.15).

Table (III.3) lists the spectral bandwidths at 1% obtained in different conditions.

	Signal (bandwidth at 1% in nm)	Idler (bandwidth at 1% in nm)
BBO 0.7 mm (red)	98	828
BBO 0.7 mm (blue)	101	848
LBO 1.9 mm (green)	143	983
LBO 2.8 mm (grey)	113	975

Table III.3 – Bandwidth of signal and idler for different types of crystals.

Again, the peculiar gain shape is observed in the case of LBO, while experiments with the BBO crystals gave mostly narrower Gaussian-shaped spectra. As a result, and as expected from the previous phase matching bandwidth analysis and numerical simulations, the LBO crystal with a length of 1.9 mm offers the largest bandwidth (983 nm at 1%), corresponding to 12.8 fs FTL, with an output energy of $1.2 \mu\text{J}$. We therefore used this crystal for the DFG stage.

2.4 Dispersion management

The idler from the DFG stage is now ready to be used as the signal for a subsequent parametric amplifier. Before amplification its spectral phase is controlled using a dispersive optical material and an AOPDF. The scheme of the dispersion management is displayed in figure (III.16).

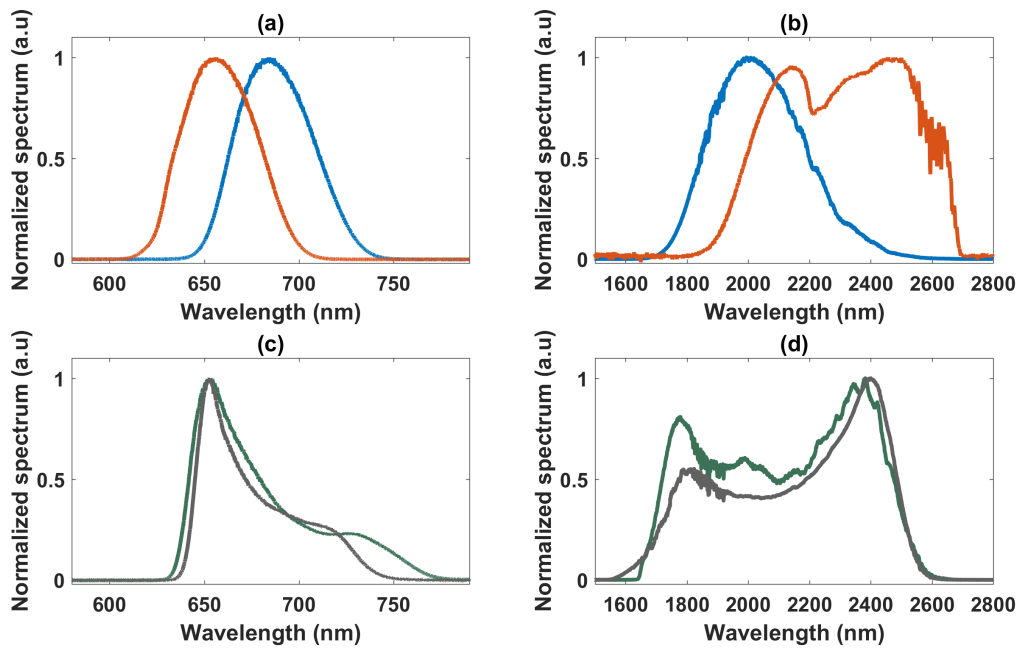


Figure III.15 – Spectra of the signal (a) and idler (b) for a 0.7 mm long BBO crystal at two different delays. (c) and (d) Signal and idler spectra for a 1.9 mm long LBO crystal (green) and a 2.8 mm long LBO crystal (grey).

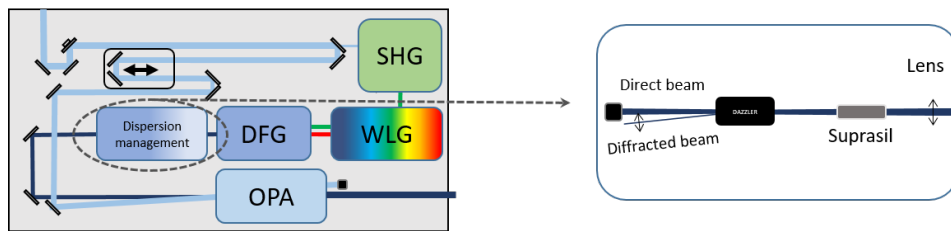


Figure III.16 – Dispersion management stage.

As explained in the first chapter, the AOPDF principle is based on the interaction of an acoustic polychromatic wave (propagating along an acoustic column) and a polychromatic light pulse (our idler at $2.1 \mu\text{m}$) co-propagating inside a birefringent crystal (LiNbO_3). A part of the incoming beam is diffracted onto the orthogonal polarization with a small angle. Two ways are used to discard the direct beam, either by using a polarizer or by physically blocking it, taking advantage of the slight angle between the cross-polarized beams.

The acoustic column has a diameter of $600 \mu\text{m}$. The incoming beam needs to respect two characteristics: its width should be below $600 \mu\text{m}$ and the beam must be collimated. As depicted in figure (III.16) we used lenses to shape the beam in order to fulfill these conditions.

In figure (III.17 a)) both idler (in orange) with $1.2 \mu\text{J}$ and signal (in blue) are represented with an energy of $5 \mu\text{J}$. That is our starting point before the dispersion management.

The diffracted spectrum exiting the Dazzler is shown in figure III.17. This spectrum exhibits a structure that is attributed to nonlinear effects inside the lithium niobate crystal. Indeed the Dazzler is composed of a 30 mm long LiNbO_3 crystal. In order to reduce these nonlinear effects, we need to reduce the peak power by temporally stretching the pulse. To do so, just before the AOPDF, we add a 50 mm long rod of suprasil. This material exhibits $-123 \text{ fs}^2/\text{mm}$ of GVD. As a consequence, the

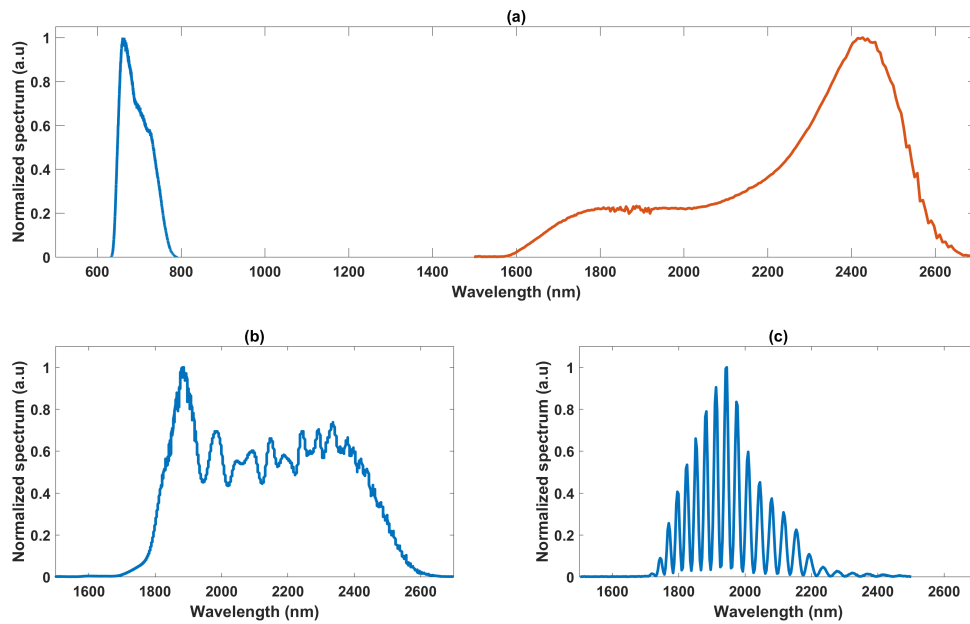


Figure III.17 – (a) Spectra from the DFG stage, signal (blue), idler (orange). (b) Spectrum output from the AOPDF. (c) Alignment spectrum for the AOPDF.

spectrum in figure (III.18 a)) is obtained at the output of the AOPDF, free of the previously observed structure.

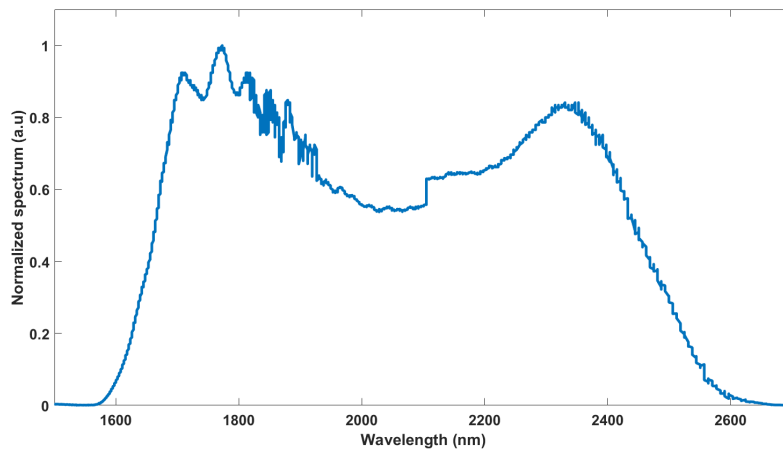


Figure III.18 – Output spectrum from the AOPDF.

The Dazzler is a device that can be difficult to properly align since both the pulse and the acoustic wave need to co-propagate with a small error margin. To do so properly, the device is mounted on a 5-axis translation stage. One way to perform this delicate alignment is to generate two pulses with the device, delayed by a few hundreds of femtosecond. That creates an interference pattern in the spectrum as shown on figure (III.17 c)). Then the measured diffracted spectrum is compared to the spectrum calculated by the device software that takes into account the acoustic wave sent to the crystal. These spectra are matched by adjusting the alignment. Using this procedure we make sure that the acousto-optic process is phase-matched and that we can diffract the whole bandwidth of the idler. The

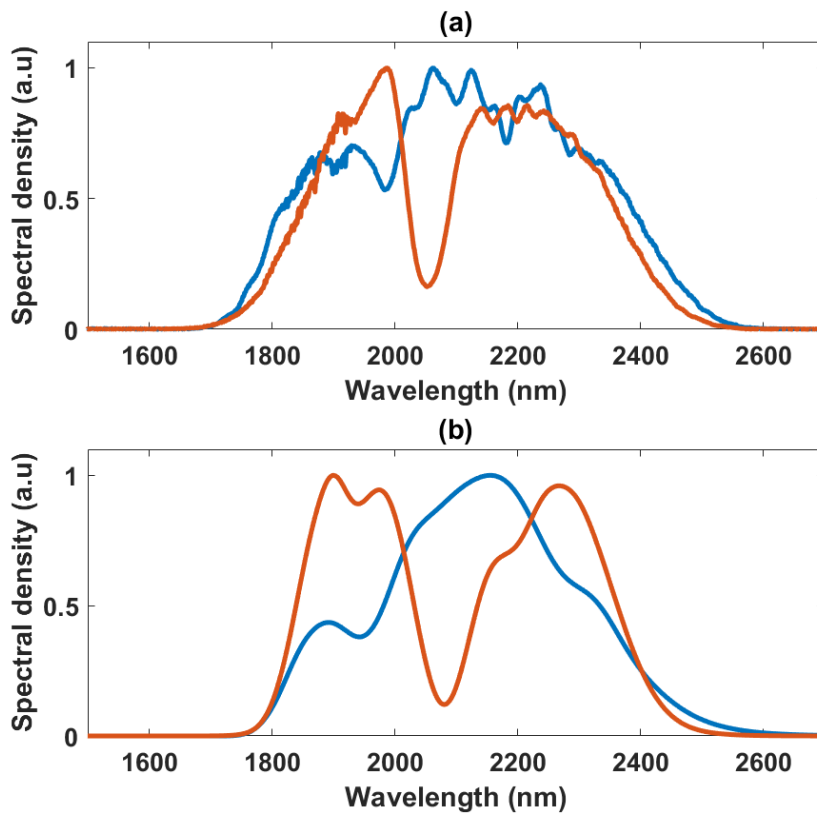


Figure III.20 – (a) (orange) Measured output spectrum with a small noncollinear angle, (blue) Output spectrum with a 5° noncollinear angle (external). (b) Numerical simulations of the second amplifier stage, with a small noncollinear angle and with a 5° noncollinear angle respectively in (orange) and (blue).

tal output spectrum is shown in (figure III.20 b)) in blue. The noncollinear geometry has two benefits: first, the hole at 2060 nm disappears, and the spectrum is slightly broader which leads to shorter FTL duration. Regarding the energy, $33 \mu\text{J}$ are available at the output of the system. That corresponds to a gain of 825.

2.6 Overall system results and discussions

Although I participated in all experimental developments described earlier, the final results presented in this section were obtained in my absence by the team at Fastlite. Nevertheless, all the methods employed to perform these measurements are explained in this section, and are the same as the one I used for the characterization of the second system in section 3.

2.6.1 Central wavelength

The output spectrum of the OPCPA is shown in figure (III.21). The spectrum presented here was recorded during the compression optimization tests and corresponds to Dazzler settings optimized for the best compression. Central wavelength of this spectrum is defined as the centroid of the spectral density function. The measured central wavelength is 2059 nm, the spectrum RMS width is 172 nm, and the FWHM is 461 nm. This spectrum supports a pulse duration of 18.9 fs.

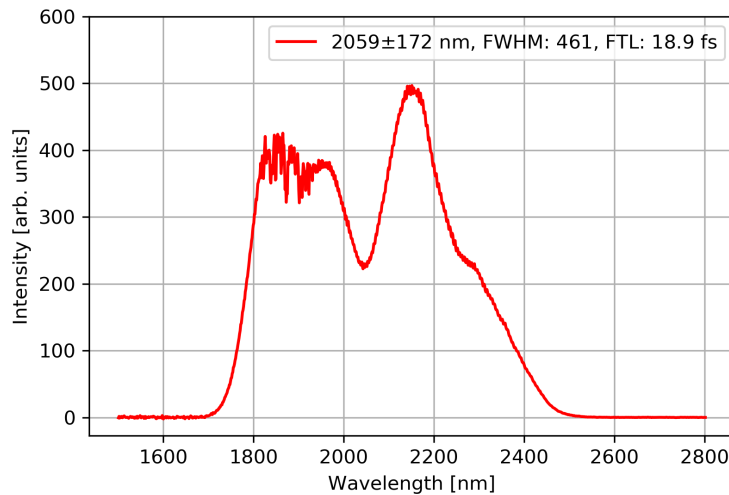


Figure III.21 – OPCPA output spectrum after compression.

2.6.2 Compressed pulse energy

The compressed output power is measured after the compressor which consists in 10 bounces off chirped mirrors (imparting -250 fs^2 per bounce) with a powermeter (Gentec). The compressed output power measured over 20 mn is shown in figure (III.22). The mean output power is 66 mW with 0.94 % RMS which corresponds to $33 \mu\text{J}$ of energy at 2 kHz.

2.6.3 Pulse duration

Temporal measurement: Wizzler

All output OPCPA pulse duration measurements are performed with a Wizzler (Fastlite). This method of measurement is based on the XPW effect (Cross-polarized Wave generation). This effect is a third-order nonlinear process that generates a pulse with orthogonal polarization upon propagation of a high intensity pulse through a medium with a non-isotropic nonlinear tensor (most of the time BaF_2). The XPW pulse is equivalent to the input pulse amplitude, filtered by its own temporal intensity. This pulse has a broader spectrum and a flatter phase with respect to the input pulse. As a consequence it can

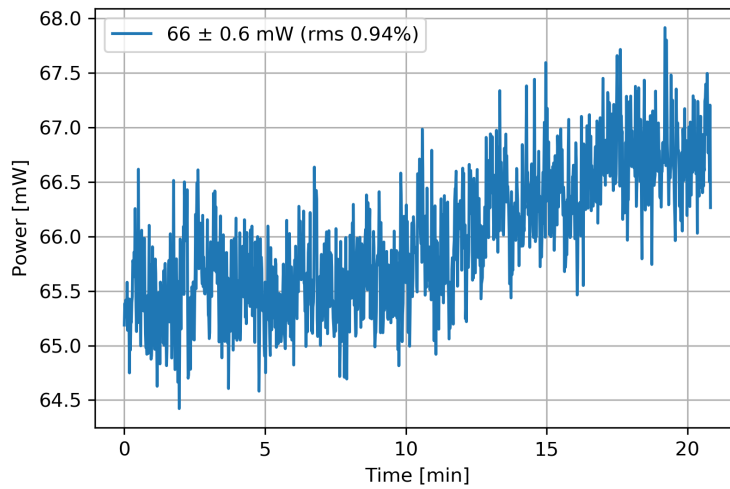


Figure III.22 – Compressed output power measured at 2 kHz, corresponding to an average pulse energy of 33 μJ .

be used as a reference for measuring the input pulse duration, using a measurement technique called Self-Referenced Spectral Interferometry (SRSI) as shown in figure (III.26).

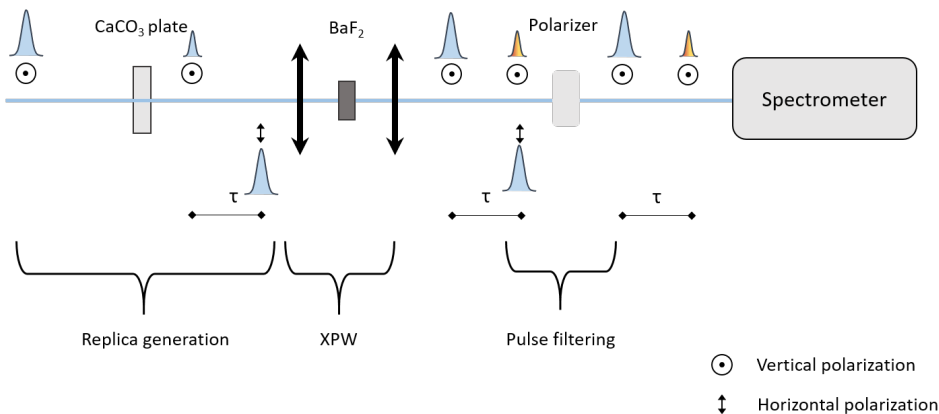


Figure III.23 – Wizzler working principle.

The main pulse is first going through a birefringent calcite plate and a small replica is created, delayed and with an orthogonal polarization with respect to the input pulse. The main pulse is then used to create an XPW signal with a broader spectrum, flatter phase and with an orthogonal polarization. Then the polarizer filters out the main pulse and lets through the replica and the XPW pulse. Both of these pulses are delayed by τ and propagate toward a spectrometer. The spectrometer then detects the interference spectrum between the first replica and the XPW reference signal.

Then an algorithm, the Fourier Transform Spectral Interferometry explained in section (2.6.5) is applied on this signal and both spectral phase and spectral intensity of the input pulse is extracted. This measurement technique works with almost compressed pulses. Indeed, its temporal duration should not exceed twice its FTL duration. This system is compact and allows pulse duration measurement below 20 fs. It pairs efficiently with the Dazzler since the measured spectral phase can be fed back to reach the FTL duration of the pulse.

The retrieved pulse duration is 18.5 fs and it is FTL after a few measurement feedback to the

Dazzler. Figure (III.24) depicts the output spectrum and spectral phase in the upper part and in the lower part the time intensity and phase.

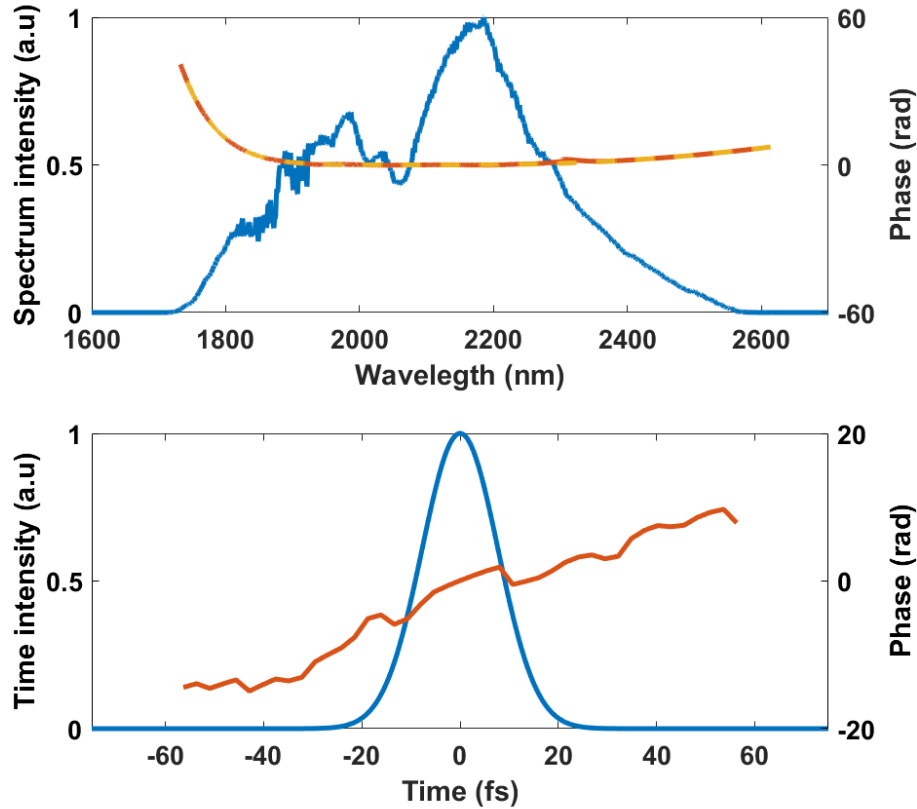


Figure III.24 – Top: spectral phase and intensity of the pulse. Bottom: temporal phase and intensity.

2.6.4 Pulse-to-pulse and long term power stability

Pulse-to-pulse stability was measured with a fraction (1 % RMS) of the output reflected beam from the output window. Parasitic SHG is filtered out with a plate of germanium. The output signal is recorded at the repetition rate of the laser by the high speed acquisition device named BigBrozzer. The specified pulse-to-pulse output stability is relative to the pump pulse-to-pulse stability, the latter was also measured by BigBrozzer.

From figures (III.25), the energy stability of the output was 1.79 % RMS over one hour whereas the pump energy stability was 1.35 % RMS during the same period. That corresponds to a relative stability of 1.33 % RMS over one hour.

The pulse energy of the output and the pump are recorded by BigBrozzer, results are shown in figure (III.25) for a duration time of 4 hours.

The output power of the OPCPA system follows the pump energy variation. The total stability over 4 hours, corresponding to the RMS of all pulses, is 3.65 % RMS for the output and 1.65 % RMS for the pump. As a conclusion, the output OPCPA energy varies twice as more as that of the pump laser.

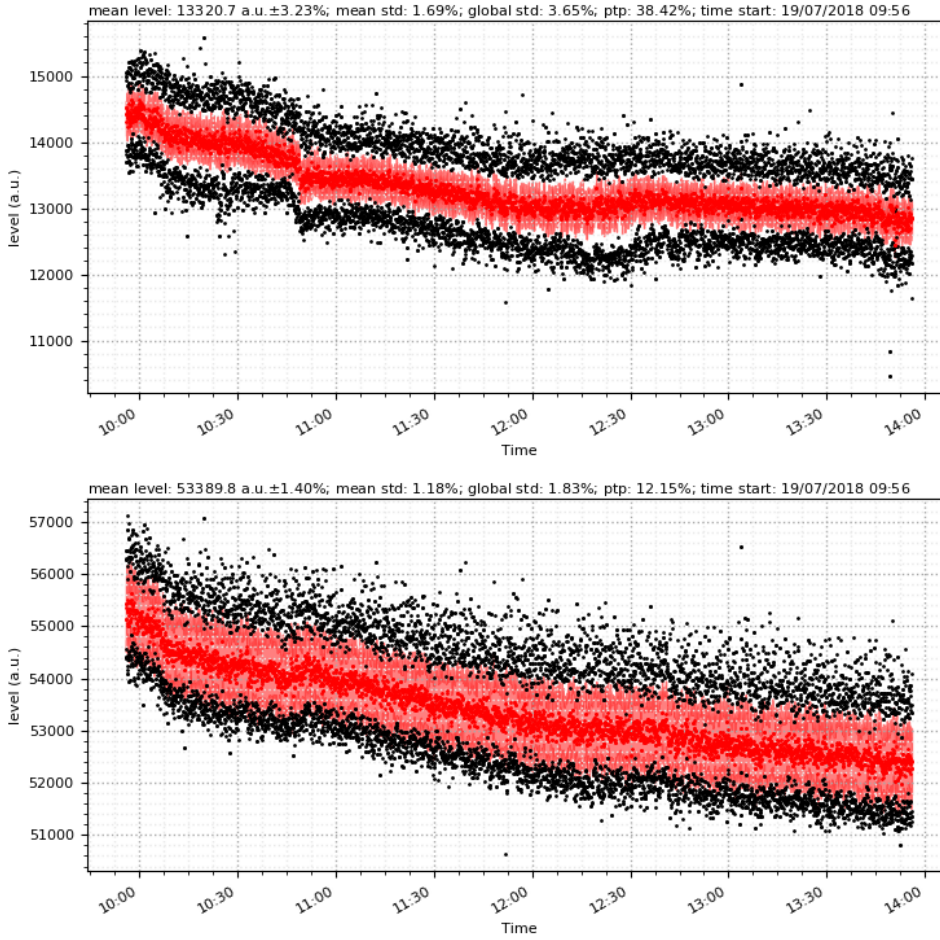


Figure III.25 – Red dots: mean energy for 5 seconds, filled area: standard deviation calculated for 5 seconds, black dots: minimum and maximum pulse energies for 5 seconds periods. Top: Long term output energy stability recorder for 4 hours. Bottom: Long term pump energy stability recorder for 4 hours.

2.6.5 CEP stability

CEP characterization

In this section we realize the measurement of CEP fluctuations of the OPCPA system. In order to do so, we implemented a f-2f scheme with an appropriate detection setup. In order to understand the principle of the measurement, let us consider the fundamental electric field from our OPCPA in the frequency domain:

$$E(\omega) = |E(\omega)|e^{i\Phi_{CEP}}. \quad (\text{III.1})$$

And the second harmonic of the fundamental delayed by a time τ , obtained in the same frequency range as the fundamental (which requires an octave-spanning spectrum)

$$E(\omega) = |E_2(\omega)|e^{i(2\Phi_{CEP}+\omega\tau)}. \quad (\text{III.2})$$

The delay τ is induced by the fact that each wave does not travel at the same speed while propagating inside materials. The detector acquires the intensity of the sum of these two components meaning that:

$$I(\omega) = |E(\omega) + E_2(\omega)|^2 = |E(\omega)|^2 + |E_2(\omega)|^2 + 2|E(\omega)||E_2(\omega)|\cos(\omega\tau + \Phi_{CEP}). \quad (\text{III.3})$$

The two first terms in the equation (III.3) are not spectrally modulated but the last term exhibits spectral fringes with a period determined by the delay and a position determined by the CEP phase. The drawing in figure (III.26) explains the FTSI principle and shows these fringes a) obtained directly from the f-2f interferometer.

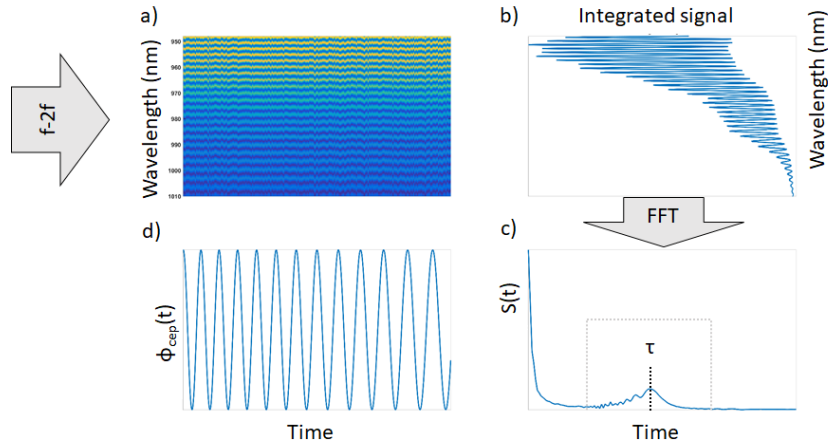


Figure III.26 – Schematic representation of the CEP measurement technique based on spectral detection at the output of an f-2f interferometer.

The signals received by the detector are spectral fringes as shown in figure (III.26). If the detector is slow compared to the repetition rate of the laser, the signal is integrated (III.26 b)). Then a Fast Fourier Transform (FFT) is applied on the acquired spectrum (integrated or not). Figure (III.26 c)) shows its magnitude square. The first peak is centered at τ (corresponding to the delay between the two pulses coming from the f-2f). Then, the CEP phase changing as a function of time is displayed in figure (III.26 d)) by selecting the peak centered at τ and measuring its phase variation in time.

This measurement technique requires that the detector be carefully chosen. Two main characteristics have to be taken into account, the integration time and the sampling rate.

The integration time corresponds to the time during which the detector is illuminated by the beam to acquire a single fringe pattern. If we want to estimate the CEP fluctuations for a single pulse of the laser, this time must be lower than the period T_R (corresponding to $1/f_R$). The sampling rate corresponds to the number of acquisitions per given time interval. It is limited by the connection between the spectrometer and the computer (order of ms). Once the CEP phase is acquired as a function of time it is interesting to look at the Power Spectral Density (PSD) to identify the frequency characteristics of the noise contributing to CEP RMS stability. Nevertheless, the PSD is limited to half the sampling frequency (due to the Nyquist-Shannon sampling theorem). In our case, if the sampling rate is equal to the repetition rate of the laser (2 kHz), f_{max} of the PSD is 1 kHz.

To detect the fringe pattern we used a Fringeazz (Fastlite). This device has an integration time low enough for our system (less than 100 μs) and a sampling rate up to 10 kHz (meaning that the maximum frequency for the PSD is $f_{max}=5$ kHz). That device suits our needs in term of single shot, every shot acquisition.

CEP stability is measured with a fringe detector (Fringeazz) fed by an 2f-to-f interferometer. The measured CEP is fed back to Dazzler. As a consequence, the presented results are in-loop measurements. The evolution of the CEP is shown in figure (III.27).

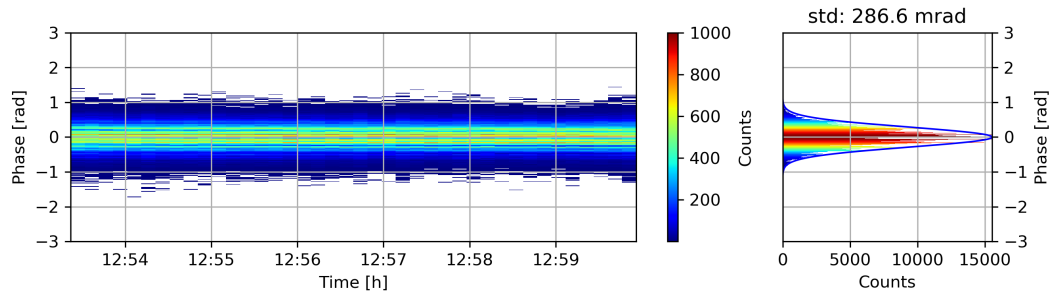


Figure III.27 – Left: evolution of the carrier-envelope phase during the best five minutes. Each column corresponds to 20 k laser shots, corresponding to 10 seconds at 2 kHz. Right: total histogram of measured CEP.

The best RMS CEP stability is 287 mrad. The pulse-to-pulse intensity stability plays an important role in the CEP stability because of intensity-to-phase noise transfer mechanisms such as SPM. As a consequence, with better pulse-to-pulse stability of the pump, a better CEP stability is expected.

2.6.6 Spatial profile: Strehl ratio

Strehl ratio was calculated by comparing the measured far-field profile to the theoretical far-field profile obtained from the experimental near field beam profile. Far-field profile was measured by inserting a plano-convex lens with a focal length of 500 mm at the location where the near-field profile was recorded. The measurements are shown in figure (III.28).

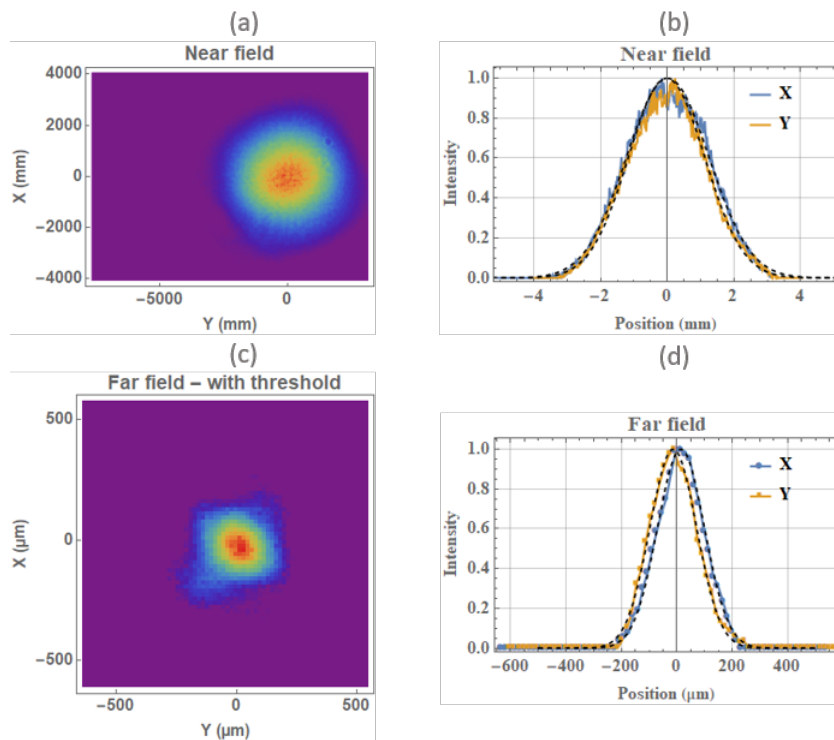


Figure III.28 – (a) Spatial near-field profile, (b) X and Y profiles with corresponding Gaussian fits with radii of 2.5 mm and 2.3 mm. (c) Recorded and filtered spatial far-field profile, (d) X and Y profiles with corresponding Gaussian fits with radii of 170 μm and 170 μm .

As a result, by comparing the peak fluence of the measured far-field beam profile to the calculated

one, the Strehl ratio is 0.75.

2.6.7 Pointing stability

In order to measure the pointing stability the same setup as the Strehl ratio is used. The output beam of the OPCPA is focused with a plano-convex lens with a focal lens $f=500$ mm. Results are shown in figure (III.29).

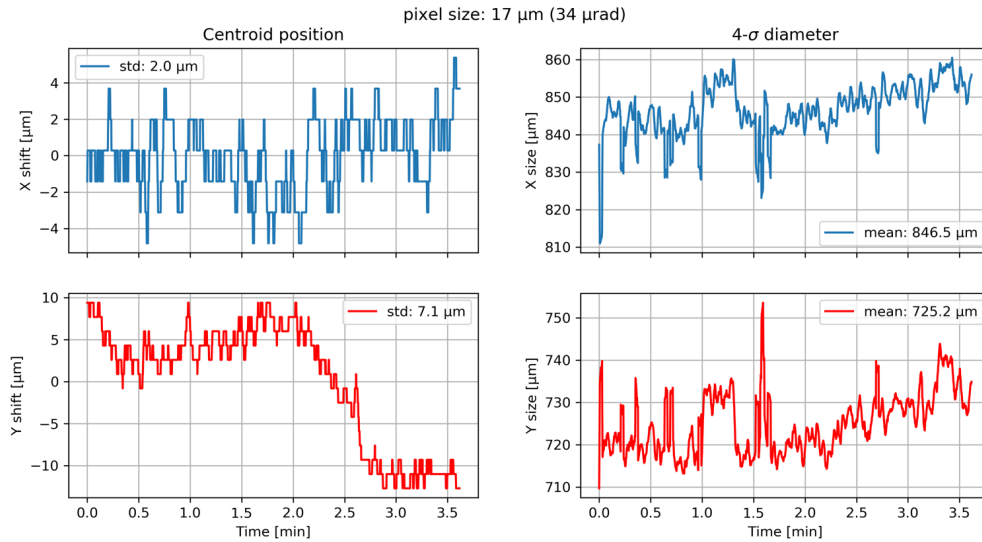


Figure III.29 – Left plots: Centroid position as a function of time in the horizontal and vertical directions. Right plots: horizontal and vertical diameters measured at 4σ as a function of time.

During the test of a few minutes, the centroid of the focused beam remained within $\pm 2 \mu\text{m}$ in the X direction and $\pm 7 \mu\text{m}$ in the Y direction. Comparing the 4σ diameters of $846 \mu\text{m}$ and $725 \mu\text{m}$, the RMS pointing stability is between 0.25 % and 1 %. Although the pointing stability measurement is not done on the long term, the far-field spot does not change its position from one day to another.

2.6.8 Uninterrupted operation

The longest recorded operation of the OPCPA is 8 hours. Figure (III.30) shows the energy output measured by Bigbrozzer. The interruption in the data record is due to some perturbation in the electric network. The region of high instability is associated to an un-synchronized operation of BigBrozzer following the network electric perturbation.

2.6.9 Conclusion

All the values measured are presented in table (III.4):

To summarize this part, all specifications are not reached, so the design of a new source is needed. In particular, the CEP stability is about twice as worse as the specification, calling for another frontend design. The second part of this chapter is dedicated to this new source.

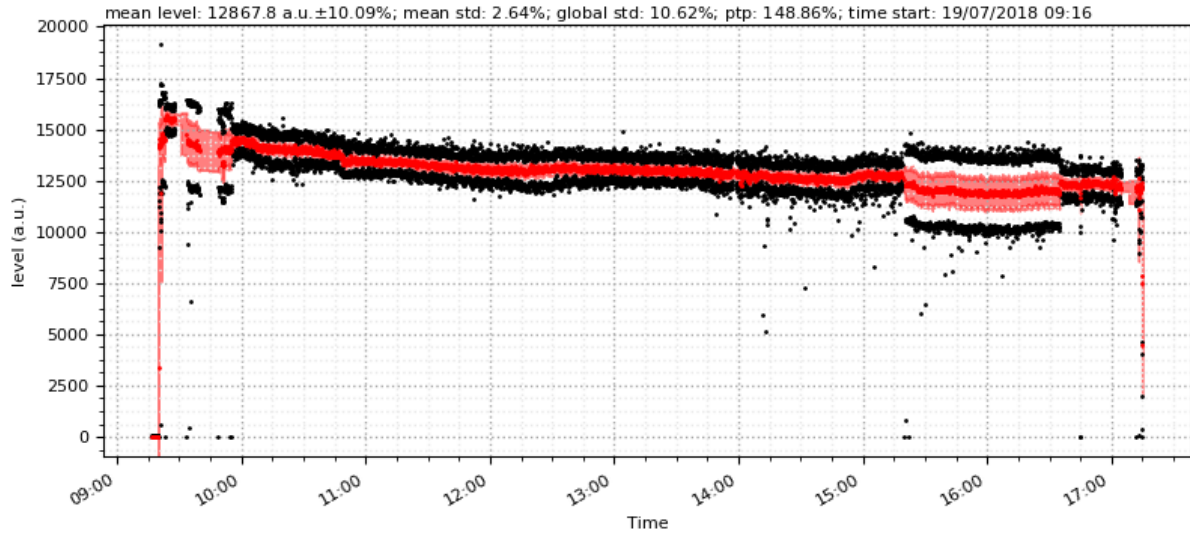


Figure III.30 – Output energy recorded over 8 hours.

Specifications	Values	Measured	Units
Central wavelength	2100 ±100	2059	nm
Compressed pulse energy	> 30	33	μJ
Repetition rate	10 or 20	Not tested	kHz
Pulse duration FWHM	< 20	18.5	fs
Pulse-to-pulse stability (over 1000 shots)	1.5 times the pump stability	<1.5	% RMS
Long term power stability (8h)	1.5 times the pump stability	2	% RMS
CEP stability	< 150	290	mrads RMS, single-shot
Strehl Ratio	> 0.8	0.75	-
Pointing stability	0.1x diffracted limited beam divergence	0.01	RMS
Uninterrupted operation	>8	8	hours
Warm up time	<1	few minutes	hours

Table III.4 – Summary of measured specifications for the first OPCPA architecture.

3 Second architecture: DFG from a 1030 nm pump laser

As explained in the first part of this chapter, the source will be installed on a different laser pump than the one where it is developed. This time, we use another laser source (Tangor, Amplitude). This system has a variable output energy and average power (up to 100 W at 140 kHz), and we can change the repetition rate to integer submultiple of 140 kHz. For this development, the laser is running at 10 kHz with an energy of 500 μJ per pulse. This laser generates FTL pulses with a duration of 300 fs at 1030 nm. Again, in order to be in the same conditions as with the final pump laser, the output compressor is tuned in order to reach a pulse duration of 890 fs. Figure (III.31) shows a SHG-FROG temporal and spectral measurement of the pump pulse.

The spatial profile of the laser is presented in figure (III.32). The beam is almost Gaussian with an elliptical ratio of 89 % in the near field and 87.5 % in the far field. The beam size measured in the near-field is 3.99x4.48 mm² (III.32, top). The far-field measured with a 750 mm long focal length has a Gaussian shape with 536x469 μm² dimensions (III.4 b)). Both measurements were done using a silicon-based camera (Basler with a pixel size of 9.9 μm).

A scheme of this second implementation of the OPCPA is presented in figure (III.33). The ar-

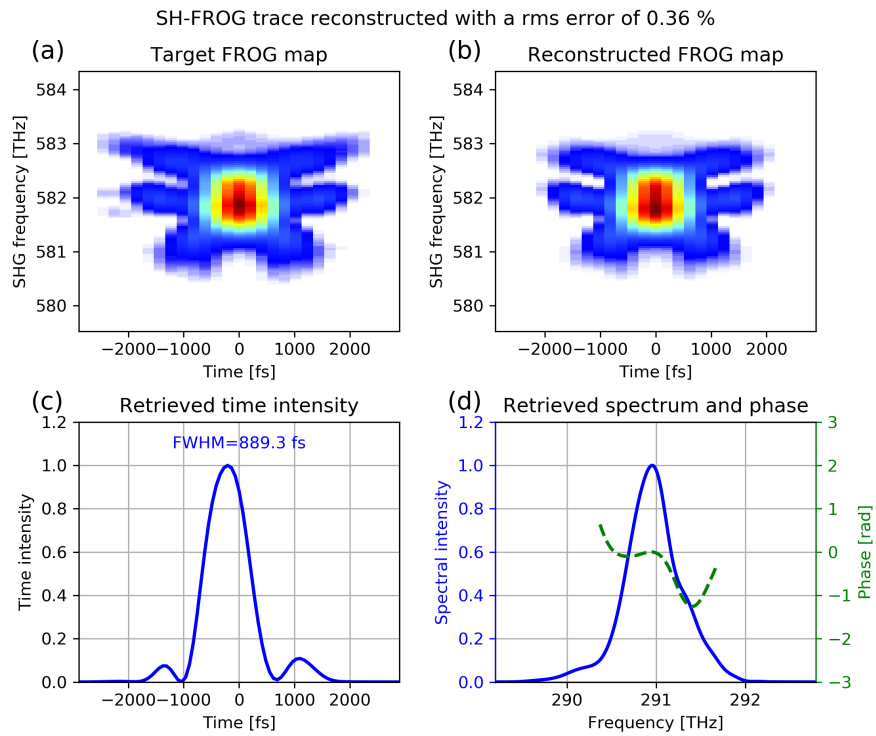


Figure III.31 – SH-FROG of the stretched pump laser. (a) Measured FROG trace (b) Reconstructed FROG with a RMS error of 0.36 % (c) Retrieved temporal intensity of the pulse with a duration of 889 fs (d) Retrieved spectrum and phase of the pump laser.

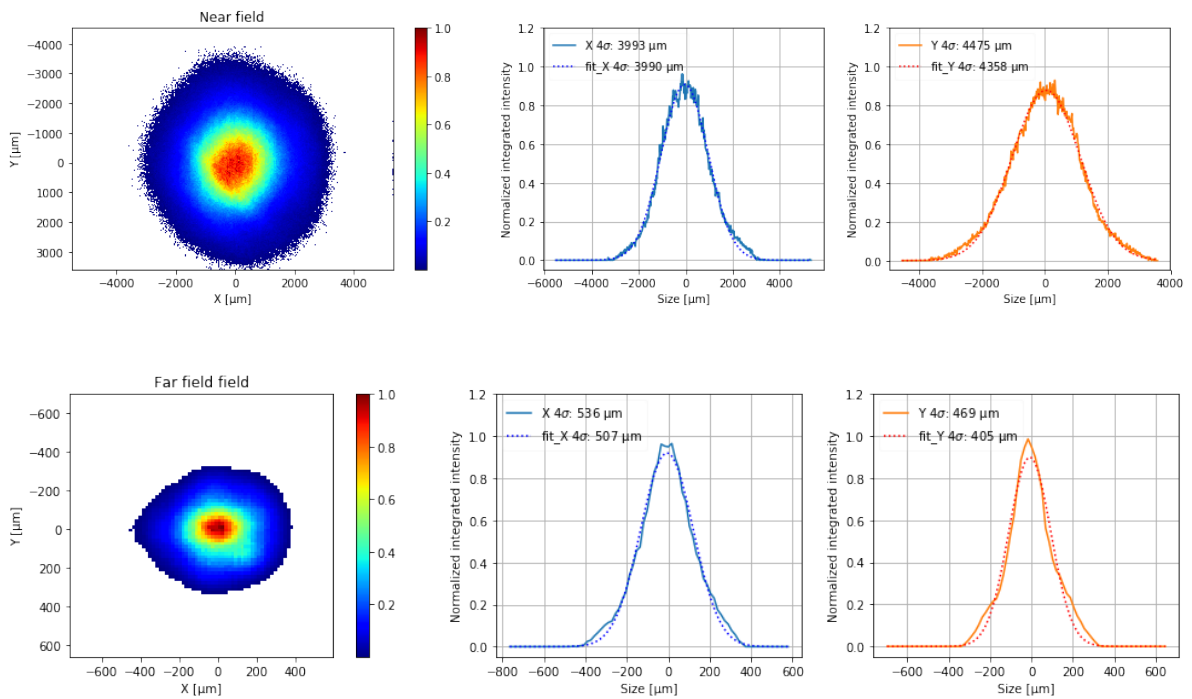


Figure III.32 – Top: Spatial profile in the near field of the pump laser. Bottom Spatial profile in the far field of the pump laser focus with 750 mm lens.

chitecture is less complex than the previous one because the SHG stage is removed. Moreover, the CEP-stable seed generation architecture, aiming at a better stability, is proposed for the first time to our best knowledge. It has been filed as a patent in 2018. In the first part of this section, this new technique is presented in details. Then the rest of the OPCPA layout, almost identical to the previous one, is presented.

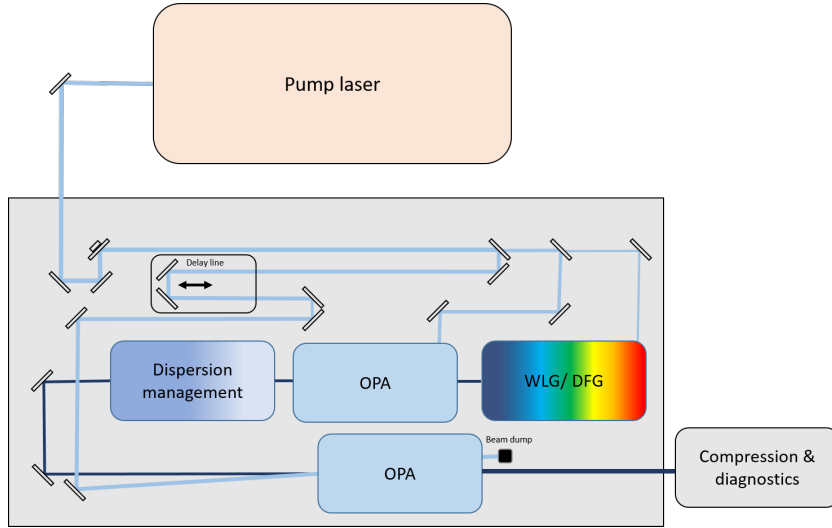


Figure III.33 – Second layout of the OPCPA, with the signal generated by an all inline DFG scheme.

3.1 Seed generation from an all inline DFG scheme

3.1.1 Layout

The CEP fluctuations are due to different factors such as the variations inside the interferometer formed by both arms of the DFG scheme. In the previous scheme, both signal and pump pulses travel down two different paths, and the phase variations along these paths can cause fluctuations on the CEP stability. We implemented a new technique to mitigate these fluctuations. The scheme is depicted in figure (III.34).

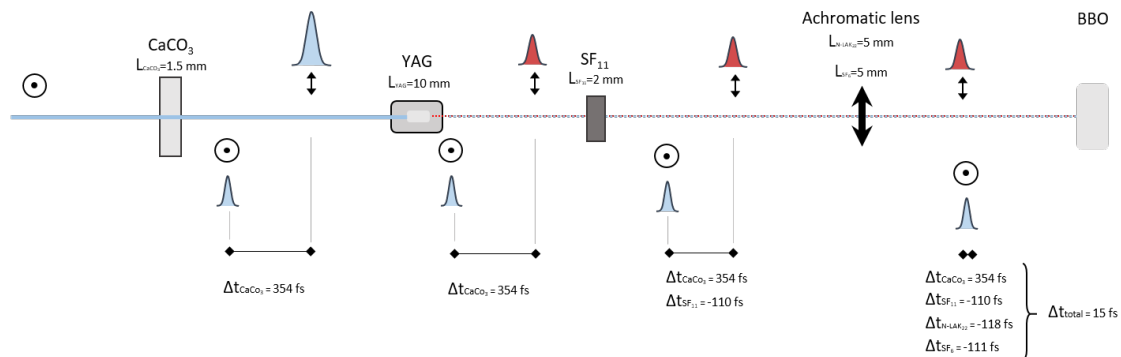


Figure III.34 – All inline CEP stable DFG scheme.

The pump beam at 1030 nm is split and delayed into two different polarizations after passing through a birefringent plate of calcite (CaCO_3). Table III.5 summarizes the group refractive indices of four relevant materials for this setup.

	$\lambda= 670 \text{ nm}$	$\lambda= 1030 \text{ nm}$
$n_{og} (\text{CaCO}_3)$	/	1.6625
$n_{eg} (\text{CaCO}_3)$	/	1.4875
$n_g(\text{SF}_{11})$	1.8413	1.7869
$n_g (\text{SF}_6)$	1.863	1.807
$n_g (\text{N-LAK}_{22})$	1.6746	1.655

Table III.5 – Group refractive indices of CaCO_3 , SF_{11} , SF_6 and N-LAK_{22} at wavelengths 670 nm and 1030 nm.

	DFG	OPA 1 and OPA 2
Pump frequency	ω_0	ω_0
Pump phase	$\Phi_p = \Phi_0 - \frac{\pi}{2}$	$\Phi_p = \Phi_0$
Signal phase	$\Phi_s = \Phi_0$	$\Phi_{s \text{ out}} = 0$
Idler phase	$\Phi_i = 0$	$\Phi_{i \text{ out}} = \Phi_0 - \frac{\pi}{2}$

Table III.6 – Phases and frequencies of each beams in the OPCPA. Fundamental frequency and phase are ω_0 and Φ_0 at the output of the pump laser.

For a thickness of 1.5 mm of CaCO_3 , the orthogonally polarized pulses are delayed by:

$$\Delta\tau = \frac{L_{\text{CaCO}_3}}{c} \left(\frac{1}{n_{eg}} - \frac{1}{n_{og}} \right) = 354 \text{ fs}. \quad (\text{III.4})$$

The calcite plate axes are oriented to create an intense replica, and a low intensity one. The beam is then focused in a 10 mm long YAG crystal, triggering WLJ for the most intense pulse. If we consider that the signal around 670 nm is generated at the output facet of the crystal the delay between the signal and the pump (less intense replica at 1030 nm) is unchanged. In order to reduce this delay we use a 2 mm plate of SF_{11} , this decreases it by 110 fs. Then the beam is focused into a 1 mm long BBO with an achromatic lens composed of two different materials, SF_6 (2 mm) and N-LAK_{22} (5 mm). This lens, with these two materials reduce the delay by 118 fs for the LAK_{22} and 111 fs for the SF_6 . Just before the amplification, both pulses are therefore almost synchronized. A small delay of 15 fs is still present and can be neglected compared to the pump duration (850 fs). In this all inline scheme, the pump and signal share the exact same optical path, and we expect this to reduce considerably technical noise due to vibrations and air movement. The mechanism for CEP stability is summarized in table III.6.

The system is passively CEP stable, the next sections will detail the building process of the OPCPA.

3.1.2 Experimental results

The WLJ spectrum obtained at the output of the YAG (10 mm) crystal is plotted in figure (III.35).

This spectrum is a solid starting point for the DFG inside a BBO crystal because it covers more than the required bandwidth from 600 nm to 900 nm.

The DFG is achieved using a 1 mm long BBO crystal in type I configuration, the phase-matching curve is shown in figure (III.36)

The acceptance bandwidth of the crystal cut at 20.1° pumped at 670 nm wavelength to amplify a

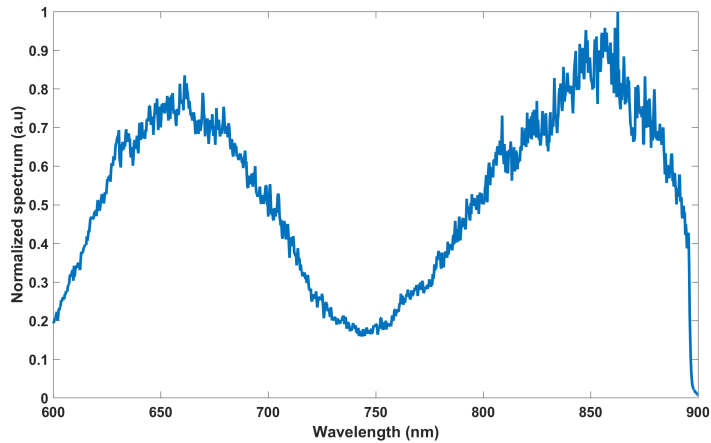


Figure III.35 – WL spectrum filtered with a short pass filter at 905 nm and a long pass filter at 515 nm obtained in a 10 mm YAG crystal.

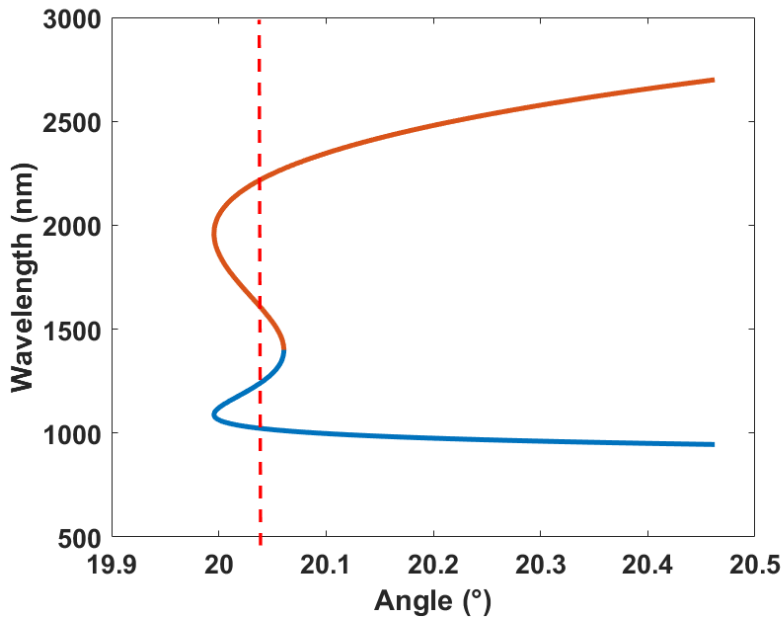


Figure III.36 – Phase matching curve for a BBO crystal pumped with a 700 nm beam.

signal centered at 1030 nm is $\Delta\lambda=612$ nm. This crystal is therefore well suited to generate a broadband CEP stable idler.

3.2 First amplifier stage

Because the energy of the CEP-stable seed is lower than in the first version of the system, two amplifiers stages are needed. The first amplifier stage has the same geometry as in the first architecture (figure (2.5)). The configuration is used for the same reasons as before. The noncollinear geometry is needed to separate the degenerate CEP-stable signal and the idler. The nonlinear crystal is a 1 mm fanout MgO:PPLN. Its periods spans continuously from 24 μm to 32 μm . Before the amplifier, a silicon plate is used at 45° angle in order to absorb the amplified signal of the DFG stage and the pump at 1030 nm. The reflected part of the beam is used as a diagnostic to feed BigBrozzer with the spectrum and energy of the DFG stage.

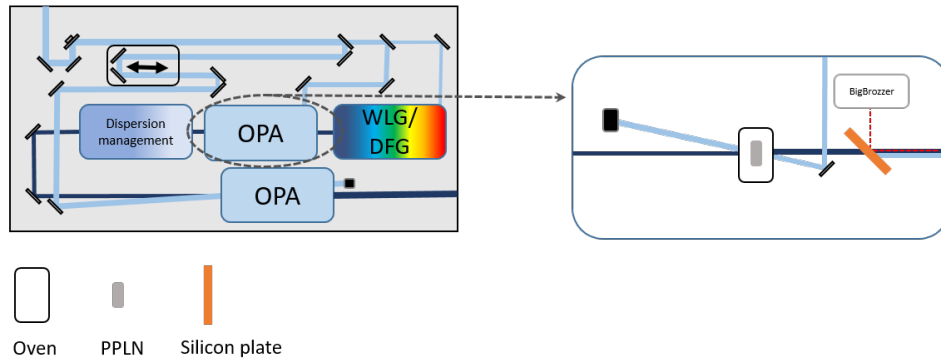


Figure III.37 – First amplification stage.

The pump and signal have a respective size in the crystal of $211 \times 210 \mu\text{m}^2$ and $454 \times 280 \mu\text{m}^2$. At that stage, the pump energy is $40 \mu\text{J}$. The resulting spectrum is plotted in the same figure (III.38) with an output energy of $1.9 \mu\text{J}$.

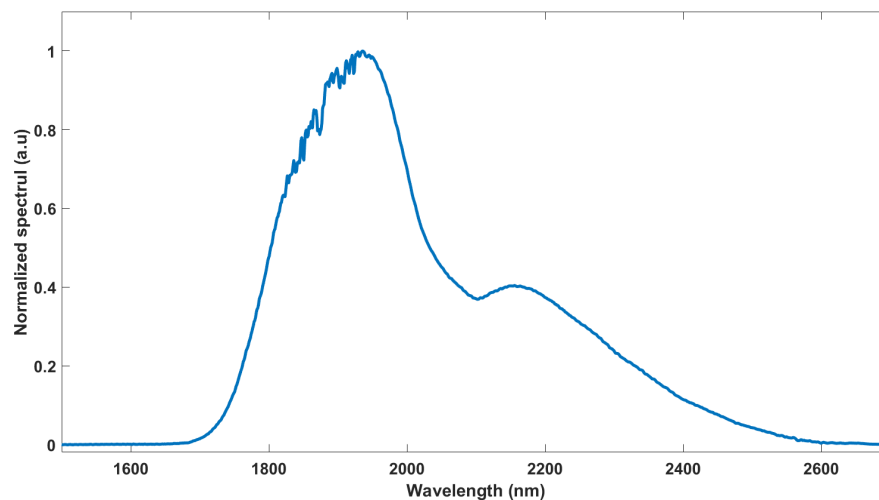


Figure III.38 – Output spectrum of the first amplifier stage.

3.3 Dispersion management

In this part, the scheme is quasi identical to the one discussed in the first version of the system figure (2.4). One difference is that the bulk material is now a 18 mm-long piece of silicon. This material exhibits (at $2.1 \mu\text{m}$) $766 \text{ fs}^2/\text{mm}$. As a consequence, the signal is stretched with 13788 fs^2 . The Dazzler second order spectral phase is set to -10600 fs^2 in order to compress the signal close to the pump duration. At the output, chirped mirrors are used to compress the pulses. These chirped mirrors exhibit -250 fs^2 per bounce. In that particular case, only 10 bounces (-2500 fs^2) allow the compression of the pulse to the FTL. All the settings of the Dazzler are shown in figure (III.39). The device exhibits -10600 fs^2 , -49000 fs^3 and -100000 fs^4 . The third and fourth order are first calculated (taking into account all the materials in the chain). Then they are adjusted while measuring the output pulse duration.

At the very end, the pulse are characterized using a Wizzler and the resulting spectral phase is fed back to the AOPDF to achieve FTL pulses.

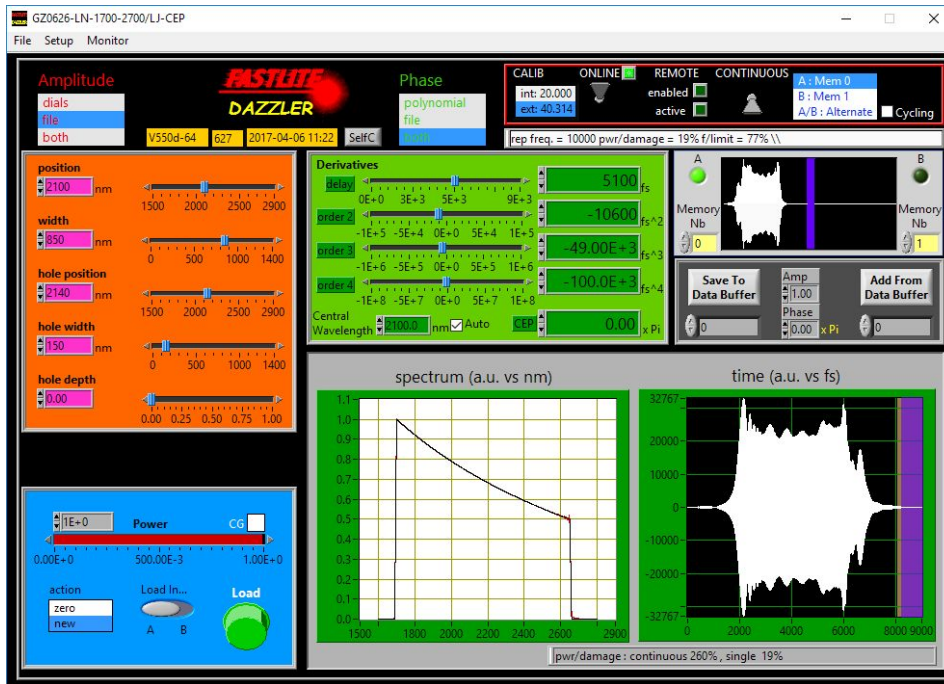


Figure III.39 – Screen capture of Dazzler settings used in the OPCPA.

3.4 Second amplifier

The scheme of the second amplifier is the same as depicted in section (2.5) for the first version of the architecture. The pump and signal are temporally and spatially overlapped in three periods (29.2/29.62/30.16 μm), 1 mm long MgO:PPLN. An external angle of 5° is formed between the pump and the signal. We used the longer period of 30.16 μm in the crystal for the amplification/. The pump and beam size have a size of 1275x934 μm^2 and 879x934 μm^2 respectively.

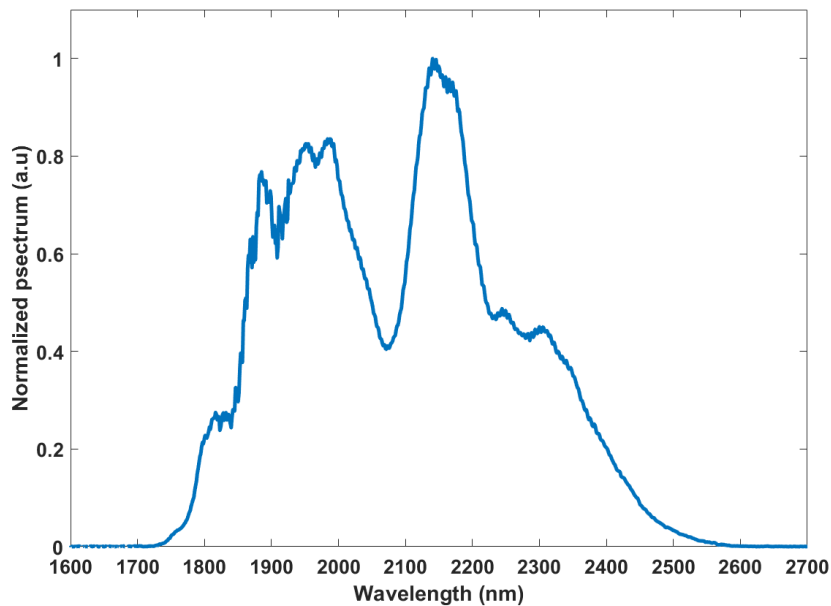


Figure III.40 – Output spectrum of the second amplifier stage.

The amplifier is seeded with an energy of 100 nJ and amplifies to 37 μJ . That represents a gain in

single pass of 370. The spectrum is plotted in figure (III.40) and spans from 1700 nm to 2650 nm. The next section summarizes all the results obtained during the specification characterization.

3.5 Output measurements and discussion

In this section all measurements performed at the output of the system are described. Figure (III.41) shows all the measurement devices used during these characterizations. The beam is routed to the

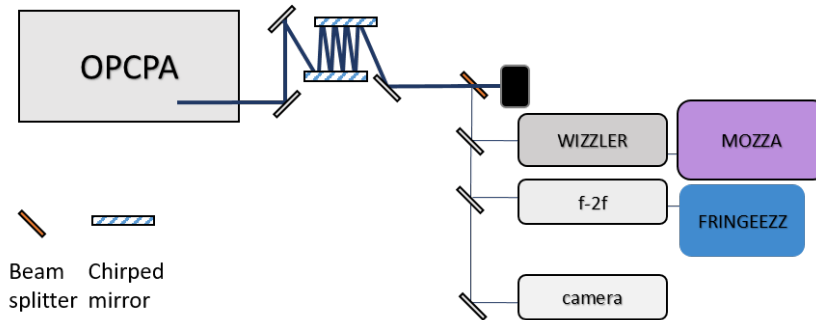


Figure III.41 – Schematic of the diagnostics at the output of the system.

compressor composed of chirped mirrors. After 8 bounces, the beam is split into two parts, the major part of the energy is directly sent into a powermeter to monitor the energy fluctuations. The reflected part of the beam is sent to the diagnostics: Wizzler, f-2f interferometer, and spatial diagnostics (beam profile, pointing stability and Strehl ratio).

3.5.1 Pulse duration

The best results in term of pulse duration and output energy were achieved with 8 bounces (-250 fs^2 per bounce). The output beam contains parasitic SHG (even with the angle between the pump and the signal in the last amplifier stage), that represents 12 % of the total energy. That energy is removed by dichroic mirrors used to route the beam to the compressor. At the input of the compressor $32.5 \mu\text{J}$ are available. After 8 bounces, the energy drops down to $31 \mu\text{J}$, corresponding to 95 % of efficiency for the compressor.

The pulse is measured with a temporal characterization device (Wizzler, Fastlite) coupled with a spectrometer (Mozza, Fastlite). The measured spectral phase was feedback to the Dazzler until the measured pulse duration was equal to FTL pulse duration. Figure (III.42) shows the retrieved spectrum and its phase and the temporal profile of the pulse. The measured time duration is 19.4 fs.

3.5.2 Strehl ratio

In order to perform the Strehl ratio measurement the spatial profile of the beam is measured in the near and far field. In that case we used a silicon camera (Basler ACE) in Two-Photon Absorption (TPA) mode. As a consequence, to obtain an equivalent beam profile intensity, an operation of square root was applied to the measurement.

To validate the TPA measurement with the silicon camera we performed another set of measurement. A 500 mm focal lens is used. Two different cameras were used, the same silicon camera used to perform the Strehl ratio measurement and a microbolometer camera (DIAS). Both of these measurements are presented in figure III.43.

For the silicon camera, the beam size is $300 \times 265 \mu\text{m}^2$ with the square root factor and for the microbolometer, the beam size is $274 \times 272 \mu\text{m}^2$. The ratio of these beams exceed 0.96, which confirms

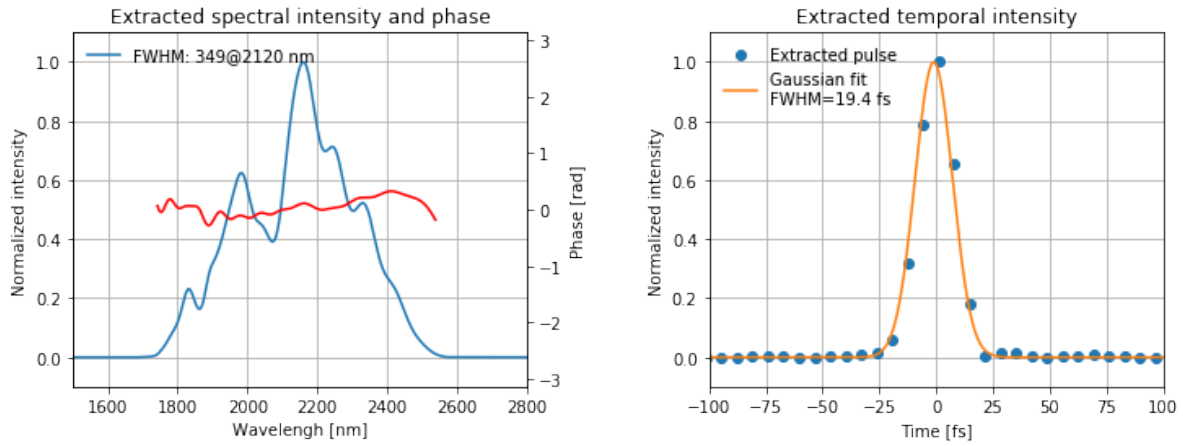


Figure III.42 – Compressed output power measured at 10 kHz, corresponding to an average pulse energy of $31 \mu\text{J}$ with a pulse duration of 19.4 fs. Left, spectral phase and spectral intensity, right time intensity.

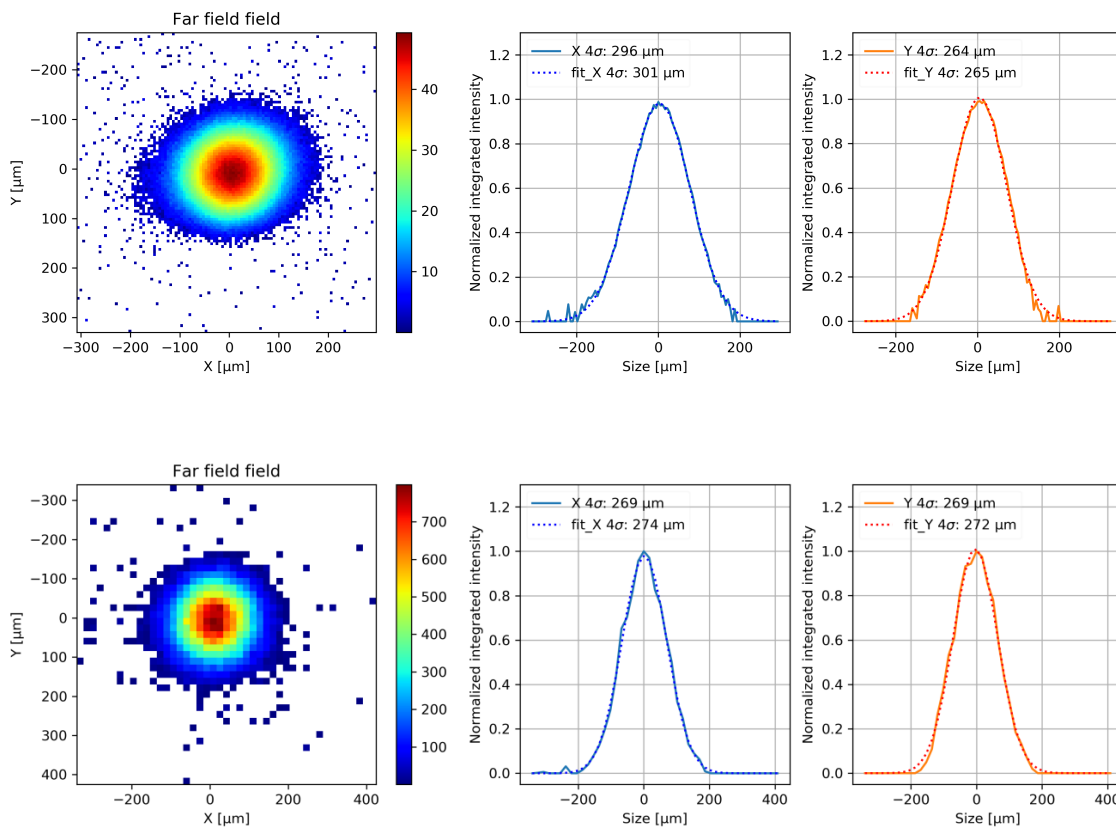


Figure III.43 – Top: Spatial profile in the far field of the OPCPA output obtained with a silicon camera via TPA. Bottom: spatial profile in the far field of the OPCPA output obtained with a microbolometer camera. Both measurements are made at the focal plane of a 500 mm focal lens.

the usability of the TPA measurement.

In order to perform the Strehl ratio measurement, a 200 mm focal length is used. Figure (III.44) shows the near and far field profiles of the output of the laser.

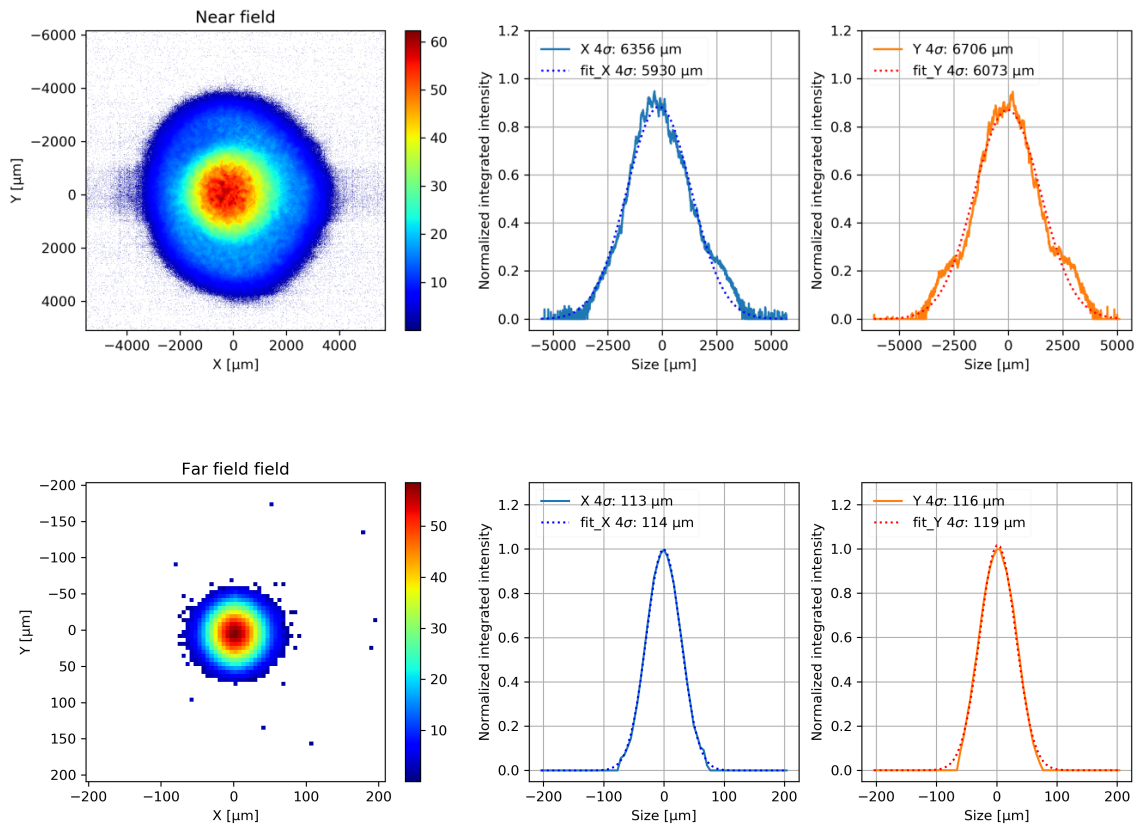


Figure III.44 – Top: spatial profile in the near field of the OPCPA output. Bottom: spatial profile in the far field of the OPCPA output focused with a 200 mm lens.

The near field profile diameter is $6 \times 6 \text{ mm}^2$ and the far field profile is $114 \times 119 \mu\text{m}^2$. Theoretical focused spot width corresponding to the near field is $103 \times 99 \mu\text{m}^2$. By comparing relative peak fluence of the measured far field and the computed far field, the Strehl ratio is 0.91.

3.5.3 Pointing stability

The pointing stability is measured at the focal plane of a 500 mm focal lens at the output of the OPCPA with a silicon camera (Basler) using TPA.

Both the longitudinal and vertical coordinates experience small fluctuations of position as a function of time. For the vertical axis, Y, standard deviation shows 3.17 μm over 180 minutes and the horizontal axis, X only 1.45 μm . By comparing these data to the beam size (as shown in figure III.43) that represents 1.1 % and 0.05 % respectively for the vertical and horizontal axis. These measurements are within the required specifications.

3.5.4 Energy and CEP stability

To detect the fringe pattern we used a Fringezzz (Fastlite) device, which is essentially a low resolution fast acquisition spectrometer, as explained previously.

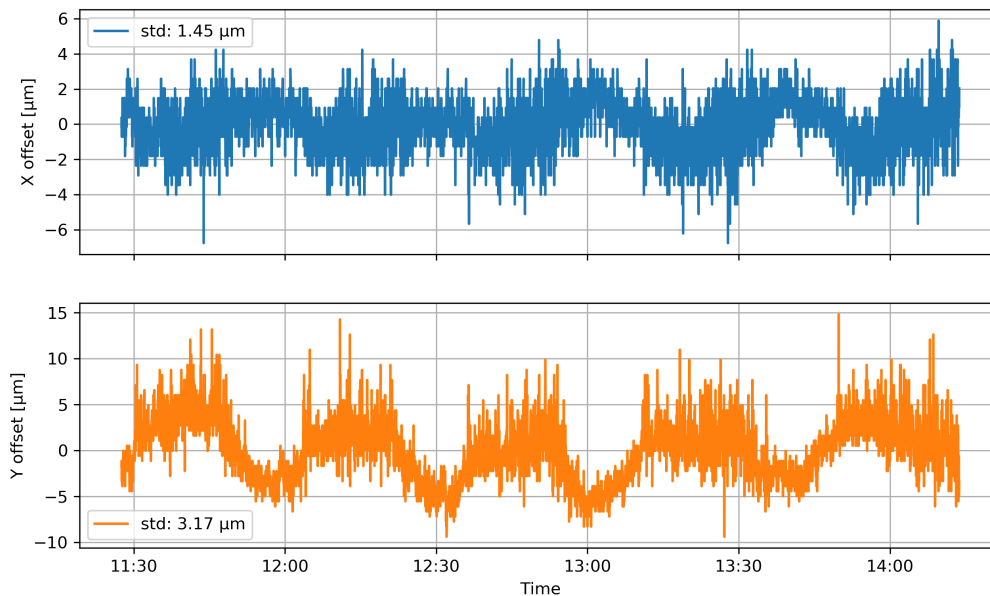


Figure III.45 – Pointing stability at the output of the OPCPA measured at the focal plane of a 500 mm lens. Top: offset position of the X axis as a function of time. Bottom: offset position of the Y axis as a function of time.

f-2f interferometer setup description

To generate the fringes to feed the detector in order to characterize the CEP fluctuations of our system we built the setup depicted in figure (III.46).

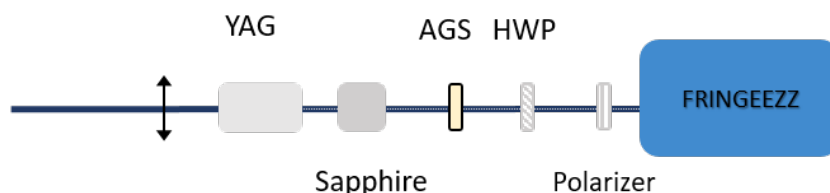


Figure III.46 – Schematic representation of the f-2f interferometer used to characterize CEP fluctuations.

The interferometer is composed of a 4 mm-long YAG crystal for WLG that generates a spectrum that expands from 1400 nm to more than 3000 nm. Then a sapphire plate is used to delay both extreme parts of the WL spectrum. The SHG crystal (AGS) is tuned in order to generate the second harmonic of the WL around 1500 nm. Then a half-wave plate (HWP) and a polarizer are used to project both components in order for them to interfere.

This all inline configuration allows a compact and stable setup (as the inline DFG generation presented at the beginning of this section). All the components are carefully chosen to create a delay between both frequency components f and $2f$. In this case the delay is determined by the difference of group velocity of the f and $2f$ beams.

The first measurement is realized with FringeZZ, an integration time of 10 μ s and a sampling rate of 10 kHz. It is synchronized with the Octopuzz synchronization unit. The results are plotted in figure

(III.47), over four minutes, representing 2.4×10^5 pulses.

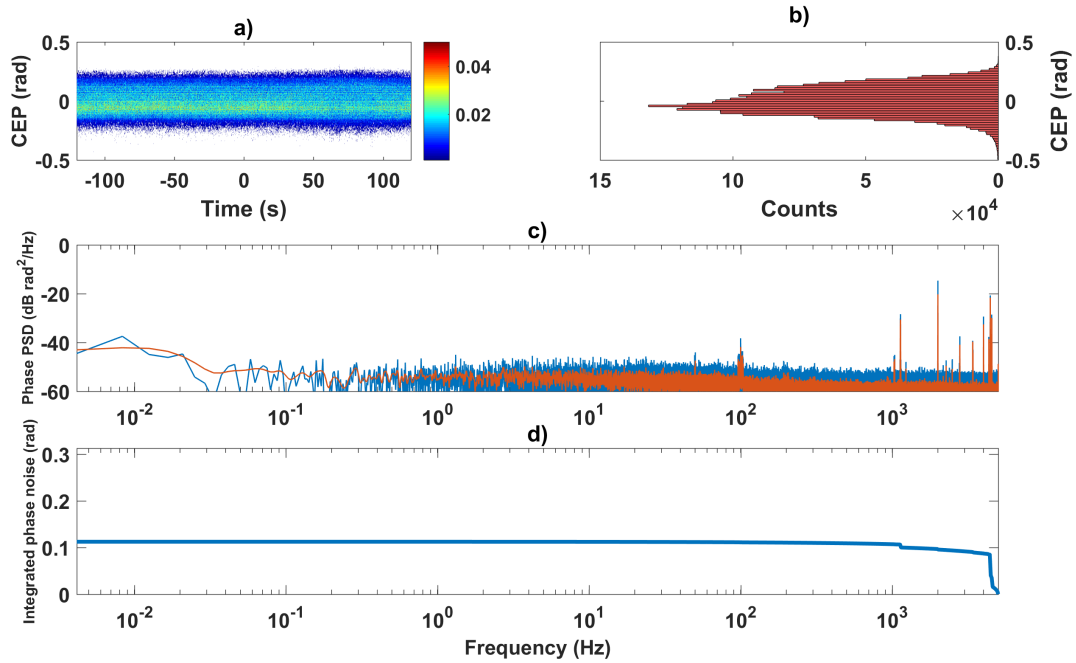


Figure III.47 – a) CEP fluctuation as a function of time and b) CEP histogram. c) In blue raw PSD (in orange filtered PSD) of the CEP fluctuations. d) Integrated CEP noise. All these measurements were recorded during 4 minutes.

In figure (III.47 a) and b)) the CEP phase probability density function is plotted as a function of time, the PSD is plotted in figure (III.47 c), allowing to identify the frequencies that contribute to the CEP noise. A large contribution of noise is observed at high frequencies, above 1 kHz. In (III.47 d)) the integrated noise is represented corresponding to 112 mrad RMS fluctuations. All these measurements are done with a feedback loop connected to the Dazzler.

The long term measurement is done over 4 hours, and records simultaneously pump energy fluctuations, CEP fluctuations, output energy fluctuations and room temperature. All these data are plotted and shown in figure (III.48).

The CEP stability is 107 mrad RMS for 4 hours, and the output energy has an RMS fluctuation of 0.58 % (0.54 % for the pump laser). The temperature room oscillates from 21.75 to 22.75 °, and the CEP, pump and output energies follow the same tendency. It is important to keep in mind that the laboratory environment has an influence on the laser system.

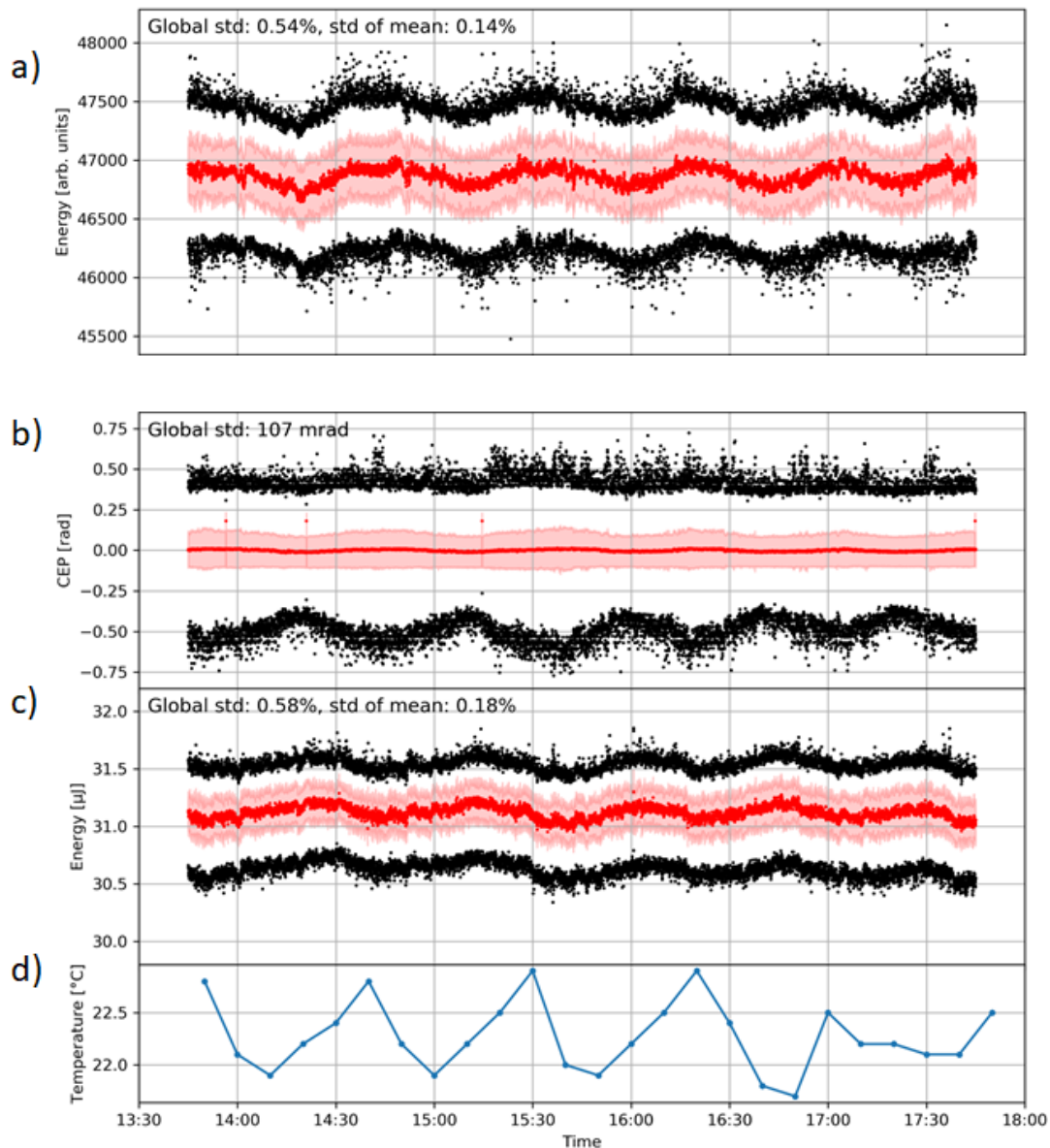


Figure III.48 – a), b), c) Red dots: mean measurement for 5 seconds, filled area is the standard deviation calculated for 5 seconds, black dots: minimum and maximum measurement for 5 seconds. a) Output energy fluctuation of the pump maser. b) CEP fluctuation at the output of the system. c) Output pulse energy fluctuation. d) Room temperature fluctuation.

3.5.5 Conclusion

All measurements are summarized in table (III.7).

All specifications are reached except for the uninterrupted operation that lasts only 4 hours. This system has several interesting characteristics such as the energy per pulse, the pulse duration and the CEP stability. Moreover it is paired with a lot of diagnostic devices that help to run it over long times.

During my thesis work, another group has worked on the same topic and developed a mid-IR CEP

Specifications	Values	Measured	Units
Central wavelength	2100 ±100	2120	nm
Compressed pulse energy	> 30	31	μJ
Repetition rate	10 or 20	10	kHz
Pulse duration FWHM	< 20	19.4	fs
Pulse-to-pulse stability (over 1000 shots)	1.5 times the pump stability	1.07	% RMS
Long term power stability (8h)	1.5 times the pump stability	1.06	% RMS
CEP stability	< 150	107	mrad RMS, single-shot
Strehl Ratio	> 0.8	0.91	-
Pointing stability	0.1x diffracted limited beam divergence	0.01	RMS
Uninterrupted operation	>8	4	hours
Warm up time	<1	few minutes	hours

Table III.7 – Measured values for the second OPCPA architecture.

stable system. They produced [Neuhaus 18] pulses with 100 μJ of energy at 100 kHz repetition rate. This system provides pulses with almost identical duration as our system, 17 fs compared to 19.4 fs. Comparing that to the total amount of energy available (1 mJ), that corresponds to a transfer of 10 % from the pump to the signal. In our case we managed to transfer 31 μJ from 500 μJ which is 6 %. Since in our case, this system is a front-end, it will be amplified by other stages in the future. For the CEP stability, this group measured 240 mrad RMS over 30 minutes at 80 Hz with an integration time of 4 ms (400 laser shots). Comparing these results to our system, we managed to measure 107 mrad RMS over 4 hours single shot every shot. It is well known that averaging over a large number of shots reduces drastically the RMS phase fluctuations, by a factor of square root of n if n is the number of average shots for uncorrelated fluctuations. The system presented in this work, thanks to a careful inline DFG stage design, is therefore at the state of the art regarding CEP stability.

This chapter has been an example of using nonlinear crystals, with a corresponding broad phase matching to generate ultrashort pulses. Nevertheless, nonlinear crystals do not always offer these features. So a temporal compression setup can be required in the case of extremely short pulses. The next chapter is dedicated to the presentation and implementation of an original nonlinear compression setup at the output of an OPCPA system.

Chapter IV

Self-compression in a MultiPass Cell

Objectives

This chapter presents the design and the development of an ultrashort SWIR OPCPA source. This system is self-compressed with a new nonlinear setup: a multipass cell (MPC) used in anomalous dispersion regime, thereby triggering soliton compression. The chapter first presents briefly the SWIR OPCPA source. In the second section, the principle, design, and development of the MPC in self-compression regime is presented.

Contents

1 Introduction	100
2 SWIR OPCPA architecture	101
3 MultiPass Cell concept	102
3.1 Principle	102
3.1.1 B-integral calculation	103
3.2 State of the art	105
4 MPC in anomalous dispersion regime: self-compression regime	105
4.1 Experimental setup	105
4.2 Nonlinear propagation regime	106
4.3 Numerical simulations	106
4.4 Experimental results	108
5 Conclusion	111

1 Introduction

In the previous chapter, we presented a front-end with an extremely short time duration output (19.4 fs, 2.8 optical cycles). We showed that the crystals available in this spectral region can provide extremely large bandwidths to be amplified. As a consequence we managed to obtain an ultrashort pulse duration. Here we mainly describe a way to temporally compress the pulses when such broadband phase matchings are not available.

The work described in this chapter was done in the framework of the STAR (meaning: "Source laser femToseconde Amplifiee pour application de Recherche scientifique") project gathering two laboratories and three companies: Amplitude systemes, Amplitude Technologies, Fastlite, LIDYL and LCF. Fastlite and the LCF have provided the design and implementation of OPCPAs in the SWIR/Mid-IR. I was directly involved in the development of the source. Let us specify the characteristics requirements for this source shown in table(IV.1).

Specifications	Goal
• Few-cycle pulses	• < 30 fs (~6cycles)
• High energy	• 20 – 50 μ J
• Repetition rate	• < 100 kHz
• Mid-IR/SWIR	• 1.55 or 3 μ m
• CEP stable	• < 300 mrad

Table IV.1 – Requirements for the SWIR OPCPA source.

This source's first aim is to generate high harmonics. The mechanism of HHG in gases is triggered by intensities of the order of 10^{14} W/m². To reach these intensities we need an ultrashort and energetic source. Moreover the cutoff energy strongly depends on the wavelength of the driving laser as $h\nu_{cutoff} \propto \lambda^{1.7}$. We can therefore imagine designing a coherent source in the THz region to reach a high photon energy at the cutoff. Nonetheless, another scaling rule applies when increasing the wavelength of the driving source: the recombination probability of an ionized electron during the HHG process scales with the following law: $\lambda^{-6.5}$ with regard to the driving wavelength laser [Popmintchev 12]. This limits drastically the XUV photon flux when increasing the driver laser's wavelength. Moreover, some applications require a high repetition rate or high flux of generated photons. A good example are experiments using a coincidence detection scheme on atomic systems e.g COLTRIMS [Jahnke 04]. The optimal tradeoff in terms of the driving wavelength is an open question, especially for repetition rate laser HHG drivers that are still rare.

Taking into account this scientific case, we used an Yb-doped fiber pump laser with a repetition rate of 125 kHz. An OPCPA at the output generates a signal centered at 1.55 μ m (with an idler wave at 3.1 μ m) with an ultrashort pulse duration.

2 SWIR OPCPA architecture

The next section quickly describes the design of the OPCPA system which uses the same building blocks as the one presented in chapter 3. A scheme of the setup is depicted in figure IV.1. The OPCPA architecture is also based on the previous work done at LCF [Rigaud 16].

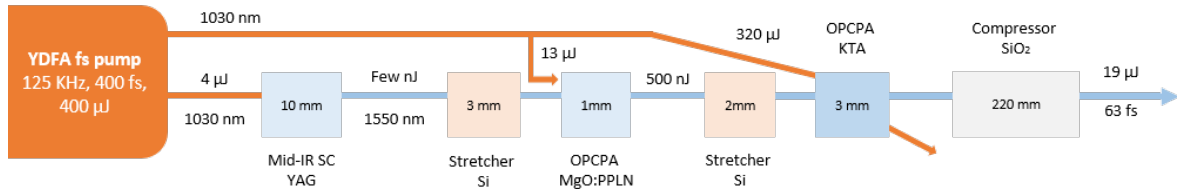


Figure IV.1 – Scheme of the SWIR OPCPA.

The pump laser is provided by Amplitude Systemes. This system delivers pulses with 400 μJ of energy at 125 kHz, with 400 fs pulses duration. The seed is generated in a 10 mm long YAG crystal by focusing a small amount of energy (4 μJ) through WLG. The bandwidth of interest around 1550 nm is sent into the OPCPA stages with an few nJ of energy. The seed is stretched in time with a 3 mm bulk plate of silicon that adds positive dispersion in order to reach the best trade-off between gain and bandwidth in the first amplifier. The seed is amplified into a 1 mm long MgO:PPLN. This OPCPA stage is pumped with 13 μJ of 1030 nm. At the output of this stage, the seed reaches an energy of 500 nJ with a spectrum centered at 1550 nm. The idler produced during this amplification stage is dumped.

The signal is one more time stretched with a 2 mm piece of silicon. It is sent into a 3 mm long KTA crystal used in type II non-collinear phase matching configuration pumped with 320 μJ . The signal is amplified to 22.5 μJ .

Finally the spatially expanded signal beam is compressed through a 220 mm long fused silica rod with a transmission efficiency of 86 %. As a consequence the pulse energy is 19 μJ corresponding to an average power of 2.4 W. The OPCPA output is spatially and temporally characterized, as plotted on figure IV.2. The output time duration measured with a FROG is 63 fs (FWHM) with a spectrum centered at 1550 nm. It has a bandwidth at -10 dB of 120 nm. The spatial profile measured with an InGaAs camera is plotted in the inset on the left figure in IV.2. The beam presents a slightly elliptical profile.

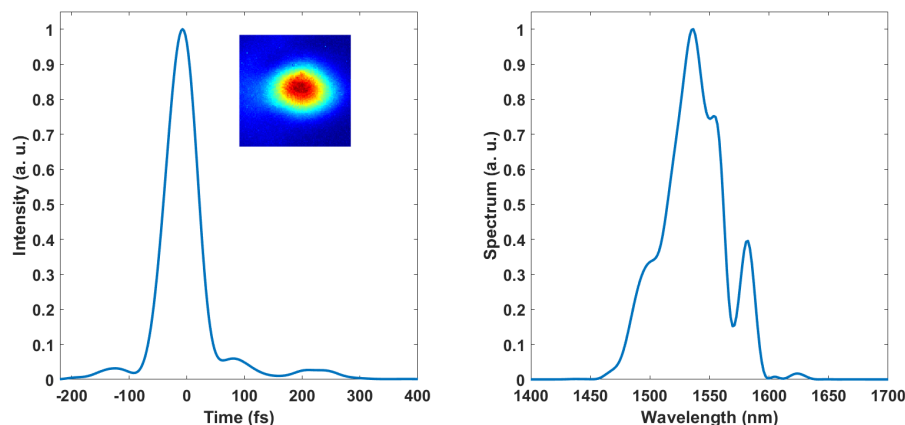


Figure IV.2 – Temporal and spatial (inset) profile (left) of the output OPCPA. Spectrum of the output of the OPCPA.

The output of the OPCPA is suitable for scientific applications but a shorter pulse duration would allow a more flexible use of the source. As a consequence, we implemented a nonlinear compression setup at the output of the source that is presented and described in the following section.

3 MultiPass Cell concept

3.1 Principle

Nonlinear compression stages after lasers output have been around for a long time. As explained in chapter 2, the first demonstration was performed in the late sixties [Fisher 69]. Since the first demonstration of nonlinear compression, lots of different setups have emerged, most of them detailed in chapter 2, in waveguides filled with gas or inside bulk plates. For the latter one, compression factors are limited due to the spatial Kerr effect. Rapidly, the idea emerges that distributing the nonlinearity over several pieces of bulk medium, reduces the spatial Kerr effect. A new concept has been implemented in 2016 called MultiPass Cell (MPC) [Schulte 16]. It is based on a Herriott type cell [Herriott 64]. This cell is based on two concave mirrors facing each other, the beam is focused on the same transverse plane but at different places in this plane. Propagation in the cell is periodic and preserves the beam parameter if the input beam is matched to the stationary beam. The beam is sent into the cell on the edge of one mirror and propagates inside the cell before being extracted. As an example [Schulte 16], the authors allow 18 roundtrips inside the MPC. In that case, the mirror substrates were used as the nonlinear medium. That configuration allows the authors to compress the pulses from 850 fs to 170 fs with an efficiency of 94 %. The authors measured the spatial beam quality and did not report any deterioration.

Let us have a brief look at the theory of MPCs. The typical configuration of a MPC is depicted in figure (IV.3). Two curved mirrors are facing each other in a Herriott configuration [Herriott 64].

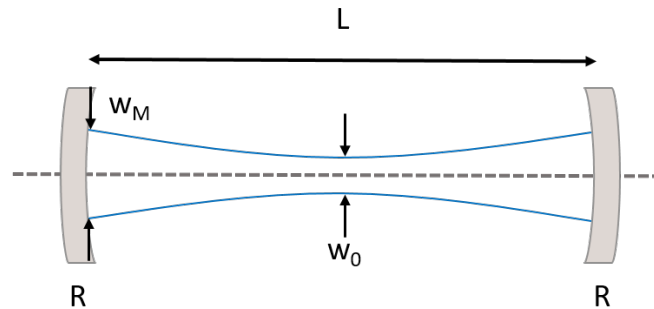


Figure IV.3 – Schematic of a MPC. Represented in blue is the caustic evolution of the beam while propagating inside the Herriott cell. R is the mirror radius of curvature, w_0 is the waist of the beam at the center of the MPC and w_M is the waist of the beam on the mirrors. L is the length separating both concave mirrors.

The radius of curvature R for each mirror can be different or equal, it depends on the chosen configuration. These two mirrors are separated by a distance L . If the beam satisfies a steady-state operation the propagation of the beam inside the MPC is periodic. The MPC can be thought of as a cavity (without resonances) meaning that the input beam needs to be mode-matched to the MPC. As a direct consequence, the B-integral per round trip is constant if the temporal profile is not affected by propagation ie if the dispersion and losses can be neglected.

For experimental convenience we used two mirrors with the same radius of curvature R . The beam size at the MPC waist (in the middle) and the mirrors are denoted by w_0 and w_M respectively. When the radius of curvature is fixed, three configurations appear while L increases.

- $L < R$: Both waist diameters (w_0 and w_M) are small. The propagation of the beam is below twice the Rayleigh distance inside the MPC.
- $L = R$: The cavity is confocal, meaning that for a fixed R , the waist w_0 is the biggest and the beam propagates over twice the Rayleigh distance inside the MPC.
- $L = 2R$: It corresponds to the cavity stability limit, the waist at the center of the MPC w_0 is decreasing to zero and the waist on the mirrors w_M increases to infinity.

Waists sizes are related by the following equation (IV.1):

$$\left(\frac{w_M}{w_0}\right)^2 = \frac{2R}{2R - L}. \quad (\text{IV.1})$$

Moreover, another equation connects the beam diameter at the center of the MPC, the radius of the mirrors and the wavelength by:

$$w_0^2 = \frac{\lambda L}{2\pi} \sqrt{\frac{2R}{2R - L}}. \quad (\text{IV.2})$$

In figure IV.4, w_0 and w_M are plotted as a function of L for a fixed radius of curvature $R=200$ mm. That figure illustrates the three configurations explained above.

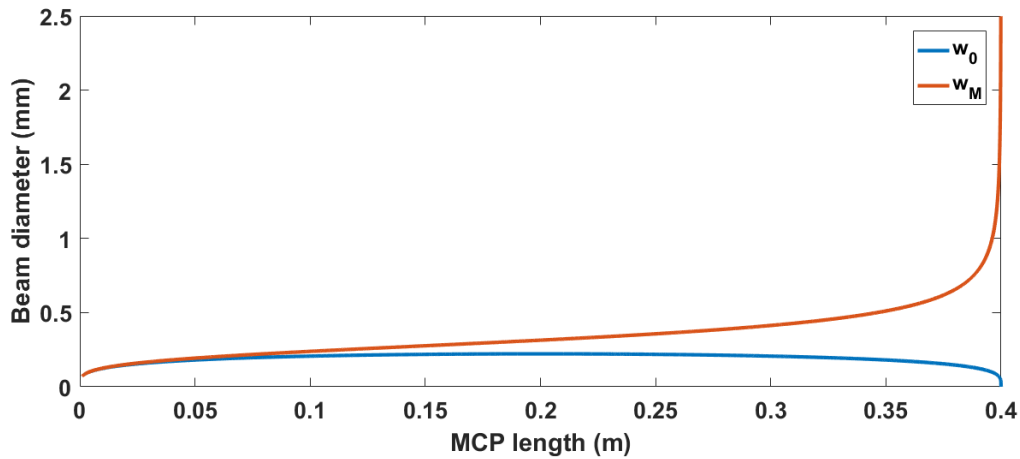


Figure IV.4 – Beam diameters as a function of the MPC length for a fixed radius of curvature $R=200$ mm. In blue w_0 , beam diameter at the center of the cavity, in orange w_M , beam diameter on the mirrors.

Experimentally, to inject and extract the beam inside the MPC two small mirrors (with a rectangular shape 3×10 mm²) are used at the edge of the curved cell mirrors.

3.1.1 B-integral calculation

In this section the question of the B-integral calculation is studied. Two cases are reviewed, first, the calculation of the B-integral with a MPC filled with gas and the calculation of the B-integral with a bulk medium used as a nonlinear medium.

In a MPC filled with gas

The B-integral depends on the MPC geometric configuration. As an example, before the confocal configuration, when $L < R$, the diameter of the beam does not change much along the cavity. However, when the cavity is at the stability limit $L = 2R$, the beam diameter at the center of the MPC is very small, while it goes to infinity on the mirrors.

In order to evaluate the B-integral per round trip, we consider the nonlinear phase accumulation homogeneous over the beam and use the definition applied in waveguides established in chapter 1. The MPC roundtrip can be divided into four identical parts given that it is symmetric, which reduces the B-integral calculation over half its size:

$$B_{roundtrip} = 4 \frac{2\pi n_2 P_{peak}}{\lambda} \int_0^{L/2} \frac{1}{A_{eff}(z)} dz. \quad (IV.3)$$

The beam is considered as Gaussian so $A_{eff} = \pi w^2(z)$, n_2 is the nonlinear refractive index of the gas, λ is the central wavelength. Since the beam does not experience any dispersion, P_{peak} is the peak power assumed independent along the propagation axis. The B-integral per round trip can be evaluated as a function of the MPC parameters as:

$$B_{roundtrip} = \pi \frac{P_{peak}}{P_{crit}} \operatorname{atan}\left(\sqrt{\frac{L}{2R - L}}\right). \quad (IV.4)$$

The quantity $B_{roundtrip}$ can be plotted as a function of the cavity length for a given radius of curvature. As explained in [Hanna 17] the B-integral increases as the MPC length is increased. Moreover, for a given n_2 , the range of B-integral accessible does not depend on the radius of curvature of the mirrors. These MPCs filled with gas present a real interest for the community because of their large transmission and energy scaling potential. A state of the art will be presented hereunder.

With a bulk medium as a nonlinear medium

Previously, we considered nonlinearities all along the propagation axis in the MPC. In this section, let us look at a discrete nonlinear medium. We consider a bulk plate inside the cavity to broaden the spectrum as depicted in figure (IV.5). The nonlinearity accumulated outside of the bulk nonlinear medium is considered negligible.

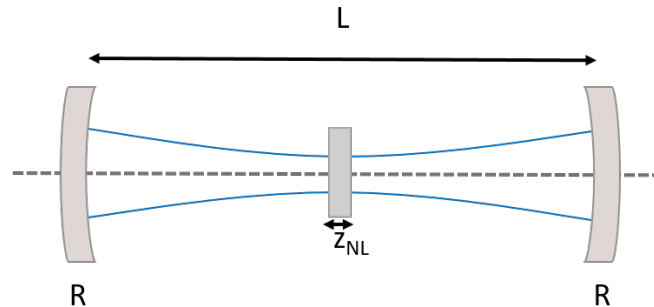


Figure IV.5 – Schematic of a MPC with a bulk medium to generate the nonlinearities.

Considering that the beam size is constant in the nonlinear medium with a waist w_{NL} . The B integral over a roundtrip is simply given by:

$$B_{roundtrip} = \frac{\lambda z_{NL}}{2n_0 w_{NL}^2} \frac{P_{peak}}{P_{crit}}. \quad (IV.5)$$

Ref	Input output pulse duration (fs)	Compression factor	Output energy (μJ)	Transmission %
[Schulte 16]	850 170	5	44.6	90
[Weitenberg 17b]	860 115	7.5	7.5	90
[Weitenberg 17a]	230 35	6.6	4.5	88
[Lavenu 18]	275 33	8.3	135	85
[Ueffing 18]	210 37	5.7	1860	93
[Kaumanns 18]	1300 41	31.8	1780	95.7
[Fritsch 18]	220 18	12.2	2.1	60
[Tsai 19]	534 88	6.1	112	91

Table IV.2 – State of the art of MPC compression setup.

There is however a big difference compared to the gas-filled case: since nonlinear propagation takes place in the plate only, the peak power can exceed the critical power as long as catastrophic collapse does not occur within the medium. Several experiments have reported the successful use of bulk-based MPC with peak powers well above the critical power.

3.2 State of the art

In this section we present the state of the art of MPC compression setup. Table IV.2 lists all the publications based on MPC.

These nonlinear compression setups are recent, with the first implementation in 2016. However the concept was proposed as early as 2000 [Milosevic 00]. All these experiments rely on the same principle which comprises two steps. First, spectral broadening is performed in the nonlinear MPC which exhibits overall normal (or negligible) dispersion. In a second time, the spectral phase induced by the broadening is compensated with negative dispersion obtained with chirped mirrors. Our framework is slightly different: we combined these two steps into one, in order to perform self-compression as shown in figure (II.18). Nonlinear propagation will take place in the anomalous dispersion regime, thereby triggering soliton dynamics. As discussed in chapter 1, this can lead to an initial step of temporal compression.

4 MPC in anomalous dispersion regime: self-compression regime

In this section all parameters used in this multipass cell setup are discussed.

4.1 Experimental setup

The MPC that we implemented is based on two concave mirrors with a radius of curvature of 200 mm. These mirrors have a diameter of one inch and are coated to be highly reflective (>99.8%) in the 1400-1700 nm region and introducing a low group delay dispersion. Mirrors are separated by 280 mm and a plate of 2 mm of fused silica is introduced inside the MPC. This plate has an anti reflective coating across the 1300-1700 nm bandwidth in order to perform the self-compression. In order to couple the beam inside and outside the MPC two rectangular shape mirrors are used in front of one of the curved mirrors. The plate is placed asymmetrically inside the MPC at a distance of 100 mm from one MPC mirror.

For the beam characteristics inside the cell, stationary beam propagation requires a beam radius at

$1/e^2$ of $212 \mu\text{m}$ at the waist of the cell and expanding to $388 \mu\text{m}$ radius on the mirrors. In order to couple the beam inside the MPC, experimentally an arrangement of two lenses with a focal length $f = 150 \text{ mm}$ and $f = -100 \text{ mm}$ at the input of the nonlinear setup allows us to mode match the cavity with a measured radius beam of $225 \times 270 \mu\text{m}$.

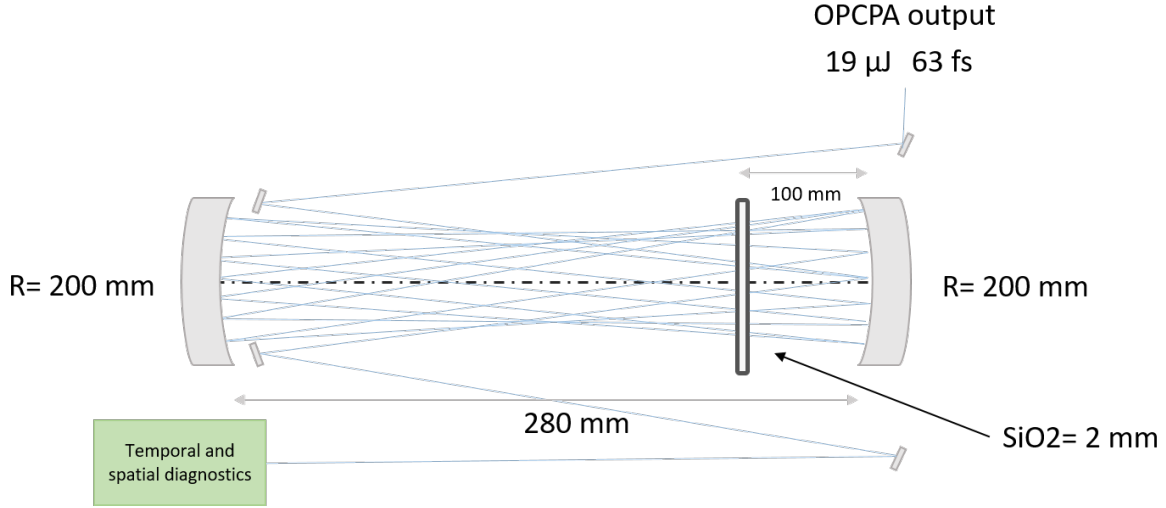


Figure IV.6 – Scheme of the implemented MPC at the output of the OPCPA.

The position and orientation of the input and the two mirrors of the MPC allow us to select the exact number of passes needed. They are adjusted to 10 roundtrips inside the MPC. Then the compressed beam is ejected and collimated with a $f = 750 \text{ mm}$ lens and routed to spatial and temporal diagnostics. The scheme in figure IV.6 shows the experimental setup of the nonlinear setup.

4.2 Nonlinear propagation regime

The output laser provides a beam centered at 1550 nm . In this wavelength region, some materials exhibit anomalous dispersion such as SiO_2 ($-28 \text{ fs}^2/\text{mm}^2$). Another important parameter to look at is the nonlinear refractive index. Fused silica exhibits a nonlinear refractive index $n_2 = 2.7 \times 10^{-20} \text{ m}^2/\text{W}$. In terms of soliton parameters, the MPC geometry translates to $L_D = 45 \text{ mm}$ and $L_{NL} = 5.9 \text{ mm}$ giving a soliton parameter of 2.7. Nevertheless, the number fluctuates due to the imperfections of the beam profile which are not present in single-mode optical fibers and the introduction of higher-order of dispersion and spectral filtering at the mirrors.

4.3 Numerical simulations

The simulation is based on the approach in [Hanna 17], where the 3D propagation envelope equation is solved using a split-step Fourier algorithm. As explained in the previous chapter, linear effects (diffraction, dispersion) are taken into account in the frequency domain and nonlinear effect (Kerr effect including self-steepening) is modeled in the space-time domain. In the Fourier domain, the linear complex envelope field propagation is computed according to:

$$E(\omega, f_x, f_y, z + dz) = E(\omega, f_x, f_y, z) \times \exp \left(ik(\omega) \sqrt{1 - \frac{4\pi^2}{k(\omega)^2} (f_x^2 + f_y^2) dz} \right), \quad (\text{IV.6})$$

where ω is the angular frequency, f_x and f_y are the transverse spatial frequencies and z the propagating distance. The wave vector $k(\omega)$ is equal to $\omega(\omega)n/c$, where c is the speed of light in vacuum.

The wave vector takes into account the dispersion by using the Sellmeier equation describing the frequency dependence of the linear refractive index of the nonlinear material of interest. Moreover, in the space-time domain the nonlinear propagation of the field is described as:

$$E(t, x, y, z + dz) = E(t, x, y, z) \times \exp \left(k_0 n_2 (iI(t, x, y, z) - \frac{1}{\omega_0 E(t, x, y, z)} \frac{\partial I(t, x, y, z)}{\partial t}) dz \right). \quad (\text{IV.7})$$

In the previous equation t is time, x and y are transverse dimensions, k_0 is the wave vector at the central wavelength in vacuum and I is the local intensity with $I = 2c\epsilon_0|E|^2$. In order to provide an accurate representation of the physical phenomenon, the model is applied with a transverse grid size of 128×128 and 256 for the time domain. The model takes into account the spectral phase and losses provided by the curved mirrors. The input beam of the cavity matches the stationary beam of the MPC, with a perfect Gaussian shape in the spatial domain.

We performed numerical simulations with a 2 mm long SiO_2 plate at the center of the MPC. The total energy of $12 \mu\text{J}$ is used for the simulations. This lower energy level compared to the experiment ($19 \mu\text{J}$) was found to provide the best agreement. This mismatch between the theoretical and experimental input energy is probably due to the fact that the spatial beam profile is not perfect, resulting in a beam bigger than expected at the nonlinear medium. That transfers directly to a lower level of nonlinearities observed in the experimental results. Imperfect mode matching might also explain this.

Regarding the temporal domain, the pulse initial condition corresponds to the measured profile at the OPCPA output, with a duration of 63 fs. The simulations were performed with 10 round trips inside the MPC that corresponds to a total propagation distance in SiO_2 of 40 mm. That length of material shows exactly the benefits of the method. Indeed if the broadening was performed directly into a 40 mm long piece of fused silica, the beam would self-collapse because the peak power is much higher than the critical power.

Let us analyze the numerical simulation of the MPC plotted in figure IV.7.

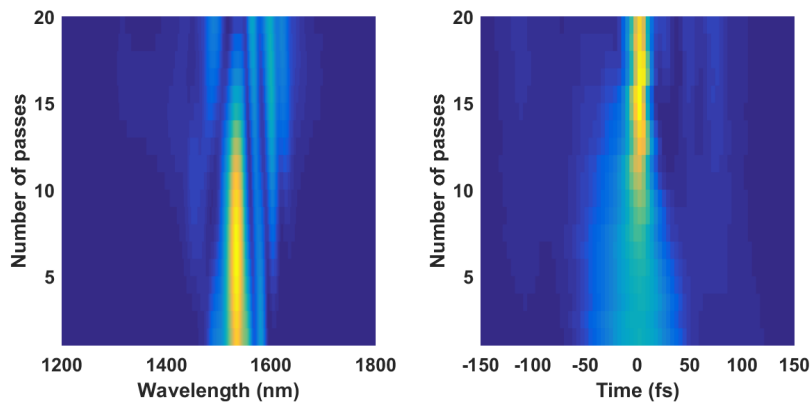


Figure IV.7 – Numerical simulation of the MPC for an input energy of $12 \mu\text{J}$. Left: Spectra evolution as a function of number of passes in the MPC. Right: Temporal profile as a function of number of passes in the MPC.

Figure IV.7 shows the spectral and temporal evolution as the pulse propagates in the MPC. At the beginning, the pulse duration is the one injected inside the nonlinear setup. As the number of passes increases, the pulse duration gets shorter due to the fact that the spectrum is broadening and because of the anomalous dispersion induced by the fused silica. We can observe that the shortest pulse duration

is obtained for 20 passes inside the nonlinear medium. In order to be able to post compress the pulse with the maximum peak power at the output of the MPC we should extract the beam after 20 passes. The on axis B-integral increases from 0.4 rad to 1 rad per round trip because of the self-compressing temporal profile. The integrated value of the B-integral is 13.5 rad.

Figure IV.8 shows a more complete picture of the output beam, including spatio-temporal and spatio-spectral profiles, and beam profiles. The simulation shows that the spatial nonlinearities have been essentially homogenized over the whole beam, leaving only the desired temporal compression in the output beam.

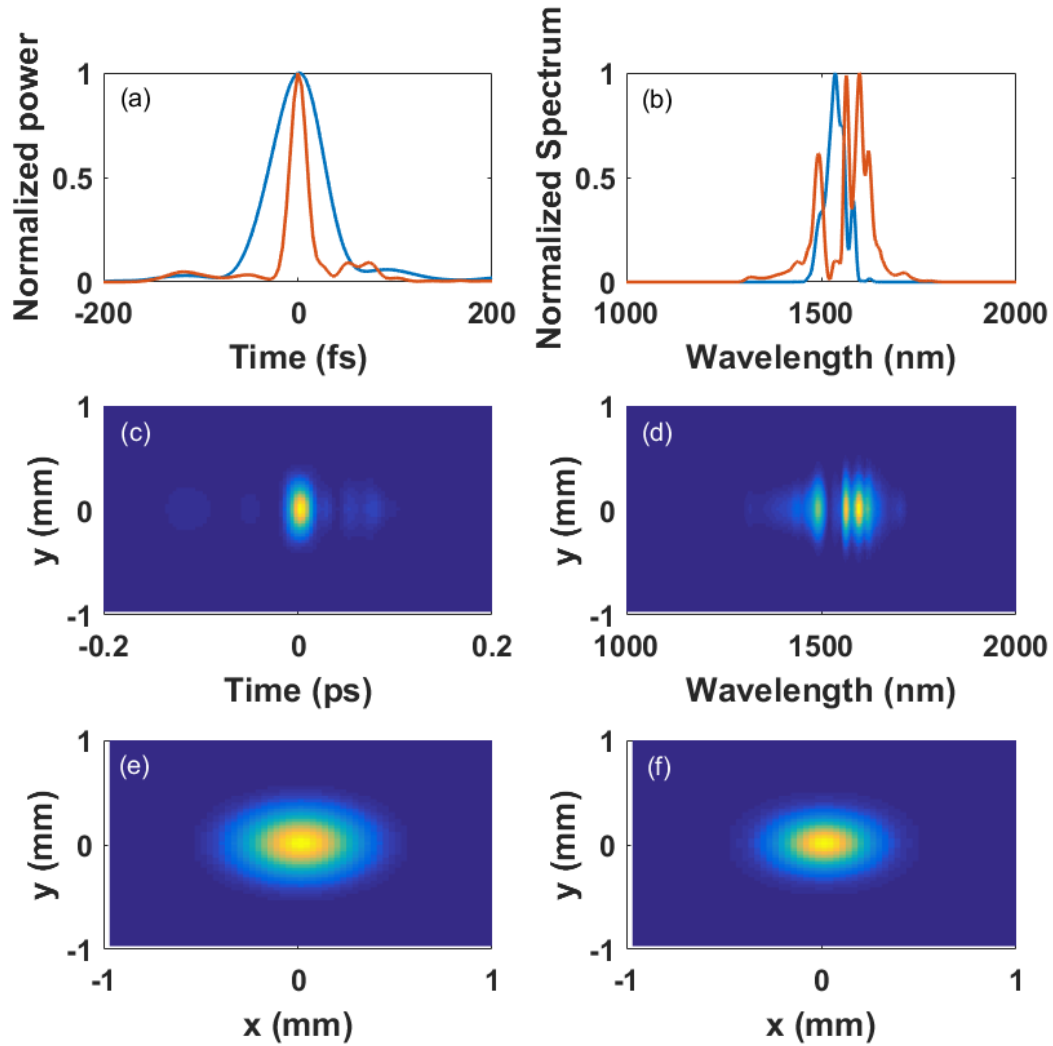


Figure IV.8 – Numerical simulation of the MPC for an input energy of $12 \mu\text{J}$ with a pulse duration of 63 fs. (a) Input (blue) and output (orange) temporal profile. (b) Input (blue) and output (orange) normalized spectrum. (c) Output spatio-temporal profile and (d) output spatio-spectral temporal profile. Input (e) and output (f) spatial beam profile

4.4 Experimental results

On figure IV.9 are plotted the measured spectra for different input energies. As the energy increases, the spectrum clearly broadens. At the maximum energy of $19 \mu\text{J}$, it extends over the whole bandwidth

supported by the mirrors.

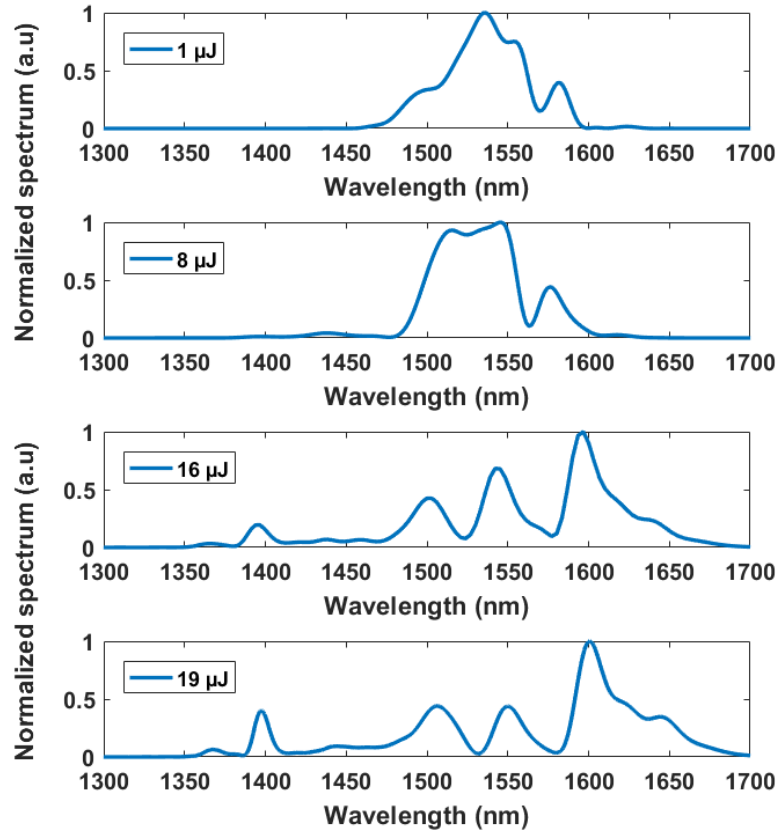


Figure IV.9 – Measured spectra as a function of input energy.

We now characterize the output beam of the MPC operating at full power, as shown in figure IV.10. The output pulse duration is 22 fs corresponding to a compression ratio of 2.8. The output spectrum expands over the full bandwidth of the mirrors from 1300 nm to 1700 nm. The bandwidth at -10 dB is 310 nm that corresponds of a Fourier transformed-limited pulse duration of 20 fs. The simulated temporal profile and spectrum are plotted along with the experimental results, and show qualitative agreement. However, the exact spectral structure is not reproduced accurately. This could be due to a number of reasons, including uncertainty in the dispersion profile of the mirror coatings, non-perfect spatial profile in the experiment, or the fact that air was not included in the simulation as a dispersive and nonlinear medium.

The experimentally measured transmission of the compression setup is 73%, the input energy of 19 μJ drops to 14 μJ. This loss of energy can be attributed to the mirror bandwidth that is not able to reflect the full spectral content generated through soliton compression. The estimated peak power of the output pulse using the temporal profile and energy is 440 MW. The peak intensity is 40 times higher than the critical power in bulk silica. That feature highlights perfectly the advantage of this technique. Indeed, it allows nonlinear propagation over an accumulated distance that is greater than the self-focusing distance in the material. In this experiment, we estimated it to be 15 mm.

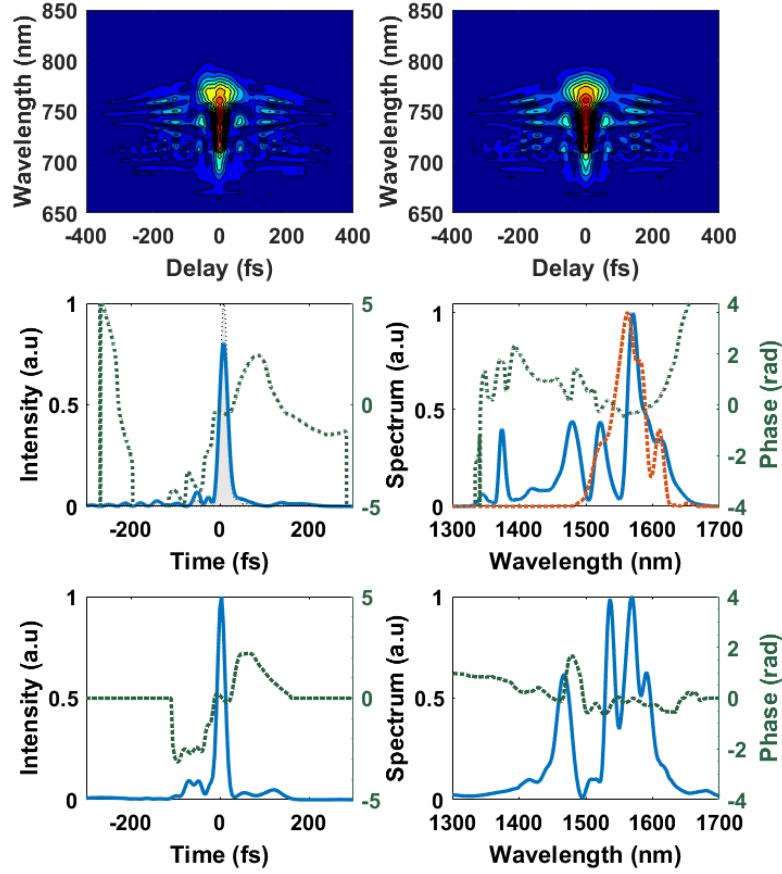


Figure IV.10 – In figure IV.10 on the first row is plotted the measured (left) and retrieved (right) FROG trace. The FROG error is 57×10^{-4} on a 256×256 grid. On the second row the FROG-retrieved temporal profile in blue, temporal phase profile in dashed green and the Fourier transformed-limited profile in gray (left) in regard to the numerical simulation in the third row (left). And the right part of the second row is plotted the FROG-retrieved spectrum in blue, spectral phase profile in dashed green and the input OPCPA spectrum in dashed red comparing to the numerical simulations in the third row (right).

We now focus on the characterization of the spatial profile of the beam at the output of the MPC. M^2 parameters are measured at the output of the nonlinear compression setup, using an InGaAs camera and a lens at low energy (linear regime) and full energy (nonlinear regime). The spatial quality remains almost the same as plotted at the top of the figure IV.11. At low power, the measured M^2 is 1.53×1.15 and 1.49×1.24 at full power.

We also evaluated the spatio-spectral homogeneity by measuring the spectral content at different locations in the compressed output beam. The so-called overlap factor is calculated as follows:

$$V = \frac{[\int (I(\lambda)I_0(\lambda))^{1/2}d\lambda]^2}{[\int I(\lambda)d\lambda \int I_0(\lambda)d\lambda]} \quad (IV.8)$$

This number aims at assessing the MPC-induced spatial homogenization of nonlinearities. To measure it we used a multimode fiber with a $200 \mu\text{m}$ core coupled to a spectrometer. The fiber can be translated in the beam transverse profile using translation stages. Once the spectra are acquired, we compute the V parameter. The result of this measure is plotted at the bottom of figure IV.11. The

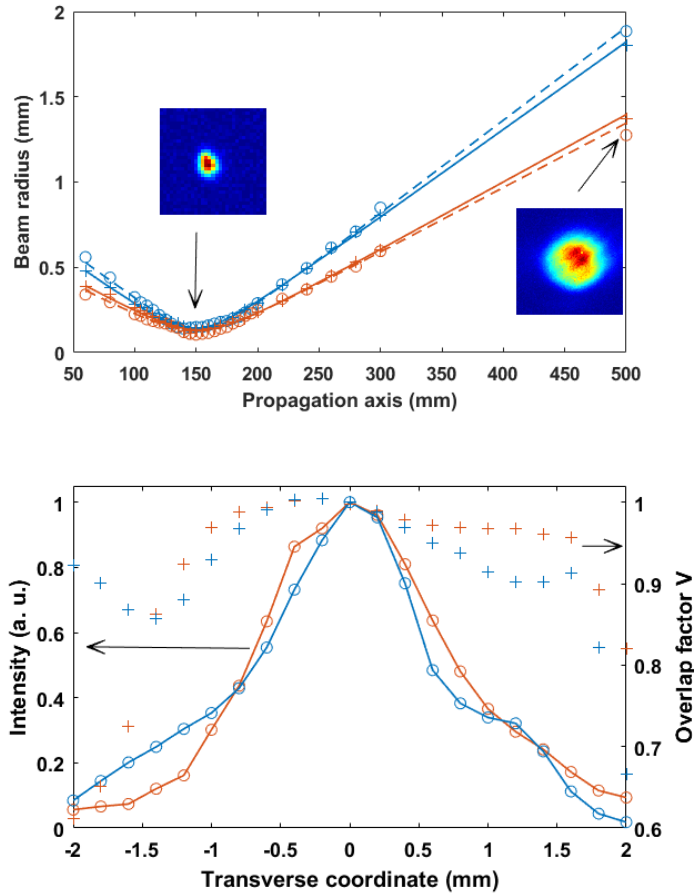


Figure IV.11 – Top: M^2 measurements of the output beam at low energy (dashed line) and full energy (solid line) in the horizontal (blue) and vertical (red) direction. Bottom: Spectrum overlap factor with a beam center and intensity as a function of horizontal (blue) and vertical (red) transverse dimensions.

spectral overlap with the beam center remains above 90% in the central part of the beam. This value decreases to lower values at intensity points below 10% of the maximum value. This decrease is attributed to a halo present at the input that is not compressed inside the MPC, and to the decrease of the signal-to-noise ratio that artificially degrades the overlap. The mean value of the overlap over the entire beam is 93% compared to 99% in simulation.

5 Conclusion

This chapter has presented a high repetition rate SWIR OPCPA with a compact self-compression setup at its output. This represents the first demonstration of self-compression using a MPC setup. This results in the generation of 14 μJ , 22 fs output pulses at 125 kHz. A picture of the MPC is shown in IV.12, highlighting the simplicity and compactness of the implementation.

That experiment enables to establish MPCs as a general nonlinear optic tool that allows to homogenize the spatial Kerr effect while providing temporal nonlinearities, and was recently published [Jargot 18]. Nonetheless, the mirror coating technology is crucial to allow high energy transmission

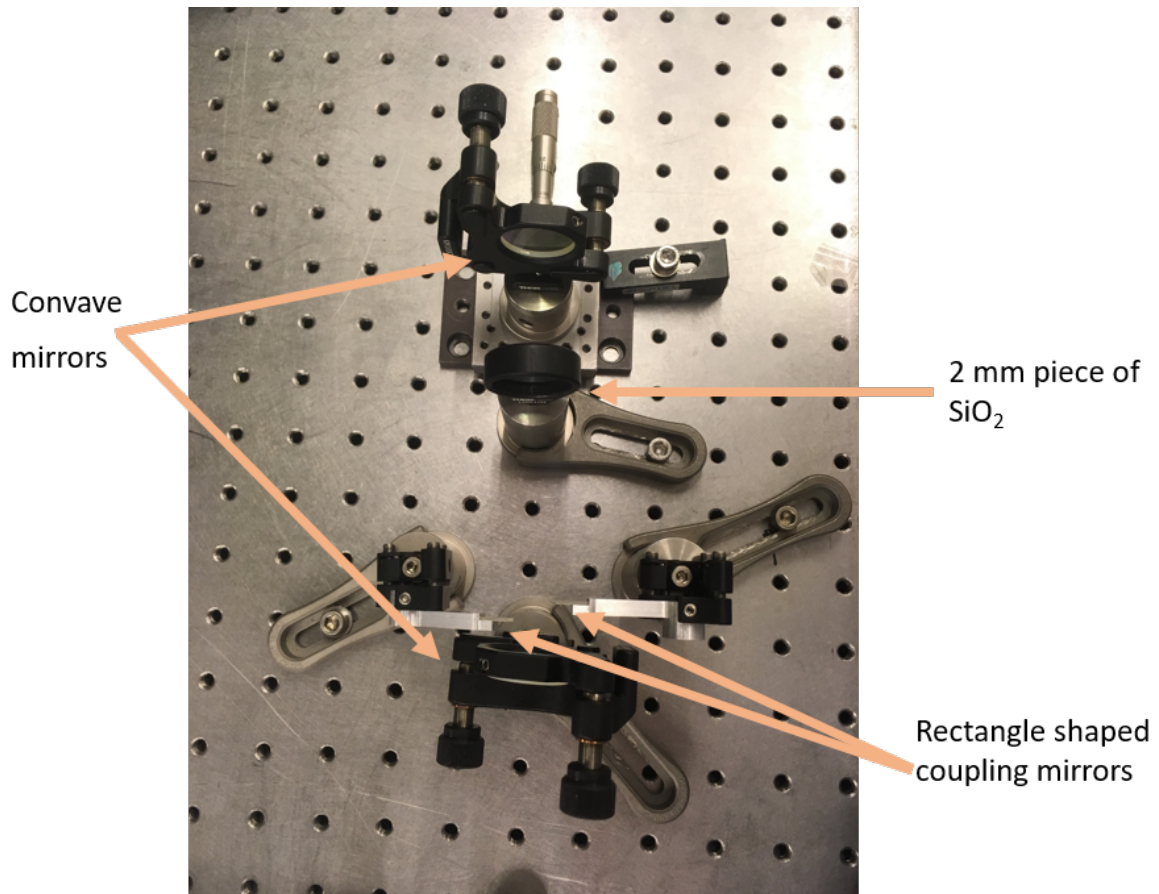


Figure IV.12 – Picture of the implemented MPC.

in order to access the few-cycle regime. That was the main limitation in our experiment. We are convinced that with advanced mirror designs, the scaling to few-cycle regime and higher energy in a robust experimental setup can be reached. A picture representing the entire experiment is shown in [IV.13](#).

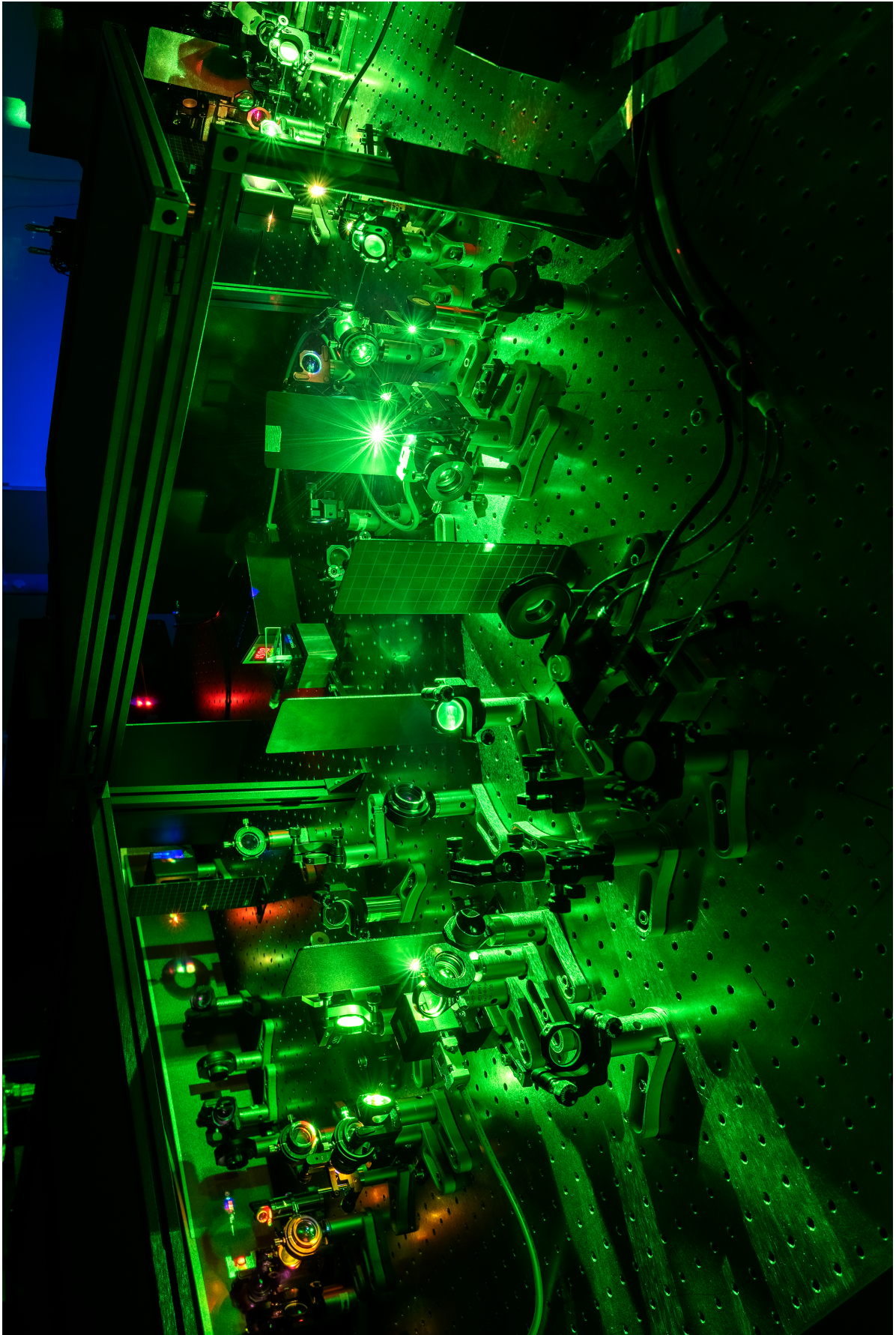


Figure IV.13 – Picture of the entire experimental setup.

Conclusion and perspective

During this thesis work, we focused on the generation of CEP-stable few-cycle pulses in the SWIR/Mid-IR at high repetition rate by OPCPA. The Yb-doped laser technology has provided us suitable pump lasers to achieve this goal.

We presented a CEP-stable frontend providing few-cycle pulses at $2\ \mu\text{m}$. Its salient feature resides in a novel all-inline implementation of the DFG stage allowing an unprecedented CEP stability. This experimental development took place in an industrial context and turned out to become a product for the company. This part of the thesis took place at the headquarters of Fastlite in Valbonne.

The second focus of this thesis work was on a new type of nonlinear compression scheme based on a MPC, allowing compression down to few-cycle pulse duration. It relies on soliton dynamics in a bulk medium located inside a MPC, allowing to use peak powers well beyond the critical power. The development of this source was made at Laboratory Charles Fabry.

As mentioned in the introduction, these sources were developed with the aim to be used in scientific applications, more precisely for HHG in gases or solids. Although not described in this manuscript since it was not the core of my work, a number of iterations of the source at LCF have been used for HHG experiments during the course of this Ph.D. First, the SWIR source was used to produce HHG in a gas jet of argon, in collaboration with a team from the Laboratoire Interaction Dynamique et Laser (LIDyL, Saclay). This experiment allowed us to observe spatio-spectral structures in the XUV beam that result from the atomic dipole phase term in the HHG process [Gonzalez 18]. A second experiment of HHG in zinc oxide (ZnO) allowed us to observe how orbital angular momentum is transferred from the driving laser to the high harmonics emitted in the deep UV [Gauthier 19]. Finally a third experiment was performed to study how doping modifies the properties of high harmonics generated in magnesium oxide (MgO) in the XUV [Nefedova 19]. Since I have been involved in the development of the sources and assisted during the experiments, I have included the corresponding publications at the end of the manuscript.

As a perspective, scaling the energy and the average power is an obvious first goal to address other applications such as electron acceleration. As a striking recent example of this capability, reference [Budriūnas 17] reports on a system that provides 50 mJ with 8 fs pulse duration at 53 W average power. This system was delivered to the large research facility ELI-ALPS in Hungary. Another remarkable work in this direction is reported in [Windeler 19], with a 100 kHz 1 mJ source, corresponding to an average power of 100 W. This source is implemented at SLAC, and seems to be extremely relevant for pump-probe experiment used in conjunction with a free electron laser. It is clear that the ongoing development in laser sources will lead to exciting new results to unravel physics at the smallest temporal and spatial scales.

Bibliography

- [Agrawal 06] G. P. Agrawal. *Nonlinear Fiber Optics*. In G. P. Agrawal, editeur, Nonlinear Fiber Optics (Fourth Edition). Academic Press, San Diego, fourth edition edition, 2006.
- [Alfano 70] R. R. Alfano et S. L. Shapiro. *Emission in the Region 4000 to 7000 cm Via Four-Photon Coupling in Glass*. Phys. Rev. Lett., vol. 24, pages 584–587, Mar 1970.
- [Armstrong 62] J. A. Armstrong, N. Bloembergen, J. Ducuing, et P. S. Pershan. *Interactions between Light Waves in a Nonlinear Dielectric*. Phys. Rev., vol. 127, pages 1918–1939, 1962.
- [Baltuska 02] A. Baltuska, T. Fuji, et T. Kobayashi. *Controlling the Carrier-Envelope Phase of Ultrashort Light Pulses with Optical Parametric Amplifiers*. Phys. Rev. Lett., vol. 88, page 133901, Mar 2002.
- [Barnes 76] N. P. Barnes et V. J. Corcoran. *Parametric generation processes: spectral bandwidth and acceptance angles*. Appl. Opt., vol. 15, no. 3, pages 696–699, Mar 1976.
- [Baudisch 14] M. Baudisch, M. Hemmer, H. Pires, et J. Biegert. *Performance of MgO:PPLN, KTA, and KNbO₃ for mid-wave infrared broadband parametric amplification at high average power*. Opt. Lett., vol. 39, no. 20, pages 5802–5805, Oct 2014.
- [Beetar 18] J. E. Beetar, S. Gholam-Mirzaei, et M. Chini. *Spectral broadening and pulse compression of a 400 μ J, 20 W Yb:KGW laser using a multi-plate medium*. Applied Physics Letters, vol. 112, no. 5, page 051102, 2018.
- [Biegert 12] J. Biegert, P. K. Bates, et O. Chalus. *New Mid-Infrared Light Sources*. IEEE Journal of Selected Topics in Quantum Electronics, vol. 18, no. 1, pages 531–540, Jan 2012.
- [Bohle 14] F. Bohle, M. Kretschmar, A. Jullien, M. Kovacs, M. Miranda, R. Romero, H. Crespo, U. Morgner, P. Simon, R. Lopez-Martens, et T. Nagy. *Compression of CEP-stable multi-mJ laser pulses down to 4 fs in long hollow fibers*. Laser Physics Letters, vol. 11, no. 9, page 095401, jun 2014.
- [Boyd 03] R. W. Boyd. Nonlinear optics; 2nd ed. Elsevier, 2003.
- [Bradler 09] M. Bradler, P. Baum, et E. Riedle. *Femtosecond continuum generation in bulk laser host materials with sub- μ J pump pulses*. Applied Physics B, vol. 97, no. 3, page 561, Aug 2009.
- [Bradler 14] M. Bradler et E. Riedle. *Sub-20 fs μ J-energy pulses tunable down to the near-UV from a 1 MHz Yb-fiber laser system*. Opt. Lett., vol. 39, no. 9, pages 2588–2591, May 2014.
- [Brodeur 99] A. Brodeur et S. L. Chin. *Ultrafast white-light continuum generation and self-focusing in transparent condensed media*. J. Opt. Soc. Am. B, vol. 16, no. 4, pages 637–650, Apr 1999.

- [Bromage 11] J. Bromage, J. Rothhardt, S. Hadrich, C. Dorrer, C. Jocher, S. Demmler, J. Limpert, A. Tunnermann, et J. D. Zuegel. *Analysis and suppression of parasitic processes in noncollinear optical parametric amplifiers*. Opt. Express, vol. 19, no. 18, pages 16797–16808, Aug 2011.
- [Budriūnas 17] R. Budriūnas, T. Stanislauskas, J. Adamonis, A. Aleknavičius, G. Veitas, D. Gadonas, S. Balickas, A. Michailovas, et A. Varanavičius. *53 W average power CEP-stabilized OPCPA system delivering 5.5 TW few cycle pulses at 1 kHz repetition rate*. Opt. Express, vol. 25, no. 5, pages 5797–5806, Mar 2017.
- [Cerullo 03] G. Cerullo et S. De Silvestri. *Ultrafast optical parametric amplifiers*. Review of Scientific Instruments, vol. 74, no. 1, pages 1–18, 2003.
- [Cerullo 10] G. Cerullo, A. Baltuska, O. Mucke, et C. Vozzi. *Few-optical-cycle light pulses with passive carrier-envelope phase stabilization*. Laser & Photonics Reviews, vol. 5, no. 3, pages 323–351, 2010.
- [Chen 09] X. Chen, A. Jullien, A. Malvache, L. Canova, A. Borot, A. Trisorio, C. G. Durfee, et R. Lopez-Martens. *Generation of 4.3 fs, 1 mJ laser pulses via compression of circularly polarized pulses in a gas-filled hollow-core fiber*. Opt. Lett., vol. 34, no. 10, pages 1588–1590, May 2009.
- [de Walle 15] A. V. de Walle, M. Hanna, F. Guichard, Y. Zaouter, A. Thai, N. Forget, et P. Georges. *Spectral and spatial full-bandwidth correlation analysis of bulk-generated supercontinuum in the mid-infrared*. Opt. Lett., vol. 40, no. 4, pages 673–676, Feb 2015.
- [Dubietis 17] A. Dubietis, G. Tamosauskas, R. Suminas, V. Jukna, et A. Couairon. *Ultrafast supercontinuum generation in bulk condensed media*. Lithuanian Journal of Physics, vol. 57, 10 2017.
- [Dudley 06] J. M. Dudley, G. Genty, et S. Coen. *Supercontinuum generation in photonic crystal fiber*. Rev. Mod. Phys., vol. 78, pages 1135–1184, Oct 2006.
- [Eidam 11] T. Eidam, J. Rothhardt, F. Stutzki, F. Jansen, S. Hadrich, H. Carstens, C. Jauregui, J. Limpert, et A. Tunnermann. *Fiber chirped-pulse amplification system emitting 3.8 GW peak power*. Opt. Express, vol. 19, no. 1, pages 255–260, Jan 2011.
- [Elu 17] U. Elu, M. Baudisch, H. Pires, F. Tani, M. H. Frosz, F. Kottig, A. Ermolov, P. S. Russell, et J. Biegert. *High average power and single-cycle pulses from a mid-IR optical parametric chirped pulse amplifier*. Optica, vol. 4, no. 9, pages 1024–1029, Sep 2017.
- [Emaury 13] F. Emaury, C. F. Dutin, C. J. Saraceno, M. Trant, O. H. Heckl, Y. Y. Wang, C. Schriber, F. Gerome, T. Sudmeyer, F. Benabid, et U. Keller. *Beam delivery and pulse compression to sub-50 fs of a modelocked thin-disk laser in a gas-filled Kagome-type HC-PCF fiber*. Opt. Express, vol. 21, no. 4, pages 4986–4994, Feb 2013.
- [Ferray 88] M. Ferray, A. L’Huillier, X. Li, L. Lompre, G. Mainfray, et C. Manus. *Multiple-harmonic conversion of 1064 nm radiation in rare gases*. Journal of Physics B: Atomic, Molecular and Optical Physics, vol. 21, no. 3, page L31, 1988.

- [Fisher 69] R. A. Fisher, P. L. Kelley, et T. K. Gustafson. *Subpicosecond pulse generation using the optical Kerr effect*. Applied Physics Letters, vol. 14, no. 4, pages 140–143, 1969.
- [Fritsch 18] K. Fritsch, M. Poetzlberger, V. Pervak, J. Brons, et O. Pronin. *All-solid-state multipass spectral broadening to sub 20 fs*. Opt. Lett., vol. 43, no. 19, pages 4643–4646, Oct 2018.
- [Fuji 06] T. Fuji, N. Ishii, C. Y. Teisset, X. Gu, T. Metzger, A. Baltuska, N. Forget, D. Kaplan, A. Galvanauskas, et F. Krausz. *Parametric amplification of few-cycle carrier-envelope phase-stable pulses at 2.1 μm* . Opt. Lett., vol. 31, no. 8, pages 1103–1105, Apr 2006.
- [Gauthier 19] D. Gauthier, S. Kaassamani, D. Franz, R. Nicolas, J.-T. Gomes, L. Lavoute, D. Gaponov, S. Février, G. Jargot, M. Hanna, W. Boutu, et H. Merdji. *Orbital angular momentum from semiconductor high-order harmonics*. Opt. Lett., vol. 44, no. 3, pages 546–549, Feb 2019.
- [Giesen 94] A. Giesen, H. Hügel, A. Voss, K. Wittig, U. Brauch, et H. Opower. *Scalable concept for diode-pumped high-power solid-state lasers*. Applied Physics B, vol. 58, no. 5, pages 365–372, May 1994.
- [Gires 64] F. Gires et P. Tournoi. *Interféromètre utilisable pour la compression d'impulsions lumineuses modulées en fréquence*. C. R. Acad. Sci. Paris, 1964.
- [Gonzalez 18] A. I. Gonzalez, G. Jargot, P. Rigaud, L. Lavenue, F. Guichard, A. Comby, T. Auguste, O. Sublemontier, M. Bougeard, Y. Zaouter, P. Georges, M. Hanna, et T. Ruchon. *Spatio-spectral structures in high harmonic generation driven by tightly focused high repetition rate lasers*. J. Opt. Soc. Am. B, vol. 35, no. 4, pages A6–A14, Apr 2018.
- [Hadrich 16] S. Hadrich, M. Kienel, M. Muller, A. Klenke, J. Rothhardt, R. Klas, T. Gottschall, T. Eidam, A. Drozdy, P. Jojart, Z. Varallyay, E. Cormier, K. Osvay, A. Tunnermann, et J. Limpert. *Energetic sub-2-cycle laser with 216 W average power*. Opt. Lett., vol. 41, no. 18, pages 4332–4335, Sep 2016.
- [Hanna 17] M. Hanna, X. Délen, L. Lavenue, F. Guichard, Y. Zaouter, F. Druon, et P. Georges. *Non-linear temporal compression in multipass cells: theory*. J. Opt. Soc. Am. B, vol. 34, no. 7, pages 1340–1347, Jul 2017.
- [Herriott 64] D. Herriott, H. Kogelnik, et R. Kompfner. *Off-Axis Paths in Spherical Mirror Interferometers*. Appl. Opt., vol. 3, no. 4, pages 523–526, Apr 1964.
- [Jahnke 04] T. Jahnke, T. Weber, T. Osipov, A. Landers, O. Jagutzki, L. Schmidt, C. Cocke, M. Prior, H. Schmidt-Bocking, et R. Dorner. *Multicoincidence studies of photo and Auger electrons from fixed-in-space molecules using the COLTRIMS technique*. Journal of Electron Spectroscopy and Related Phenomena, vol. 141, no. 2, pages 229 – 238, 2004.
- [Jargot 18] G. Jargot, N. Daher, L. Lavenue, X. Delen, N. Forget, M. Hanna, et P. Georges. *Self-compression in a multipass cell*. Opt. Lett., vol. 43, no. 22, pages 5643–5646, Nov 2018.
- [Jeong 18] Y.-G. Jeong, R. Piccoli, D. Ferachou, V. Cardin, M. Chini, S. Hadrich, J. Limpert, R. Morandotti, F. Legare, B. E. Fmidt, et L. Razzari. *Direct compression of 170-fs*

50-cycle pulses down to 1.5 cycles with 70% transmission. Scientific Reports, vol. 8, no. 1, page 11794, 2018.

- [Jukna 14] V. Jukna, J. Galinis, G. Tamosauskas, D. Majus, et A. Dubietis. *Infrared extension of femtosecond supercontinuum generated by filamentation in solid-state media.* Applied Physics B, vol. 116, no. 2, pages 477–483, Aug 2014.
- [Kaumanns 18] M. Kaumanns, V. Pervak, D. Kormin, V. Leshchenko, A. Kessel, M. Ueffing, Y. Chen, et T. Nubbemeyer. *Multipass spectral broadening of 18 mJ pulses compressible from 1.3 ps to 41 fs.* Opt. Lett., vol. 43, no. 23, pages 5877–5880, Dec 2018.
- [Kienel 16] M. Kienel, M. Muller, A. Klenke, J. Limpert, et A. Tunnermann. *12 mJ kW class ultrafast fiber laser system using multidimensional coherent pulse addition.* Opt. Lett., vol. 41, no. 14, pages 3343–3346, Jul 2016.
- [Krause 92] J. L. Krause, K. J. Schafer, et K. C. Kulander. *High-order harmonic generation from atoms and ions in the high intensity regime.* Phys. Rev. Lett., vol. 68, pages 3535–3538, Jun 1992.
- [Lavenu 17] L. Lavenu, M. Natile, F. Guichard, Y. Zaouter, M. Hanna, E. Mottay, et P. Georges. *High-energy few-cycle Yb-doped fiber amplifier source based on a single nonlinear compression stage.* Opt. Express, vol. 25, no. 7, pages 7530–7537, Apr 2017.
- [Lavenu 18] L. Lavenu, M. Natile, F. Guichard, Y. Zaouter, X. Delen, M. Hanna, E. Mottay, et P. Georges. *Nonlinear pulse compression based on a gas-filled multipass cell.* Opt. Lett., vol. 43, no. 10, pages 2252–2255, May 2018.
- [Lavenu 19] L. Lavenu, M. Natile, F. Guichard, X. Délen, M. Hanna, Y. Zaouter, et P. Georges. *High-power two-cycle ultrafast source based on hybrid nonlinear compression.* Opt. Express, vol. 27, no. 3, pages 1958–1967, Feb 2019.
- [Lim 89] E.-j. Lim, M. Fejer, et R. Byer. *Second-harmonic generation of green light in periodically poled planar lithium niobate waveguide.* Electronics Letters, vol. 25, pages 174 – 175, 03 1989.
- [Lu 18a] C.-H. Lu, T. Witting, A. Husakou, M. J. Vrakking, A. H. Kung, et F. J. Furch. *Sub-4 fs laser pulses at high average power and high repetition rate from an all-solid-state setup.* Opt. Express, vol. 26, no. 7, pages 8941–8956, Apr 2018.
- [Lu 18b] F. Lu, P. Xia, Y. Matsumoto, T. Kanai, N. Ishii, et J. Itatani. *Generation of sub-two-cycle CEP-stable optical pulses at 3.5 μm from a KTA-based optical parametric amplifier with multiple-plate compression.* Opt. Lett., vol. 43, no. 11, pages 2720–2723, Jun 2018.
- [Maiman 60] T. Maiman. *Stimulated optical radiation in ruby.* Nature, 1960.
- [Mak 13] K. F. Mak, J. C. Travers, N. Y. Joly, A. Abdolvand, et P. S. J. Russell. *Two techniques for temporal pulse compression in gas-filled hollow-core kagome photonic crystal fiber.* Opt. Lett., vol. 38, no. 18, pages 3592–3595, Sep 2013.
- [Mero 18] M. Mero, Z. Heiner, V. Petrov, H. Rottke, F. Branchi, G. M. Thomas, et M. J. J. Vrakking. *43 W, 1.55 μm and 12.5 W, 3.1 μm dual-beam, sub-10 cycle, 100 kHz*

optical parametric chirped pulse amplifier. *Opt. Lett.*, vol. 43, no. 21, pages 5246–5249, Nov 2018.

- [Milosevic 00] N. Milosevic, G. Tempea, et T. Brabec. *Optical pulse compression bulk media versus hollow waveguides*. *Opt. Lett.*, vol. 25, no. 9, pages 672–674, May 2000.
- [Moses 11] J. Moses et S.-W. Huang. *Conformal profile theory for performance scaling of ultra-broadband optical parametric chirped pulse amplification*. *J. Opt. Soc. Am. B*, vol. 28, no. 4, pages 812–831, Apr 2011.
- [Muller 16] M. Muller, M. Kienel, A. Klenke, T. Gottschall, E. ShestaeV, M. Plotner, J. Limpert, et A. Tunnermann. *1 kW 1 mJ eight-channel ultrafast fiber laser*. *Opt. Lett.*, vol. 41, no. 15, pages 3439–3442, Aug 2016.
- [Nefedova 19] V. Nefedova, S. Frohlich, D. Gauthier, S. Kaassamani, R. Nicolas, D. Franz, W. Boutu, A. Hamdou, F. Navarrete, M. Ciappina, G. Jargot, M. Hanna, N. Tancogne-Dejean, A. Rubio, et H. Merdji. *High-harmonic generation from chromium-doped and pristine magnesium oxide*. Manuscript in preparation, 2019.
- [Neuhaus 18] M. Neuhaus, H. Fuest, M. Seeger, J. Schötz, M. Trubetskov, P. Russbuedt, H. Hoffmann, E. Riedle, Z. Major, V. Pervak, M. F. Kling, et P. Wnuk. *10 W CEP-stable few-cycle source at 2 μm with 100 kHz repetition rate*. *Opt. Express*, vol. 26, no. 13, pages 16074–16085, Jun 2018.
- [Nubbemeyer 17] T. Nubbemeyer, M. Kaumanns, M. Ueffing, M. Gorjan, A. Alismail, H. Fattahi, J. Brons, O. Pronin, H. G. Barros, Z. Major, T. Metzger, D. Sutter, et F. Krausz. *1 kW, 200 mJ picosecond thin-disk laser system*. *Opt. Lett.*, vol. 42, no. 7, pages 1381–1384, Apr 2017.
- [Park 09] J. Park, J. hwan Lee, et C. H. Nam. *Generation of 1.5 cycle 0.3 TW laser pulses using a hollow-fiber pulse compressor*. *Opt. Lett.*, vol. 34, no. 15, pages 2342–2344, Aug 2009.
- [Paschotta 97] R. Paschotta, J. Nilsson, A. C. Tropper, et D. C. Hanna. *Ytterbium-doped fiber amplifiers*. *IEEE Journal of Quantum Electronics*, vol. 33, no. 7, pages 1049–1056, July 1997.
- [Pires 15] H. Pires, M. Baudisch, D. Sanchez, M. Hemmer, et J. Biegert. *Ultrashort pulse generation in the mid-IR*. *Progress in Quantum Electronics*, vol. 43, pages 1 – 30, 2015.
- [Popmintchev 12] T. Popmintchev, M.-C. Chen, D. Popmintchev, P. Arpin, S. Brown, S. Ališauskas, G. Andriukaitis, T. Balčiunas, O. D. Mücke, A. Pugzlys, A. Baltuška, B. Shim, S. E. Schrauth, A. Gaeta, C. Hernández-García, L. Plaja, A. Becker, A. Jaron-Becker, M. M. Murnane, et H. C. Kapteyn. *Bright Coherent Ultrahigh Harmonics in the keV X-ray Regime from Mid-Infrared Femtosecond Lasers*. *Science*, vol. 336, no. 6086, pages 1287–1291, 2012.
- [Pupeza 15] I. Pupeza, D. Sanchez, J. Zhang, N. Lilienfein, M. Seidel, N. Karpowicz, T. Paasch-Colberg, I. Znakovskaya, M. Pescher, W. Schweinberger, V. Pervak, E. Fill, O. Pronin, Z. Wei, F. Krausz, A. Apolonski, et J. Biegert. *High-power sub-two-cycle mid-infrared pulses at 100 MHz repetition rate*. *Nature Photonics*, vol. 9, page 721, 2015.

- [Reed 94] M. K. Reed, M. K. Steiner-Shepard, et D. K. Negus. *Widely tunable femtosecond optical parametric amplifier at 250 kHz with a Ti:sapphire regenerative amplifier*. Opt. Lett., vol. 19, no. 22, pages 1855–1857, Nov 1994.
- [Rigaud 16] P. Rigaud, A. V. de Walle, M. Hanna, N. Forget, F. Guichard, Y. Zaouter, K. Guesmi, F. Druon, et P. Georges. *Supercontinuum-seeded few-cycle mid-infrared OPCPA system*. Opt. Express, vol. 24, no. 23, pages 26494–26502, Nov 2016.
- [Rolland 88] C. Rolland et P. B. Corkum. *Compression of high-power optical pulses*. J. Opt. Soc. Am. B, vol. 5, no. 3, pages 641–647, Mar 1988.
- [Roso 17] Roso. *Advanced laser facilities and scientific applications*, pages 157–180. Springer International Publishing, Cham, 2017.
- [Russbuehdt 10] P. Russbuehdt, T. Mans, J. Weitenberg, H. D. Hoffmann, et R. Poprawe. *Compact diode-pumped 1.1 kW Yb:YAG Innoslab femtosecond amplifier*. Opt. Lett., vol. 35, no. 24, pages 4169–4171, Dec 2010.
- [Saraceno 19] C. J. Saraceno, D. Sutter, T. Metzger, et M. Abdou Ahmed. *The amazing progress of high-power ultrafast thin-disk lasers*. Journal of the European Optical Society-Rapid Publications, vol. 15, no. 1, page 15, Jun 2019.
- [Schmidt 10] B. E. Schmidt, P. Bejot, M. Giguere, A. D. Shiner, C. Trallero-Herrero, E. Bisson, J. Kasparian, J.-P. Wolf, D. M. Villeneuve, J.-C. Kieffer, P. B. Corkum, et F. Legare. *Compression of 1.8 μm laser pulses to sub two optical cycles with bulk material*. Applied Physics Letters, vol. 96, no. 12, page 121109, 2010.
- [Schulte 16] J. Schulte, T. Sartorius, J. Weitenberg, A. Vernaleken, et P. Russbuehdt. *Nonlinear pulse compression in a multi-pass cell*. Opt. Lett., vol. 41, no. 19, pages 4511–4514, Oct 2016.
- [Seidel 16] M. Seidel, G. Arisholm, J. Brons, V. Pervak, et O. Pronin. *All solid-state spectral broadening: an average and peak power scalable method for compression of ultrashort pulses*. Opt. Express, vol. 24, no. 9, pages 9412–9428, May 2016.
- [Shen 84] Y. R. Shen. *The principles of nonlinear optics*. Wiley Classics Library, 1984.
- [Strickland 85] D. Strickland et G. Mourou. *Compression of amplified chirped optical pulses*. Optics Communications, vol. 55, no. 6, pages 447 – 449, 1985.
- [Telle 99] H. Telle, G. Steinmeyer, A. Dunlop, J. Stenger, D. Sutter, et U. Keller. *Carrier-envelope offset phase control: A novel concept for absolute optical frequency measurement and ultrashort pulse generation*. Applied Physics B, vol. 69, no. 4, pages 327–332, Oct 1999.
- [Thai 11] A. Thai, M. Hemmer, P. K. Bates, O. Chalus, et J. Biegert. *Sub-250-mrad, passively carrier-envelope-phase-stable mid-infrared OPCPA source at high repetition rate*. Opt. Lett., vol. 36, no. 19, pages 3918–3920, Oct 2011.
- [Thiré 17] N. Thiré, R. Maksimenka, B. Kiss, C. Ferchaud, P. Bizouard, E. Cormier, K. Osvay, et N. Forget. *4-W, 100-kHz, few-cycle mid-infrared source with sub-100-mrad carrier-envelope phase noise*. Opt. Express, vol. 25, no. 2, pages 1505–1514, Jan 2017.

-
- [Thiré 18] N. Thiré, R. Maksimenka, B. Kiss, C. Ferchaud, G. Gitzinger, T. Pinoteau, H. Jous-selin, S. Jarosch, P. Bizouard, V. D. Pietro, E. Cormier, K. Osvay, et N. Forget. *Highly stable, 15 W, few-cycle, 65 mrad CEP-noise mid-IR OPCPA for statistical physics*. Opt. Express, vol. 26, no. 21, pages 26907–26915, Oct 2018.
- [Tomlinson 84] W. J. Tomlinson, R. H. Stolen, et C. V. Shank. *Compression of optical pulses chirped by self-phase modulation in fibers*. J. Opt. Soc. Am. B, vol. 1, no. 2, pages 139–149, Apr 1984.
- [Tournois 97] P. Tournois. *Acousto-optic programmable dispersive filter for adaptive compensation of group delay time dispersion in laser systems*. Optics Communications, vol. 140, no. 4, pages 245 – 249, 1997.
- [Trebino 97] R. Trebino, K. W. DeLong, D. N. Fittinghoff, J. N. Sweetser, M. A. Krumbugel, B. A. Richman, et D. J. Kane. *Measuring ultrashort laser pulses in the time-frequency domain using frequency-resolved optical gating*. Review of Scientific Instruments, vol. 68, no. 9, pages 3277–3295, 1997.
- [Tsai 19] C.-L. Tsai, F. Meyer, A. Omar, Y. Wang, A.-Y. Liang, C.-H. Lu, M. Hoffmann, S.-D. Yang, et C. J. Saraceno. *Efficient nonlinear compression of a mode-locked thin-disk oscillator to 27fs at 98W average power*. Opt. Lett., vol. 44, no. 17, pages 4115–4118, Sep 2019.
- [Ueffing 18] M. Ueffing, S. Reiger, M. Kaumanns, V. Pervak, M. Trubetskov, T. Nubbemeyer, et F. Krausz. *Nonlinear pulse compression in a gas-filled multipass cell*. Opt. Lett., vol. 43, no. 9, pages 2070–2073, May 2018.
- [Van de Walle 16] A. Van de Walle. *Parametric mid-IR source at high repetition*. Theses, Université Paris-Saclay, November 2016.
- [Wall 90] K. F. Wall et A. Sanchez. *Titanium sapphire lasers*. Lincoln Laboratory Journal, vol. 3, pages 447–462, 1990.
- [Weitenberg 17a] J. Weitenberg, T. Saule, J. Schulte, et P. Rusbuldt. *Nonlinear pulse compression to Sub-40 fs at 4.5 μ J pulse energy by multi-pass-cell spectral broadening*. IEEE Journal of Quantum Electronics, vol. 53, no. 6, pages 1–4, December 2017.
- [Weitenberg 17b] J. Weitenberg, A. Vernaleken, J. Schulte, A. Ozawa, T. Sartorius, V. Pervak, H.-D. Hoffmann, T. Udem, P. Russbuldt, et T. W. Hansch. *Multi-pass-cell-based nonlinear pulse compression to 115 fs at 75 μ J pulse energy and 300 W average power*. Optics Express, vol. 25, no. 17, page 20502, August 2017.
- [Windeler 19] M. K. R. Windeler, K. Mecseki, A. Miahnahri, J. S. Robinson, J. M. Fraser, A. R. Fry, et F. Tavella. *100W high-repetition-rate near-infrared optical parametric chirped pulse amplifier*. Opt. Lett., vol. 44, no. 17, pages 4287–4290, Sep 2019.
- [Xu 96] L. Xu, C. Spielmann, A. Poppe, T. Brabec, F. Krausz, et T. W. Hänsch. *Route to phase control of ultrashort light pulses*. Opt. Lett., vol. 21, no. 24, pages 2008–2010, Dec 1996.
- [Zysset 86] B. Zysset, W. Hodel, P. Beaud, et H. P. Weber. *200-femtosecond pulses at 1.06 μ m generated with a double-stage pulse compressor*. Opt. Lett., vol. 11, no. 3, pages 156–158, Mar 1986.



Spatio-spectral structures in high harmonic generation driven by tightly focused high repetition rate lasers

AURA INÉS GONZALEZ,^{1,2,3,*} GAËTAN JARGOT,^{1,4} PHILIPPE RIGAUD,¹ LOÏC LAVENU,^{1,5} FLORENT GUICHARD,⁵ ANTOINE COMBY,⁶ THIERRY AUGUSTE,² OLIVIER SUBLEMONTIER,⁷ MICHEL BOUGEARD,² YOANN ZAOUTER,⁵ PATRICK GEORGES,¹ MARC HANNA,¹ AND THIERRY RUCHON²

¹Laboratoire Charles Fabry, Institut d'Optique Graduate School, CNRS, Université Paris Saclay, 2 Avenue Augustin Fresnel, 91127 Palaiseau, France

²LIDYL, CEA, CNRS, Université Paris-Saclay, CEA Saclay 91191 Gif-sur-Yvette, France

³Amplitude Technologies, 2 rue du Bois Chaland, 91090 Lisses, France

⁴Fastlite, 1900 route des Crêtes, 06560 Valbonne, Sophia Antipolis, France

⁵Amplitude Systemes, 11 Avenue de Canteranne, Cité de la Photonique, 33600 Pessac, France

⁶Université de Bordeaux-CNRS-CEA, CELIA, UMR5107, F33405 Talence, France

⁷NIMBE, CEA, CNRS, Université Paris-Saclay, CEA Saclay 91191 Gif-sur-Yvette, France

*Corresponding author: aura.gonzalez@amplitude-laser.com

Received 30 October 2017; revised 25 January 2018; accepted 25 January 2018; posted 25 January 2018 (Doc. ID 310222); published 27 February 2018

We investigate the spatio-spectral properties of extreme ultraviolet (XUV) high harmonic radiation driven by high repetition rate femtosecond laser systems. In the spatio-spectral domain, ring-shaped structures at each harmonic order associated with long-trajectory electrons are found to form arrow-shaped structures at the cutoff. These structures are observed with two different laser systems: an optical parametric chirped-pulse amplifier system at a central wavelength of 1.55 μm and 125 kHz repetition rate, and a temporally compressed femtosecond ytterbium fiber amplifier at 1.03 μm wavelength and 100 kHz repetition rate. As recently pointed out, the observed structures are well explained by considering the space-time atomic dipole-induced phase for short and long electron trajectories in the generation plane. The tighter focusing geometry and longer wavelength associated with these emerging driving laser systems increase the ring-like divergence and spectral broadening for high harmonics. Cutoff energies and photon fluxes obtained in argon and neon are also reported. Overall, these results shed new light on the properties of XUV radiation driven by these recently developed high average power laser systems, paving the way to high photon-flux XUV beamlines. © 2018 Optical Society of America

OCIS codes: (340.7480) X-rays, soft x-rays, extreme ultraviolet (EUV); (320.7110) Ultrafast nonlinear optics; (320.7090) Ultrafast lasers.

<https://doi.org/10.1364/JOSAB.35.0000A6>

1. INTRODUCTION

The process of high harmonic generation (HHG) allows the generation of coherent femtosecond to attosecond extreme ultraviolet (XUV) beams by focusing a high-intensity femtosecond laser in a gas medium [1,2]. The associated XUV spectrum is typically composed of odd harmonics of the driving laser of approximately constant amplitude, extending up to the photon energy cutoff [3]. Depending on the experimental parameters, such as driving laser pulse duration and central wavelength, interaction geometry, and ionization potential of the gas, the spatial and temporal/spectral properties of the XUV beams can be vastly different [4]. The HHG process can be described using

the classical three-step model [3], where the laser field distorts the Coulomb potential of the atom, allowing tunneling of an electron wave packet from the valence shell. This electron is then freely accelerated by the electric field, and can recombine with the parent ion, releasing the acquired potential and kinetic energy in the form of an attosecond XUV burst. This process is repeated every half-cycle of the driving laser, inducing the odd harmonic structure of the radiated XUV beam. Both the semi-classical and quantum [5] analyses of this picture allows a good understanding of this intricate process, which leads to rich spatial and spectral features of the HHG beam. Since HHG is seen nowadays as a unique way to provide XUV photons, enabling

numerous applications including ultrafast spectroscopy, nano-scale imaging, and attosecond science [6–8], it is essential to understand these spectral and spatial properties to be able to tailor the XUV beam for specific applications.

The majority of recent HHG experiments have been performed with Ti:Sa laser systems that are able to deliver short (<30 fs) energetic pulses (few millijoules) at repetition rates limited to a few kilohertz, corresponding to average powers about 10 W. However, there is currently considerable technological and research effort toward efficient HHG setups compatible with emerging laser systems [9] that are scalable to higher average powers, and typically operate at much higher repetition rate (≥ 100 kHz) and lower energy per pulse. In particular, ytterbium-doped fiber-based amplifier (YDFA) sources have allowed unprecedented XUV photon fluxes [10–13]. Optical parametric chirped-pulse amplifier (OPCPA) systems add the possibility to operate at longer central wavelengths in order to reach higher cutoff energies, and are also increasingly used to drive HHG [14]. The lower pulse energy delivered by these systems requires a tighter focusing geometry to reach intensities of a few 10^{14} W/cm² typically required for HHG. The short-associated Rayleigh range asks for short and dense gas targets. These high repetition rate XUV systems are of great interest for several applications, such as coincidence detection of ionization fragments [15] and photoemission spectroscopy [16].

There has been a large number of reports of the spatio-spectral features of HHG, including various physical effects such as multiple quantum paths interference [17–20], Maker fringes related to phase-matching effects [21], and space–time atomic dipole phase [22]. These works have been done with Ti:Sa systems at a central wavelength of 800 nm. In this paper, we investigate spatio-spectral HHG features generated with two high repetition rate laser systems: (i) an OPCPA operating at a wavelength $\lambda = 1.55$ μm and delivering pulses with an energy $E = 20$ μJ and duration $\tau = 50$ fs at a repetition rate of 125 kHz, and (ii) a temporally compressed YDFA delivering $\lambda = 1.03$ μm , $\tau = 30$ fs, $E = 150$ μJ pulses at a repetition rate of 100 kHz. The experimentally observed structures are compared to theoretical results obtained considering a single longitudinal plane, neglecting phase-matching-related effects. All the observed features are compatible with a temporal and purely transverse spatial dependence of the dipole phase. The effects are more pronounced than in the case of Ti:Sa driven HHG because the dipole phase impact increases with stronger focusing and larger driving wavelengths. In addition to these observations, we provide cutoff energies and photon fluxes obtained with these sources, and conclude by discussing implications for users in terms of possible XUV beamline parameters.

2. EXPERIMENTAL SETUP FOR HIGH HARMONIC GENERATION

A. OPCPA System at $\lambda = 1.55$ μm

The OPCPA system is based on a commercial high-energy femtosecond ytterbium-doped fiber amplifier (Amplitude Systems Tangerine) that delivers 400 μJ , 400 fs pulses at 125 kHz and a central wavelength of 1.03 μm . A small fraction of the pulse

energy is used to generate a supercontinuum, constituting the seed for further amplification at a central wavelength of 1550 nm. This allows robust temporal synchronization between the pump and signal. Stretching and compression is achieved using bulk materials, silicon, and fused silica. Three optical parametric amplifier stages based on periodically poled magnesium-doped lithium niobate are implemented. The collinear interaction geometry results in simultaneously usable signal and idler beams at $\lambda = 1.55$ μm and $\lambda = 3.07$ μm , respectively. Only the $\lambda = 1.55$ μm beam is used in this work. More details on this source are available in [23]. The output parameters at $\lambda = 1.55$ μm are as follows: pulse duration 50 fs, pulse energy 20 μJ , and repetition rate 125 kHz.

B. Temporally Compressed YDFA System at $\lambda = 1.03$ μm

The second source is also based on a commercial high-energy femtosecond ytterbium-doped fiber amplifier (Amplitude Systems Tangerine), but the beam at $\lambda = 1.03$ μm is directly used to perform HHG. However, since shorter pulse durations allow overall better HHG performance, special care has been taken to counteract gain narrowing, allowing the generation of 150 fs pulses at the output of the laser [24]. These pulses are sent to a temporal compression stage that consists of a xenon-filled capillary inducing self-phase modulation followed by chirped mirrors. This compression stage can be entirely bypassed to drive the HHG with 150 fs pulses, or used with various Xe pressures and number of bounces on the chirped mirrors to provide tunable pulse duration at the output, from 16 fs to 30 fs in this work. More information on this source can be found in [24].

C. HHG Setup

The HHG setup is depicted in Fig. 1. It consists of a generation chamber and a detection chamber, connected through a 3 mm

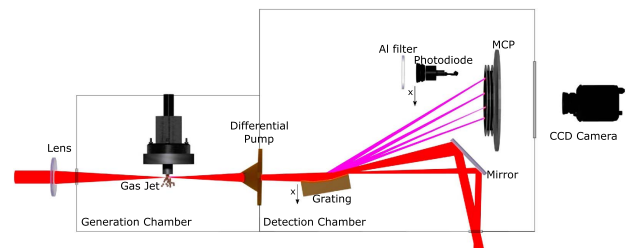


Fig. 1. Experimental setup. The XUV source is composed of two vacuum chambers. The generation chamber has been designed to evacuate the maximum of gas injected at backing pressures up to 12 bars, allowing overall pressures in the chamber of $\sim 10^{-3}$ mbar. The detection chamber hosts an XUV spectrometer with a grating placed on a motorized holder with nanometer precision of the rotation and transversal position. A motorized holder allows insertion of a 200 nm thick aluminum filter and a calibrated photodiode in the beam path. The spectrum is finally detected on a two-stage MCP in chevron configuration of 77 mm diameter coupled to a phosphore screen (P43 type). Part of the IR beam is filtered out by a water-cooled skimmer that also acts as a differential pumping between the chambers. The residual IR beam is sent out of the detection chamber with a silver mirror. This part of the IR beam can be used to monitor the IR parameters and beamline alignment.

diameter skimmer hole that allows propagation of the harmonic beam. It also allows us to establish a differential pressure between the chambers (typically 10^{-3} mbar in the generation chamber and 10^{-5} mbar in the detection chamber). The generating medium is a continuous flow of gas (argon or neon) emitted from a 100 μm nozzle backed with a pressure of 3–12 bars. The laser beam is expanded to a diameter of 7 mm before being focused with a 75 mm or 150 mm focal length lens through a 3 mm thick fused silica window at the output of the gas nozzle. The longitudinal gas jet position with respect to the laser focus is adjustable as an optimization parameter for the experiments; however, its absolute position is not accessible. The HHG beam passes through the skimmer and enters a spectrometer, composed of a 1200 lines per mm Hitachi aberration-corrected grating (001-0266) at grazing incidence and a micro-channel plate (MCP) detector, equipped with a phosphor screen. This screen is imaged onto a CCD camera. This detector is located 50 cm away from the HHG generation point.

To calibrate the spectrometer in photon energy, a fit is performed considering the grating characteristics and geometry of the setup in terms of angle and distance. This fit is checked using a 200 nm thick Al filter with a band edge at 75 eV that can be inserted in the XUV beam path. Finally, photon flux measurements are performed using a calibrated XUV photodiode placed downstream the Al filter, after removal of the spectrometer grating. Its current is read by a precision picoammeter and corrected for a small offset due to the remaining infrared light passing the Al filter. To measure this offset, a differential measurement of the photodiode current with and without generating gas, and in linear or circular polarization, is carried out. The signal is measured as a function of photodiode lateral position with respect to the optical axis, and the XUV signal shows up as a very localized contribution, while the IR background (representing typically 5% of the signal) is always present. This total photon flux is then used to calibrate the spectra recorded on the CCD camera in terms of photon flux spectral density. Uncertainties on the spectral responses of the photodiode, grating, and MCP/phosphor screen result in error bars for the measured photon flux densities of $\pm 30\%$.

3. DIPOLE MODEL AND SIMULATIONS

A. Atomic Phase Model

The harmonic generation process can be described by a very simple model [22] where the source term for a given harmonic number q and trajectory class (short or long) is written in the spatio-temporal domain at the interaction point as

$$d_q(x, t) = E^{q_{\text{eff}}}(x, t) \exp(-i\alpha I(x, t)), \quad (1)$$

where t is time, x is the resolved transverse spatial coordinate, E and I are the driver laser field and intensity, and q_{eff} and α are considered as constant for a fixed harmonic number, type of trajectory, and maximum laser intensity. The q_{eff} constant describes how the dipole response intensity varies as a function of fundamental field intensity, while α describes the strength of the atomic response-induced phase, which can be shown to be proportional to the driving laser intensity. The value of α (expressed in 10^{-14} rad \cdot cm 2 /W throughout this paper) is related to the time of flight of the electron wave packet in the

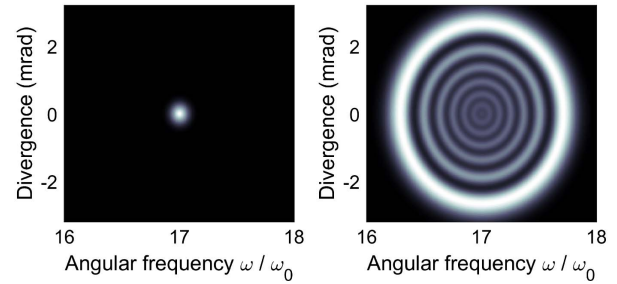


Fig. 2. Intensity in the spatio-spectral domain in the far field calculated using the simple atomic phase model for short trajectories (left, $q_{\text{eff}} = 4$, $\alpha = 2$) and long trajectories (right, $q_{\text{eff}} = 4$, $\alpha = 20$).

continuum, and therefore increases with longer driving wavelength with a λ^3 dependence [25]. For short trajectories, this value increases (in absolute value) with harmonic number, while for long trajectories the absolute value of α decreases with harmonic number, merging at the cutoff energy.

To illustrate the consequences of this model, the intensity of the 17th harmonic order (26.3 eV) in the spatio-spectral plane in the far field is plotted in Fig. 2. The driving laser is considered to deliver 40 fs pulses at 800 nm, focused on a 120 μm waist radius at a maximum intensity of 2×10^{14} W/cm 2 . The q_{eff} value is taken to be 4 for both trajectory types, and we have taken $\alpha = 2$ for short trajectories and $\alpha = 20$ for long trajectories, typical values for argon at 800 nm [22]. For large values of the dipole-induced phase (long trajectories), the atomic phase term in the near-field temporal domain translates into a ring structure in the far-field spatio-spectral domain. To understand this feature, an interesting analogy with self-phase modulation (SPM) in nonlinear optics can be drawn: in both cases, a phase proportional to the intensity profile is induced. It is well known that for smooth Fourier transform-limited pulses, SPM imparts a spectral broadening that exhibits multiple lobes, which are more prominent on the spectral edges. The overall width of the spectrum and number of lobes increases with the nonlinear phase excursion. The exact same behavior is observed for the atomic phase (in 2D in the case of Fig. 2), with the slight modification that the intensity of the radiating source term is also modified through the value of q_{eff} . Overall, this simple model predicts two contributions to the intensity pattern in the far-field spatio-spectral domain. The short trajectories bring a localized contribution. In contrast, the long trajectories contribute to a more dilute ring pattern, and specific numbers for the divergence and harmonic spectral width depend on the exact values of q_{eff} and α , together with the driving field parameters, such as pulse duration, focal spot size, position, and intensity.

B. Numerical Simulations (SFA Model)

To obtain more accurate theoretical results, a software package was used to compute the HHG far-field spatio-spectral intensity [26]. This package solves the time-dependent Schrödinger equation under the strong-field approximation (SFA) [5] to compute the nonlinear dipole response to the pulsed driving field at discrete locations in the gas target. Contributions from all the volume regions in the target are then propagated to

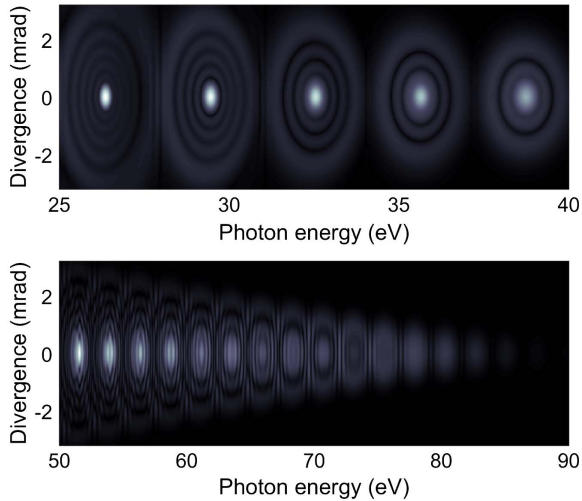


Fig. 3. Intensity in the spatio-spectral domain in the far field calculated using the numerical model based on SFA for central wavelengths of 800 nm (top), and 1030 nm (bottom).

include macroscopic effects such as phase matching. Finally, the resulting HHG far field at a specific distance can be obtained. To validate this model, it was first run with a set of parameters used in [22]: generation in a single longitudinal plane of argon with a central wavelength of 800 nm, waist 120 μm , pulse duration 40 fs, and intensity $2 \times 10^{14} \text{ W/cm}^2$. The result is shown in Fig. 3, and is in excellent agreement with the data from [22]. In addition, there is also a remarkable agreement with the simple model described above (the 17th harmonic is the leftmost harmonic in Fig. 3 top).

To get a first illustration of the effect of the central wavelength shift toward longer values, the simulation is reproduced with the same parameters except for the central wavelength, which is changed to 1030 nm. The result is plotted near the energy cutoff in Fig. 3 (bottom). The shift to a longer wavelength results in an extended cutoff energy, and the ring structures associated with neighboring harmonics start to overlap. This is both due to the fact that the value of α increases with wavelength, and to the fact that in a constant spectral zone, the separation of the harmonic orders decreases with the driving wavelength. The overlap between structures induces an interference pattern, whose location is sensitive to the carrier-envelope phase (CEP). They appear as a series of vertical fringes in the spectrum in Fig. 3. This interference will therefore be washed out if observed with a laser that is not CEP-stabilized. Note that since a single transverse plane was considered in these simulations, longitudinal phase matching plays no role in the appearance of the spatio-spectral structures.

These two theoretical tools are used to analyze the experimental data obtained in various conditions, presented hereafter.

4. EXPERIMENTAL RESULTS

A. Results Obtained with the YDFA in Argon

We first describe results obtained using the YDFA laser temporally compressed down to 30 fs. For this part, the input pulse (115 μJ energy) was focused using a 150 mm lens in an argon

gas jet with a backing pressure of 6.5 bar. The goal of this section is to identify experimentally the origin of the ring structure, and check that our models can predict them with reasonable accuracy. The generating conditions (intensity, position of the gas nozzle, backing pressure) are therefore optimized to observe a clear spatio-spectral pattern. A pinhole is used at the input of the chamber to reduce the input beam size and pulse energy, resulting in a 30 μm waist radius at the gas target location and an estimated intensity of $0.7 \times 10^{14} \text{ W/cm}^2$. The spectrometer is aligned to observe photon energies from 20 to 65 eV.

Figure 4 shows the experimentally observed spatio-spectral structure in these conditions, along with results from the SFA and atomic phase models. To obtain the spatio-spectral structure with the atomic phase model, the contribution of each harmonic and trajectory is calculated independently using α values obtained from the SFA code, and the contributions' intensities are summed to obtain the final result.

The α values used in this result are plotted in Fig. 5, showing that the longer driving wavelength compared to Ti:Sa systems results in significantly higher transverse spatial phases.

Overall, the agreement between the experimental data and both models is good in terms of divergence observed for each harmonic. In particular, as the photon energy increases, since α for the long and short trajectories converge to the same value, the spatio-spectral structures converge as well to end at the energy cutoff. This confirms that the ring-like structures are indeed well explained by a purely spatial transverse and spectral phase, even with numerical apertures of 0.03. The number and contrast of the rings predicted by each model do not match. It is not overly surprising, since the atomic phase model is very rudimentary: both q_{eff} and α depend on the intensity, which is a time-varying quantity. They are taken as constant and equal to the SFA value at the peak intensity in the atomic phase model, which is a very rough assumption. We still see a value in using this model because it allows a useful analogy to the Kerr effect and indicates well the trends, but it has limited predictive value. The SFA model on the other hand matches much better the experimentally observed pattern.

Another feature that can be observed in Fig. 4(a) is a lateral asymmetry of the ring patterns. While this is not fully

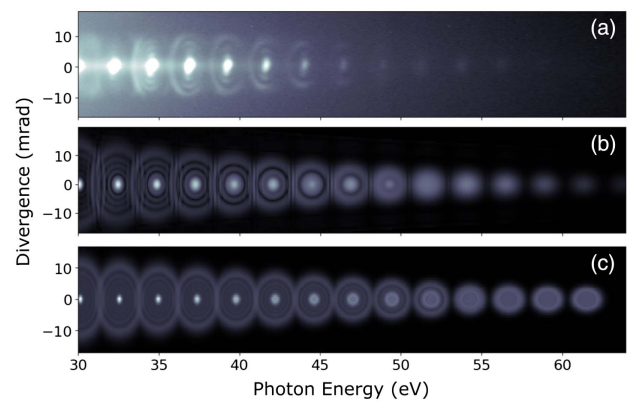


Fig. 4. Spatio-spectral structures obtained with the YDFA in argon. (a) Experiment, (b) SFA model, (c) atomic phase model.

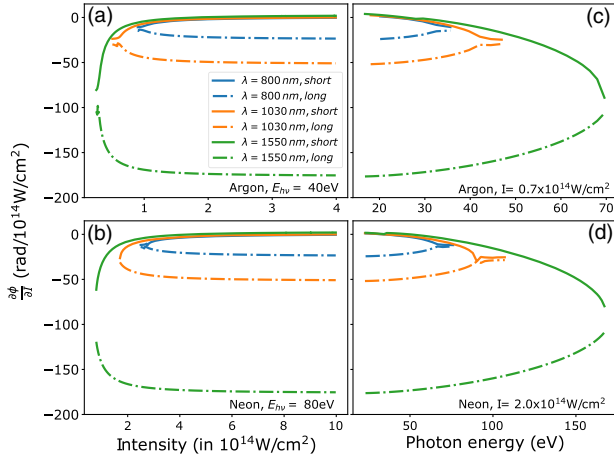


Fig. 5. Atomic phase-intensity coupling constants obtained from the SFA adiabatic model used in the simplified model for three different wavelengths: 800 nm (blue), 1030 nm (orange), and 1550 nm (green) and the two first quantum trajectories labeled short (plain line) and long (dashed line). (Top line) Argon gas. (Bottom line) Neon gas. Left column: variation of α against the laser intensity at a photon energy of (a) 40 eV in argon and (b) 80 eV in neon. Right column: variation of α against the photon energy at an intensity of (c) 0.7×10^{14} W/cm² in argon and (d) 2.0×10^{14} W/cm² in neon.

understood yet, a possible explanation is related to the temporal profile of the driving pulse: asymmetric pulses will lead to an asymmetry in the XUV spectral broadening. Another source of dissymmetry is the dispersion due to electrons which are being created in the medium as the pulse passes. This changes phase-matching conditions but also reshapes the driving pulse. Even with a perfectly symmetric incoming pulse, asymmetric spectral structures might thus appear.

B. Results Obtained with the OPCPA in Argon

To study the influence of the driving wavelength on these spatio-spectral structures, we now report on experiments performed with the same HHG setup using the OPCPA source at 1.55 μm . The focus of this part is also to observe the dependence of the spatio-spectral structures on phase-matching conditions; however, the setup is first optimized to obtain the maximum cutoff photon energy. The input beam is focused using a 75 mm lens in the argon gas jet, resulting in a waist radius of 15 μm at the gas target, and an estimated intensity of 1.0×10^{14} W/cm². The spectrometer is aligned to observe photon energies from 50 to 100 eV.

Figure 6 shows two spatio-spectral structures observed at backing pressures of 7.2 bar and 11.4 bar. A lineout shows the normalized photon flux spectral density obtained, revealing an energy cutoff around 95 eV for both backing pressures. The absolute value of photon flux spectral density obtained at 11.4 bar is also given using the right-hand side vertical scale in Fig. 6(b). As well established in the literature, the gas pressure is an essential parameter that changes longitudinal phase-matching conditions by changing the dispersion and absorption of the medium. This is particularly important in tightly focused configurations [27]. A salient feature of the data shown in Fig. 6

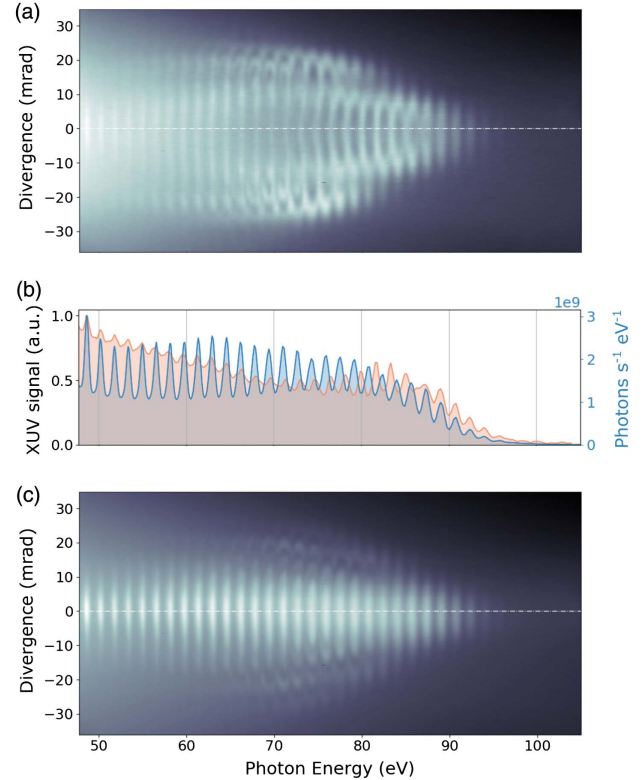


Fig. 6. Experimental spatio-spectral intensity distribution of the XUV beam generated in argon with the OPCPA at (a) 7.2 bar and (c) 11.4 bar. (b) Lineouts of the spectra at 7.2 bar (orange) and 11.4 bar (blue). Both lineouts are normalized on the left axis. In addition, for the blue curve corresponding to panel (c), the right axis indicates the photon flux spectral scale.

is that the change in pressure redistributes the intensity between the more diverging components at angle above 10 mrad, associated with the long trajectories, and the central components, associated with the short trajectories, while keeping the underlying structures. This behavior is expected since phase matching is trajectory-specific, while we attribute the geometrical structures to temporal and spatial atomic dipole phase modulation, which is pressure independent.

This allows a direct comparison between the long and short trajectories. The long trajectories observed in Fig. 6(a) follow an increasing divergence as the photon energy decreases from the cutoff value, as already observed in Fig. 4. The ring structure can be distinguished, for example in the region around 70 eV at 10, 20, and 25 mrad. The effect of the overlap between the different harmonics increased by the long driving laser wavelength (1550 nm) is evident in the central lineout of Fig. 6(b). The central ring structure of long trajectories (orange line) is symmetrically located around the short trajectories (blue line) between 75 eV and 82 eV and they overlap for smaller photon energies because the diameter of the ring structures increases. The divergence of the ring structures is more important than in the case of Fig. 4, since the value of α is much higher (typically -150×10^{-14} rad \cdot cm²/W for long trajectories and low-order harmonics). As the photon energy increases through the cutoff, the contributions from the short

trajectories present an increasing divergence [Fig. 6(c)], and long and short trajectories contributions merge at the cutoff.

Since the SFA model gives the contributions of both trajectories, short and long, we used a backing pressure of 6.2 bar that experimentally allows clear observation of both trajectories and compared the result to the SFA model in Fig. 7. Again, the model considers a single plane of Ar atoms located at the input beam waist, thereby neglecting phase-matching effects. The code was run for eight values of the CEP and intensity-averaged, since the experiment was performed with a non-CEP-stabilized laser. The results are in reasonable agreement, and it is clear that the ring features converging at the energy cutoff form the overall arrow shape at the cutoff. The values of divergence are also well reproduced. It is noteworthy that simulation results for a given CEP show interference effects between neighboring spatio-spectral structures, a feature that has been previously observed [28,29].

The ring structures observed in Fig. 7(a) are not perfectly regular, compared to the simulation. Possible experimental causes for irregular ring structures include phase-matching effects that redistribute the intensity among structures, non-perfect temporal or spatial beam profiles of the driving laser leading to asymmetric rings, and slight dissymmetry in the gas expansion, among others.

From an XUV beam user perspective, this experiment shows that using a long-wavelength driver indeed allows us to reach higher energy cutoffs [90 eV in argon is not possible with a 800 nm laser with the same number of cycles (10 cycles ~ 27 fs) due to the much lower ponderomotive energy], at the cost of increasing divergence due to a large atomic-induced transverse spatial phase.

This strong phase modulation in both the temporal and spatial domains may have far-reaching consequences for potential users. To study the consequence on the temporal attosecond structure, we performed more complete SFA simulations, now taking into account the phase-matching effects. The model, which is described in [30], includes the dispersion and absorption by neutral atoms, electrons, and ions of both

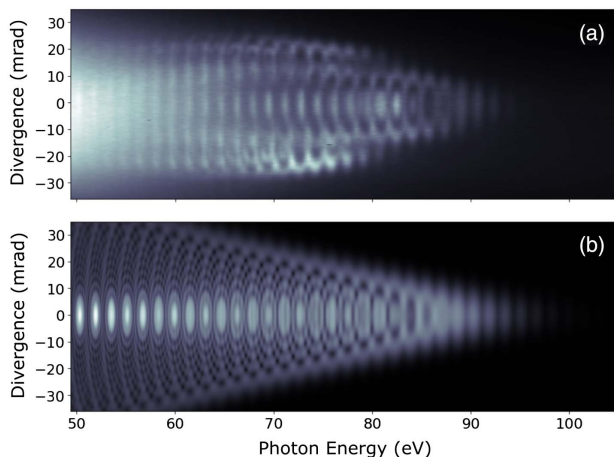


Fig. 7. (a) Experimental spatio-spectral intensity distribution of the XUV beam generated in argon with the OPCPA at 6.2 bar. (b) Result from the SFA simulation code.

the fundamental beam and the XUV radiation. The simulation has been done with a $\lambda = 1.55 \mu\text{m}$ driving laser, with 50 fs duration, focused down to a $w_0 = 10 \mu\text{m}$ spot size and a peak intensity of $1 \times 10^{14} \text{ W/cm}^2$. The argon gas jet is $300 \mu\text{m}$ long, with a density of $3.75 \times 10^{17} \text{ atoms/cm}^3$. The result, considering a single value of CEP, is plotted in Fig. 8. The intensity of HHG radiation is plotted in the time-divergence domain after numerical filtering by a 200 nm thick aluminum foil and propagation over 1 m. At each angular position, a train of about 1 fs long pulses is obtained. This is consistent with a bandpass of aluminum extending from 15 eV to 70 eV and a regular attochirp [31]. Indeed, a Fourier transformed pulse would yield $\tau_{\text{FT}} = 25$ as long pulses. Now, the chirp scales as λ and in our conditions, may be estimated as $\phi_2 = \frac{\partial^2 \phi}{\partial \omega^2} \simeq 1 \times 10^{-32} \text{ s}^2$. Plugging this value in the duration of a chirped pulse, $\tau_{\text{out}} = \sqrt{\frac{\tau_{\text{FT}}^4 + 16(\ln 2)^2 \phi_2^2}{\tau_{\text{FT}}}}$, gives a duration of 1.1 fs, compatible with this numerical observation. The pulse train should thus be compressible using standard methods. In addition, a strong curvature of the wavefront is observed. This is well described by the propagation of a $10 \mu\text{m}$ waist Gaussian beam at a 1 m distance (legend in Fig. 8). A series of lineouts displayed in Fig. 8(b) evidences the similarity of the intensities once corrected for the spherical phase, with slight shifts in time. The time discretization does not allow us to perform reliable summations of these pulses, as it would appear when focused by, e.g., a toroidal mirror. However, it seems that even though the spectrum is very

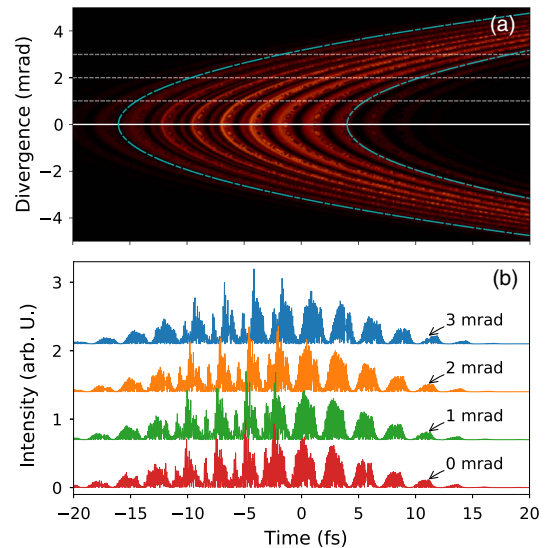


Fig. 8. (a) Spatio-temporal map of the electric field intensity at $z = 1 \text{ m}$ from the gas jet, plotted in false colors. The blue dashed lines are two parabolic phase profiles corresponding to a Gaussian beam with $w_0 = 10 \mu\text{m}$ waist at this distance, given by $t + \frac{1}{2c} \frac{z}{1 + \frac{z^2}{w_0^2}} \theta^2 = \text{cst}$, where θ is the divergence. The white lines are the locations of the lineouts displayed in panel (b). (b) Temporal profiles in the far field at three transverse locations. The lineouts have been shifted horizontally by the time lag corresponding to the trivial Gaussian quadratic phase corresponding to each angle [displayed in blue in panel (a)] and vertically by 0.7 from one another for the sake of clarity.

structured, after adequate spatial filtering in the far field, the attosecond structure might remain controllable at the focal point of an instrument.

To investigate further the properties of the XUV beam driven by high-power emerging drivers from a user perspective, we now focus on experiments performed in neon.

C. Results Obtained with the YDFA in Neon

In particular, we explore the energy cutoff and photon flux scalability, using the YDFA laser temporally compressed to the shortest duration of 16 fs with the current setup. Here the setup is aligned to favor short trajectories and obtain maximum photon flux. The laser pulse (70 μJ energy) is focused in a neon gas jet backed by a pressure of 9 bar using a 75 mm lens. The spectrometer is aligned to observe photon energies up to 160 eV. The measured spatio-spectral intensity distribution is shown in Fig. 9, along with the associated photon flux spectral density.

At this pressure level, it is clear from Fig. 9 that phase matching is optimized for the short trajectories, resulting in a low divergence beam. The overall spatio-spectral structure exhibits low couplings, although a slight increase of the divergence is observed as the photon energy approaches the cutoff energy around 140 eV. The photon flux spectral density associated with the 73th harmonic at 58 eV is 1.4×10^{12} photons \cdot s $^{-1}$ \cdot eV $^{-1}$. This corresponds to an average power in this harmonic of 6 μW , the largest average power reported to our knowledge in this spectral range [10,27]. This highlights the fact that these compact laser sources have a great potential for numerous applications that require large photon flux and/or high repetition rates.

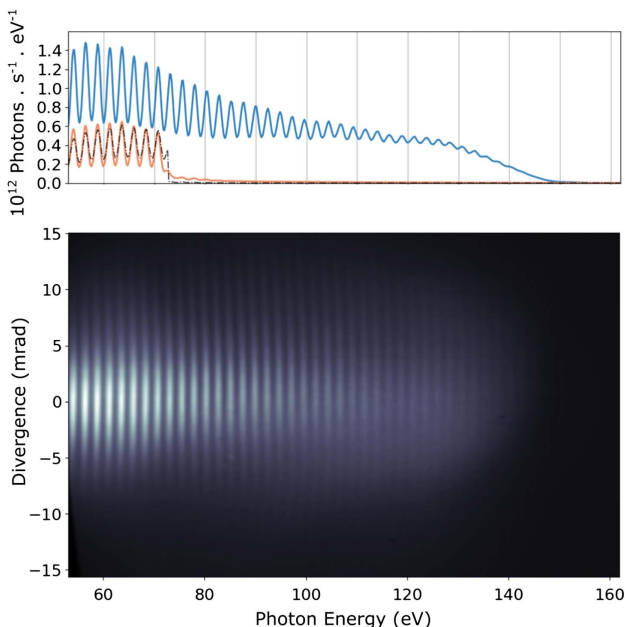


Fig. 9. Bottom: experimental spatio-spectral intensity distribution of the XUV beam generated in neon with the temporally compressed YDFA. Top: measured photon flux spectral density of XUV beam unfiltered (blue) and transmitted through a 200 nm thick Al filter (orange). Dashed line: measured unfiltered spectrum multiplied by the transmission curve of 200 nm Al filter with 20 nm Al_2O_3 layer.

5. CONCLUSION

We studied the spatio-spectral intensity distribution of XUV beams generated through HHG using high repetition rate laser systems at 1.03 μm and 1.55 μm wavelengths. The observed structures are rings at each harmonic with decreasing divergence for increasing photon energies for the long trajectories. For short trajectories, the structures form homogeneous lines with increasing divergence as the photon energy approaches the cutoff. These observations are in line with a simple model that connects these structures to the atomic dipole phase induced in the near field/temporal domain [22]. Since the phase-intensity coupling constant α scales as λ^3 , these effects are more prominent as the driver wavelength increases.

At constant peak intensity and pulse duration, the use of a longer-wavelength high repetition rate system results in two effects for the spatio-spectral structures. First, tighter focusing leads to an increased divergence that, in the far field, broadens the ring structure in the spatial dimension, without affecting the photon energy spread. The structure in itself is not modified by the focusing condition, just a scaling is applied. However, in that case, phase matching necessitates higher gas pressure than in loose focusing conditions. Second, the increased driving wavelength leads to a larger spatio-temporal phase modulation that both increases the spatial divergence and photon energy spread and modifies the structure by adding ring patterns. In all cases it is possible to phase match the HHG process to isolate the short trajectories contribution, where these effects are much less pronounced because of the lower value of the phase-intensity coupling constant. Although such an optimization might result in conditions where the overall photon flux is not maximum, this optimization results in usable XUV beams for numerous applications. From this perspective, we have obtained a cutoff energy of 95 eV in argon using the OPCPA driver at 1.55 μm , and by using the YDFA driver at 1.03 μm we achieved a cutoff energy of 140 eV in neon, with photon flux spectral densities up to 3×10^9 photon \cdot s $^{-1}$ \cdot eV $^{-1}$ and 1.4×10^{12} photon \cdot s $^{-1}$ \cdot eV $^{-1}$, respectively. These values are extremely promising for a wide range of applications from gas phase and condensed matter physics.

For instance, the use of coincidence detection devices [32–34] typically requires about 10^5 – 10^8 photons/pulse [32], which matches the number of photons obtained in a single harmonic in the plateau when the short trajectory is phase matched with our sources. This opens the route to the investigation of, e.g., time delays in molecular photoionization [35]. The same applies to solid-state applications, such as, for instance, the attosecond PhotoElectron Emission microscope, which promises the dynamical imaging of localized nanoscale structures, e.g., surface plasmons [36,37]. Also, femtosecond Angularly Resolved PhotoEmission Spectroscopy (FemtoArpes) [38–41] will benefit from these emerging sources with high photon fluxes but low photon number per pulse. Upon delivering the same order of magnitude of photons per pulse, the full Brillouin zone becomes accessible, while keeping a femtosecond to attosecond time resolution [42,43]. It should be noted that for these applications that require a high spectral purity of the XUV beam, the atomic dipole-induced spectral phase has important consequence in terms of each harmonic

bandwidth. Applications of high repetition rate XUV sources may extend to spin resolved Arpes [44], opening a new route to the study of attosecond and femtosecond dynamics of magnetism. These emerging compact high repetition rate drivers are therefore very promising to broaden the range of applications and spread the use of XUV beams generated through HHG.

Funding. Fonds Unique Interministériel (FUI) (STAR); Conseil départemental de l'Essonne (SOPHIE) (SOPHIE); Agence Nationale de la Recherche (ANR) (ANR-10-LABX-0039-PALM, ANR-11-EQPX0005-ATTOLAB, ANR-16-CE30-0027-01-HELLIX).

REFERENCES

1. A. McPherson, G. Gibson, H. Jara, U. Johann, T. S. Luk, I. A. McIntyre, K. Boyer, and C. K. Rhodes, "Studies of multiphoton production of vacuum-ultraviolet radiation in the rare gases," *J. Opt. Soc. Am. B* **4**, 595–601 (1987).
2. M. Ferray, A. L'Huillier, X. F. Li, G. Mainfray, and C. Manus, "Multiple-harmonic conversion of 1064 nm radiation in rare gases," *J. Phys. B* **21**, L31–L35 (1988).
3. P. B. Corkum, "Plasma perspective on strong-field multiphoton ionization," *Phys. Rev. Lett.* **71**, 1994–1997 (1993).
4. P. Balcou, P. Salieres, A. L'Huillier, and M. Lewenstein, "Generalized phase-matching conditions for high harmonics: the role of field-gradient forces," *Phys. Rev. A* **55**, 3204–3210 (1997).
5. M. Lewenstein, P. Balcou, M. Ivanov, A. L'Huillier, and P. B. Corkum, "Theory of high-order harmonic generation by low-frequency laser fields," *Phys. Rev. A* **49**, 2117–2132 (1994).
6. F. Lépine, M. Y. Ivanov, and M. J. J. Vrakking, "Attosecond molecular dynamics: fact or fiction?" *Nat. Photonics* **8**, 195–204 (2014).
7. M. F. Ciappina, J. A. Pérez-Hernández, A. S. Landsman, W. A. Okell, S. Zherebtsov, B. Förg, J. Schötz, L. Seiffert, T. Fennel, T. Shaaran, T. Zimmermann, A. Chacón, R. Guichard, A. Zair, J. W. G. Tisch, J. P. Marangos, T. Witting, A. Braun, S. A. Maier, L. Roso, M. Krüger, P. Hommelhoff, M. F. Kling, F. Krausz, and M. Lewenstein, "Attosecond physics at the nanoscale," *Rep. Prog. Phys.* **80**, 054401 (2017).
8. F. Calegari, G. Sansone, S. Stagira, C. Vozzi, and M. Nisoli, "Advances in attosecond science," *J. Phys. B* **49**, 062001 (2016).
9. E. Lorek, E. W. Larsen, C. M. Heyl, S. Carlström, D. Paleček, D. Zigmantas, and J. Mauritsson, "High-order harmonic generation using a high-repetition-rate turnkey laser," *Rev. Sci. Instrum.* **85**, 123106 (2014).
10. S. Hädrich, J. Rothhardt, M. Krebs, S. Demmler, A. Klenke, A. Tünnermann, and J. Limpert, "Single-pass high harmonic generation at high repetition rate and photon flux," *J. Phys. B* **49**, 172002 (2016).
11. A. Cabasse, G. Machinet, A. Dubrouil, E. Cormier, and E. Constant, "Optimization and phase matching of fiber-laser-driven high-order harmonic generation at high repetition rate," *Opt. Lett.* **37**, 4618–4620 (2012).
12. S. Hädrich, M. Krebs, J. Rothhardt, H. Carstens, S. Demmler, J. Limpert, and A. Tünnermann, "Generation of μW level plateau harmonics at high repetition rate," *Opt. Express* **19**, 19374–19383 (2011).
13. J. Bouillet, Y. Zaouter, J. Limpert, S. Petit, Y. Mairesse, B. Fabre, J. Higuët, E. Mével, E. Constant, and E. Cormier, "High-order harmonic generation at a megahertz-level repetition rate directly driven by an ytterbium-doped-fiber chirped-pulse amplification system," *Opt. Lett.* **34**, 1489–1491 (2009).
14. K.-H. Hong, C.-J. Lai, J. P. Siqueira, P. Krogen, J. Moses, C.-L. Chang, G. J. Stein, L. E. Zapata, and F. X. Kärtner, "Multi-mJ, kHz, 2.1 μm optical parametric chirped-pulse amplifier and high-flux soft x-ray high-harmonic generation," *Opt. Lett.* **39**, 3145–3148 (2014).
15. X. Zhou, P. Ranitovic, C. Hogle, J. Eland, H. Kapteyn, and M. Murnane, "Probing and controlling non-Born-Oppenheimer dynamics in highly excited molecular ions," *Nat. Phys.* **8**, 232–237 (2012).
16. C.-T. Chiang, M. Huth, A. Trützschler, M. Kiel, F. O. Schumann, J. Kirschner, and W. Widdra, "Boosting laboratory photoelectron spectroscopy by megahertz high-order harmonics," *New J. Phys.* **17**, 013035 (2015).
17. L. He, P. Lan, Q. Zhang, C. Zhai, F. Wang, W. Shi, and P. Lu, "Spectrally resolved spatiotemporal features of quantum paths in high-order-harmonic generation," *Phys. Rev. A* **92**, 043403 (2015).
18. A. Dubrouil, O. Hort, F. Catoire, D. Descamps, S. Petit, E. Mével, V. Strelkov, and E. Constant, "Spatio-spectral structures in high-order harmonic beams generated with terawatt 10-fs pulses," *Nat. Commun.* **5**, 4637 (2014).
19. F. Schapper, M. Holler, T. Auguste, A. Zar, M. Weger, P. Salières, L. Gallmann, and U. Keller, "Spatial fingerprint of quantum path interferences in high order harmonic generation," *Opt. Express* **18**, 2987–2994 (2010).
20. S. Carlström, J. Preclíková, E. Lorek, E. W. Larsen, C. M. Heyl, D. Paleček, D. Zigmantas, K. J. Schager, M. B. Gaarde, and J. Mauritsson, "Spatially and spectrally resolved quantum path interference with chirped driving pulses," *New J. Phys.* **18**, 123032 (2016).
21. C. M. Heyl, J. Gädde, U. Höfer, and A. L'Huillier, "Spectrally resolved maker fringes in high-order harmonic generation," *Phys. Rev. Lett.* **107**, 033903 (2011).
22. F. Catoire, A. Ferré, O. Hort, A. Dubrouil, L. Quintard, D. Descamps, S. Petit, F. Burgy, E. Mével, Y. Mairesse, and E. Constant, "Complex structure of spatially resolved high-order-harmonic spectra," *Phys. Rev. A* **94**, 063401 (2016).
23. P. Rigaud, A. Van de Walle, M. Hanna, N. Forget, F. Guichard, Y. Zaouter, K. Guesmi, F. Druon, and P. Georges, "Supercontinuum-seeded few-cycle mid-infrared OPCPA system," *Opt. Express* **24**, 26494–26502 (2016).
24. L. Lavenue, M. Natile, F. Guichard, Y. Zaouter, M. Hanna, E. Mottay, and P. Georges, "High-energy few-cycle Yb-doped fiber amplifier source based on a single nonlinear compression stage," *Opt. Express* **25**, 7530–7537 (2017).
25. H. Bandulet, D. Comtois, A. Shiner, C. Trallero-Herrero, N. Kajumba, T. Ozaki, P. Corkum, D. Villeneuve, J. Kieffer, and F. Légaré, "High harmonic generation with a spatially filtered optical parametric amplifier," *J. Phys. B* **41**, 245602 (2008).
26. M. Högner, "HHG max code," <https://github.com/Leberwurscht/HHGmax>.
27. C. M. Heyl, C. L. Arnold, A. Couairon, and A. L'Huillier, "Introduction to macroscopic power scaling principles for high-order harmonic generation," *J. Phys. B* **50**, 013001 (2017).
28. E. Mansten, J. M. Dahlstrom, J. Mauritsson, T. Ruchon, A. L'Huillier, J. Tate, M. B. Gaarde, P. Eckle, A. Guandalini, M. Holler, F. Schapper, L. Gallmann, and U. Keller, "Spectral signature of short attosecond pulse trains," *Phys. Rev. Lett.* **102**, 083002 (2009).
29. G. Sansone, E. Benedetti, J.-P. Caumes, S. Stagira, C. Vozzi, M. Pascolini, L. Poletto, P. Villoresi, S. De Silvestri, and M. Nisoli, "Measurement of harmonic phase differences by interference of attosecond light pulses," *Phys. Rev. Lett.* **94**, 193903 (2005).
30. T. Auguste, O. Gobert, T. Ruchon, and F. Quéré, "Attosecond light-houses in gases: a theoretical and numerical study," *Phys. Rev. Lett.* **A 93**, 033825 (2016).
31. S. B. Schoun, R. Chirla, J. Wheeler, C. Roedig, P. Agostini, L. F. DiMauro, K. J. Shafer, and M. B. Gaarde, "Attosecond pulse shaping around a Cooper minimum," *Phys. Rev. Lett.* **112**, 153001 (2014).
32. P. Billaud, M. Géléoc, Y. J. Picard, K. Veyrinas, J. F. Hergott, S. M. Poullain, P. Breger, T. Ruchon, M. Roullay, F. Delmotte, F. Lepetit, A. Huetz, B. Carré, and D. Dowek, "Molecular frame photoemission in dissociative ionization of H_2 and D_2 induced by high harmonic generation femtosecond XUV pulses," *J. Phys. B* **45**, 194013 (2012).
33. Y. J. Picard, B. Manschwetus, M. Géléoc, M. Böttcher, E. M. S. Casagrande, N. Lin, T. Ruchon, B. Carré, J.-F. Hergott, F. Lepetit, R. Taëb, A. Maquet, and A. Huetz, "Attosecond evolution of energy- and angle-resolved photoemission spectra in two-color (XUV + IR) ionization of rare gases," *Phys. Rev. A* **89**, 031401 (2014).
34. K. Veyrinas, V. Gruson, S. Weber, L. Barreau, T. Ruchon, J.-F. Hergott, J.-C. Houver, R. Lucchese, P. Salières, and D. Dowek, "Molecular frame photoemission by a comb of elliptical high-order

- harmonics: a sensitive probe of both photodynamics and harmonic complete polarization state," *Faraday Discuss.* **194**, 161–183 (2016).
35. P. Hockett, E. Frumker, D. M. Villeneuve, and P. B. Corkum, "Time delay in molecular photoionization," *J. Phys. B* **49**, 095602 (2016).
 36. S. H. Chew, K. Pearce, C. Späth, A. Guggenmos, J. Schmidt, F. Süßmann, M. F. Kling, U. Kleineberg, E. Mårsell, C. L. Arnold, E. Lorek, P. Rudawski, C. Guo, M. Miranda, F. Ardana, J. Mauritsson, A. L'Huillier, and A. Mikkelsen, "*Imaging Localized Surface Plasmons by Femtosecond to Attosecond Time-Resolved Photoelectron Emission Microscopy-ATTO-PEEM*," (Wiley-VCH Verlag GmbH & Co. KGaA, 2014), pp. 325–364.
 37. A. Mikkelsen, J. Schwenke, T. Fordell, G. Luo, K. Klünder, E. Hilner, N. Anttu, A. Zakharov, E. Lundgren, J. Mauritsson, J. N. Andersen, H. Q. Xu, and A. L'Huillier, "Photoemission electron microscopy using extreme ultraviolet attosecond pulse trains," *Rev. Sci. Instrum.* **80**, 123703 (2009).
 38. S. Eich, A. Stange, A. Carr, J. Urbancic, T. Popmintchev, M. Wiesenmayer, K. Jansen, A. Ruffing, S. Jakobs, T. Rohwer, S. Hellmann, C. Chen, P. Matyba, L. Kipp, K. Rossnagel, M. Bauer, M. Murnane, H. Kapteyn, S. Mathias, and M. Aeschlimann, "Time- and angle-resolved photoemission spectroscopy with optimized high-harmonic pulses using frequency-doubled Ti:sapphire lasers," *J. Electron Spectrosc. Relat. Phenom.* **195**, 231–236 (2014).
 39. M. Puppin, Y. Deng, O. Prochnow, J. Ahrens, T. Binhammer, U. Morgner, M. Krenz, M. Wolf, and R. Ernstorfer, "500 kHz OPCPA delivering tunable sub-20 fs pulses with 15 W average power based on an all-ytterbium laser," *Opt. Express* **23**, 1491–1497 (2015).
 40. R. Locher, L. Castiglioni, M. Lucchini, M. Greif, L. Gallmann, J. Osterwalder, M. Hengsberger, and U. Keller, "Energy-dependent photoemission delays from noble metal surfaces by attosecond interferometry," *Optica* **2**, 405–410 (2015).
 41. G. Rohde, A. Hendel, A. Stange, K. Hanff, L.-P. Oloff, L. X. Yang, K. Rossnagel, and M. Bauer, "Time-resolved ARPES with sub-15 fs temporal and near Fourier-limited spectral resolution," *Rev. Sci. Instrum.* **87**, 103102 (2016).
 42. Z. Tao, C. Chen, T. Szilvasi, M. Keller, M. Mavrikakis, H. Kapteyn, and M. Murnane, "Direct time-domain observation of attosecond final-state lifetimes in photoemission from solids," *Science* **353**, 62–67 (2016).
 43. M. Lucchini, L. Castiglioni, L. Kasmi, P. Kliuiev, A. Ludwig, M. Greif, J. Osterwalder, M. Hengsberger, L. Gallmann, and U. Keller, "Light-matter interaction at surfaces in the spatiotemporal limit of macroscopic models," *Phys. Rev. Lett.* **115**, 137401 (2015).
 44. C. Nicholson, C. Monney, R. Carley, B. Frietsch, J. Bowlan, M. Weinelt, and M. Wolf, "Ultrafast spin density wave transition in chromium governed by thermalized electron gas," *Phys. Rev. Lett.* **117**, 136801 (2016).



Optics Letters

Self-compression in a multipass cell

GAËTAN JARGOT,^{1,2,*} NOUR DAHER,¹ LOÏC LAVENU,^{1,3} XAVIER DELEN,¹ NICOLAS FORGET,²  MARC HANNA,¹ AND PATRICK GEORGES¹

¹Laboratoire Charles Fabry, Institut d'Optique Graduate School, CNRS, Université Paris-Saclay, 91127 Palaiseau Cedex, France

²Fastlite, 165 rue des Cistes Pôle entreprise 95 06600 Antibes, Sophia Antipolis, France

³Amplitude Laser, Cité de la Photonique, 11 avenue de Canteranne, 33600 Pessac, France

*Corresponding author: gaetan.jargot@institutoptique.fr

Received 18 July 2018; revised 17 October 2018; accepted 22 October 2018; posted 26 October 2018 (Doc. ID 340161); published 14 November 2018

We demonstrate self-compression of short-wavelength infrared pulses in a multipass cell (MPC) containing a plate of silica. Nonlinear propagation in the cell in the anomalous dispersion regime results in the generation of 14 μJ 22 fs pulses at 125 kHz repetition rate and 1550 nm wavelength. Periodic focusing inside the cell allows us to circumvent catastrophic self-focusing, despite an output peak power of 440 MW well beyond the critical power in silica of 10 MW. This technique allows straightforward energy scaling of self-compression setups and control over the spatial manifestation of Kerr nonlinearity. More generally, MPCs can be used to perform, at higher energy levels, temporal manipulations of pulses that have been previously demonstrated in waveguides. © 2018 Optical Society of America

<https://doi.org/10.1364/OL.43.005643>

Ultrafast lasers have allowed a plethora of applications, ranging from industrial processing to a large number of scientific advances such as multiphoton imaging, ultrafast dynamics studies, and strong field physics. In the short-wavelength infrared (SWIR) and mid-infrared (MIR) wavelength ranges, applications such as high-harmonic generation in gases [1], solids [2], and multidimensional molecular spectroscopy [3] are pushing the development of high-power microjoule–millijoule laser systems with pulse durations in the few-cycle regime. In this wavelength range, the most widespread sources of ultrashort pulses are optical parametric chirped pulse amplifiers (OPCPAs) that readily deliver pulses with sub-100 fs durations at high repetition rates [4–8].

Access to shorter pulse durations is often allowed by implementing a nonlinear compression setup at the output of the laser system. Propagation of the pulse in a solid or gas material induces spectral broadening through self-phase modulation (SPM), corresponding to a shorter Fourier-transform limited pulse. For sources in the near-infrared, where material dispersion is normal, additional negative dispersion must be added after the SPM stage [9]. For sources in the SWIR and MIR, most optical materials exhibit anomalous dispersion, and soliton dynamics results in compression in the initial stage of propagation. Although self-compression can be performed in

gaseous [10] and bulk solid [11] media, these experiments often show low energy transfer to the compressed pulse and more difficult experimental control because of the complex spatio-temporal dynamics. Alternatively, the use of a waveguide allows large interaction lengths and negates the spatial Kerr effect, resulting in efficient and well-controlled setups. Energy scaling in waveguides is challenging, requiring, for instance, the use of gas-filled anti-resonant photonic crystal fiber designs to increase the critical power for self-focusing, ensure low losses, and induce anomalous dispersion [12].

Recently, a concept allowing the use of a bulk nonlinear medium while retaining the advantages of waveguides has emerged [13]. It consists of placing the nonlinear medium inside a multipass cell (MPC) and accumulating the nonlinearity over a large number of passes, so that nonlinear propagation in the medium can be seen as a small perturbation to free-space propagation as far as spatial effects are concerned. This can be compared to waveguides where spatial nonlinear effects change slightly the mode structure [14] without significant physical impact. It can also be considered as an extension of multi-plate setups [15–17] with a distribution of the nonlinearity over tens of passes in the material instead of a few. Although it was proposed as early as 2000 [18], it is only recently that this idea has been demonstrated [13].

The concept was first implemented with a solid nonlinear medium [13,19,20], where it was shown that the peak power can exceed the critical power in the medium without affecting the spatial profile at the output. The MPC idea was then used with a gas medium [21,22], at higher energy levels of 140 μJ and 2 mJ, respectively. These demonstrations have all been done in setups where the net dispersion in the MPC was either negligible or slightly normal, resulting in an essentially stationary temporal profile during propagation and necessitating negative dispersion at the output to compress the pulse.

Here we report the use of an MPC in net anomalous dispersion regime to take advantage of soliton dynamics and self-compress 19 μJ 63 fs pulses generated by an OPCPA at 1.55 μm down to a 22 fs pulse duration with a transmission of 73%. The experimental data are compared to a 3D numerical model, and the output beam is characterized in terms of spatio-spectral couplings. This experiment establishes the use of MPCs as a simple way to scale the energy of nonlinear

functions usually performed in waveguides, essentially opening ultrafast nonlinear fiber optics to higher pulse energies.

Figure 1 depicts the SWIR OPCPA operated at 125 kHz and 1550 nm that follows the overall architecture reported in Ref. [7], with some modifications. The setup is based on a femtosecond ytterbium-doped fiber amplifier system (Tangerine, Amplitude Systèmes) that delivers 400 μJ 400 fs pulses at a 125 kHz repetition rate with a central wavelength at 1030 nm. A small fraction (4 μJ) of the pump beam is used to generate a stable seed extending from 1300 to 1700 nm through supercontinuum generation in a 10 mm long YAG crystal [23]. This signal is temporally stretched by passing through 3 mm of silicon in order to reach the best trade-off between the gain and bandwidth in the first parametric amplification stage, carried out in a 1 mm long Mgo:PPLN fanout crystal. At the output of this stage, pumped with 13 μJ , the signal energy is 500 nJ, with a spectrum centered at 1550 nm. After propagation through 2 mm of additional silicon, the signal is sent to the second and last stage of parametric amplification, based on a 3 mm long KTA crystal used in type II non-collinear phase matching. The signal pulses are amplified to 22.5 μJ . Compression is achieved by propagation in 210 mm of silica, with a transmission of 86%. The compressed pulse energy is 19 μJ , corresponding to 2.4 W average power.

The OPCPA output properties are shown in Fig. 2. The temporal profile and spectrum are measured with a second-harmonic generation frequency-resolved optical gating (FROG) apparatus. The full width at half-maximum (FWHM) pulse duration is 63 fs, with a 120 nm bandwidth at -10 dB. The spatial beam profile is measured using an InGaAs camera, showing a slightly elliptic beam, as shown in the inset Fig. 2(a).

In optical fibers, soliton dynamics in the anomalous dispersion regime induces self-compression for soliton number $N = \sqrt{L_d/L_{SPM}} > 1$, where $L_d = T_0^2/\beta_2$ is the dispersion length, T_0 is the input pulse duration, and β_2 is the group-velocity dispersion. The characteristic length for SPM is $L_{SPM} = cA_{\text{eff}}/\omega_0 n_2 P_{\text{peak}}$, where c is the speed of light, A_{eff} is the effective area, ω_0 is the optical angular frequency, n_2 is the nonlinear index, and P_{peak} is the input peak power. In order to keep a clean compressed pulse, small values of N are required ($N \leq 5$), since larger values of N result in a reduced fraction of energy contained in the compressed temporal feature at the output. The compression ratio and optimal compression distance are found to scale like N and $1/N$, respectively [24].

Deviations from these scaling laws depend on the influence of higher-order effects such as higher-order dispersion and self-steepening.

Here we use an MPC that includes a 2 mm plate of anti-reflection coated (1300–1700 nm) silica to perform self-compression. The output beam from the OPCPA is coupled in and out of the MPC using rectangular-shaped mirrors (3 mm \times 10 mm) located in front of one of the MPC mirrors. These mirrors (Layertec coating 113504) have a diameter of 25.4 mm and a radius of curvature of 200 mm, and are coated to be highly reflective (>99.8%) in the 1400–1700 nm range while introducing low group delay dispersion. The MPC is 280 mm long, and the silica plate is located asymmetrically at a distance of 100 mm from one of the MPC mirror. This adjustment is an experimentally convenient way to tune the level of nonlinearity, since the beam width increases from the MPC center to the mirrors. Stationary beam propagation in this MPC requires a beam radius at $1/e^2$ of 212 μm at the MPC waist, expanding to 388 μm radius at the MPC mirrors. Experimentally, an arrangement of two lenses with a focal length $f = 150$ mm and $f = -100$ mm at the input of the cell allows us to match this value, with a measured radius of 225×270 μm . At the output of the MPC, the beam is collimated with a $f = 750$ mm

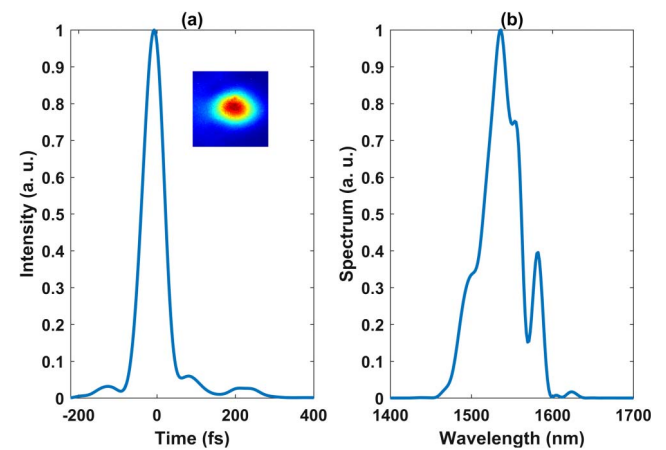


Fig. 2. (a) Temporal profile at the output of the OPCPA. Inset: spatial profile. (b) Spectrum at the OPCPA output. The FROG error is 61×10^{-4} on a 256×256 grid.

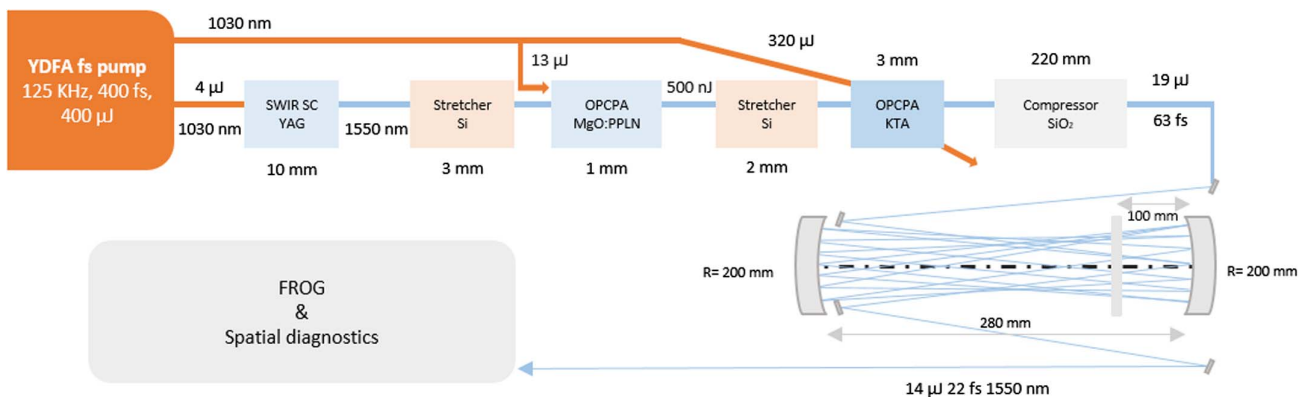


Fig. 1. Experimental setup.

lens, and silver-protected mirrors are used to route it to diagnostics.

In terms of soliton parameters, using the input pulse parameters from the OPCPA, the dispersion and nonlinear index of silica at 1550 nm $\beta_2 = -28 \text{ fs}^2/\text{mm}$ and $n_2 = 2.7 \times 10^{-20} \text{ m}^2/\text{W}$, this MPC geometry translates in $L_D = 45 \text{ mm}$ and $L_{NL} = 5.9 \text{ mm}$, giving a soliton parameter $N = 2.7$. The most obvious deviations from the theoretical soliton framework are the spatial imperfections that are not present in a single-mode optical fiber, and the introduction of higher-order dispersion and spectral filtering at the mirrors. This dispersion results in a net zero dispersion wavelength shifted from 1300 nm for pure silica to 1450 nm for the MPC, so that the spectral content generated below this value will not participate further in the soliton dynamics.

The position and orientation of the input and output coupling mirrors allow us to select the number of roundtrips in the MPC. They are adjusted to make 10 roundtrips, resulting in an overall propagation distance in the silica of 40 mm. Figure 3 shows the measured and retrieved FROG traces and the related temporal profile and spectrum, when the input pulse energy is 19 μJ , without any additional dispersion added between the MPC and diagnostics. The FWHM pulse width is 22 fs, corresponding to a compression ratio of 2.8. The spectrum extends over the full bandwidth of the mirrors from 1300 to 1700 nm, with a bandwidth at -10 dB of 310 nm corresponding to a Fourier transform-limited pulse duration of 20 fs. The energy

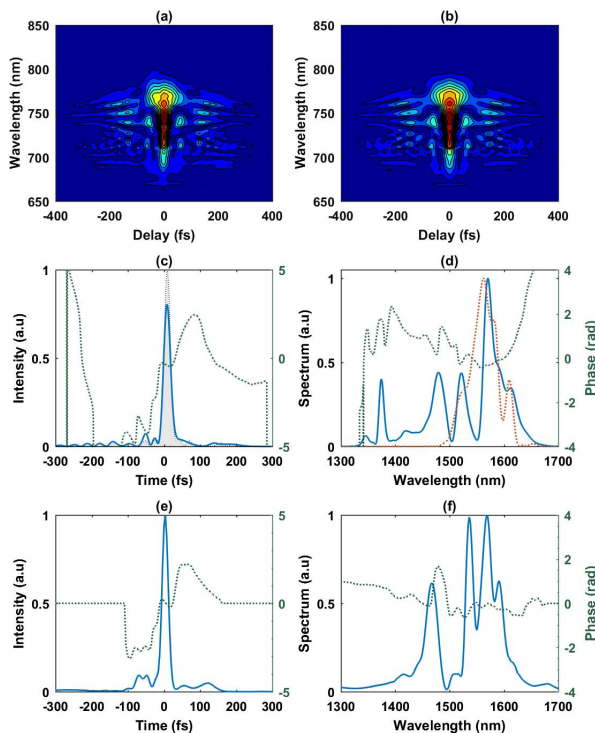


Fig. 3. (a) Measured and (b) retrieved FROG traces at the output of the compression setup at maximum input energy of 19 μJ . The FROG error is 57×10^{-4} on a 256×256 grid. (c) FROG-retrieved temporal profile (blue), temporal phase profile (dashed green), and Fourier transform-limited profile (gray) compared to (e) the numerical model. (d) FROG-retrieved spectrum (solid blue), spectral phase profile (dashed green), and initial OPCPA spectrum (dashed red) compared to (f) the numerical model.

transmission of the MPC starts at 80% at low input energy, and drops down to 73% at the highest energy of 19 μJ , resulting in 14 μJ output pulses. This drop can be confidently attributed to the mirror bandwidths that are not able to reflect the full spectral content generated through soliton compression. The estimated peak power using the measured temporal profile and energy at the output is 440 MW, 40 times higher than the critical power in bulk silica. This highlights the main advantage of this geometry, first pointed out in Ref. [13]: it allows nonlinear propagation over an accumulated distance that is greater than the self-focusing distance (estimated to 15 mm in this experiment) in the material, with minor impact on the spatial profile, as will be described hereafter.

Numerical simulations are performed to ensure that the physics underlying the compression is well captured by a 3D model based on an envelope equation described in Ref. [25], solved using the split-step method described in Ref. [26]. This model includes self-steepening, in addition to diffraction, dispersion to all orders, and instantaneous Kerr effect. The mirror dispersion and reflection curves are fitted to the supplier data to account for this deviation from the ideal soliton model. The temporal initial condition is taken from the FROG-retrieved field at the output of the OPCPA. The input spatial profile is a perfect Gaussian function that matches the stationary MPC beam. The input energy is adjusted to 12 μJ to match the experimentally obtained optimal compression point of 10 roundtrips. This discrepancy is most probably due to the non-perfect spatial quality and mode matching which translate into an experimentally lower level of nonlinearity. The simulated temporal profile and spectrum are plotted along with the experimental results in Fig. 3, and show qualitative agreement. However, the exact spectral structure is not reproduced accurately. This could be due to a number of reasons, including uncertainty in the dispersion profile of the mirror coatings, a non-perfect spatial profile in the experiment, or the fact that air was not included in the simulation as a dispersive and nonlinear medium. The on-axis B-integral per pass through the silica plate grows from 0.4 to 1 rad because of the self-compressing temporal profile, with an integrated value of 13.5 rad. This model also allows us to point out what limits the pulse duration in the current experiment: if the realistically dispersive and filtering mirrors are replaced with dispersionless infinitely broadband mirrors, compression down to sub -10 fs (two optical cycles at 1550 nm) should be achievable.

We now focus on the spatial properties of the output beam, of particular importance in MPC-based nonlinear optics setups. The M^2 parameter is measured at the output of the MPC using a lens and InGaAs camera, both in linear (low energy) and nonlinear (full energy) propagation regimes. The collimated spatial beam profile is observed to slightly decrease in size as the energy is increased, an effect also observed in simulations. However, as shown in Fig. 4, the spatial quality remains essentially constant with M^2 values of 1.53×1.15 at low power going to 1.49×1.24 at the highest energy.

We also assess the spatio-spectral homogeneity by measuring the spectral content at different locations in the compressed output beam. This is an important point to assess the MPC-induced spatial homogenization of nonlinearities. A multimode fiber with a 200 μm core is translated into the output beam and coupled to a spectrometer. The result of this measurement is plotted in Fig. 4. The plotted quantity is the spectral overlap

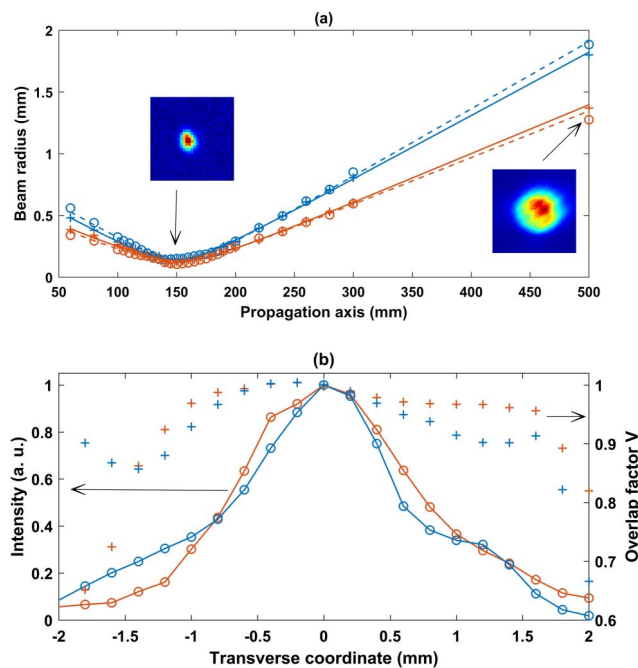


Fig. 4. (a) M^2 measurements of the output beam at low energy (dashed line) and at full energy (solid line) in the horizontal (blue) and vertical (red) directions. (b) Spectral overlap factor with a beam center and intensity as a function of horizontal (blue) and vertical (red) transverse dimensions.

with the beam center [19] that remains above 90% in the central part of the beam. It decreases to lower values at intensity points below 10% of the maximum value. We attribute this decrease to both a decreasing signal-to-noise ratio that artificially degrades the overlap and to a halo that is present in the input beam that is not compressed in the MPC. The mean value of the spectral overlap over the entire beam is 93%, to be compared with a value of 99% in simulations. Again, the input spatial imperfections might explain this discrepancy. Overall, the spatial and spatio-temporal quality at the output is well controlled.

To conclude, we demonstrate for the first time, to the best of our knowledge, self-compression of ultrashort pulses in the SWIR using an MPC setup. This results in the generation of 14 μJ 22 fs output pulses at 125 kHz. This experiment establishes MPCs as a general nonlinear optics tool that allows retaining temporal nonlinearities while homogenizing the spatial Kerr effect. It also allows straightforward energy scaling by adjusting the MPC geometry, mirrors, and nonlinear material to fit the input pulse characteristics. Mirror coating technology is crucial to allow high energy transmission and access to the few-cycle regime, and limits the pulse duration in this demonstration. These coatings can be engineered to introduce a net anomalous dispersion in the cell so that self-compression can be achieved in a large variety of media (gases, solids) and wavelength ranges. We believe that MPCs with advanced mirror designs will allow the scaling of self-compression setups to high energy and few-cycle pulses in a robust experimental setup. This should enable applications in the SWIR and

MIR wavelength range, and we more generally expect the number of nonlinear MPC applications to grow, since it constitutes a unique tool in the current ultrafast technology landscape.

Funding. Agence Nationale de la Recherche (ANR) (ANR-10-LABX-0039-PALM, ANR-16-CE30-0027-01); Conseil Départemental de l'Yvelines (Sophie).

REFERENCES

1. T. Popmintchev, M.-C. Chen, D. Popmintchev, P. Arpin, S. Brown, S. Ališauskas, G. Andriukaitis, T. Balčiūnas, O. D. Mücke, A. Pugžlys, A. Baltuška, B. Shim, S. E. Schrauth, A. Gaeta, C. Hernández-García, L. Plaja, A. Becker, A. Jaron-Becker, M. M. Murnane, and H. C. Kapteyn, *Science* **336**, 1287 (2012).
2. S. Ghimire, A. D. DiChiara, E. Sistrunk, P. Agostini, L. F. DiMauro, and D. A. Reis, *Nat. Phys.* **7**, 138 (2011).
3. B. M. Luther, K. M. Tracy, M. Gerrity, S. Brown, and A. T. Krummel, *Opt. Express* **24**, 4117 (2016).
4. N. Thiré, R. Maksimenka, B. Kiss, C. Ferchaud, P. Bizouard, E. Cormier, K. Osvay, and N. Forget, *Opt. Express* **25**, 1505 (2017).
5. M. Neuhaus, H. Fuest, M. Seeger, J. Schötz, M. Trubetskov, P. Russbuedt, H. D. Hoffmann, E. Riedle, Z. Major, V. Pervak, M. F. Kling, and P. Wnuk, *Opt. Express* **26**, 16074 (2018).
6. M. Mero, F. Noack, F. Bach, V. Petrov, and M. J. J. Vrakking, *Opt. Express* **23**, 33157 (2015).
7. P. Rigaud, A. V. de Walle, M. Hanna, N. Forget, F. Guichard, Y. Zaouter, K. Guesmi, F. Druon, and P. Georges, *Opt. Express* **24**, 26494 (2016).
8. O. Chalus, P. K. Bates, M. Smolarski, and J. Biegert, *Opt. Express* **17**, 3587 (2009).
9. W. J. Tomlinson, R. H. Stolen, and C. V. Shank, *J. Opt. Soc. Am. B* **1**, 139 (1984).
10. A. V. Mitrofanov, A. A. Voronin, M. V. Rozhko, D. A. Sidorov-Biryukov, A. B. Fedotov, A. Pugžlys, V. Shumakova, S. Ališauskas, A. Baltuška, and A. M. Zheltikov, *Optica* **4**, 1405 (2017).
11. D. Majus, G. Tamošauskas, I. Gražulevičiūtė, N. Garejev, A. Lotti, A. Couairon, D. Faccio, and A. Dubietis, *Phys. Rev. Lett.* **112**, 193901 (2014).
12. U. Elu, M. Baudisch, H. Pires, F. Tani, M. H. Frosz, F. Köttig, A. Ermolov, P. St.J. Russell, and J. Biegert, *Optica* **4**, 1024 (2017).
13. J. Schulte, T. Sartorius, J. Weitenberg, A. Vernaleken, and P. Russbuedt, *Opt. Lett.* **41**, 4511 (2016).
14. L. Dong, *J. Lightwave Technol.* **26**, 3476 (2008).
15. F. Lu, P. Xia, Y. Matsumoto, T. Kanai, N. Ishii, and J. Itatani, *Opt. Lett.* **43**, 2720 (2018).
16. J. E. Beetar, S. Gholam-Mirzaei, and M. Chini, *Appl. Phys. Lett.* **112**, 051102 (2018).
17. M. Seidel, G. Arisholm, J. Brons, V. Pervak, and O. Pronin, *Opt. Express* **24**, 9412 (2016).
18. N. Milosevic, G. Tempea, and T. Brabec, *Opt. Lett.* **25**, 672 (2000).
19. J. Weitenberg, A. Vernaleken, J. Schulte, A. Ozawa, T. Sartorius, V. Pervak, H.-D. Hoffmann, T. Udem, P. Russbuedt, and T. W. Hänsch, *Opt. Express* **25**, 20502 (2017).
20. K. Fritsch, M. Poetzlberger, V. Pervak, J. Brons, and O. Pronin, *Opt. Lett.* **43**, 4643 (2018).
21. L. Lavenue, M. Natile, F. Guichard, Y. Zaouter, X. Delen, M. Hanna, E. Mottay, and P. Georges, *Opt. Lett.* **43**, 2252 (2018).
22. M. Jeuffing, S. Reiger, M. Kaumanns, V. Pervak, M. Trubetskov, T. Nubbemeyer, and F. Krausz, *Opt. Lett.* **43**, 2070 (2018).
23. A. van de Walle, M. Hanna, F. Guichard, Y. Zaouter, A. Thai, N. Forget, and P. Georges, *Opt. Lett.* **40**, 673 (2015).
24. G. Agrawal, *Nonlinear Fiber Optics* (2007).
25. T. Brabec and F. Krausz, *Phys. Rev. Lett.* **78**, 3282 (1997).
26. M. Hanna, X. Délen, L. Lavenue, F. Guichard, Y. Zaouter, F. Druon, and P. Georges, *J. Opt. Soc. Am. B* **34**, 1340 (2017).



Optics Letters

Orbital angular momentum from semiconductor high-order harmonics

DAVID GAUTHIER,^{1,*} SHATHA KAASSAMANI,¹ DOMINIK FRANZ,¹ RANA NICOLAS,¹ JEAN-THOMAS GOMES,² LAURE LAVOUTE,² DMITRY GAPONOV,² SÉBASTIEN FÉVRIER,³ GAËTAN JARGOT,^{4,5} MARC HANNA,⁴ WILLEM BOUTU,¹ AND HAMED MERDJI¹

¹LIDYL, CEA, CNRS, Université Paris-Saclay, CEA-Saclay, 91191 Gif-sur-Yvette, France

²Novae, ZI du Moulin Cheyroux, 87700 Aix-sur-Vienne, France

³Université de Limoges, CNRS, XLIM, UMR 7252, 87000 Limoges, France

⁴Laboratoire Charles Fabry, Institut d'Optique Graduate School, CNRS, Université Paris-Saclay, 91127 Palaiseau, France

⁵Fastlite, 165 rue des Cistes, Pôle entreprise 95, 06600 Antibes, Sophia Antipolis, France

*Corresponding author: david.gauthier@cea.fr

Received 20 September 2018; revised 20 December 2018; accepted 25 December 2018; posted 2 January 2019 (Doc. ID 346402); published 23 January 2019

Light beams carrying orbital angular momentum (OAM) have led to stunning applications in various fields from quantum information to microscopy. We examine OAM from the recently observed high-harmonic generation (HHG) in semiconductor crystals. HHG from solids could be a valuable approach for integrated high-flux short-wavelength coherent light sources. First, we verify the transfer and conservation of the OAM in the strong-field regime of interaction from the generation laser to the harmonics. Secondly, we create OAM beams by etching a spiral zone structure directly at the surface of a zinc oxide crystal. Such diffractive optics act on the generated harmonics and produces focused optical vortices with sub-micrometric size. © 2019 Optical Society of America

<https://doi.org/10.1364/OL.44.000546>

Interaction between matter and photons carrying an orbital angular momentum (OAM) is an intensively studied topic in a large variety of applications [1]. Light beams carrying OAM have a helical wavefront accompanied by a phase singularity in their center [2]. They show an azimuthal phase dependence $\exp(-il\phi)$, where l is the topological charge, and ϕ is the azimuthal coordinate in the plane perpendicular to the beam propagation. Such beams carry an OAM of $l\hbar$ per photon [3]. The most common light beams carrying OAM display Laguerre–Gaussian modes characterized by a donut-shaped intensity profile. There is currently a large theoretical and experimental effort towards the generation of vortex beams with new coherent light sources [4–8]. Among the challenges involving OAM beams, increasing attention is devoted to the fundamental studies in highly nonlinear light-matter interactions. High-harmonic generation (HHG) based on frequency upconversion of a high intensity visible-IR femtosecond laser can generate coherent beams down to few nanometer wavelength and attosecond pulse duration [9]. This light source is now very common, and the underlying mechanisms are well understood

for generation in various media, particularly for atomic gases and plasma targets. Recently, in both media, the transfer and conservation of the OAM from the driving laser to the high harmonics has been verified [10–12].

Reported for the first time in 2011 [13], HHG in solids, namely, bulk semiconductor crystals, has triggered numerous studies focused on the understanding of the phenomenon, proposing different models, and pushing experimental setups [14,15]. The harmonic generation mechanism is different from the dilute matter due to the high density, band structure, and periodicity of the crystal. Moreover, it requires a relatively lower intensity compared to HHG in gases, which makes it well suited for high-repetition-rate (multi-megahertz) nanoscale integrated light sources [16,17]. An all solid-state HHG source would open vast applications in science, but also in industry. An interesting feature specific to the generation of high harmonics in solids is the possibility to tailor the generation medium; the solid can be patterned to control the process of generation and the emission of radiation [18–20]. In comparison to HHG in gases, this offers a significant additional degree of freedom. Moreover, the pulse properties can be shaped directly at the source of the HHG emission by changing the characteristics of the generation medium.

In this Letter, we investigate HHG beams in solids carrying OAM using two approaches as illustrated in Fig. 1. The first case considers the generation by means of a Laguerre–Gaussian laser beam in a bare crystal [Fig. 1(a)]. Similar to HHG in gases, we show that the OAM of the harmonic beams is conserved such that their topological charge l_q is a multiple of the harmonic order q following the relation $l_q = l_l \times q$, with l_l being the topological charge of the driving laser. The second case exploits the solid-state nature of the generation medium to macroscopically control the harmonic beams. By patterning the surface of the crystal, one can design either refractive or diffractive optics. For example, nanostructured surfaces can be designed and arranged spatially in such a way that the harmonics generated in the bulk diffract and build a new mode of the light.

Figure 1(b) shows a diffractive optic, specifically a spiral zone plate (SZP) [21–23], etched at the surface of the crystal. The SZP combines beam focusing, just like an ordinary Fresnel zone plate, together with the OAM mode conversion to produce focused optical vortices carrying an arbitrary topological charge.

The first experiment was performed with an optical parametric chirped pulse amplification laser system emitting at 1550 nm [24]. It provides pulses with a duration of ≈ 80 fs and energy of ≈ 2 μ J at the repetition rate of 125 kHz. The laser beam is converted from a Gaussian to a Laguerre–Gaussian mode, with a unitary topological charge, using a q -plate combined with a quarter-wave plate (QWP) [25]. The linear polarization recommended for HHG in the crystal is induced by the second QWP. The laser is focused by a 5 cm focal length off-axis parabola ($f/15$) in a 500 μ m thick zinc oxide (ZnO) crystal (laser propagation along the optical axis of the crystal) reaching intensities ranging from 0.2 to 1.5 TW/cm². An aspheric lens (numerical aperture NA = 0.63) and a CCD camera are used to image the harmonic beams at the exit of the crystal (see Fig. 2). Figure 2(a) displays the modes at the exit of the crystal for the fundamental and the generated harmonics h3 (517 nm), h5 (310 nm), and h7 (221 nm). The modes show the expected ring-shaped distribution with a radius of about 15 μ m. The thickness of the rings decreases with an increase of the harmonic order, as a consequence of the nonlinear response to the annular fundamental intensity distribution in the sample. The imperfections in the fundamental mode are enhanced for high harmonics and suggest a decrease of the Laguerre–Gaussian mode purity. To determine the topological charge of each mode we performed self-referenced spatial interferometric measurements [26]. The principle is illustrated in Fig. 2(b). A rectangular slit (15 \times 1 μ m size) patterned on the crystal front surface diffracts a part of the harmonic beam generated in the crystal. At a distance of about 100 μ m from the crystal, the diffraction spreads over the harmonic beam (not affected by the slit) that propagates outside the crystal. The slit is small enough with respect to the OAM mode such that the diffracted wavefront does not contain any phase singularity and can be approximated by a spherical wavefront. The interference of the latter with the helical wavefront of the main beam gives a characteristic fork grating pattern, as depicted Fig. 2(c). The topological charge of the mode is deduced directly from the number of bifurcations. Figures 2(d) and 2(e) display the experimental results for the third and fifth harmonics, respectively. In Fig. 2(d), one fringe splits into four fringes which gives a topological charge of 3. For the 5th harmonic, one fringe splits into six fringes, corresponding to a topological charge of 5. These results validate the *multiplicative* rule for the OAM transfer from the generation laser to the harmonics.

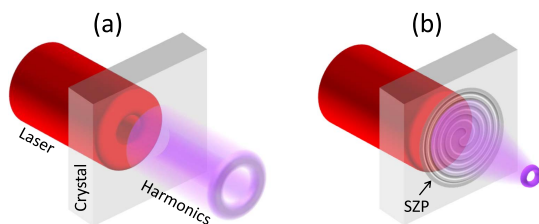


Fig. 1. Sketch of two approaches to create HHG beams carrying an OAM in semiconductor crystals: (a) transfer of the OAM from the driving laser to the harmonics; (b) diffraction of the harmonics by a SZP patterned at the surface of the generation crystal.

They have been obtained with laser peak intensity estimated (in vacuum) to 0.8 TW/cm² which corresponds to a Keldysh parameter near the tunneling limit of strong-field ionization [14]. We conclude that in this highly nonlinear regime, the mechanisms related to HHG in semiconductors do not affect the conservation rules of OAMs for harmonics having photon energies below and above the ZnO bandgap (3.3 eV).

The second experiment was performed with a commercial all-fiber (oscillator and amplifier) femtosecond mode-locked laser emitting at 2100 nm [27]. It provides pulses with a duration of ≈ 85 fs and energy of ≈ 8 nJ at a repetition rate of 18.66 MHz. The laser beam is directly focused at the rear side of the sample by a 2.5 cm focal length off-axis parabola ($f/6$) at a peak intensity of 0.3 TW/cm². The sample is a ZnO crystal with various SZPs etched at its surface using a nano-focused ion beam. The image of the beam diffracted by the SZP is obtained with an objective

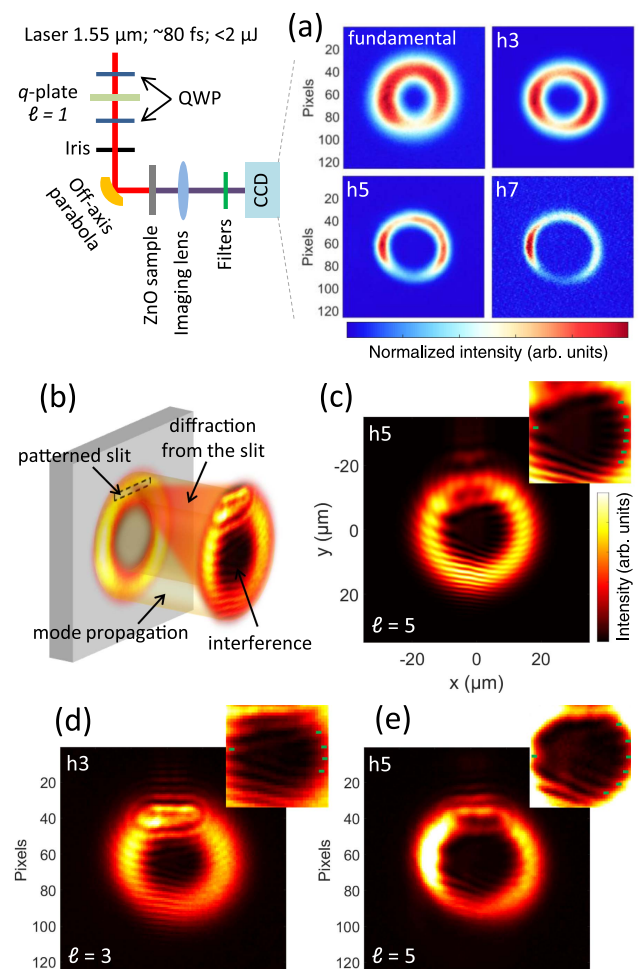


Fig. 2. OAM conservation of HHG in semiconductor crystals. Sketch of the experimental setup; a q -plate between two QWPs imparts an OAM with a topological charge $l = 1$ on the laser. The beam is then focused by a parabolic mirror in a ZnO crystal. The generated harmonics are collected by a lens to image the mode at the exit of the crystal (a). Each harmonic order is selected using bandpass filters. (b) Topological charge of the modes is defined using self-referenced interferences. (c) Simulation result with the experimental parameters of the self-referenced interferogram for harmonic h5. (d) and (e) Experimental results for harmonics h3 and h5. The insets show the detail of the fork grating pattern. The green dots highlight the extremity of each fringe.

lens (numerical aperture $NA = 0.65$) coupled to a CCD camera (see Fig. 3). The desired SZPs are pure phase objects computed numerically by combining the phase profiles of a helical and spherical waves following the relation $P = \exp(-il\phi) \exp(i2\pi\sqrt{R^2 + r^2}/\lambda)$, where λ is the wavelength of the spherical wave of the radius of curvature R (determining the focal length of the SZP), and r is the radial coordinate. All the SZPs have been designed to generate optical vortices with a topological charge $l = 1$. From the computed phase P , two types of etching profile have been defined: the *non-binary* SZP directly corresponds to the wrapping of P within $0 - 2\pi$, and the *binary* SZP is the binarization of the latter at 0 and π . For below bandgap energies, the harmonic radiation is generated in the bulk, and the etching depth d in the crystal can be defined as $d = \lambda P / 2\pi(n - 1)$, where n is the index of refraction of the ZnO material at the relevant wavelength. For the data in Figs. 3 and 4 showing harmonic h5 (420 nm), $n \approx 2.1$.

Figure 3(a) shows the binary SZP and the intensity distribution measured at the focal plane of the first diffraction order located at $6 \mu\text{m}$ from the sample. Although imperfect, the mode shows the characteristic donut-shaped profile. The main cause of the imperfection is the restricted number of illuminated zones (grooves) of the SZP that limit an efficient build-up of the diffracted wave. Indeed, only the central part of the structure is actually illuminated by the $3 \mu\text{m}$ diameter (FWHM) harmonic beam generated in the bulk. Increasing the number of illuminated zones would imply either increasing the size of the laser beam or decreasing the zone periodicity. In the first case, one has to ensure that the laser intensity stays

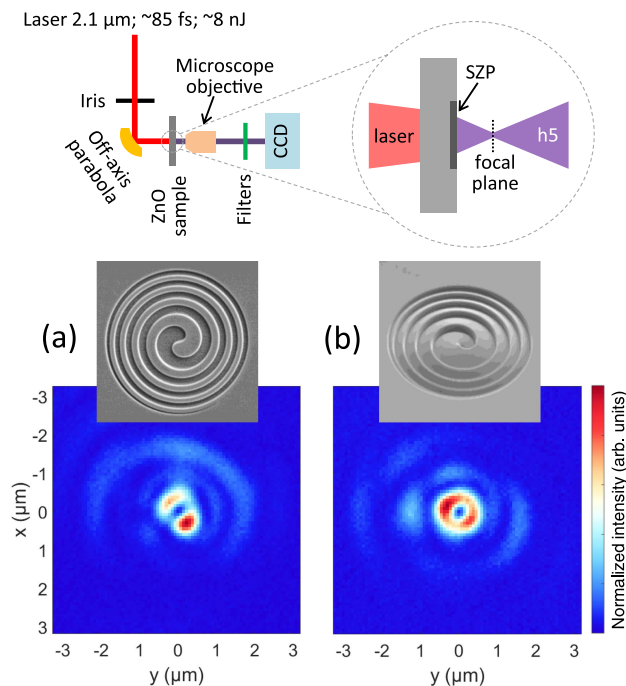


Fig. 3. Spatial beam shaping using a SZP that combines beam focusing and OAM manipulation. Sketch of the experimental setup; a microscope objective is used to image the focal plane of the SZP. Experimental results for (a) a binary and (b) a non-binary SZP etched at the surface of a ZnO crystal. Scanning electron microscope images of each diffractive structure (diameter = $10 \mu\text{m}$); (a) normal incidence and (b) perspective view and resulting intensity distributions at the focal plane for harmonic h5.

large enough for HHG, while the latter would result in decreasing the focal length of the SZP, leading to a tighter focus. However, the design of the SZP was a tradeoff between the laser energy available and the image resolution allowed with our objective lens. Another source of imperfection is coming from the fabrication defaults; the etched depth is about 205 nm , inducing a phase step about 7% larger than requested. Moreover, the gallium ions contamination and the ruggedness induced by the etching process with the focused ion beam might have modified the transmittance of the optics. The last source of imperfection is coming from residual aberrations in the generating laser and misalignments. Figure 3(b) shows the design of the non-binary version of the previous SZP and the resulting mode. This non-binary SZP is not rigorously a diffractive optics, because it is based on the principle of a Fresnel lens. For this reason, it does not suffer from the problem of the limited number of illuminated zones, and the donut-shaped profile, with a radius of 380 nm , is better defined. However, due to small errors in the etching depth, it also shows a diffractive behavior with presence of diffraction orders, which explains the parasitic signal surrounding the main mode similar to the binary SZP.

Figure 4 displays the results obtained with a binary and a non-binary off-axis SZP. The computed pattern of off-axis SZPs is achieved by a transversal shift between the centers of the spherical and helical waves. The shift is of $6 \mu\text{m}$ for a radius of curvature of $10 \mu\text{m}$. Consequently, the first order of diffraction is tilted from the main optical axis by an angle of 31 deg (see sketch in Fig. 4). Figure 4(a) shows the etched binary off-axis SZP and the intensity distribution in the focal plane of the first order of diffraction. Compared to the previous binary on-axis SZP, the mode quality is significantly improved, because the off-axis design leads to a larger density of zones illuminated in the center of the optics. Off-axis SZPs have other advantages: the diffraction orders are spatially separated, so there is no parasitic signal surrounding the main mode; for properly chosen parameters, beams from different harmonic orders can be split as well. The latter is particularly interesting for fully integrated and compact sources of optical vortices. Notice that OAM beams from adjacent harmonic orders are generated from the same SZP and share the same topological charge. However, the efficiency is rather low, because the etching is not optimized for a broad wavelength range. For the non-binary off-axis SZP [Fig. 4(b)], the blazed grating profile optimizes the flux diffracted in the first order, which contains 76% of the detected photons, when this number is only of 9% for the binary case. Finally, we performed interferometric measurements in order to verify the topological charge of the beam shaped by the SZP. In this case, the reference beam is provided by the zero order that spreads over the first order by means of a knife edge, as depicted in Fig. 4(c). We find a fork grating pattern with one bifurcation, which confirms the unitary topological charge of the OAM beam.

In conclusion, we reviewed and demonstrated two different methods to generate high-harmonic photons carrying an OAM from a semiconductor crystal. First, the conservation rule of OAM beam is verified for below and above bandgap harmonics in the strong-field regime of interaction. Then, we show that the integration of a SZP to the generation medium can produce focused optical vortices with sub-micrometric size. Structured surfaces have been established for below bandgap harmonics. Shaping the crystal surface can change the intensity distribution of the driving laser with the appearance of local field confinements that modify the properties of the generated harmonics

and possibly enhance the emission [20]. This is particularly relevant for above bandgap harmonics that are not efficiently generated in the bulk crystal due to absorption. Therefore, structured surfaces for above bandgap harmonic generation have to consider together the action on the generating laser and on the harmonics. The resulting 2-in-1 design can combine enhancement and spatial shaping of the harmonic emission. Pushing the idea of integrated devices can also merge with other nano-technologies such as nano-plasmonics [28]. For example, the generating medium could be arranged as a metamaterial. Planar devices based on metasurfaces enable various manipulations beyond the simple light diffraction, including the control of the polarization (spin) and orbital angular momentum of light [29]. HHG in solids would take advantage of the numerous possibilities offered by the metasurfaces for the control of the light.

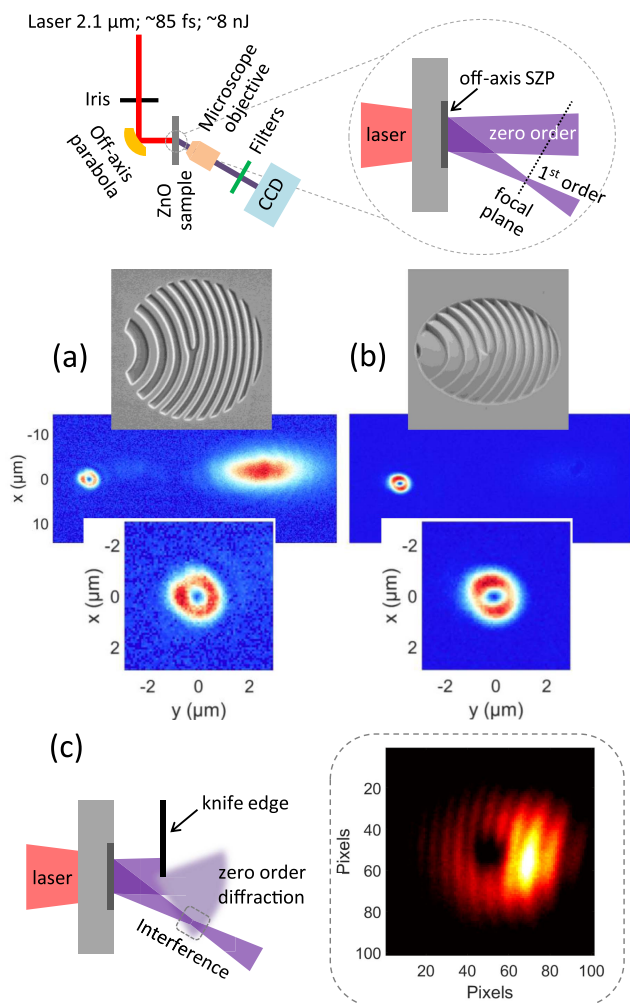


Fig. 4. Off-axis SZP. Sketch of the experimental setup; the microscope objective is tilted by an angle of 31 deg to be aligned along the optical axis of the first diffraction order. Experimental results for (a) a binary and (b) a non-binary off-axis SZP. Scanning electron microscope images of each diffractive structure (diameter = 10 μm) with the resulting intensity distributions at the focal plane of the first order, showing the zeroth and first orders of diffraction. The first order is magnified in the inset. The zeroth order shows strong aberrations due to the coupling with the microscope objective. (c) Sketch of the procedure used to measure the topological charge by the interference of the first order with the zeroth order and the resulting fork grating.

Funding. Agence Nationale de la Recherche (ANR) (2014 IPEX, 2016 BISCOT, 2017 PACHA, ANR-10-LABX-0039-PALM); French ASTRE program (NanoLight grant); Direction Générale de l'Armement (DGA) (2017 SWIM LASER grant); Laserlab-Europe (EU-H2020 654148).

REFERENCES

- J. P. Torres and L. Torner, *Twisted Photons* (Wiley, 2011).
- M. Padgett, J. Courtial, and L. Allen, *Phys. Today* **57**(5), 35 (2004).
- L. Allen, M. W. Beijersbergen, R. J. C. Spreeuw, and J. P. Woerdman, *Phys. Rev. A* **45**, 8185 (1992).
- C. Hernandez-Garcia, J. Vieira, T. J. Mendonça, L. Rego, J. San Roman, L. Plaja, P. R. Ribic, D. Gauthier, and A. Picon, *Photonics* **4**, 28 (2017).
- D. Gauthier, P. R. Ribic, G. Adhikary, A. Camper, C. Chappuis, R. Cucini, L. F. DiMauro, G. Dovillaire, F. Frassetto, R. Géneaux, P. Miotti, L. Poletto, B. Ressel, C. Spezzani, M. Stupar, T. Ruchon, and G. De Ninno, *Nat. Commun.* **8**, 14971 (2017).
- P. R. Ribic, B. Rösner, D. Gauthier, E. Allaria, F. Döring, L. Foglia, L. Giannessi, N. Mahne, M. Manfreda, C. Masciovecchio, R. Mincigrucci, N. Mirian, E. Principi, E. Roussel, A. Simoncig, S. Spampinati, C. David, and G. De Ninno, *Phys. Rev. X* **7**, 031036 (2017).
- J. Vieira, R. M. G. M. Trines, E. P. Alves, R. A. Fonseca, J. T. Mendonça, R. Bingham, P. Norreys, and L. O. Silva, *Phys. Rev. Lett.* **117**, 265001 (2016).
- V. Petrillo, G. Dattoli, I. Drebot, and F. Nguyenal, *Phys. Rev. Lett.* **117**, 123903 (2016).
- T. Brabec and F. Krausz, *Rev. Mod. Phys.* **72**, 545 (2000).
- G. Gariepy, J. Leach, K. T. Kim, T. J. Hammond, E. Frumker, R. W. Boyd, and P. B. Corkum, *Phys. Rev. Lett.* **113**, 153901 (2014).
- R. Geneaux, A. Camper, T. Auguste, O. Gobert, J. Caillat, R. Taeib, and T. Ruchon, *Nat. Commun.* **7**, 12583 (2016).
- A. Denoëud, L. Chopineau, A. Leblanc, and F. Quéré, *Phys. Rev. Lett.* **118**, 033902 (2017).
- S. Ghimire, A. D. DiChiara, E. Sistrunk, P. Agostini, L. F. DiMauro, and D. A. Reis, *Nat. Phys.* **7**, 138 (2011).
- S. Ghimire, G. Ndbashimiye, A. D. DiChiara, E. Sistrunk, M. I. Stockman, P. Agostini, L. F. DiMauro, and D. A. Reis, *J. Phys. B* **47**, 204030 (2014).
- G. Vampa and T. Brabec, *J. Phys. B* **50**, 083001 (2017).
- K. F. Lee, X. Ding, T. J. Hammond, M. E. Fermann, G. Vampa, and P. B. Corkum, *Opt. Lett.* **42**, 1113 (2017).
- T. T. Luu, V. Scagnoli, S. Saha, L. J. Heyderman, and H. J. Wörner, *Opt. Lett.* **43**, 1790 (2018).
- S. Han, H. Kim, Y. W. Kim, Y.-J. Kim, S. Kim, I.-Y. Park, and S.-W. Kim, *Nat. Commun.* **7**, 13105 (2016).
- H. Kim, S. Han, Y. W. Kim, S. Kim, and S.-W. Kim, *ACS Photonics* **4**, 1627 (2017).
- M. Sivilis, M. Taucer, G. Vampa, K. Johnston, A. Staudte, A. Y. Naumov, D. M. Villeneuve, C. Ropers, and P. B. Corkum, *Science* **357**, 303 (2017).
- N. R. Heckenberg, R. McDuff, C. P. Smith, and A. G. White, *Opt. Lett.* **17**, 221 (1992).
- V. Y. Bazhenov, M. S. Soskin, and M. V. Vasnetsov, *J. Mod. Opt.* **39**, 985 (1992).
- A. Sakdinawat and Y. Liu, *Opt. Lett.* **32**, 2635 (2007).
- P. Rigaud, A. Van de Walle, M. Hanna, N. Forget, F. Guichard, Y. Zaouter, K. Guesmi, F. Druon, and P. Georges, *Opt. Express* **24**, 26494 (2016).
- L. Marrucci, C. Manzo, and D. Paparo, *Phys. Rev. Lett.* **96**, 163905 (2006).
- D. G. Lee, J. J. Park, J. H. Sung, and C. H. Nam, *Opt. Lett.* **28**, 480 (2003).
- <https://www.novae-laser.com/brevity/>.
- G. Vampa, B. G. Ghamsari, S. S. Mousavi, T. J. Hammond, A. Olivieri, E. Lisicka-Skrek, A. Y. Naumov, D. M. Villeneuve, A. Staudte, P. Berini, and P. B. Corkum, *Nat. Phys.* **13**, 659 (2017).
- N. Yu and F. Capasso, *Nat. Mater.* **13**, 139 (2014).

Titre : Source paramétrique optique de quelques cycles optiques dans le moyen infrarouge stabilisée en CEP à haut taux de répétition

Mots clés : Amplification paramétrique, stabilisation de la CEP, compression non-linéaire, cellule multi-passage

Résumé : La génération d'impulsions de quelques cycles optiques stabilisées en CEP dans le moyen infrarouge utilisant la technique d'amplification paramétrique optique à fort taux de répétition est d'un grand intérêt pour diverses études de dynamiques ultra-brèves. Les travaux de cette thèse sont directement inscrits dans ce cadre. Nous décrivons un système émettant des impulsions dont le spectre est centré à $2.1 \mu\text{m}$ avec une durée de 19.5 fs et une énergie de $31 \mu\text{J}$ opérant à 10 kHz avec une stabilité RMS de 0.54% . Ce système se distingue de l'état de l'art par la mise en œuvre d'une technique de différence de fréquence en ligne permettant d'obtenir une stabilité de la CEP tir-à-tir de 107 mrad pendant quatre heures.

De plus cette thèse a permis le développement d'un dispositif émettant des impulsions de quelques cycles optiques à $1.55 \mu\text{m}$ opérant à haut taux de répétition (125 kHz). Ce système est le résultat de l'assemblage d'un amplificateur paramétrique optique et d'un système de compression non-linéaire dans une cellule multi-passage. La propagation non linéaire périodique dans la cellule en régime de dispersion anormale permet une compression solitonique, tout en moyennant les effets spatiaux de la nonlinéarité sur le faisceau. Nous démontrons ainsi l'autocompression d'impulsions initiales de $19 \mu\text{J}$ 63 fs vers des impulsions en sortie de $14 \mu\text{J}$ 22 fs .

Title: High-repetition rate CEP-stable few-cycle OPCPA sources in the short wave infrared/mid-infrared

Keywords : Carrier envelope phase, few-cycle pulses, optical parametric amplification, Multipass cell.

Abstract : The generation of carrier envelope phase (CEP) stable few-cycle pulses in the SWIR/Mid-IR using optical parametric chirped pulse amplification (OPCPA) at high repetition rate is of great interest for several applications in ultrafast dynamics. During this thesis the work was primarily focused on the development of OPCPA sources for attosecond science. We present an OPCPA operating at $2.1 \mu\text{m}$ delivering 19.5 fs pulse duration with an energy of $31 \mu\text{J}$ at 10 kHz with a RMS energy stability of 0.54% . An original architecture using an all-inline difference frequency generation stage allows performances beyond the state of the art in terms of CEP stability. We report RMS CEP fluctuations of 107 mrad RMS measured shot-to-shot over four hours.

On another hand, the development of a high repetition rate (125 kHz) OPCPA coupled with an innovative nonlinear compression scheme is described. The OPCPA provides pulses centered at $1.55 \mu\text{m}$, with a pulse duration of 63 fs with an energy of $19 \mu\text{J}$ after compression. Then a nonlinear compression stage based on a soliton dynamics in a multipass cell is implemented. The periodic propagation inside the cell allows to retain the temporal nonlinear effects, while the spatial nonlinear effects are washed out by the distributed nature of the nonlinearity over a large number of passes. We report the self-compression of 63 fs pulse at $1.5 \mu\text{m}$ down to 22 fs with an energy of $14 \mu\text{J}$.



